

ARS

JOURNAL

A PUBLICATION OF THE AMERICAN ROCKET SOCIETY

VOLUME 31 NUMBER 3

MARCH 1961

LOS ANGELES PUBLIC LIBRARY

APR 18 1961

BIND

CONTRIBUTED ARTICLES

Anomalies of the Geomagnetic Retardation of the Spin of Satellite Vanguard I (1958 Beta)	P. R. Arendt	286
Eddy Current Torque Compensation in a Spin Stabilized Earth Satellite	L. H. Grasshoff	290
A Capacitance Densitometer for Determination of the Transient Densities of Cryogenic Liquids	A. Harry Sharbaugh and Maxwell W. Lippitt Jr.	294
Analysis of Partial Admission Axial Impulse Turbines	Hans D. Linhardt and David H. Silvern	297
Stresses Owing to Internal Pressure in Solid Propellant Rocket Grains	Howard B. Wilson Jr.	309
Generalized Heat Transfer Formulas and Graphs for Nose Cone Re-Entry into the Atmosphere	R. W. Detra and H. Hidalgo	318
Voltage-Current Characteristics of Tungsten Electrodes in Cesium Vapor	L. H. Stauffer	322
Solar Collectors for Use in Thermionic Power Supply Systems in Space	D. Wing and K. E. Cameron	327
Linearized Magnetohydrodynamic Channel Flow With Axial Symmetry	F. Edward Ehlers	334
Optimum Staging Technique to Maximize Payload Total Energy	Edgar R. Cobb	342
Characteristic Velocity Requirements for Impulsive Thrust Transfers Between Non Co-Planar Circular Orbits	L. Rider	346
Probability of Satellite Interception by an Air Launched Pre-Guided Missile	Edgar M. Jacobs, George W. Morgenthaler and Robert A. Sebastian	352
Alignment of an Inertial Autonavigator	L. R. McMurray	356
Effect of Geometrical Libration on the Damped Motion of an Earth Satellite	L. N. Rowell and M. C. Smith	361
Variables That Are Determinate for Any Orbit	Robert R. Newton	364

TECHNICAL NOTES

Heat Release Rate, Temperature and Pressure in Solid Rocket Instability	F. T. McClure, R. W. Hart and J. F. Bird	367
Advanced Uncooled Nozzle for Solid Propellant Rocket	Chun-Ching Ma	368
Stagnation Point Radiative Transfer	H. Kanno and S. L. Strach	370
Calibration of Hypersonic High Temperature Wind Tunnels	S. E. Neale and R. W. Rutowski	372
Calculation of C^* for Highly Dissociated Propellant Combustion Products	L. J. Gordon	374
Entrance Effects in the High Temperature Heat Transfer From Dissociated Gases	P. Lee and S. Steinberg	375
Comparison of Some Approximate Methods for Calculating Re-Entry Ablation of a Subliming Material	Sheldon Blocher and George W. Sutton	433
Minimum Time Ballistic Interplanetary Trajectories	Vernon A. Lee and Dwight E. Flanagan	436
Approximate Velocity, Position and Time Relationship for Ballistic Re-Entry	S. P. Miller	437
Scattering Effects on the Moon's Surface	G. K. Wehner	438
Celestial Rate Sensing	Hans K. Karrenberg and Robert E. Robinson	440
Graphical Method for Prediction of Time in Sunlight for a Circular Orbit	G. B. Patterson	441
Aerodynamic Influences on Satellite Librations	D. M. Schuette	442
Radiated Power From a 3-In. Sphere of High Temperature Air at Pressures to 50 Atm	Domenico Ragusa	445
Effect of Two-Dimensional Heat Transfer on Wall Temperatures in a Tubular Thrust Chamber	John P. Sellers Jr.	446
Hydraulic Analog Investigation of a Ping Nozzle	R. H. Page and A. P. Meyer	447
Divergence From Equilibrium Glide Path at Supersatellite Velocities	Raymond North and Jason L. Speyer	448
Multistage Rocket Optimization	Robert V. Ragan and Paul L. Patterson	450
Effect of Scale Size on a Rocket Engine With Suddenly Frozen Nozzle Flow	Ronald Watson	452

DEPARTMENTS

Book Notes	453
New Patents	455
Technical Literature Digest	456

RUSSIAN SUPPLEMENT . . . 377-432

ENERGY CONVERSION FOR SPACE POWER
VOLUME 2, ARS PROGRESS SERIES . . . 293

The first six years of Space Technology Leadership

Since 1954, when the Air Force ballistic missile program was accorded top national priority, Space Technology Laboratories has been engaged in virtually every major phase of research, development, testing and technical management of missile and space systems • STL's contributions have hastened the day of operational capability for Air Force ballistic missiles, and have been applied as well in satellite projects and space probes • Today, as STL's activities expand in significance and scope, STL offers exceptional opportunity to the outstanding scientist and engineer whose talents and training will add to, and benefit from, the accumulated experience that has enabled STL to conceive and accomplish major advances in the state-of-the-art • STL's creative flexibility, anticipating and responding to the demands of space progress, ranges in application from abstract analysis to complex hardware fabrication for military and civilian space projects • STL invites scientists and engineers to consider career opportunities in the atmosphere of Space Technology Leadership. Resume and inquiries will receive meticulous attention.

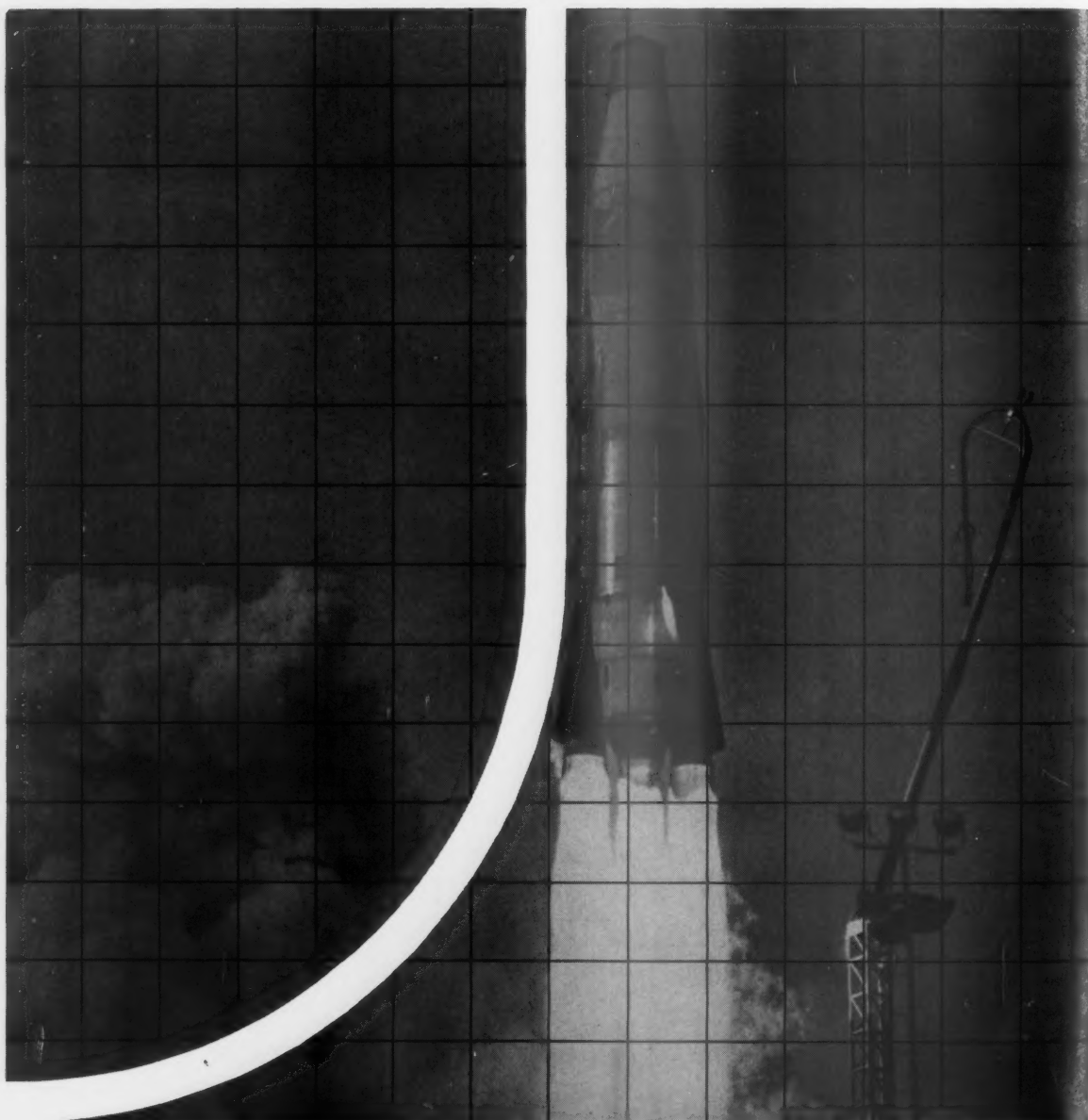
SPACE TECHNOLOGY LABORATORIES, INC. P.O. BOX 95005C LOS ANGELES 45, CALIFORNIA

a subsidiary of Thompson Ramo Wooldridge Inc.

El Segundo • Santa Maria • Edwards Rocket Base • Canoga Park



Cape Canaveral • Manchester, England • Singapore • Hawaii



ARS JOURNAL

A PUBLICATION OF THE AMERICAN ROCKET SOCIETY

EDITOR Martin Summerfield
ASSOCIATE TECHNICAL EDITOR Irvin Glassman
MANAGING EDITOR Margaret Sherman
STAFF EDITOR Barbara Nowak
ART EDITOR John Culin

ASSOCIATE EDITORS

Igor Jurkevich, *G. E. Space Sciences Laboratory, Russian Supplement*;
 George F. McLaughlin, *Patents*; Charles J. Mundo Jr., *Raytheon Co., Guidance*;
 Bernard H. Palewosky, *Aeronautical Research Associates of Princeton, Flight Mechanics*; M. H. Smith, *Princeton University, Technical Literature Digest*

ASSISTANT EDITORS

Eleanor Rosman, Carol Rubenstein, Estelle Viertel

DIRECTOR OF MARKETING

Owen A. Kean

ADVERTISING PRODUCTION MANAGER

Walter Brunke

ADVERTISING REPRESENTATIVES

New York
 D. C. Emery and Associates
 400 Madison Ave., New York, N. Y.
 Telephone: Plaza 9-7460

Chicago
 Jim Summers and Associates
 35 E. Wacker Dr., Chicago, Ill.
 Telephone: Andover 3-1154

Atlanta
 Joe H. Howell
 1776 Peachtree Bldg., Atlanta 9, Ga.
 Telephone: 873-2136

Los Angeles
 James C. Galloway and Co.
 6535 Wilshire Blvd., Los Angeles, Calif.
 Telephone: Olive 3-3223

Detroit
 R. F. Pickrell and Associates
 318 Stephenson Bldg., Detroit, Mich.
 Telephone: Trinity 1-0790

London
 B. C. Nichols
 151 Fleet St.
 London E. C. 4, England

American Rocket Society

500 Fifth Avenue, New York 36, N. Y.

Founded 1930

OFFICERS

President
 Vice-President
 Executive Secretary
 Treasurer
 General Counsel
 Director of Publications

Harold W. Ritchey
 William H. Pickering
 James J. Harford
 Robert M. Lawrence
 Andrew G. Haley
 Irwin Hersey

BOARD OF DIRECTORS

Terms expiring on dates indicated

Ali B. Campbell 1962
 Richard B. Canright 1962
 William J. Cecka Jr. 1963
 J. R. Dempsey 1961
 Herbert Friedman 1962
 George Gerard 1961
 Robert A. Gross 1962

Samuel Herrick 1963
 Arthur Kantrowitz 1963
 A. K. Oppenheim 1961
 Simon Ramo 1963
 David G. Simons 1961
 John L. Sloop 1961
 Martin Summerfield 1962

A. M. Zarem 1963

TECHNICAL COMMITTEE CHAIRMEN

William H. Avery, Ramjets
 R. M. L. Baker Jr., Astrodynamics
 G. Daniel Brewer, Solid Propellant Rockets
 Robert W. Bussard, Nuclear Propulsion
 Bernhardt L. Dorman, Test, Operations and Support
 William M. Duke, Missiles and Space Vehicles
 William H. Dorrance, Hypersonics
 James S. Farrior, Guidance and Control
 Herbert Friedman, Physics of the Atmosphere and Space
 George Gerard, Structures and Materials

Martin Goldsmith, Liquid Rockets
 Andrew G. Haley, Space Law and Sociology
 John H. Huth, Power Systems
 Eugene B. Konecni, Human Factors and Bioastronautics
 Frank W. Lehan, Communications and Instrumentation
 Peter L. Nichols Jr., Propellants and Combustion
 Milton M. Slawsky, Magnetohydrodynamics
 Herman E. Sheets, Underwater Propulsion
 Ernst Stuhlinger, Electric Propulsion

Scope of ARS JOURNAL

This Journal is devoted to the advancement of astronautics through the dissemination of original papers disclosing new scientific knowledge and basic applications of such knowledge. The sciences of astronautics are understood here to embrace selected aspects of jet and rocket propulsion, spacecraft mechanics, high speed aerodynamics, flight guidance, space communications, atmospheric and outer space physics, materials and structures, human engineering, overall system analysis and possibly certain other scientific areas. The selection of papers to be printed will be governed by the pertinence of the topic to the field of astronautics, by the current or probable future significance of the research, and by the importance of distributing the information to the members of the Society and to the profession at large.

Information for Authors

Manuscripts must be as brief as the proper presentation of the ideas will allow. Exclusion of dispensable material and conciseness of expression will influence the Editors' acceptance of a manuscript. In terms of standard-size double-spaced typed pages, a typical maximum length is 22 pages of text (including equations), 1 page of references, 1 page of abstract and 12 illustrations. Fewer illustrations permit more text, and vice versa. Greater length will be acceptable only in exceptional cases.

Short manuscripts, not more than one quarter of the maximum length stated for full articles, may qualify for publication as Technical Notes or Technical Comments. They may be devoted to new developments requiring prompt disclosure or to comments on previously published papers. Such manuscripts are published within a few months of the date of receipt.

Sponsored manuscripts are published occasionally as an ARS service to the industry. A manuscript that does not qualify for publication, according to the above-stated requirements as to subject, scope or length, but which nevertheless deserves widespread distribution among jet propulsion engineers, may be printed as an extra part of the Journal or as a special supplement, if the author or his sponsor will reimburse the Society for actual publication costs. Estimates are available on request. Acknowledgment of such financial sponsorship appears as a footnote on the first page of the article. Publication is prompt since such papers are not in the ordinary backlog.

Manuscripts must be double spaced on one side of paper only with wide margins to allow for instructions to printer. Include a 100 to 200 word abstract. State the authors' positions and affiliations in a footnote on the first page. Equations and symbols may be handwritten or typewritten; clarity for the printer is essential. Greek letters and unusual symbols should be identified in the margin. If handwritten, distinguish between capital and lower case letters, and indicate subscripts and superscripts. References are to be grouped at the end of the manuscript and are to be given as follows. For journal articles: Authors first, then title, journal, volume, year, page numbers; for books: Authors first, then title, publisher, city, edition and page or chapter numbers. Line drawings must be clear and sharp to make clear engravings. Use black ink on white paper or tracing cloth. Lettering should be large enough to be legible after reduction. Photographs should be glossy prints, not matte or semi-matte. Each illustration must have a legend; legends should be listed in order on a separate sheet.

Manuscripts must be accompanied by written assurance as to security clearance in the event the subject matter lies in a classified area or if the paper originates under government sponsorship. Full responsibility rests with the author.

Preprints of papers presented at ARS meetings are automatically considered for publication.

Submit manuscripts in duplicate (original plus first carbon, with two sets of illustrations) to the Managing Editor, ARS JOURNAL, 500 Fifth Avenue, New York 36, N. Y.

ARS JOURNAL is published monthly by the American Rocket Society, Inc. and the American Interplanetary Society at 20th & Northampton Sts., Easton, Pa., U. S. A. Editorial offices: 500 Fifth Ave., New York 36, N. Y. Price: \$18.00 per year, \$3.00 per single copy. Second-class postage paid at Easton, Pa., with additional entry at New York, N. Y. This publication is authorized to be mailed at the special rates of postage prescribed by Section 132.122. Notice of change of address should be sent to the Secretary, ARS, at least 30 days prior to publication. Opinions expressed herein are the authors' and do not necessarily reflect the views of the Editors or of the Society. © Copyright 1961 by the American Rocket Society, Inc.

PROGRESS IN ASTRONAUTICS AND ROCKETRY

Series Editor
MARTIN SUMMERFIELD
Princeton University

SPONSORED BY THE AMERICAN ROCKET SOCIETY

New in March 1961:

Volume 3 Energy Conversion for Space Power

Edited by
NATHAN W. SNYDER
Institute of Defense Analyses,
Washington, D. C.

*A Selection of Technical Papers based mainly on a Symposium of the American Rocket Society
held at Santa Monica, California, September 27-30, 1960
March 1961, 779 pp., illus., \$7.25*

Forthcoming volumes:

Volume 4 Space Power Systems

Edited by
NATHAN W. SNYDER

*A Selection of Technical Papers based mainly on a Symposium of the American Rocket Society
held at Santa Monica, California, September 27-30, 1960*

Volume 5 Electrostatic Propulsion

Edited by
DAVID M. LANGMUIR
ERNST STUHLINGER
J. M. SELLEN, JR.

*A Selection of Technical Papers based mainly on a Symposium of the American Rocket Society
held at Monterey, California, November 3, 4, 1960*

Previously published:

Volume 1 Solid Propellant Rocket Research

Edited by
MARTIN SUMMERFIELD

*A Selection of Technical Papers based mainly on a Symposium of the American Rocket Society
held at Princeton University, Princeton, New Jersey, January 28, 29, 1960
November 1960, 692 pp., illus., \$6.50*

Volume 2 Liquid Rockets and Propellants

Edited by
LOREN E. BOLLINGER
MARTIN GOLDSMITH
ALEXIS W. LEMMON, JR.

*A Selection of Technical Papers based mainly on a Symposium of the American Rocket Society
held at The Ohio State University, Columbus, Ohio, July 18, 19, 1960
December 1960, 682 pp., illus., \$6.50.*



ACADEMIC PRESS

New York and London

111 Fifth Avenue, New York 3, New York

17 Old Queen Street, London, S.W. 1

German Agency: Minerva, G.m.b.H., Holbeinstrasse 25-27, Frankfurt am Main
Indian Agency: Asia Publishing House, Nicol Road, Ballard Estate, Bombay 1

Energy Conversion for Space Power

Edited by
NATHAN W. SNYDER
Institute for Defense
Analyses, Washington, D.C.

The American Rocket Society is pleased to announce the publication of this third volume of *Progress in Astronautics and Rocketry*. Most of the papers in the volume were presented at the ARS Space Power Systems Conference held at Santa Monica, California, September 27-30, 1960. The remaining papers were invited by the editor in order to extend the coverage of various subjects.

The remaining papers presented in Santa Monica, together with others invited by the editor, will appear in Volume 4, *Space Power Systems*, also edited by Nathan W. Snyder. The papers will cover solar systems, nuclear systems, chemical systems, and power requirements. Complete contents will appear in *ARS Journal* at the time of publication.

Thermoelectricity

- A. C. BEER, Physics of Thermoelectricity
- R. C. MILLER and R. W. URE, JR., Thermoelectric Generator Materials
- S. W. KURNICK, R. L. FITZPATRICK, and J. F. LEAVY, High-Temperature Semiconductors for Thermoelectric Conversion
- S. E. MAYER and I. M. RITCHIE, The Use of High Temperature Thermoelectric Materials (Silicides) for Power Generation in Space
- J. C. DANKO, G. R. KILP, and P. V. MITCHELL, Irradiation Effects on Thermoelectric Materials
- DOUGLAS L. KERR, Thermoelectric Elements in Space Power Systems
- EDWARD E. GARDNER and EDWIN L. WOISARD, Thermoelectric Materials for Space Cooling

Thermionics

- WAYNE B. NOTTINGHAM, Review of the Physics of Thermionics
- H. W. LEWIS, Plasma Thermionics
- V. C. WILSON, Cesium Converter Studies
- N. S. RASOR, Parametric Optimization of the Emission-Limited Thermionic Converter
- KARL G. HERNQVIST, Experimental Research on Plasma Thermionic Energy Converters
- HOWARD L. STEELE, Theory of the Cesium Plasma Energy Converter with a Tungsten Cathode
- MELVIN G. BOWMAN, Chemistry of Fuel Element Cathode Materials
- R. C. HOWARD, L. YANG, H. L. GARVIN, and F. D. CARPENTER, A Nuclear-Thermionic Fuel Element Test

Photovoltaic Cells

- J. J. LOFERSKI, The Photovoltaic Effect and Solar Energy Conversion
- MARTIN WOLF, Advances in Silicon Solar Cell Development
- JAMES F. ELLIOTT, V. F. MEIKLEHAM, and C. L. KOLBE, Large Area Solar Cells
- A. E. MIDDLETON, D. A. GORSKI, and F. A. SHIRLAND, Evaporated CdS Film Photovoltaic Cells for Solar Energy Conversion
- L. E. STONE, J. E. POWDERLY, and W. E. MEDCALF, Integrally Composed Variable Energy Gap Photovoltaic Cells
- HANS J. QUEISSER and WILLIAM SHOCKLEY, Some Theoretical Aspects of the Physics of Solar Cells
- R. G. DOWNING, Electron Bombardment of Silicon Solar Cells
- J. M. DENNEY, Radiation Damage in Satellite Solar Cell Power Systems
- J. M. DENNEY, R. G. DOWNING, and A. GRENALL, High Energy Proton Radiation Damage
- ALFRED THELEN, The Use of Vacuum Deposited Coatings to Improve the Conversion Efficiency of Silicon Solar Cells in Space

Electrochemical Cells

- JAMES KING, JR., FRANK A. LUDWIG, and J. J. ROWLETTE, General Evaluation of Chemicals for Regenerative Fuel Cells
- R. E. HENDERSON, B. AGRUSS, and W. G. CAPLE, Resume of Thermally Regenerative Fuel Cell Systems
- FRANK A. LUDWIG, Regenerative Hydrogen-Oxygen Fuel Cell
- WALTER JUDA, CHARLES E. TIRRELL, and ROBERT M. LURIE, Fuel Cells with Ion Exchange Membranes
- J. S. BONE and M. D. READ, Regenerative Ion Exchange Membrane Fuel Cell Developments
- GERALD E. STARKEY, Fuel Cells for Astronautic Application
- IRWIN M. SCHULMAN, Secondary Batteries for Energy Storage in Space
- U. B. THOMAS, Battery Considerations for a Communications Satellite

Dynamic Engines

- ROBERT O. BULLOCK, Vapor Turbine for Space Power
- M. D. PARKER and C. L. SMITH, Stirling Engine Development for Space Power
- HOMER J. WOOD and NORMAND E. MORGAN, Comparative Rating of Positive-Displacement Engines and Turbines for Cryogenic Power Systems
- LLOYD M. HEDGEPEETH, Zero Gravity Boiling and Condensing
- JOHN B. ROES, An Electro-mechanical Energy Storage System for Space Application

Magnetohydrodynamics

- G. W. SUTTON and L. STEG, The Prospects for MHD Power Generation
- J. H. HUTH, Aspects of Magnetohydrodynamic (MHD) Generators for Space
- STEWART WAY, Experiments Relating to Generation of Power by Magnetohydrodynamics
- R. J. COERDT, W. C. DAVIS, R. T. CRAIG, and J. E. McCUNE, A Vortex MHD Power Generator
- JAMES E. McCUNE and COLEMAN DUP. DONALDSON, On the Magnetogasdynamics of Compressible Vortices

Electrostatic Generators

- A. S. DENHOLM, J. G. TRUMP, and A. J. GALE, High Voltage Generation in Space: The Parametric Electrostatic Machine
- DOMINIQUE GIGNOUX, Electrostatic Generators in Space Power Systems

NOTE: Orders and requests for information should be addressed to ACADEMIC PRESS, rather than to the ARS. Complete addresses are given on the facing page.

CREATIVE ELECTRONICS BY RCA



KEEPING BMEWS ON THE AIR

RCA Checkout and Automatic Monitoring Equipment Guards BMEWS Reliability Around the Clock

The incredible complexity of the BMEWS network and its vital mission in continental defense demand the ultimate in system reliability. Through unique and highly advanced developments by RCA this standard is being achieved.

The RCA Checkout Equipment installed at BMEWS sites performs a dual function—it generates and inserts realistic simulated target problems for on line exercising of the entire system. These integrated tests

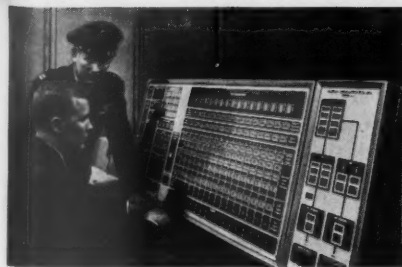
are designed to test the BMEWS early warning capability to its fullest extent. Automatic monitoring detects degradation prior to failure and isolates marginal conditions or malfunctions enabling rapid corrective maintenance.

Around-the-clock operation of this RCA equipment enables BMEWS to meet its over-all operability goal with negligible downtime, thus keeping BMEWS on the air!



The play equ

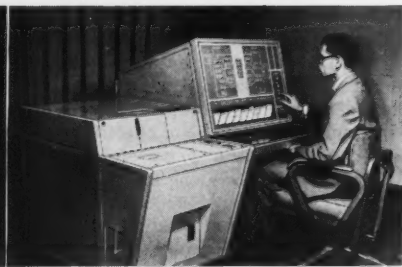
RCA enhance for use current comm RCA C Defens town,



The Central Automatic Monitoring Console displays the status of the entire site, and displays equipment degradation prior to failure.



The Checkout Data Processor generates simulated missile attacks and evaluates the BMEWS response to the simulation.



The Automatic Monitoring Console displays degradation and the location of degraded equipment.

RCA Checkout and Automatic Monitoring (CAM) Equipment has greatly enhanced the reliability of complex ground environment systems. Adaptable for use in systems already completed, and as an integration tool for systems currently being implemented, CAM equipment is available for all complex commercial, military, and government systems. For a description of the RCA Checkout and Automatic Monitoring Equipment, write to: RCA Major Defense Systems, Defense Electronic Products, CAM 127-204, Moorestown, New Jersey.



The Most Trusted Name
in Electronics

RADIO CORPORATION OF AMERICA

Anomalies of the Geomagnetic Retardation of the Spin of Satellite Vanguard I (1958 Beta)

P. R. ARENDT¹

U. S. Army Signal Research
and Development Laboratory
Fort Monmouth, N. J.

Continuous observations of the spin rate decay of satellite Vanguard I (Beta 1958) have indicated anomalies that do not fit into the picture developed from the theory of exponential magnetic damping by eddy currents. The first anomaly was detected in December 1958; the decay changed to a very low rate; a rate similar to the previous decay was observed early in 1959. Other anomalies were found later in 1959 and in 1960. Some of the anomalous low decay rates might be related to the movement of the Earth around the sun. During the 2½ years of observation the spin changed from 1 revolution in ½ sec to 1 revolution in 20 sec. The slope of the decay curve varied between 0.19 and 7.6 arbitrary log units during fall 1960; initially the slope varied between 4.1 and 5.0 units. The slope during first anomaly was 2.2 units.

Spin Fading

THE METHOD of obtaining the spin rate of an artificial satellite by the counting of maxima or minima in a satellite's CW signal is well known. These "spin fades" are produced by the lobes or zeros in the pattern of the satellite's transmitting antenna. The effects of various types of satellite antennas (such as dipoles, turnstile or slot antennas) have to be considered as well as the influence of the receiver antenna, the polarization of that antenna, and the geometry of and the ionization along the propagation path. For these reasons, the spin fading observations are easily disturbed by other fading phenomena such as multiple path reception or Faraday fading. For example, Sputnik I showed a spin fading period of about 4.6 sec. The period of Faraday fading observed was 4.4 sec at 20 mc and 15.0 sec at 40 mc. Thus, it is sometimes difficult to differentiate both phenomena. However, with frequencies in the order of 100 mc the periods of Faraday fading are in the order of minutes and will not divert spin fading observation. Further, multiple path reception is much less probable with such higher frequencies than in the 20- and 40-mc range. Therefore, the observations of Vanguard I on 108 mc are rather free from errors due to other types of fading.

When a satellite is placed into orbit, the effects of gravity are greatly reduced in the sense that the satellite can be considered a free gyroscope and under no constraint. Therefore, small forces become effective. Torques acting at the spin axis produce a decay of the spin rate. Other small torques not aligned along the spin axis cause precession and lead to tumbling. Such tumbling or precession period causes a complicated rotation of the antenna pattern with respect to the observer on Earth. The resulting ambiguity in the interpretation of the data is demonstrated by Fig. 1, which shows the spin and precession fades during the early life of Vanguard I. The ambiguity was solved in this case by independent telemetry signals measuring the initial spin before third-state separation during the launching operation.²

Received Aug. 14, 1959 and revised Dec. 21, 1960.

¹ Institute for Exploratory Research.

² The author is indebted to R. I. Easton and M. J. Votav for this communication.

Many authors have described the relationship between the radiation qualities (polarization, pattern) of the two antennas involved in the propagation process and the variation of the look angle during the passage of the spinning and tumbling vehicle (1-10).³ A comprehensive monograph of all physical effects possibly involved is given by the study of K. P. Chopra (11).

A close inspection of the spin fading intervals indicates that most of the satellites suffer from minor fluctuations of the spin rate. Over short intervals of time, often during the same passage interval of a few minutes duration, the spin rate increases or decreases slightly. Such minor changes of the spin angular momentum have been related (12) to mechanical vibrations caused by differential gravitational forces acting either on elastically mounted interior equipment or on flexible antennas, etc. Similar vibrations might also be caused by interactions between the satellite and surrounding charged particles (13) or meteorites. Another cause could be the interaction of the Earth magnetic field with electrical currents produced within the satellite during periods of instrumental operation. Our observations disclose many such minor fluctuations (Fig. 2). However, we have excluded these side effects from the present study, which is devoted to the long time retardation of the spin rate. During our observations the spin changed from 1 revolution in about ½ sec to 1 revolution in 20 sec.

Eddy Current Retardation

We started our observations during the launching phase of Vanguard I, March 17, 1958. R. I. Easton and M. J. Votav first reported measurements of the spin rate (14), which coincide with our own measurements (Fig. 3) in all details during the launching period as well as in spin rate decay during the early life of this satellite.

The Vanguard I satellite performs its orbits at such distances from the earth that air drag cannot be considered serious (perigee at about 650 km, apogee at about 3900 km). This assumption is proven by the fact that the time of the orbital period did not change remarkably during its life.

³ Numbers in parentheses indicate References at end of paper.

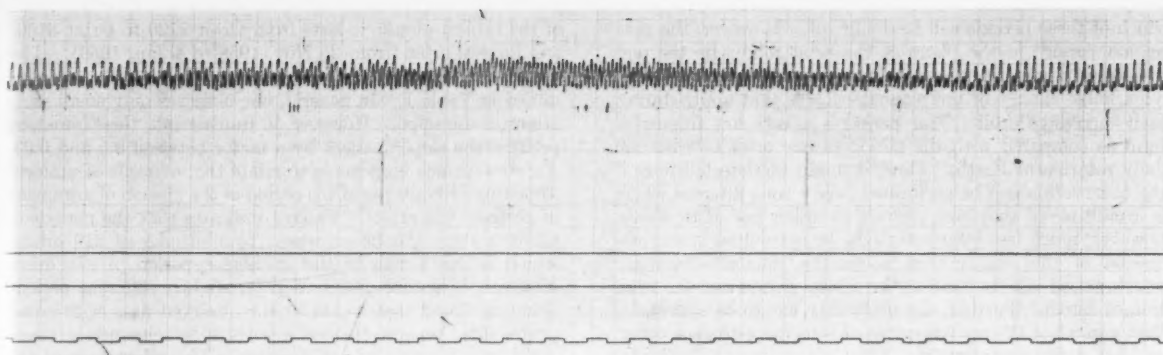


Fig. 1 Amplitude recording of spin and tumble fades during early life of Vanguard I satellite; bottom line shows time tic of 1 sec

However, St. P. Wyatt observed irregularities in the rate of period decrease during rather short time intervals in July 1959 (16). L. G. Jacchia has observed periodic fluctuations of the orbital acceleration over the interval of about one year. An attempt has been made by W. Priester to correlate these periodic alterations to the observed solar activity during the same period (17).

During 3200 orbits the period changed from 134.29 min to 134.14 min (15). Therefore, this satellite can be used to study the geomagnetic retardation of the spin rate predicted by D. P. Vinti's eddy current theory (18) and applied experimentally by R. H. Wilson Jr. (19). Vinti's study assumes that the dominant factors of the spin decay are the electromagnetic forces derived from the movement of a conductive body through the electric and magnetic fields of Earth. Gravitational forces are excluded by the assumption that the center of mass of the satellite coincides accurately with its geometrical center. Further, air drag is considered negligible. Other assumptions are: The satellite consists of a uniformly conductive, nonferromagnetic, hollow, spherical shell that has obtained an initial spin around an axis of mechanical symmetry. In first order, these assumptions apply to Vanguard I. Wilson considered the damping effect of the various electromagnetic or ferromagnetic couples in the satellite. He calculated an effective electromagnetic couple for the entire satellite, which in turn permitted a prediction of the spin decay when an assumption was made for the mean effective magnetic field. He found that the magnetic field calculated from the observed spin decay coincides with the ambient field value calculated from surface measurements. Thus, the eddy current theory has been confirmed. Therefore, for this paper we hypothesized that the long-term alterations of the spin are due to the interaction of the induced eddy currents with Earth's magnetic field. These forces produce a decay of the spin rate and also a torque tending to turn the axis of spin.

The theory describes the spin decay by an exponential function for a circular equatorial orbit. In the case of a nonequatorial, noncircular orbit large changes of the spin direction occur because of a turning torque. In this most general case, the spin movement is described by a "smooth" exponential decay function of the spin rate and by the turning of the spin axis until this axis is parallel to the magnetic axis of the earth; that is, the spin is changing until the spin axis revolves once per day around an axis parallel to the rotational axis of the earth. However, this latter quasi-stabilized condition may be achieved only in orbits that are symmetrical with respect to the shape of the magnetic field of Earth. For the most general case, Vinti predicted that the smooth decay function is disturbed by four periodic perturbations. Three of these periods are related to the orbital data and one is related to the rotation of Earth. It has not been predicted

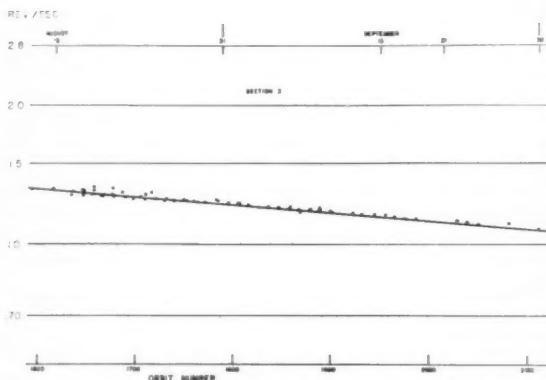


Fig. 2 Minor fluctuations of the spin rate of Vanguard I satellite

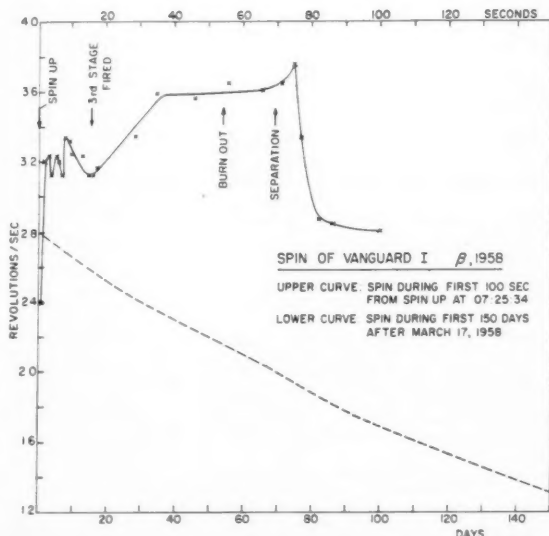


Fig. 3 Spin rate of Vanguard I satellite during launching and shortly thereafter

which of these periods will be dominant. However, the precession period⁴ in the plane of the orbit might be the one to become dominant because this movement results in a very remarkable change of the magnetic forces that apply during each successive orbit. This period is a very low frequency term as compared with the period of one orbit or with the daily rotation of Earth. Thus, it might be detected only if the observation can be performed over a time interval which is a multiple of that long period. Another period to which, however, much less influence might be attributed is the precession of the longitude of successive equator crossings,⁵ which period is a function of the orbital period and the rotation of Earth. Further, the possibility has to be considered that various of the periods involved coincide with each other, at least in longer intervals. These intervals may be longer than the period for the precession of the orbit, which frequency might be regarded as the basic frequency of such multiple coincidences.

Observations

It is convenient to present the observed spin rate in logarithmic scaling as a function of time and to measure time by orbit numbers. Examples of our data are given in Fig. 4, which shows the spin decay during the first year of satellite life, and in Fig. 5, which gives an enlarged section of the data during the first anomaly.

In order to find whether some of the perturbation periods previously mentioned apply, we inspected the data closely. It is interesting to note that the duration of the anomaly in December coincides with half of the period of the precession

⁴ Motion of argument of perigee, in case of Vanguard I: 4.4 deg per day; entire period equals 876 orbit; 1 (sidereal) day equals 86,164 sec.

⁵ Motion of longitude of ascending node, in case of Vanguard I: -3.0 deg per day; entire period equals 1286 orbit.

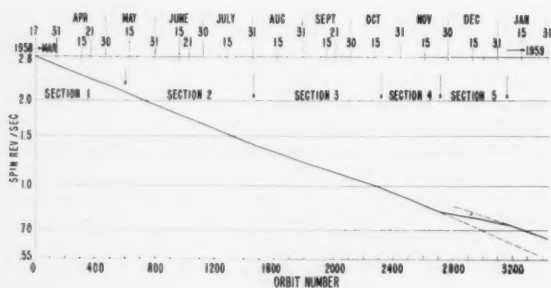


Fig. 4 Spin rate decay of Vanguard I satellite during first year

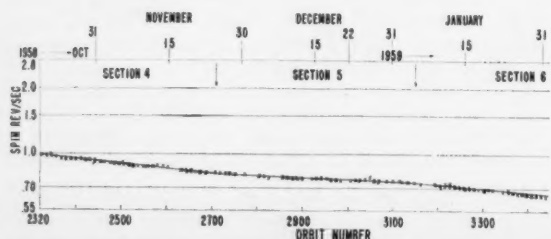


Fig. 5 Details of first anomaly of spin rate decay

of the orbital plane; it lasts from Orbit 2720 to Orbit 3160, i.e., for 440 orbit (from 25 Nov. 1958 to 4 Jan. 1959). The observed intervals of the alterations of the slope are contained in Table 1. In general, one observes only small variations of the slope. However, in transition to the anomalous periods, the slope changes by a factor between 0.5 and 0.03. An attempt has been made to relate the intervals of uniform slope to a submultiple of the period of the motion of argument of perigee (876 orbit). Table 1 indicates that the periods of uniform slope can be expressed by multiples of 219 orbits, which is one fourth of the precession period of 876 orbit. However, a similar distribution for slightly different periods could be found that would fit the observed data with equal probability, because there is a fairly wide tolerance in measuring the duration of each section. The alterations of the slope are obvious, but the variability of the measured data does not permit a better determination of the duration of each section than ± 30 orbit. If this margin is adopted at each end of all sections, a good coincidence can be stated between the observed intervals and the assumed periodic sections. For more detail see (20).

The extreme low value of the slope anomalies could be derived from an assumption that two or more perturbation functions were coinciding. But this would not account for the very long duration of the anomaly. Such a long deviation could result only from a coincidence of perturbations if the difference of the two perturbing periods is nearly equal to the duration of the anomaly. In such a case, the anomaly should be observable in regular intervals. However, such is not the case, as indicated by Table 1. This fact suggests that the cause for the anomalies may not be found exclusively from eddy current theory.

Possible Explanations

In tracking for other possible perturbations, we have to exclude all effects (21 and 22) which might influence the translatory movement of the satellite, because this movement has not been altered correspondingly. However, it is interesting to note that the center orbit of the first observed anomaly was performed on a date that is close to the Winter solstice at 21 December. (The author is indebted to H. P. Hutchinson for this observation.) Thus, one is inclined to use the hypothesis that there exists an influence of the position of Earth in its orbit or of its distance from the sun on the decay function of the spin rate. Such thesis gets some support by the fact that a similar anomaly was found near the Winter solstice 1959. However, the fact of very strong anomalies during February 1959 and July through September 1960 opposes such conclusion.

One could think about the possibility that streams of charged solar or cosmic particles were creating local magnetic fields along some part of the satellite's trajectory that could reduce the effective magnetic field at the satellite in such a manner as to produce the observed reduction of the retardation. In this case, however, there is no reason not to assume the opposite effect which might be demonstrated by the steep slope in section 12 and 14 shown in Table 1.

On the other hand, forgetting about the summer anomaly in 1960, one can argue as follows: Three anomalies were observed during fall and winter in the northern hemisphere, and steeper slopes were found during midsummer. For these cases one might admit the possibility of extraterrestrial influence on spin retardation. During perihelion of Earth and the satellite any changes of nonterrestrial suninfluenced magnetic fields are easier noticeable by the satellite than during aphelion (when Earth is far from the sun). However, if this conclusion is accepted there still remains an open question as to whether extraterrestrial or solar events can be found that coincide with the rather long periods of anomalous small retardation of the spin rate. This question will be the effort of future investigations.

Table 1 Variation of spin rate decay

Decay curve, section	Slope ^a observed	Interval observed, date	Orbit number	Duration, section in orbit observed	219 orbit, multiples
1	4.4	17 March 12 May 1958	0-600	600	...
2	5.0	12 May 31 July 1958	600-1460	860	4
3	4.1	31 July 20 Oct. 1958	1460-2320	860	4
4	5.0	20 Oct. 25 Nov. 1958	2320-2720	400	2
5	2.2	25 Nov. 1958 6 Jan. 1959	2720-3160	440	2
6	5.3	6 Jan. 30 Jan. 1959	3160-3426	266	1
7	2.1	30 Jan. 11 March 1959	3426-3844	418	2
8	4.7	11 March 1 June 1959	3844-4740 ^b	896	4
9	4.2	1 June 20 Oct. 1959	4720-6260	1520	7
10	1.0	20 Oct. 1959 1 Feb. 1960	6260-7370	1110	5
11	4.2	1 Feb. 20 April 1960	7370-8220	850	4
12	6.1	20 April 10 July 1960	8220-9094	874	4
13	0.19	10 July 24 Sept. 1960	9094-9912	818	4
14	7.6	24 Sept. ^c	9912-

^a Measured in log rps per orbit $\times 10^4$.^b Uncertain for ± 120 orbit.^c Observed until orbit 10450, 15 Nov. 1960.

Acknowledgments

The satellite recordings used in this report were performed by the USASRDL Astro-Electronics Division's radio receiving station in Deal, N. J. The recording operations were under the supervision of L. D. Manamon and D. R. Wills. The laborious task of measuring the spin-rate was performed by various groups consisting of R. Leach, P. Manno, W. A. Scott, R. Uradnicak, Elsie W. Harris, O. C. Tilton and G. Haber. The author is much indebted to all mentioned and to many other members of USASRDL for their cooperative assistance and advice, especially for the advice of J. Weinstein in checking the statistical confidence of the data, and for the continuous encouragement by E. M. Reiley.

References

- 1 Vakhmin, V. "Artificial Earth Satellites," *Radio* (Russian), no. 6, 1957, pp. 14-17, transl. by National Acad. of Sci., Sept. 1957.
- 2 Bolljahn, J. T., "Effects of Satellite Spin on Ground-Received Signal," IRE Trans. on Antennas and Propagation, vol. AP-6, no. 3, 1958, pp. 260-267.
- 3 Barr, T. A., "Explorer IV Antennas," in "Explorer IV Orbital Data Series," Issue I, Army Ballistic Missile Agency and Smithsonian Astro-Physical Observatory, Aug. 11, 1958; also R. Naumann, "Attitude Determination of Explorer IV," ABMA Rep. no. DV-TN-19-59, June 1959.
- 4 Bracewell, R. N. and Garriot, O. K., "Rotation of Artificial Earth Satellites," *Nature*, vol. 182, no. 4658, 1958, pp. 760-762.
- 5 Warwick, J. W., "High Altitude Observatory, AFCRC-TN-58-134 Scientific Rep. no. 10, 1958, pp. 30-50.
- 6 McAllister, H. M., "Satellite Propagation Observation Tracking," RCA Service Company Rep., DA 36-039 SC-72802, vol. 1, 1958, pp. 14-18.
- 7 Waterman, A. T., Jr., "Modulations Imposed on a Radio Signal by Satellite Motions," 1958 Symposium on Telemetering, June 1958.
- 8 For visual observations of spin see: Melin, M., *Sky and Telescope*, vol. 18, no. 3, 1959, pp. 82-83; Moore, D. G., *ibid.*; Carr, P. H., Stewart, R. M.,

Jr. and Senne, J. H., Flash period of 1958 Delta I, *Amer. J. Physics*, vol. 28 no. 1, 1960, pp. 64-66; Notni, P. and Oleak, H., "Die Rotation der Traegerkete von Sputnik III (1958#1)," *Veroeff. der Sternwarte in Babelsberg*, vol. 13, no. 3, 1959.

9 Arendt, P. R. and Hutchinson, H. P., "Spin Variations of Satellite Radio Emission," 3rd Nat. Conv. on Military Electronics, Conf. Proceedings 1959, pp. 407-412.

10 Vonbun, F. O., "Analysis of Satellite Motion from Radio Reception," IRE Trans., vol. Mil-4, no. 2-3, 1960, pp. 361-365.

11 Chopra, K. P., "Interactions of Rapidly Moving Bodies in Terrestrial Atmosphere," Engng. Center, Univ. of Southern California, USCEC Rep., 56-212, March 1960.

12 Roberson, R. E., "Torques on a Satellite Vehicle from Internal Moving Parts," *J. Appl. Mech.*, vol. 25, no. 2, 1958, pp. 219-200, 287-288.

13 Warwick, J. W., "Decay of Spin in Sputnik I," *Planet, Space Sci.*, vol. 1, no. 1, 1959, pp. 43.

14 Easton, R. I. and Votav, M. J., "The Vanguard I IGY Satellite (1958 Beta)," U. S. Naval Research Laboratory Rep., 1958.

15 Weekly release of the Vanguard Computing Center and the National Aeronautics and Space Administration.

16 Wyatt, St. P., "Solar Effects in the Motion of Vanguard," *Nature*, vol. 184, no. 4683, 1959, pp. 351.

17 Jacchia, L. G., "Two Atmospheric Effects in the Orbital Acceleration of Artificial Satellites," *Nature*, vol. 183, no. 4660, 1959, pp. 526-527.

18 Vinti, D. P., "Theory of the Spin of a Conducting Satellite in the Magnetic Field of the Earth," Ballistic Research Laboratories, Rep. no. 1027, July 1957.

19 Wilson, R. C., Jr., "Magnetic Damping of Rotation of Satellite (1958 Beta) *Science*, vol. 130, no. 3378, 1959, pp. 791-793; "Geomagnetic Rotational Retardation of Satellite 1959 Alpha I (Vanguard II), *Science*, vol. 131, no. 3395, 1960, pp. 223-225; La Paz, L., "Magnetic Damping of the Vanguard I Satellite," *Science*, vol. 131, no. 3397, 1960, pp. 355-356; Wilson, R. H., Jr., *ibid.*, pp. 356-357; La Paz, L., "On the Magnetic Damping of Rotation of Artificial Satellites of the Earth," *J. Geophys. Res.*, vol. 65, no. 7, 1960, pp. 2201-2202.

20 Arendt, P. R., "An Anomaly of the Spin of Satellite Vanguard I," USASRDL Tech. Rep. 2025, March 1959.

21 Musen, P., "The Influence of the Solar Radiation Pressure on the Motion of an Artificial Satellite," *J. Geophys. Res.*, vol. 65, no. 5, 1960, pp. 1391-1396.

22 Bogorodskii, A. F., "Relativistic Effects in the Motion of an Artificial Earth Satellite," *Astron. Zhur.*, vol. 36, no. 5, 1959, pp. 883-889, Engl. translation *AJ*, vol. 3, no. 5, 1960, pp. 857-862.

Eddy Current Torque Compensation in a Spin Stabilized Earth Satellite¹

L. H. GRASSHOFF²

Radio Corp. of America
Princeton, N. J.

The vector torque produced by eddy currents in a conducting body rotating in Earth's magnetic field bears a unique relation to the spin vector and the field vector. A simple coil arrangement may be made to produce a vector torque which effectively cancels the eddy current torque, thus eliminating the spin decay and precession owing to induced eddy currents. The system under consideration here consists of a sensing coil, a torque producing coil and an amplifier. The operation is as follows: The sensing coil has an induced emf proportional to the rate of change of magnetic flux through the coil. The sensing coil voltage is amplified and applied to a "torquing" coil which produces a torque opposing the eddy current torque. The appropriate magnitude is obtained by varying the amplifier gain or by switching the amplifier on and off at proper intervals. The total weight of the system is approximately 4 lb, and the power requirement is 3 milliwatts (continuous). In addition to the eddy current compensating system, a third coil may be added in a plane normal to the spin axis for the purpose of "steering" or orienting the spin axis independently of eddy current effects.

Qualitative Requirements for Compensating Torque

IT MAY be shown that the eddy current torque on a rotating body is in the plane containing the field vector and the angular velocity vector and is normal to the field vector (1).³ In addition, the spin axis component of eddy current torque must always oppose the rotation. Fig. 1 shows the direction of the eddy current torque for a spin vector along the negative z-axis.

If the field vector \mathbf{B} be resolved into a component B_{\parallel} parallel to the spin axis and a component B_{\perp} perpendicular to the spin axis, the following proportionalities hold

$$T_P \propto B_{\parallel} B_{\perp} \quad [1]$$

$$T_S \propto B_{\perp}^2 \quad [2]$$

where T_P is the precession component of the eddy current torque, and T_S is the spin axis component. In terms of the x, y, z components of \mathbf{B} (Fig. 1), the relations [1 and 2] become

$$T_P \propto B_z(B_x^2 + B_y^2)^{1/2} \quad [3]$$

$$T_S \propto (B_x^2 + B_y^2) \quad [4]$$

Thus, a system for eddy current torque compensation must produce torques in opposition to those expressed by Equations [3 and 4], where the direction of T_S and T_P is shown in Fig. 1.

Method of Producing Compensating Torque

The required compensating torque may be produced by the coil arrangement shown in Fig. 2. Earth's field is resolved into components along the axes of a coordinate system with origin fixed at the center of gravity of the satellite. The

coordinate axes are inertial in so far as orientation is concerned. Reference (2) contains all the details of field description in the coordinate system under consideration. To illustrate how a coil may be made to produce the torques of Equations [3 and 4], it will be assumed that the coil can be made to carry a current proportional to the emf induced in the sensing coil. Accomplishing this requirement will necessitate only a slight modification of coil arrangement.

The emf induced in the sensing coil as it rotates in Earth's field is given by (3).

$$\epsilon = -N_s d/dt \int \mathbf{B} \cdot d\mathbf{A} \quad [5]$$

The vector differential area of the sensing coil as it rotates with respect to the coordinate system is given by

$$-d\mathbf{A} = (i \sin \omega t + j \cos \omega t) dA \quad [6]$$

where ω is the spin angular velocity shown in Fig. 1. Then

$$\epsilon = +N_s d/dt \int (iB_z + jB_y + kB_x) \cdot (i \sin \omega t + j \cos \omega t) dA$$

$$\epsilon = +N_s A \omega (B_x \cos \omega t - B_y \sin \omega t) \text{ volts} \quad [7a]$$

Now let

$$i_c = -K\epsilon \quad [7b]$$

where K is the amplifier gain in amperes per volt, and i_c is the current in the torquing coil

$$i_c = -KN_s A \omega (B_x \cos \omega t - B_y \sin \omega t) \quad [8]$$

The resulting torque is

$$\mathbf{L} = N i_c \mathbf{A} \times \mathbf{B} \quad [9]$$

$$\mathbf{L} = +KNN_s \omega A^2 (B_x \cos \omega t - B_y \sin \omega t) \times (i \sin \omega t + j \cos \omega t) \times (iB_z + jB_y + kB_x)$$

$$\mathbf{L} = +KNN_s \omega A^2 (B_x \cos \omega t - B_y \sin \omega t) \times [i(B_x \cos \omega t) + j(-B_x \sin \omega t) +$$

$$k(-B_x \cos \omega t + B_y \sin \omega t)] \quad [10]$$

Received July 29, 1960.

¹ The material in this paper originally appeared as Technical Memorandum TM 232-13, Oct. 16, 1958, Astro-Electronics Div. of RCA.

² Senior Engineer, Advanced Projects Analysis, Astro-Electronics Div. Member ARS.

³ Numbers in parentheses indicate References at end of paper.

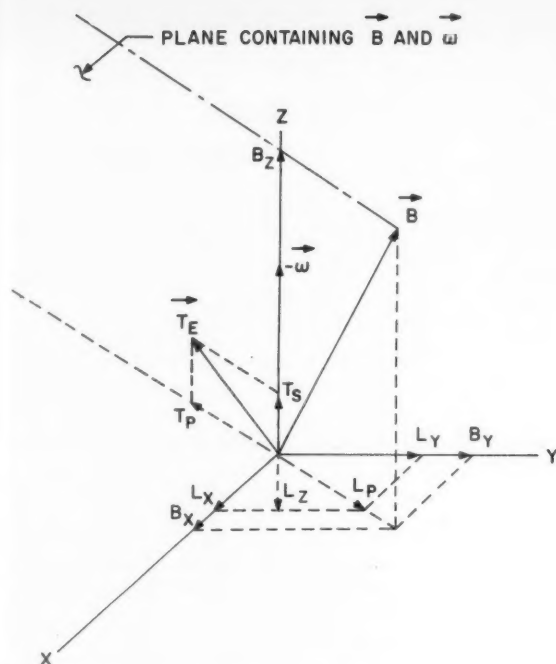


Fig. 1 Eddy current torque and control torque components

The components of \mathbf{L} are

$$L_x = KNN_s \omega A^2 (B_z B_x \cos^2 \omega t + B_z B_y \sin \omega t \cos \omega t) \quad [11]$$

$$L_y = KNN_s \omega A^2 (B_z B_y \sin^2 \omega t - B_z B_x \sin \omega t \cos \omega t) \quad [12]$$

$$L_z = -KNN_s \omega A^2 (B_x \cos \omega t + B_y \sin \omega t)^2 \quad [13]$$

The average values of the torque components over a time interval several times greater than the spin period become

$$L_x = \frac{1}{2} KNN_s \omega A^2 B_z B_x \quad [14]$$

$$L_y = \frac{1}{2} KNN_s \omega A^2 B_z B_y \quad [15]$$

$$L_z = -\frac{1}{2} KNN_s \omega A^2 (B_x^2 + B_y^2) \quad [16]$$

The precession component L_P is

$$L_P = (L_x^2 + L_y^2)^{1/2} = \frac{1}{2} KNN_s \omega A^2 B_z (B_x^2 + B_y^2)^{1/2} \quad [17]$$

Comparing Equations [16 and 17] with Equations [4 and 3], respectively, shows that the coil produces a torque in precisely the correct direction.

Circuit Analysis

Referring to Fig. 3, the following equations may be written

$$e_{11} + e_{12} + e_{10} = -i_1(R_1 + R_s) \quad [18]$$

$$e_{22} + e_{21} + e_{20} = K_s i_1 R_s - i_2 R_2 \quad [19]$$

Here K_s is the voltage gain of the amplifier.

Equations [18 and 19] become

$$L_1(di_1/dt) + M(di_2/dt) + e_{10} = -i_1(R_1 + R_s) \quad [20]$$

$$L_2(di_2/dt) + M(di_1/dt) + (N_2/N_1)e_{10} = K_s i_1 R_s - i_2 R_2 \quad [21]$$

where

- e_{10} = emf induced in the sensing coil by Earth's field
- L_1 = self-inductance of the sensing coil
- L_2 = self-inductance of the torque coil

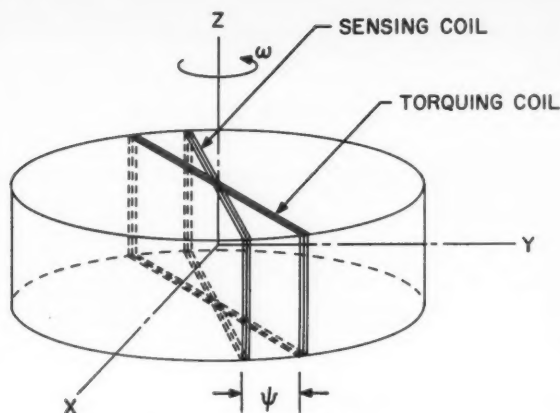


Fig. 2 Schematic diagram of coil arrangement

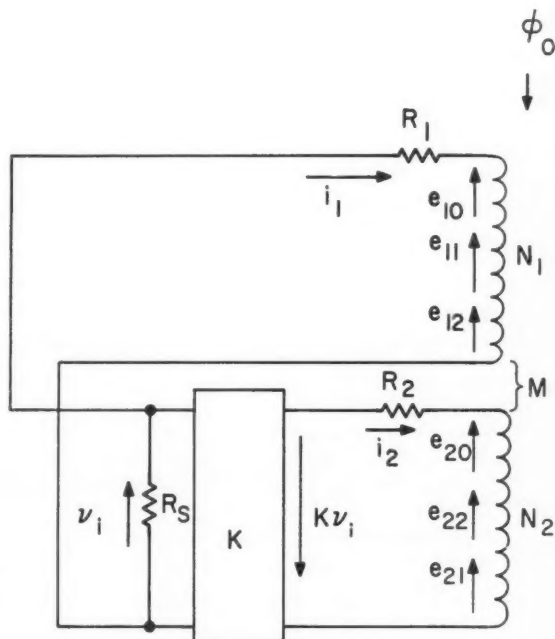


Fig. 3 Circuit diagram of coil system

M = mutual inductance
 N_2/N_1 = turns ratio

The complete solution of Equations [20 and 21] will be given in a subsequent section. The steady-state equations corresponding to Equations [20 and 21] are

$$(R_1 + R_s + j\omega L_1)I_1 + j\omega M I_2 = -E_{10} \quad [22]$$

$$(j\omega M - K_s R_s)I_1 + (R_2 + j\omega L_2)I_2 = -(N_2/N_1)E_{10} \quad [23]$$

The coefficient of coupling is k equal to $M/\sqrt{L_1 L_2}$.

Solving Equations [22 and 23] gives

$$I_2 = \frac{-E_{10} \{ [K_s R_s + (N_2/N_1)(R_1 + R_2)] + j\omega \sqrt{L_1 L_2} (1 - k) \}}{[R_2(R_1 + R_s) - \omega^2 L_1 L_2 (1 - k^2)] + j\omega [R_2 L_1 + (R_1 + R_s) L_2 + \sqrt{L_1 L_2} K_s k]} \quad [24]$$

Dividing numerator and denominator by $(R_1 + R_s)$ and setting R_1/R_s equal to a gives

$$I_2 = - \frac{E_{10} \left\{ \left[\frac{K_s}{1+a} + \frac{N_2}{N_1} \right] + j\omega \left[\frac{\sqrt{L_1 L_2} (1-k)}{R_1 + R_s} \right] \right\}}{\left[R_2 - \frac{\omega^2 L_1 L_2 (1-k^2)}{(R_1 + R_s)} \right] + j\omega \left[L_2 + \frac{R_2 L_1}{R_1 + R_s} + \frac{\sqrt{L_1 L_2} K_s k}{1+a} \right]} \quad [25]$$

Now for a low frequency ($\omega < 2$)

$$\begin{aligned} (R_1 + R_s) &\gg \omega L_1 L_2 (1 - k) \\ (R_1 + R_s) &\gg R_2 L_1 \quad K_s \gg N_2/N_1 \\ (R_1 + R_s) &\gg \omega^2 L_1 L_2 (1 - k^2) \end{aligned}$$

Then

$$I_2 \cong -E_{10} \frac{K_s/(1+a)}{R_2 + j\omega \left(L_2 + \frac{\sqrt{L_1 L_2} K_s k}{1+a} \right)} \quad [26]$$

The emf E_{10} induced in the sensing coil by Earth's field may be obtained from Equation [7a]

$$\begin{aligned} e_{10} &= -N_s A \omega (B_x^2 + B_y^2)^{1/2} \sin \left(\omega t + \tan^{-1} \frac{B_x}{B_y} \right) \\ &= -E_{0 \max} \sin (\omega t + \alpha) \end{aligned} \quad [27]$$

Typical values for B_x and B_y as obtained from (2) might be

$$\begin{aligned} B_{x \max} &\cong 1.4 (\mu_0 M_e / 4\pi r^3) \\ B_{y \max} &\cong 0.63 (\mu_0 M_e / 4\pi r^3) \end{aligned} \quad [28]$$

where M_e is the magnetic moment of Earth's dipole field.

Design Calculations

$$B_{x \max} = (\mu_0 M_e / 4\pi r^3) (1.4)$$

$$B_{y \max} = (\mu_0 M_e / 4\pi r^3) (0.63)$$

Let

$$N_s = 1000 \text{ turns}$$

$$A = 0.254 \text{ m}^2$$

$$\omega = 1.2 \text{ radians per sec}$$

$$\begin{aligned} |E_{10 \max}| &= 1000 (0.254) (1.2) (\mu_0 M_e / 4\pi r^3) (1.4^2 + 0.63^2)^{1/2} \\ &= 470 \frac{4\pi \times 10^{-7} \times 8.1 \times 10^{22}}{4\pi \times 3.08 \times 10^{20}} = 12.4 \text{ mv} \end{aligned}$$

Now for the same B_x and B_y , use Equation [16] to compute K (amperes per volt) for a given L_k . Let $L_s = 10^{-5}$ Newton meters (an estimated value for eddy current torque). Then from Equation [16]

$$\begin{aligned} 10^{-5} &= \frac{1}{2} K (100) (1000) (1.2) (0.254)^2 \left(\frac{\mu_0 M_e}{4\pi r^3} \right)^2 \times \\ &\quad (1.4^2 + 0.63^2) \\ &= 62.8 \times 10^{-7} K \\ K &= 1.59 \text{ amp/v} \end{aligned}$$

Then the required I_2 is obtained from Equation [7b]

$$i_{2 \max} = 1.59 (12.4) = 19.7 \text{ milliamps}$$

From (4), the self-inductances of sensing and torquing coils are

$$\begin{aligned} L_1 &\cong 1.3 \text{ h} \\ L_2 &\cong 0.013 \text{ h} \end{aligned}$$

Equation [26] may be used to calculate the voltage gain K_s . Variation of K_s with a or k may be plotted using the other (k or a) as a parameter. For

$$N_2 = 100 \text{ (turns, No. 20 copper wire)}$$

$$R_2 \cong 8.5 \text{ ohm}$$

Now setting k equal to 1 and a equal to $\frac{1}{3}$, Equation [26] gives

$$0.0197 = 0.0124 \frac{K_s/1.33}{[8.5^2 + 1.2^2 (0.13 K_s/1.33)^2]^{1/2}}$$

from which K_s is equal to 18.5 v per v. Variation in k has only slight effect on the required K_s .

The phase lag of I_2 behind $-E_{10}$ should be corrected by "advancing" the torquing coil ahead of the sensing coil. The right-hand side of Equation [23] should be adjusted for the new position of the torquing coil. The phase angle is

$$\psi = \tan^{-1} \frac{\omega [L_2 + (\sqrt{L_1 L_2} K_s k)/(1+a)]}{R_2}$$

For the case considered, ψ is equal to 14.3 deg.

No attempt has been made to optimize any of the parameters. The amplifier design must be carefully integrated with the system before optimization calculations can be made. Neglecting losses in the amplifier, the power requirements for this system are

$$\begin{aligned} P_{avg} &\cong 10^{-5} \times 1.2 + (0.0197)^2 (8.5) \text{ w} \\ &= 3.31 \text{ mw} \end{aligned}$$

The system weight is approximated as follows:

1000 turns, No. 36 copper wire	0.63 lb
100 turns, No. 20 copper wire	2.58 lb
structure	1.00 lb
amplifier	0.25 lb
total weight	4.46 lb

The resistances and inductances are:

$$\begin{aligned} R_1 &= 3450 \text{ ohms} \\ L_1 &= 1.3 \text{ h} \\ R_2 &= 8.5 \text{ ohms} \\ L_2 &= 0.013 \text{ h} \end{aligned}$$

Transient Response

Taking the Laplace transform of Equations [18 and 19],

the following equations are obtained:

$$L_1 s i_1(s) + (R_1 + R_s) i_1(s) + M s i_2(s) - L_1 i_1(0) - M i_2(0) = -e_{10}(s) \quad [28]$$

$$M s i_1(s) - K_s R_s i_1(s) + L_2 s i_2(s) + R_2 i_2(s) + M i_1(0) + L_2 i_2(0) = -(N_2/N_1) e_{10}(s) \quad [29]$$

For zero initial conditions

$$i_2(s) \left\{ (1 - k^2) s^2 + \left[\frac{R_2}{L_2} + \frac{R_1 + R_s}{L_1} + \frac{K_s R_s M}{L_1 L_2} \right] s + \frac{R_2(R_1 + R_s)}{L_1 L_2} \right\} = \left\{ \left(\frac{M}{L_1 L_2} - \frac{N_2}{N_1} \frac{1}{L_2} \right) s - \frac{1}{L_1 L_2} \left[\frac{N_2}{N_1} R_1 + \left(K_s + \frac{N_2}{N_1} \right) R_s \right] \right\} e_{10}(s)$$

Using $k = M/\sqrt{L_1 L_2}$ and $N_2/N_1 = \sqrt{L_2/L_1}$

$$i_2(s) = -e_{10}(s) \frac{\left\{ \frac{1}{\sqrt{L_1 L_2}} (1 - k) s + \frac{1}{L_1 L_2} \left[\left(k_s + \frac{N_2}{N_1} \right) R_s + \frac{N_2}{N_1} R_1 \right] \right\}}{\left\{ (1 - k^2) s^2 + \left[\frac{R_2}{L_2} + \frac{R_1 + R_s}{L_1} + \frac{K_s R_s M}{L_1 L_2} \right] s + \frac{R_2(R_1 + R_s)}{L_1 L_2} \right\}} \quad [30]$$

In Equation [30], e_{10} may be the emf induced in the sensing coil by any external field. The complete solution for i_2 (for zero initial conditions) is available directly from Equation [30].

Conclusions

The analysis demonstrates the feasibility of compensating for eddy current torque by electromagnetic means. The presence of spurious a-c fields should be determined, and their effects should be calculated. The necessary equations are

available by adding to e_{10} the emf induced in the sensing coil by local circuits.

References

- 1 Vinti, J. P., "Theory of the Spin of a Conducting Satellite in the Magnetic Field of the Earth," Ballistic Research Laboratories, Aberdeen, Md., Rep. no. 1020, July 1957.
- 2 Grasshoff, L. H., "A Method for Controlling the Attitude of a Spin-Stabilized Satellite," ARS preprint 1501-60, Dec., 1960.
- 3 Smythe, W. R., "Static and Dynamic Electricity," McGraw-Hill Book Co., Inc., N. Y., 1950, p. 307.
- 4 Terman, F. E., "Radio Engineer's Handbook," McGraw-Hill Book Co., Inc., N. Y., 1943, p. 56.

1960-61 ARS Meeting Schedule

Date	Meeting	Location	Abstract Deadline
March 13-16	Missile and Space Vehicle Testing Conference	Los Angeles, Calif.	Past
April 4-6	Lifting Re-Entry Vehicles: Structures, Materials, and Design Conference	Palm Springs, Calif.	Past
April 26-28	Propellants, Combustion, and Liquid Rockets Conference	Palm Beach, Fla.	Past
May 3-5	Space Nuclear Conference	Gatlinburg, Tenn.	Past
May 22-24	National Telemetry Conference	Chicago, Ill.	Past
June 13-16	National IAS-ARS Joint Meeting	Los Angeles, Calif.	Past
Aug. 7-9	Guidance and Control Conference	Palo Alto, Calif.	Past
Aug. 16-18	International Hypersonics Conference	Cambridge, Mass.	Past
Aug. 23-25	Biennial Gas Dynamics Symposium	Evanston, Ill.	Past
Oct. 2-7	XIIth International Astronautical Congress	Washington, D.C.	May 1
Oct. 9-15	ARS SPACE FLIGHT REPORT TO THE NATION	New York, N.Y.	April 15

Send all abstracts to Meetings Manager, ARS, 500 Fifth Ave., New York 36, N.Y.

A Capacitance Densitometer for Determination of the Transient Densities of Cryogenic Liquids

A. HARRY SHARBAUGH¹

Research Laboratory,
General Electric Co.
Schenectady, N. Y.

MAXWELL W. LIPPITT Jr.²

Malta Test Station,
General Electric Co.
Ballston Spa, N. Y.

In the operation and testing of rocket engines using liquid propellants, it is desirable to measure continuously the density of the flowing liquid under transient conditions where the changing temperature and pressure cause small, but important, density changes. This report describes a novel method for doing this by measuring the electrical capacitance of a calibrated concentric-cylinder capacitor which is inserted into the feed system of the rocket engine. Test results with liquid oxygen show that this capacitance densitometer will indicate changes in density to about $\pm 0.2\%$ accuracy and absolute values of density may be measured with an error of about $\pm 1\%$.

IN THE operation and testing of rocket engines using liquid propellants, it is necessary to know the mass flow rate of the fuel, i.e., the product of the density and the volume flow rate of liquid. Ordinarily, this quantity is computed with sufficient accuracy by using the nominal density as measured under room conditions, uncorrected for the effects of temperature and pressure. However, it is sometimes desirable to continuously measure a more accurate value for the density under transient conditions where the temperature and pressure of the liquid are changing and, in so doing, cause small but important changes in the density.

In principle, this quantity could be determined by making a continuous measurement of the operating temperature and pressure, from which data the corrected density could be computed from an equation of state for the liquid. This process, however, would introduce an undesirable time delay. Furthermore, the expansion and compressibility coefficients may be unavailable under the conditions of temperature and pressure which are commonly being used in modern rocketry.

We shall describe here a densitometer which overcomes this difficulty; it provides a continuous indication of the transient density of a nonpolar liquid under either flow or no flow conditions. Briefly, the method consists of the measurement of the electrical capacitance of a calibrated concentric-cylinder capacitor which is inserted in the feed system of the rocket engine. Any change in the number of molecules per cc (i.e., density) owing to pressure and/or temperature variation is reflected immediately by a change in the dielectric constant of the liquid.

We shall present here the test results of an experiment in which the instantaneous density was determined by capacitance measurement, values of the transient temperature and pressure being recorded simultaneously. From these latter quantities the density was calculated by a somewhat tedious extrapolation procedure, and these values will be compared with those determined by the capacitance measurement technique.

Received June 21, 1960.

¹ Physical Chemist.

² Development Engineer; present address, Instrument Research Div., NASA, Langley Research Center, Langley Field, Va. Member ARS.

Theory

The dielectric constant ϵ' of a nonpolar liquid, such as hydrogen or oxygen, is related to its density by the well-known Clausius-Mosotti relation

$$\frac{\epsilon' - 1}{\epsilon' + 2} = \frac{4\pi n\alpha}{3} = \frac{4\pi Nd}{3M} \alpha \quad [1]$$

Here

n = number of molecules per cm^3

M = molecular weight, gm

α = polarizability of the molecule, cm^3

N = universal constant (6.02×10^{23}) equal to the number of molecules in a gm-molecular weight of any substance

Since α and M are constant for a particular liquid

$$(\epsilon' - 1)/(\epsilon' + 2) = kd \quad [2]$$

where the proportionality constant k equals $(4/3)(\pi N\alpha/M)$.

If we expand the left-hand side of Equation [2] about the value $\epsilon' = 1.500$, the nominal dielectric constant of liquid oxygen, we obtain

$$\epsilon' - 1/\epsilon' + 2 = 0.1430 + 0.2450 (\Delta\epsilon') - 0.1650 (\Delta\epsilon')^2 \quad [3]$$

where $\Delta\epsilon' = \epsilon' - 1.500$. Thus, for the restricted range of dielectric constants with which we are concerned (1.49–1.51), the error introduced by a linear approximation is negligible.

According to Equation [1], any change in the number of molecules per unit volume owing to a pressure and/or temperature change causes a change in dielectric constant. This, in turn, causes a change in the value of capacitance C of the sensing element according to the relation $C = C_0\epsilon'$. Here C_0 is the vacuum or air capacitance of the "fillable" portion of the capacitor.

If we retain the linear term only in Equation [3] and combine with Equation [2], we may express the density by the relation

$$d = \frac{1}{k} \left(\frac{0.2450 C}{C_0} - 0.2245 \right) \quad [4]$$

For larger changes in the dielectric constant, either higher

order terms must be retained in Equation [3] or the exact relation given by Equation [2] must be used. Using Equation [1] we may evaluate k by measuring the dielectric constant and density simultaneously at a number of different temperatures. This is permissible because the polarizability of a nonpolar molecule is independent of temperature (and pressure) and is a function of the atomic and molecular structure only. The measurements of Kanda (1)³ on liquid oxygen were used to establish a value k equal to 0.1212.

Experimental

To investigate the practicability of the method outlined, a dielectric constant bridge was installed in a rocket test stand. The particular stand selected was one in which liquid oxygen is pressurized to a maximum of 900 psi, though the method should be equally applicable to any nonpolar liquid, e.g., hydrogen. During the run, liquid oxygen flowed through a 4-in. diameter pipe at a rate of about 70 lb per sec.

The capacitance cell consists of two coaxial cylinders spaced about $\frac{3}{8}$ in. apart, mounted centrally in a 6-in. diameter pipe with aluminum oxide supports. (An end view of the cell is shown in Fig. 1.) The ends of the pipe are fitted with reducing sections to connect to the flanges of conventional 4-in. diameter lines. The cell is designed so as to introduce a minimum amount of pressure drop and turbulence which might alter the flow characteristics of the test stand. The electrodes are equipped with guard rings in order to reduce fringing effects.

Capacitance was measured with a self-balancing Wheatstone-type bridge⁴ which operates at a frequency of 400 cycles. It is provided with a dial readout of the capacitance value, as well as an output voltage which may be used to indicate the capacitance continuously on a pen recorder. The ratio arms consist of a center tapped transformer with a rebalance potentiometer connected across part of the secondary winding. The third bridge arm is simply a variable air capacitor whose capacitance is adjusted to the nominal value of the liquid-filled test cell. The test capacitor constitutes the fourth arm of the bridge. Such a circuit conveniently provides an automatic balance of the guard electrode.

Calibration may be accomplished by replacing the cell with a precision three-terminal capacitor, or by filling the test cell with a liquid of known density or dielectric constant. The latter method is preferable in that it eliminates possible errors arising from changes in the geometry of the leads when transferring from the standard to the test capacitor.

Liquid oxygen boils at -183°C at one atmosphere and, under these conditions, its density (2) is accurately known to be 1.142 gm per cc and the value of its dielectric constant (2) is 1.483. Hence, under these conditions it may be conveniently used as a calibrating liquid. Accordingly, the liquid filled cell was connected to the bridge and, after temperature equilibration, the bridge was balanced and dial readout value noted. The absolute capacitance corresponding to this dial reading was determined by solving Equation [4] for C with $k = 0.1212$, $C_0 = 99.5 \mu\text{f}$, and $d = 1.142 \text{ gm per cc}$. All subsequently measured capacitance values were determined by referring the dial readout values of the bridge to this value.

The nominal capacitance of the cell filled with liquid oxygen is $(100 \times 1.5) = 150 \mu\text{f}$, and the bridge will automatically measure any capacitance within $\pm 5\%$ of this value with an error of less than 0.1%. Full scale rebalancing time is of the order of 1 sec, and this establishes the upper limit to the rate of density change which may be monitored. The bridge may be operated remotely from the cell by connection of a length of coaxial cable.

³ Numbers in parentheses indicate References at end of paper.

⁴ Designed and constructed by Magnetic Instruments Co., Thornwood, N. Y.

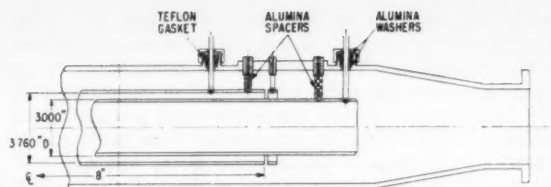


Fig. 1 Cross section of one end of capacitance cell. Material is 304 stainless steel unless otherwise noted

One end of the capacitance cell is shown in cross section in Fig. 1, where it will be noted that none of the insulating electrode supports is located within the volume whose capacitance is measured. In addition, guard electrodes are provided; hence, the absolute capacitance may be accurately calculated from the relation

$$C_0 = \frac{0.2416 l}{\log_{10} (D_1/D_2)} = 100.1 \mu\text{f}$$

(at room temperature). Here

l = length, 40.6 cm

D_1 = outer diameter, 3.760"

D_2 = inner diameter, 3.000"

The capacitance of such a geometry may be calculated more accurately than it may be measured, and measurements with air confirmed this figure within experimental error. The extra fringing capacitance arising because of the finite spacing between guard and guarded electrodes was negligible. At the boiling point of liquid O_2 (-183°C), the capacitance decreases to $99.5 \mu\text{f}$, because of the change in dimensions owing to thermal contraction.

Results and Discussion

Preliminary measurements under static conditions were attempted by mounting the test capacitor in an upright position. The cell was filled with liquid oxygen through the bottom opening. Pressure was then applied, and capacitance readings were taken at various temperatures and pressures. These results were generally unsuccessful because of the inhomogeneity in temperature owing to warming of the liquid surface by the pressurized gas. The device was then installed in the test stand and evaluated under flow conditions.

In one run liquid oxygen was forced through the capacitor at a flow rate of about 70 lb per sec for 1 min. During this time the pressure changed continuously from about 550 to 730 psi while the temperature rose from 99 to 106 K, corresponding to a net density decrease of about 3%. Pressure was measured at the liquid oxygen tank, and the temperature was indicated by a thermocouple. The flow rate was indicated by a Potter flowmeter. The test results are presented in Fig. 2, where the values computed with the aid of Equation [4] are plotted as the ordinates along with the corresponding calculated densities. The method of calculation will now be described.

The density of liquid oxygen in equilibrium with its vapor has been measured over a wide range of temperatures (2). This data and knowledge of the vapor pressure curve of liquid oxygen (3) enabled us to construct a density-temperature curve, each point of which could be identified with a known and different pressure. Next, a second curve at a constant pressure of 900 psi was plotted by extrapolation of each of the points of the previously described curve using

the method outlined by Hougen and Watson (4). This pressure was chosen so as to bracket all those encountered in our experiment. These two lines were replotted on an expanded scale in the temperature region of our experiment. The density at the precise temperature and pressure of the experiment could then be interpolated from the resulting graph. In the range of temperatures in the test run (100–105 K), the average temperature coefficient of density is -5.8×10^{-3} per deg C; the compressibility coefficient of density is 21×10^{-6} atm $^{-1}$. It is estimated that, owing to error in the measured temperature values, the absolute error in these calculated densities is about ± 0.01 gm per cc, while the relative error is about one fifth of this value.

The error in the relative changes in density will be mainly governed by the accuracy with which changes in capacitance may be measured by the bridge, namely, 0.2%. On the other hand, the absolute accuracy of the density will be largely limited by the error in C and C_0 . In a well-designed

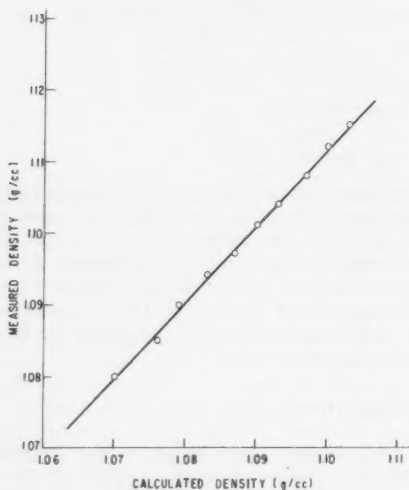


Fig. 2 Comparison of density measured by capacitance variation with calculated density

cell one may calculate a value for C_0 to about $\pm 0.2\%$; however, the error in C may well be as high as 5% unless considerable care is exercised in calibrating the bridge. As already indicated, under ideal conditions where the bridge is calibrated with the cell filled with a liquid of known dielectric constant, this error may be reduced to about 1%. In our case, we note in Fig. 2 that the measured density is consistently about 1% higher than the calculated values; this is almost certainly owing to the absolute error in the value of capacitance and/or temperature gradients in the liquid oxygen.

The standard deviation of the measured densities with respect to the straight line of Fig. 2 is only 0.00006 density unit; this shows the high accuracy of the determination of relative density. It is estimated that a significant part of this scatter is due to the error in the calculated densities. The slope of this line is about 5% higher than would be observed if there were exactly 1:1 correspondence between measured and calculated densities. This is a reasonable value in view of the estimated errors in C_0 and the calculated densities.

Conclusion

In conclusion, the capacitance densitometer described here will indicate relative changes in density to at least $\pm 0.2\%$ accuracy and absolute densities to about $\pm 1\%$, depending on the care which is exercised during calibration. The advantages of this instrument would become even greater in the case of other lower boiling and more compressible propellants; liquid hydrogen, for example, has about ten times the compressibility of liquid oxygen.

Acknowledgments

Grateful acknowledgment is made to C. P. Beauchamp and L. Stibrany of the Malta Test Station, General Electric Co., for their encouragement and help in this experiment.

References

- 1 Kanda, E., "Studies on Fluorine at Low Temperatures. VII. Determination of Dielectric Constants of Condensed Gases," *Bull. Chem. Soc. Japan*, vol. 12, 1937, p. 473.
- 2 Scott, R. B., "Cryogenic Engineering," Van Nostrand Co., Inc., Princeton, N. J., 1959, p. 275.
- 3 Scott, R. B., *ibid.*, p. 274.
- 4 Hougen, O. A., and Watson, K. M., "Chemical Process Principles," Part 2, John Wiley and Sons, Inc., N. Y., 1947, p. 502.

Analysis of Partial Admission Axial Impulse Turbines¹

HANS D. LINHARDT²

Sundstrand Aviation
Denver, Colo.

DAVID H. SILVERN³

North Hollywood, Calif.

Presented herein is a review of the analysis and design of axial partial admission turbines. The analysis utilizes the similarity concept of specific speed and specific diameter. The result of the analysis is presented in design charts which show efficiency lines and optimum geometric ratios as a function of the design parameters, specific speed and specific diameter for certain regimes of Reynolds number and Mach number. The validity of the analysis is substantiated by test data.

SUCCESSFUL designs of axial flow turbomachines depend to a considerable extent upon accurate knowledge and understanding of the flow in these devices. For a considerable time, two-dimensional, cascade theory in conjunction with boundary layer concepts have been the basis of the design of most axial compressors and pumps as indicated in (1 and 2).⁴ However, axial flow impulse turbines are not susceptible to the same rigorous analysis because of the complex flow phenomena found in high solidity cascades with large turning angles and relative, small flow passages. Impulse turbines are defined as turbines which expand completely the available energy in the nozzle and then extract the kinetic energy in the following rotor by turning of the relative flow (110 to 140 deg) under constant static pressure. A typical blade section of an impulse turbine is shown in Fig. 1 together with a design velocity diagram. In view of the complex flow phenomena, turbine design practice made use of one-dimensional streamline concepts (3). The one-dimensional streamline concept is based on the Euler equation of change of momentum. The state of the art was gradually refined by introducing empirical corrections for three-dimensional effects and other losses which were determined by extensive test programs. An excellent review of these design procedures initiated by the work of Stodola (3) is given in (4) and several NACA reports, for example (5). Altogether, in the state of the art, the analysis of full admission impulse turbines is fairly well documented and has led to successful designs.

The performance of gas turbines is usually characterized by the velocity ratio (u/c_0) which denotes the ratio of the tip speed to the spouting velocity of the gas. The optimum performance of impulse turbines is achievable with (u/c_0) \approx 0.50 as demonstrated by Stodola (3). However, the development of high energy propellants and other high energy working fluids for lightweight accessory power units provided extreme high spouting velocities which do not allow turbine operation at (u/c_0) = 0.5. This is owing to stress limitations of present turbine materials. For example, Fig. 2, taken

from (6), demonstrates the limitations on tip speed according to the present technology. It can be seen that a tip speed of about 2000 fps is the highest value for accessory power units above 2000 deg inlet temperature and about 1000 hr continuous operation. In view of these stress limits, turbines are in demand which can operate efficiently at speed ratios between 0.15 and 0.3. This initiated the design of partial admission turbines and drag turbines as reviewed in (7).

In the gas turbine field, partial admission turbines were designed in the beginning by application of the well-established design philosophy of full admission turbines. This approach apparently was responsible for poor performance results. In view of this fact, detailed loss investigations were

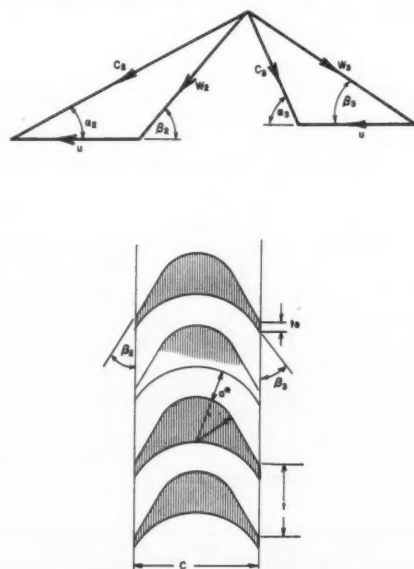


Fig. 1 Typical velocity triangle and blade section of impulse turbine

Presented at the ARS Semi-Annual Meeting, Los Angeles, Calif., May 9-12, 1960.

¹ The work reported herein was supported by the Department of the Navy, Office of Naval Research, under Contract no. NONR 2292(00), Task no. NR 094-343.

² Manager, Turbomachinery Section. Member ARS.

³ Engineering Consultant. Member ARS.

⁴ Numbers in parentheses indicate References at end of paper.

conducted in this country at MIT, leading to the work of Stenning (8). He demonstrated that additional losses occur in partial admission impulse turbines. These losses are caused by filling and emptying losses of the blade passages, pumping losses of the unadmitted part of the turbine, scavenging losses and pronounced secondary flow losses. His work found widespread use in the industry, but somehow lacked the necessary generalization for the solution of design problems. The generalization of analysis of partial admission impulse turbines and the correlation of all basic design parameters, as diameter, speed, blade height to diameter ratio, per cent of admission, aspect ratio, solidity, etc., is the objective of this paper, which summarizes the basic work of Silvern and Balje (9) for single stage turbines and of Linhardt (10) for high pressure ratio two-stage re-entry turbines. The analysis technique presented is based on the similarity concept of specific speed and specific diameter. Cordier (11) established experimentally the optimum regime of turbomachines as a function of specific speed and specific diameter, while the correlation of experiment and theory was demonstrated by Dickmann (12) for optimum ducted propellers, Buehning (13) for optimum high specific speed fans, by Bowerman (14) for high specific speed pumps, and by Silvern and Balje (9) for low specific speed turbines. Balje also showed the usefulness of this concept for matching of gas turbine components in a recent paper (15).

Design Point Analysis of Single Stage Partial Admission Impulse Turbines

The similarity parameter, specific speed, was introduced first by Thoma and co-workers in the field of hydroelectric powerplants (16). The specific speed is defined as

$$N_s = N\sqrt{Q_s}/(H_{ad})^{3/4} \quad [1]$$

and interrelates the rotative speed N (rpm), the volume flow Q_s (cfs) and the available energy H_{ad} . The specific speed can

also be expressed in terms of horsepower, resulting in the well-known relation

$$N_s = \frac{N}{(H_{ad})^{3/4}} \cdot \sqrt{\frac{550 \text{ HP } R T_s}{\eta_T P_s}} \quad [2]$$

Inspection of both equations indicates that low values of specific speed describe turbines operating at low volume flow, or low horsepower levels, using high energy propellants. For example, typical open cycle accessory power units for space vehicles or missiles operate in the low specific speed region, $N_s = 3$ to $N_s = 12$. This specific speed regime is the design area of the partial admission impulse turbines dealt within this paper.

The specific diameter as stated by Cordier connects the rotor diameter D with the volume flow Q and the available energy according to the relation

$$D_s = [D \cdot (H_{ad})^{1/4}] / \sqrt{Q_s} \quad [3]$$

The definition of the specific diameter indicates, for example, that relative large diameters are necessary for expanding high energy level propellants with small flow rates at a constant value of D_s .

A generalized analysis of partial admission turbines is now confronted with the problem of establishing the optimum relation of specific speed and specific diameter for the practical design areas of this turbine type. After completion of such an analysis, the optimum specific speed and specific diameter relation obtained determines immediately the optimum rotative speed and the optimum diameter for any given set of head and flow requirements. The following section presents a solution of this problem for single stage, partial admission impulse turbines. The mathematical solution of the problem is demonstrated in Fig. 3. The derivation of these equations is discussed in detail.

Generally, the turbine efficiency or overall efficiency is defined by

$$\eta_T = \eta_h(1 - L_t) - \sum L \quad [4]$$

where

- η_h = hydraulic efficiency
- L_t = total leakage as percentage of total mass flow
- $\sum L$ = sum of other loss terms (as percentage of available power)

The hydraulic efficiency of axial, full admission impulse turbines is given at design point by the well-known relation

$$\eta_h = 2 \left(\frac{u}{c_0} \right) (1 + \psi_R) \left(\psi_N \cos \alpha - \frac{u}{c_0} \right) \quad [5]$$

where

- ψ_N = nozzle coefficient or velocity loss coefficient of nozzle
- ψ_R = velocity coefficient of rotor
- α = nozzle angle
- (u/c_0) = velocity ratio

For calculating the overall efficiency, all occurring losses have to be subtracted from the hydraulic efficiency, as shown in Equation [4]. The losses included in the $\sum L$ term of Equation [4] are L_d the disk friction losses, L_b the blade pumping losses and L_{se} the scavenging losses. In addition, filling and emptying losses have to be considered as demonstrated in (8). Filling and emptying losses are caused by sudden ex-

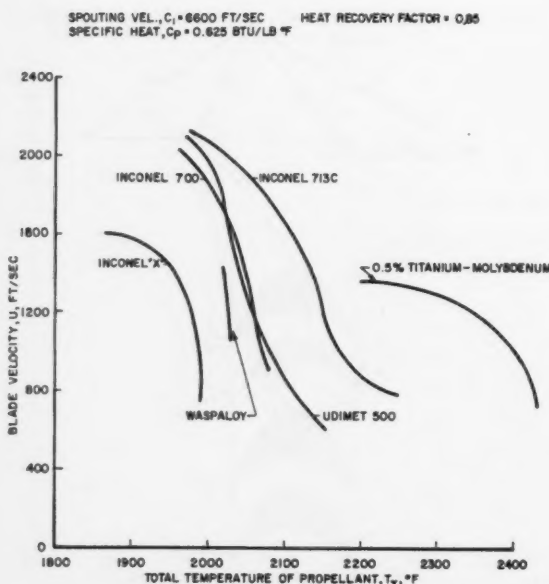


Fig. 2 Allowable blade speeds for constant stress turbine disks for 1000 hr stress rupture life

A. SINGLE STAGE TURBINE

$$\eta_T = \eta_h (1 - L_f) - \Sigma L \quad (1A)$$

$$\eta_h = 2 \frac{u}{c_0} \left(1 + \psi_R \right) \left(\psi_N \cos \alpha_2 - \frac{u}{c_0} \right) \quad (2A)$$

$$\eta_T = 2 \frac{u}{c_0} \left[1 + \psi_R \left(1 - \frac{t}{2a} \right) \right] \left[\psi_N \cos \alpha_2 - \frac{u}{c_0} \right] - \quad (3A)$$

$$\underbrace{\left(\frac{u}{c_0} \right)^3 \left(\frac{c}{a} \right) \frac{f}{\psi_N \sin \alpha_2}}_{\text{Scavenging Loss}} - \underbrace{2 \left(\frac{u}{c_0} \right)^3 \frac{u}{D} \gamma \left\{ K_w + K_p \left(1 - \frac{h}{D} \right) \left(\frac{h}{D} \right)^{1.5} \right\}}_{\text{Disc friction and pumping loss}}$$

$$\left(\frac{u}{c_0} \right) = \frac{N_s D_s}{154} \quad (4A)$$

$$\frac{t}{2a} = D_s^2 \sin \alpha_2 \psi_N \sqrt{2g} \left(\frac{h}{D} \right) \frac{\pi}{2Z} \quad (5A)$$

$$\frac{a}{\pi D} = \frac{1}{\pi h/D D_s^2 \psi_N \sin \alpha_2 \sqrt{2g}} \quad (6A)$$

$$\frac{c}{a} = \psi_N \sin \alpha_2 D_s^2 \sqrt{2g} \frac{c}{D} \frac{h}{D} \quad (7A)$$

$$\psi_R = \left[1 - 0.228 \left(1 - \frac{B}{9D} \right)^3 \right] \left[1 - 0.05 (M_w - 1)^2 \right] \left[1 - 0.06 \frac{c}{h} \right] \quad (8A)$$

$$\eta_T = \frac{N_s D_s}{77} \left\{ 1 + \psi_R \left(1 - D_s^2 \sin \alpha_2 0.96 \sqrt{2g} \frac{h}{D} \frac{\pi}{2Z} \right) \right\} \left\{ 0.96 \cos \alpha_2 - \frac{N_s D_s}{154} \right\}$$

$$\underbrace{- \frac{N_s^3 D_s^3}{154^3} 1.4 \sqrt{2g} \left(\frac{c}{D} \right) \left(\frac{h}{D} \right)}_{\text{Scavenging Loss}} - \underbrace{\frac{2 N_s^3 D_s^3}{154^3} \left\{ K_w + K_p \left(1 - \frac{1}{D_s^2 h/D \pi \sin \alpha_2 0.96 \sqrt{2g}} \frac{h}{D} \right) \left(\frac{h}{D} \right)^{1.5} \right\}}_{\text{Disc friction and pumping loss}} \quad (9A)$$

$$(\eta_T)_{\text{opt}} = \frac{\sqrt{\sin 2\beta}}{4 D_s^2 \sin \alpha_2 \sqrt{2g}} \quad (10A)$$

$$Z = \frac{\pi \sin \beta}{a/D} \quad (11A)$$

$$\eta_T = F(N_s, D_s, M_w, R_s, \alpha_2, \frac{a}{D}) \quad (12A)$$

Fig. 3 Analysis of single stage turbine

pansion of the nozzle jet when the blade passage moves from the unadmitted arc into the admitted portion of the arc and offers a larger flow area than defined by the nozzle area. This leads to a decrease of the total turning of the relative flow within the rotor or, in other words, the guidance effect of partial admission cascades is less than that of full admission cascades. Stenning's work (8) suggests that the filling and emptying losses, or cascade losses, decrease the rotor coefficient by a factor $K_f = (1 - t/2a)$, where t denotes the blade spacing and a is the nozzle arc in peripheral direction. Hence, the rotor velocity coefficient ψ_R has to be multiplied by the factor K_f for calculating the hydraulic efficiency of a partial admission turbine as shown by the first term of Equation [3A], Fig. 3. Inspection of the hydraulic efficiency indicates that partial admission losses can be decreased by using larger blade numbers than usually experienced in the field of full admission turbines.

The scavenging loss is caused by mixing of the supersonic nozzle jet and the relatively stagnant amount of fluid which is trapped in the unadmitted blade passages. The scavenging loss derived by (8) and quoted in (9) as per cent of the available power amounts to

$$L_{ss} = \frac{f}{\psi_N \sin \alpha_2} \left(\frac{c}{a} \right) \left(\frac{u}{c_0} \right)^3 \quad (6)$$

where

c = chord length

a = arc of admission

f = mixing coefficient [quoted in (8) to be equal to 1.5]

The disk friction loss is derived by Stodola (3) and can be expressed as per cent of the available energy by writing

$$L_d = 2 K_w \gamma D^2 (u/\dot{w}) (u/c_0)^2 \quad (7)$$

where

γ = density of gas surrounding wheel disk

D = disk diameter

K_w = a factor representing influence of distance of stationary shrouds and influence of disk Reynolds number

The factor K_w is evaluated in (17) for a large range of Reynolds numbers. Further loss to be considered in partial admission turbines is the blade pumping loss of the blades in the unadmitted arc of the turbine periphery. This loss can be expressed according to (9) as loss of the percentage of the available energy by the following equation

$$L_b = 2 K_b D^2 \gamma \left(\frac{u}{\dot{w}} \right) \left(\frac{u}{c_0} \right)^2 \left[\left(1 - \frac{a}{\pi D} \right) \left(\frac{h}{D} \right)^{1.5} \right] \quad (8)$$

where

(h/D) = blade height to diameter ratio

u = tip speed

$(a/\pi D)$ = per cent of admission

Combining now Equations [4 through 8], the shaft efficiency of partial admission turbines is found to be

$$\eta_T = 2 \left(\frac{u}{c_0} \right) \left[1 + \psi_R \left(1 - \frac{t}{2a} \right) \right] \left(\psi_N \cos \alpha - \frac{u}{c_0} \right) - \frac{f}{\psi_N \sin \alpha} \left(\frac{c}{a} \right) \left(\frac{u}{c_0} \right)^3 - 2 \gamma D^2 \left(\frac{u}{\dot{w}} \right) \left(\frac{u}{c_0} \right)^2 \times \left[K_w + K_b \left(1 - \frac{a}{\pi D} \right) \left(\frac{h}{D} \right)^{1.5} \right] \quad (9)$$

The next step is now the generalization of this efficiency expression by introducing the similarity parameters, specific speed and specific diameter. In this way the velocity coefficient (u/c_0) is related to specific speed and specific diameter by

$$u/c_0 = N_s D_s / 154 \quad (10)$$

Considering now that definite interrelationships exist between the degree of admission, weight flow, the ratio of spacing to arc of admission, and the ratio of chord lengths to arc of admission, the efficiency can be expressed as a function of the basic similarity parameters. The individual relations are given in Fig. 3, Equations [4A through 8A]. Combining these equations, the following general equation for the turbine efficiency is obtained

$$\eta_T = \frac{N_s D_s}{77} \left\{ 1 + \psi_R \left[1 - D_s^2 \sin \alpha_2 \psi_N \sqrt{2g} \left(\frac{h}{D} \right) \left(\frac{\pi}{2Z} \right) \right] \right\} \cdot \left\{ \psi_N \cos \alpha - \frac{N_s D_s}{154} \right\} - 1.4 \sqrt{2g} \left(\frac{c}{D} \right) \left(\frac{h}{D} \right) \frac{N_s^3 D_s^5}{154^3} - \frac{2 N_s^3 D_s^5}{154^3} \left\{ K_w + K_b \left(1 - \frac{1}{D_s^2 (h/D) \pi \sin \alpha_2 \psi_N \sqrt{2g}} \right) \left(\frac{h}{D} \right)^{1.5} \right\} \quad (11)$$

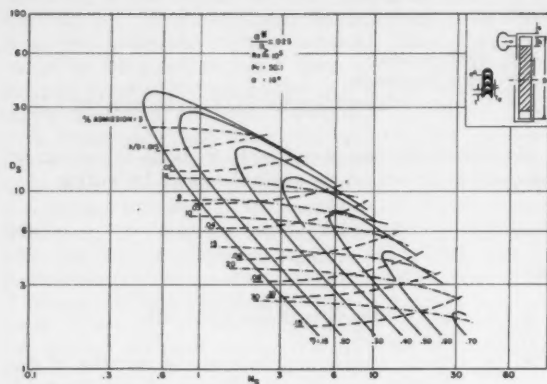


Fig. 4 $N_s D_s$ diagram for axial turbines with small blade numbers

Equation [11] indicates that it is sufficient to determine the interrelationship between ψ_R , ψ_N , (h/D) , (c/D) and z in order to calculate the maximum obtainable efficiency of all axial impulse turbines. Thereby, it is to be noted that ψ_R is a function of β , which is related to α_2 according to

$$\cot \beta = \cot \alpha_2 - (u/c_0)/(\psi_N \sin \alpha_2) \quad [12]$$

A detailed analysis and literature search was conducted and reported in (9) in order to estimate the effect of profile losses, leakage losses, Mach number and Reynolds number influences on the rotor coefficient ψ_R . The results of this investigation led to the following equation, which is suitable for expressing

$$\eta_T = \frac{N_s D_s}{77} \left\{ 1 + \left[1 - 0.228 \left(1 - \frac{\beta^\circ}{90^\circ} \right)^3 \right] \left[1 - 0.05 (M_w - 1)^2 \right] \left[1 - \frac{0.24 D_s}{z} \sqrt{\pi \sin \alpha \sin 3 \beta \sqrt{2g}} \right]^2 \right\} \times \\ \left(0.96 \cos \alpha_2 - \frac{N_s D_s}{154} \right) - 1.4 \frac{N_s D_s^4}{z} \frac{(\sin 2\beta\pi)^{1.5}}{\sqrt{\sin \alpha} (154)^3} \sqrt{2g} - \frac{2 N_s D_s^5}{154^3} \sqrt{2g} \times \\ \left[K_w + K_b \left(1 - \frac{1}{D_s \sqrt{\sin \alpha_2 \sin 3 \beta \pi \sqrt{2g} 0.48}} \right) \left(\frac{\sqrt{\sin 2\beta\pi}}{2 D_s \sqrt{\sin \alpha \sqrt{2g}}} \right)^{1.5} \right] \quad [15]$$

the velocity coefficient of impulse blades as a function of deflection angle, Mach number and aspect ratio (h/c)

$$\psi_R = \left[1 - 0.228 \left(1 - \frac{\beta^\circ}{90^\circ} \right)^3 \right] \times \\ \left[1 - 0.05 (M_w - 1)^2 \right] \left[1 - 0.06 \left(\frac{c}{h} \right) \right] \quad [13]$$

From this equation it can be seen that the relative Mach number M_w and the aspect ratio have pronounced effects on the blade coefficient ψ_R . The Reynolds number effect is neglected in Equation [13] owing to lack of pertinent information for Reynolds numbers smaller than 10^4 . This equation is also based on the assumption that the ratio of the trailing edge thickness to the spacing (in circumferential direction) is smaller than 0.02 and that the clearance ratio of the tip clearance to the blade height is smaller than 0.02. The nozzle coefficient ψ_N is very well established as a function of Mach number. The experiments of Keenan (18) and the investigations of (9) demonstrated that the nozzle velocity coefficient can, in almost all cases, be assumed ψ_N equal to 0.96, as long as pitch chord ratios of 0.6 to 0.9 are achieved.

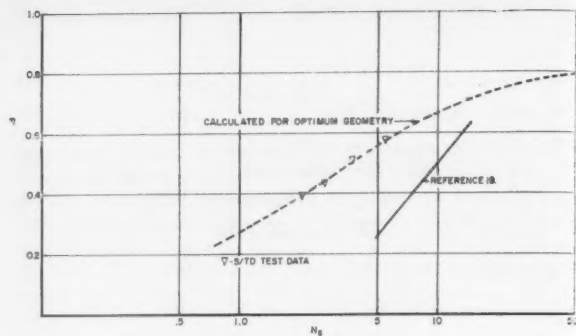


Fig. 5 Comparison of test data with theory of low specific speed axial turbines

Combining Equations [11 and 13], an approximate optimization analysis was conducted by partial differentiation (9). This resulted in the following equation for optimum blade height to diameter ratio

$$\left(\frac{h}{D} \right)_{opt} = \sqrt{\frac{\sin 2 \beta}{4 D_s^2 \sin \alpha \sqrt{2g}}} \quad [14]$$

This equation indicates that the optimum blade height to diameter ratio is not an independent parameter but is determined by specific diameter and the nozzle angle. Using the optimum blade height to diameter relation the maximum efficiency of single stage axial turbines can be written in the final form

This final equation demonstrates that the maximum obtainable efficiency is a definite function of specific speed and specific diameter. The nozzle angle α and the number of blades or the ratio of cutter diameter to rotor diameter (see Eq. [11A], Fig. 3) are secondary parameters. Selecting an average nozzle angle of about 16 deg (9) and using a practical ratio of cutter to rotor diameter ($a^*/D = 0.01$ to 0.025) Equation [15] can be evaluated and lines of constant efficiency as a function of specific speed and specific diameter can be plotted. This leads to a general design chart called $N_s D_s$ diagram, as shown in Fig. 4 for partial admission, axial impulse turbines. An inspection of this diagram reveals the following trends: The optimum degree of admission decreases with decreasing specific speed. In order to obtain higher efficiencies at decreasing specific speeds, the specific diameter has to be increased, and the ratio of blade height to rotor diameter has to be decreased. This means that turbines with low degrees of admission must show comparatively large rotor diameters with comparatively short blades. The ratio of cutter diameter to rotor diameter should be minimized, and it also follows that the number of blades should be maximized, which means that low specific speed turbines

show optimum efficiencies only if the maximum possible number of blades is selected. In contrast, full admission turbines show best efficiencies at considerably smaller specific diameters and considerably larger ratios of blade height to rotor diameter. This also means that full admission turbines usually show a comparatively low number of blades for optimum efficiency and also comparatively long blades. Therefore, it becomes evident that only inefficient, partial admission turbines are obtained if the design philosophy of full admission turbines is adopted for designing partial admission impulse turbines.

Finally, the predicted efficiencies and optimum geometries are compared with test data of turbines built according to the outlined theory and turbines mentioned in the literature (19). The result of this comparison is shown in Fig. 5. It can be seen that turbines of optimized geometries perform closely to the theory presented. The agreement of experiment and theory is achieved in the low specific speed region $N_s = 2$ to 8. For the specific speed of 3, an efficiency of about 45% is achieved. Comparing the results of (19), which shows far less efficient machines in that specific speed range, the usefulness of the optimum analysis is clearly demonstrated. For practical purposes of design, it is now sufficient to use the $N_s D_s$ diagram of Fig. 4 for solving a given problem. For more detailed analysis, the mathematical formulation of the analysis may be useful, as is summarized in Fig. 3.

Analysis of Pressure Staged, Impulse Re-Entry Turbines

For the lightweight accessory power units, certain improvements of the overall efficiency are still desirable in the low specific speed region from 2 to 12. This can be achieved by multistaging. However, by designing multistage turbines in the conventional fashion of multidisk designs, greater turbine weights and increased rotor complexities are the consequence. Hence, such a design would not be feasible for serious consideration in small accessory power units where simplicity inherent in single disk turbines must be retained. An attractive solution of combining single disk designs with the multistage performance is offered by so-called "re-entry-type turbines," where several partial admission impulse stages are combined within one single disk, as shown in Fig. 6. The stages themselves are pressure staged. Fig. 6 demonstrates the design geometry of a two-stage re-entry turbine without crossover ducts. This means that the gas is admitted on one side of the rotor, passes through the rotor, is collected and passed through the rotor again, and hence, leaves the turbine at the same side where the first stage is located. In other words, the design consists of two stages with opposed flow directions. Since both stages operate as partial admission turbines, it is evident that partial admission losses such as filling and emptying losses, pumping losses, etc., will appear in this turbine type. However, disk friction will be smaller in the single disk turbine than in the conventional multidisk turbine, so that the single disk turbine does not only show disadvantages, but also some aerodynamic advantages (9). The performance analysis of this arrangement was presented first by Silvern (9) for the case of moderate pressure ratios and different number of stages. The theoretical and experimental analysis of high pressure ratio two-stage re-entry turbines is discussed in the following section.

The potential of high pressure ratio, two-stage re-entry turbines was investigated (10), applying the same technique of analysis which has proved fruitful for single stage, partial admission turbines. This technique of analysis was demonstrated in detail in the foregoing sections. Briefly, the analysis of two-stage re-entry turbines consists of the summa-

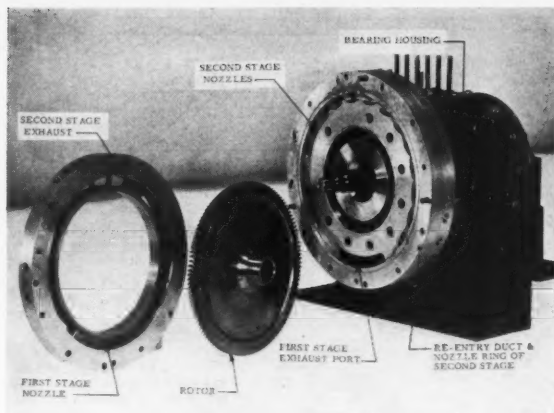


Fig. 6 Exploded view of two-stage re-entry turbine

tion of the partial admission losses experienced by each stage, and the results of theoretical and experimental investigations of additional losses less predominant in single stage turbines. Then, the overall efficiency can be calculated from the definition

$$\eta_T = \bar{\eta}_h(1 - L_l) - L_b - L_d \quad [16]$$

where

- $\bar{\eta}_h$ = average hydraulic efficiency
- L_l = sum of all leakage losses
- L_d = disk friction loss
- L_b = pumping loss of both stages

The average hydraulic efficiency of a two-stage partial admission turbine is derived (10) yielding the following expression

$$\bar{\eta}_h = 4 \left(\frac{u}{c_0} \right) \times \left\{ 1 + \bar{\psi}_R \left[1 - \frac{t}{4a_1} \left(1 + \frac{a_1}{a_{11}} \right) \right] \right\} \left\{ \bar{\psi}_N \cos \alpha - \frac{u}{c_0} \right\} \quad [17]$$

where

- $\bar{\psi}_R$ = average blade coefficient
- $\bar{\psi}_N$ = average nozzle coefficient
- (a_1/a_{11}) = ratio of arc of admission of first stage to arc of admission of second stage

The average blade coefficient is readily determined from the algebraic mean of both blade coefficients, which can be calculated for each Mach number level, according to the general relation stated by Equation [13]. The average nozzle coefficient is defined according to

$$\bar{\psi}_N = \frac{1}{2} \left[\psi_{N1} \left(\frac{c_{01}}{c_0} \right) + \psi_{N2} \left(\frac{c_{02}}{c_0} \right) \right] \quad [18]$$

where

- ψ_{N1}, ψ_{N2} = individual stage nozzle coefficients
- c_{01}, c_{02} = spouting velocities of first and second stage
- c_0 = total spouting velocity of turbine

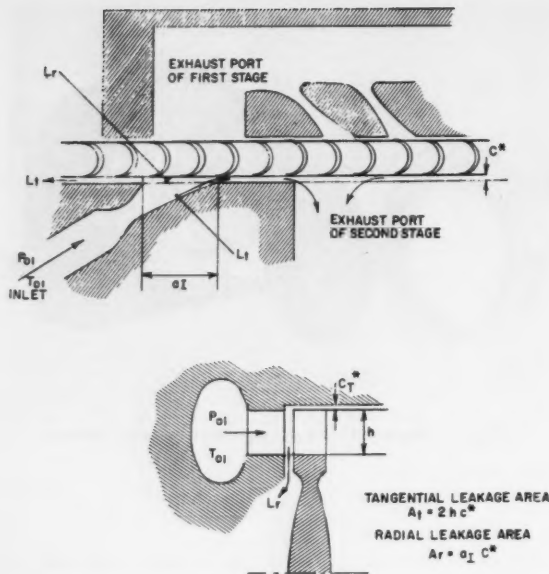


Fig. 7 Leakage paths of two-stage re-entry turbine with opposed flows in both stages

The summation of disk friction and windage losses is immediately obtained from the single stage relations, and hence, does not have to be repeated here. The scavenging loss becomes nearly negligible for two-stage re-entry turbines as outlined by (10). Leakage appeared to be the predominant loss in two-stage re-entry turbines as already stated in (9). Therefore, a special effort was made to analyze the leakage paths and subsequent leakage losses. The analysis was conducted for the case of a two-stage re-entry turbine without crossover duct, as shown in Fig. 7, where the first stage nozzle is located on the same side as the exhaust port of the second stage. This figure illustrates that tangential and radial leakage flow occur between the first stage nozzle exit and the exhaust port of the second stage. This leakage loss is caused by the pressure gradient between rotor inlet and exhaust of the turbine. In the case of high pressure ratio turbines, the pressure ratio between the nozzle exit of the first stage and the exhaust of the second stage is always higher than the critical pressure ratio and hence, the leakage flow is determined by the choked flow relation

$$\dot{w} = C_F \sqrt{2g \frac{k}{k+1} \left(\frac{2}{k+1} \right)^{\frac{1}{k-1}}} A^* \frac{P_0}{\sqrt{RT_0}} \quad [19]$$

where P_0 and T_0 describe the total conditions in front of the leakage throat area A^* . For the preliminary analysis, it was assumed that the static conditions at the nozzle exit represent the total condition in front of the tangential leakage area A_t , equals $2C^*h$, and the radial leakage area A_r , equals

C^*a_1 . Then, the total leakage loss for the design geometry chosen is determined by the following relation, where the leakage loss is expressed as ratio of the total mass flow

$$L_t = C_F \left(\frac{C^*}{D} \right) \left(\frac{D^2}{A^*} \right) \left[2 \frac{h}{D} + \frac{a_1}{D} \right] F_1(M_{a1}) \quad [20]$$

The function F_1 denotes the ratio of static condition in front of the leakage area to the total conditions in front of the nozzle throat area of the first stage. (D^2/A_1^*) is the ratio of the wheel diameter squared to the nozzle throat of the first stage, and C_F is the restriction factor which is usually found to be in the order of $C_F = \frac{2}{3}$, as reported (9). Substituting all loss relations in Equation [16], the basic efficiency equation of two-stage re-entry turbines is obtained.

In the next step, the equation is generalized by use of the similarity concept of specific speed and specific diameter. The analysis of single stage turbines has shown that only four parameters are necessary for describing completely the design and performance parameters of single stage turbines. These parameters are: The specific speed N_s , specific diameter D_s , the relative Mach number M_w and the Reynolds number Re . In the case of the two-stage re-entry turbine, another independent variable exists. That is, the pressure split between both stages or, in other words, the ratio of the specific diameters of both stages. For the analysis of two-stage re-entry turbines, it was found convenient to use the alternative expression of specific diameter, as derived in (9)

$$D_s = \frac{\sqrt[4]{\frac{k}{k-1}} \sqrt[4]{1 - \delta_{tot} \frac{k-1}{k}}}{\sqrt{\frac{A_1^*}{D^2}} \sqrt{\psi} \sqrt{P_{r,tot}} \sqrt{1 - \eta_T} \left(1 - \delta_{tot} \frac{k-1}{k} \right)} \quad [21]$$

where

- δ_{tot} = reciprocal of overall total pressure ratio
- η_T = turbine efficiency
- k = specific heat ratio
- ψ = nozzle function for choked flow

$$\psi = \sqrt{2g \frac{k}{k+1} \left(\frac{2}{k+1} \right)^{\frac{k}{k-1}}} \quad [22a]$$

In the case of unchoked flow, ψ amounts to

$$\psi = \sqrt{2g \frac{k}{k-1} \left[\left(\frac{1}{P_r} \right)^{2/k} - \left(\frac{1}{P_r} \right)^{\frac{k+1}{k}} \right]} \quad [22b]$$

where P_r denotes the stage pressure ratio. (A_1^*/D^2) is the ratio of the throat area of the first stage nozzle to the rotor diameter squared. The specific diameter of each stage can now be expressed analogous to Equation [21], resulting in the following relations for D_{sI} and D_{sII} . The specific diameter of the first stage is

$$D_{sI} = \frac{\sqrt[4]{\frac{k}{k-1}} \sqrt[4]{1 - \delta_{I1} \frac{k-1}{k}} \delta_{I1}}{\sqrt{\left(\frac{A_1^*}{D^2} \right) \psi \left[1 - \psi_N^2 \left(1 - \delta_{I1} \frac{k-1}{k} \right) \right]}} \quad [23]$$

and the specific diameter of the second stage amounts to

$$D_{sII} = \frac{\sqrt[4]{\frac{k}{k-1}} \sqrt[4]{1 - \delta_{II} \frac{k-1}{k}} \delta_{II}}{\sqrt{\left(\frac{A_1^*}{D^2} \right) \psi \left[1 - \eta_I \left(1 - \delta_{II} \frac{k-1}{k} \right) \right] \left[1 - \psi_N^2 \left(1 - \delta_{II} \frac{k-1}{k} \right) \right]}} \quad [24]$$

where

- δ_I = reciprocal of pressure ratio of first stage
 δ_{II} = reciprocal of pressure ratio of second stage
 η_I = efficiency of first stage
 ψ_N = nozzle coefficient

It is to be noted that the equations shown present only approximate relations which neglect leakage and assume the static pressure at the exhaust of each stage similar to that at each nozzle exit. For further calculations, it was found convenient (10) to define the ratios of the stage specific diameters to the overall specific diameter ($D_{s1}/D_{s\text{ tot}}$) and ($D_{s11}/D_{s\text{ tot}}$), which can easily be derived by combinations of Equations [21, 23 and 24]. These stage to overall specific diameter ratios are shown in Fig. 8, Equations [5B] and [6B]. The specific diameter ratio ($D_{s1}/D_{s\text{ tot}}$)² of the first stage is denoted k_1 , and that of the second stage k_2 . In addition, a function k_3 is used, as defined by Equation [7B], Fig. 8. It can be seen that k_3 is dependent only on the overall pressure ratio and specific heat ratio of the gas k or, in other words, k_3 is a function of $D_{s\text{ tot}}$. Combining now the N_s - D_s relations of the single stage turbine and using the specific diameter ratios k_1 , k_2 and k_3 , the turbine efficiency can be expressed exclusively as a function of the specific diameter, ratio of specific diameter of the first stage to specific diameter of the second stage, specific speed, Mach number and Reynolds number range of the turbine. For calculating now an N_s - D_s diagram of two-stage re-entry turbines, it is necessary to determine the optimum pressure split or the optimum ratio of the specific diameters. However, owing to the mathematical complexity of the equations involved, the general optimization of pressure split as a function of N_s and D_s was not obtained by (10). The problem was only solved approximately by calculating N_s - D_s diagrams for the cases of equal work and equal pressure ratios in both stages. The calculations were conducted for Reynolds numbers larger than $Re = 10^4$ and for the overall pressure ratio $Pr = 300:1$. The result of this analysis is shown in Fig. 9, where the optimum efficiency obtainable with turbines having equal pressure ratios and equal heads in both stages is compared for the range of specific speed between 3 and 15. It can be seen that turbines having equal pressure ratios in both stages are more efficient in the specific speed range from 4 to 15.

In order to substantiate the analysis of two-stage re-entry turbines, a turbine was designed having equal pressure ratios in both stages. The performance was then evaluated and is described in detail (10). The turbine configuration used is shown in Fig. 6 and is characterized by an aspect ratio of $c/h = 0.855$, a blade height to diameter ratio $h/D = 0.055$ and the stage pressure ratio $Pr = 17.3:1$. The blade angle is $\beta = 30$ deg, and the number of blades amounts to 120. Due to speed limitations of the test facility at that time, the turbine was designed for the specific speed $N_s = 11.9$ instead, for the optimum specific speed of about 19 for the design specific diameter $D_s = 2.58$. Tests were conducted with nitrogen of 716 R inlet temperature and 90 psia inlet pressure. The performance of the turbine was evaluated by torque measurements and by temperature measurements between inlet and exhaust stations. Pressure pickups and several thermocouples were installed at the exhaust of the first stage nozzle, exhaust of the first stage, inlet of the second stage and at the exhaust of the second stage. The instrumentation was necessary in order to evaluate approximately the stage performance. The turbine efficiency measured is plotted vs. the velocity coefficient u/c_0 in Fig. 10, showing the test results for clearance 0.005 in. and clearance 0.017 in. The test result of clearance 0.005 in. is compared in this diagram with the prediction of the preliminary N_s - D_s diagram. It can be seen that the measured performance differs about

B. TWO-STAGE RE-ENTRY TURBINE

$$\eta_T = \eta_h (1 - L_1) - L_d - L_b \quad (1B)$$

$$\eta_h = \left(\frac{4}{154} \right) N_s D_s \left\{ 1 + \frac{\pi}{4} \left[1 - \frac{1 + \frac{\pi}{2}}{4} \left(1 + \frac{\pi}{2} \right) \right] \right\} \left(\frac{\psi_N \cos \alpha}{154} \right) \quad (2B)$$

$$\frac{\psi_N}{\psi_R} = \left(\frac{\psi_{N1} + \psi_{N2}}{2} \right) \quad \text{Hydraulic efficiency} \quad (3B)$$

$$\psi_N = \frac{1}{2} \left[\sqrt{1 - \delta_I \frac{\pi-1}{\pi}} \psi_{N1} + \sqrt{1 - \delta_{II} \frac{\pi-1}{\pi}} \psi_{N2} \right] \quad (4B)$$

$$k_1 = \left(\frac{D_{s1}}{D_{s\text{ tot}}} \right)^2 = \frac{\sqrt{1 - \delta_I \frac{\pi-1}{\pi}}}{\sqrt{1 - \delta_{\text{tot}} \frac{\pi-1}{\pi}}} \left[\frac{1 - \eta_{\text{tot}} (1 - \delta_{\text{tot}} \frac{\pi-1}{\pi})}{1 - \psi_N^2 (1 - \delta_{\text{tot}} \frac{\pi-1}{\pi})} \right] \left(\frac{Pr_{\text{tot}}}{Pr I} \right) \quad (5B)$$

$$k_2 = \left(\frac{D_{s2}}{D_{s\text{ tot}}} \right)^2 = \frac{\sqrt{1 - \eta_I (1 - \delta_I \frac{\pi-1}{\pi})} \sqrt{1 - \delta_{II} \frac{\pi-1}{\pi}}}{\sqrt{1 - \delta_{\text{tot}} \frac{\pi-1}{\pi}}} \quad (6B)$$

$$k_3 = \frac{Pr_{\text{tot}} \sqrt{2g \frac{\pi}{\pi-1}} \left(\frac{2}{\pi-1} \right)^{\frac{1}{\pi-1}} \left[1 - \eta_T (1 - \delta_{\text{tot}} \frac{\pi-1}{\pi}) \right]}{\sqrt{1 - \delta_{\text{tot}} \frac{\pi-1}{\pi}}} \quad (7B)$$

$$L_1 = L_{s1} + L_d \quad (8B)$$

$$L_1 = C_F \left(\frac{C}{D} \right) \left\{ \frac{K_3}{K_1} \left[1 + \frac{K_2}{K_1} \right] \frac{(F_1 + F_2)}{\psi_N \sin \alpha \sqrt{2g}} \right. \quad (9B)$$

$$+ \frac{\text{Static leakage in axial and } \pi \text{ } K_3}{\left[1 + \frac{K_2}{K_1} \right] D_{s\text{ tot}} F_1} + 2 C_{F_T} \left(\frac{C}{D} \right) K_3 D_{s\text{ tot}} \left(\frac{C}{D} \right) F_1$$

radial direction tip leakage

$$+ C_D \frac{N_s D_s}{154} \left[\left(\frac{C}{D} \right) \sqrt{\frac{1 - \delta_{\text{tot}} \frac{\pi-1}{\pi}}{1 - \delta_I \frac{\pi-1}{\pi}}} \frac{\left[1 + \frac{\pi}{2} \right]}{\psi_N \sin \alpha \sqrt{2g}} \right]$$

Dynamic leakage

$$L_d = K_d \frac{\sqrt{2g}}{154^3} N_s^3 D_{s\text{ tot}}^3 \quad (10B)$$

Disc friction loss

$$L_b = K_b \sqrt{2g} \sqrt{\frac{1 - \delta_{\text{tot}} \frac{\pi-1}{\pi}}{1 - \delta_I \frac{\pi-1}{\pi}}} \psi_N (1 - \epsilon) \frac{N_s^3 D_{s\text{ tot}}^3}{154^3} \left[\frac{1}{\epsilon \sin \alpha \sqrt{2g} K_1 D_{s\text{ tot}}} \left(1 + \frac{\pi}{2} \right) \right]^{1.8} K_1 \quad (11B)$$

Blade pumping loss

$$\epsilon_{\text{opt}} = \frac{\alpha_I + \alpha_{II}}{\pi D} \left(\frac{1 + \frac{\pi}{2}}{\frac{\pi}{2}} \right) \frac{\sqrt{F_2(MI)}}{\psi_N D_{s\text{ tot}} \sqrt{K_1 \psi_N \sin \alpha \sqrt{2g}}} \quad (12B)$$

$$F_1 = (M_{s1}) = \frac{\sqrt{1 + \frac{\pi-1}{2} \psi_{N1}^2 M_{12}^2}}{\left(1 + \frac{\pi-1}{2} \psi_{N1}^2 M_{12}^2 \right)^{\frac{1}{\pi-1}}} \quad (13B)$$

$$F_2 = \left[\frac{1 + \frac{\pi-1}{2} \psi_N^2 M_{12}^2 \left\{ (\cos^2 \alpha + 1) + \frac{\pi-1}{2} \cos^2 \alpha \psi_N^2 M_{12}^2 \right\}}{1 + \frac{\pi-1}{2} M_{12}^2 \left\{ (\psi_N^2 + 1) + \frac{\pi-1}{2} \psi_N^2 M_{12}^2 \right\}} \right]^{\frac{\pi}{\pi-1}} \quad (14B)$$

$$\eta_T = F \left(N_{s\text{ tot}}, D_{s\text{ tot}}, \frac{D_{s1}}{D_{s2}}, Mw(Pr), Re \right) \quad (15B)$$

Fig. 8 Analysis of two-stage re-entry turbine

10 points from the predicted performance for the design point $u/c_0 = 0.2$. The maximum efficiency occurs about at $u/c_0 = 0.3$ and amounts to about $\eta_T = 0.62$. The torque efficiency and temperature efficiency are compared in Fig. 11, which illustrates good agreement at the design point. The discrepancy between preliminary analysis and test was somewhat surprising. In order to locate the source of additional losses not encountered in the preliminary performance analysis, detailed tests of the components were conducted. The nozzles were tested separately under static and dynamic conditions, leakage was measured during stalled and running conditions, the re-entry duct was calibrated and

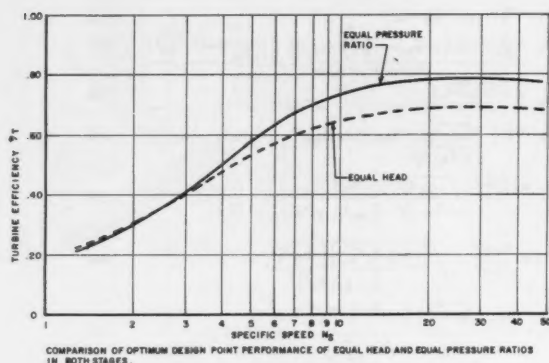


Fig. 9 Two-stage re-entry turbine for $P_r = 300:1$

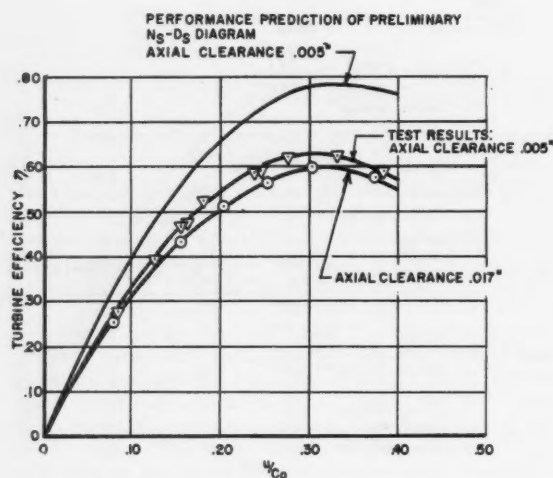


Fig. 10 Performance of two-stage re-entry turbine for pressure ratio $P_r = 300:1$

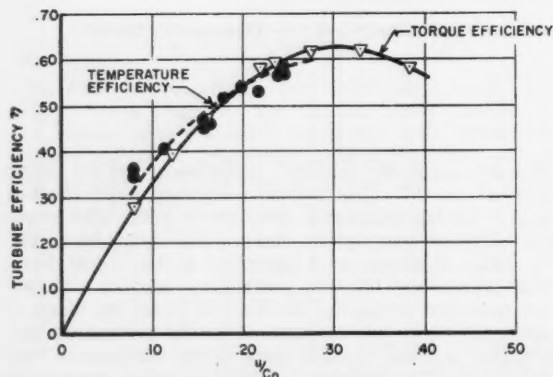


Fig. 11 Comparison of torque and temperature efficiency for clearance $C^* = 0.005$ in.

the pressure losses evaluated. Analysis of the component performance demonstrated clearly (10) that the discrepancy was mainly caused by leakage and less effective blade and nozzle performance. It was found that the leakage of high pressure ratio turbines is strongly influenced by the tangential jet component of the first stage nozzle. Analysis revealed that in the case of supersonic tangential jet velocities, shocks occur in front of the leakage gap, such increasing the density and, hence, increasing the leakage flow from first stage nozzle to exhaust. To account approximately for this complex effect, it was assumed (10) that total conditions are governing the leakage flow in direction of the tangential jet component, whereas static conditions are still valid for calculating the leakage through all other clearance gaps. This concept led to the following equation for predicting the actual measured leakage values

$$L_t = C_F \left(\frac{c^*}{D} \right) \left(\frac{D^2}{A_1^*} \right) \left[\left(\frac{h}{D} + \frac{a_1}{D} \right) F_1 + \left(\frac{h}{D} \right) F_2 \right] + 2C_{FT} \left(\frac{C_T^*}{D} \right) \left(\frac{D^2}{A_1^*} \right) \left(\frac{c}{D} \right) F_1 \quad [25]$$

This equation is of similar structure as the leakage Equation [20]. The only difference is that the function F_2 is introduced which describes the total conditions in front of the leakage gap in direction of rotation. The leakage function $F_2 (Mi_1)$ is presented by Equation [14B], Fig. 8. The second term of Equation [25] accounts approximately for the tip leakage. The restriction factor C_F or C_{FT} amounts about to $C_F = \frac{2}{3}$. Evaluation of Equation [25] resulted in an excellent correlation between experiment and theory, as demonstrated by Fig. 12. In addition to the increased static leakage, it was found that "dynamic leakage" occurred in the turbine. This is illustrated in Fig. 13, where the measured leakage is plotted vs. the velocity ratio u/c_0 . The dynamic and static leakage is indicated in that figure. The analysis of (10) has shown that dynamic leakage is caused by an amount of fluid of the first stage

$$\Delta \dot{w}_d = C_D \cdot \chi \cdot \rho \cdot h \cdot c \cdot u \quad [26]$$

which is trapped in the blade passage. χ denotes the blade density ratio, and C_D is a restriction factor, which depends on exhaust geometry of the first stage and the density before and after it is trapped. Considering that vacuum cannot exist in the blades passage of a partial admission turbine, it appears that dynamic leakage will always occur, regardless how large the exhaust port is designed. The dynamic leakage can be expressed as ratio of the total mass flow by the following relation

$$L_d = C_D \chi \left(\frac{u}{c_0} \right) \left(\frac{c_0}{c_{01}} \right) \frac{(c/a_1)}{\psi_N \sin \alpha_1} \quad [27]$$

The test result shown in Fig. 12 can be predicted by Equation [27] when a restriction factor of $C_D = 0.35$ is used in connection with the measured blade density of $\chi = 0.60$. It is to be mentioned that C_D is generally not a constant but a variable dependent on the interstage pressure ratio. Further analysis of the dynamic leakage is in preparation.

Investigation of the stage performance also indicated that a nozzle coefficient of $\psi_N = 0.96$, assumed as achievable in the preliminary analysis, is somewhat optimistic and that usual designs achieve only nozzle coefficients in the order of $\psi_N = 0.92$. This is mainly due to manufacturing errors and incident losses caused by interference of the moving cascades and

the nozzle jet. Furthermore, the measured blade coefficients seemed to be somewhat lower than predicted by Equation [8A], Fig. 3. Fig. 14 compares the blade coefficients determined from the test data with the predicted blade coefficients of Equation [8A], Fig. 3. The analysis implied that the lower values of the blade coefficients are caused by shock and separation phenomena within the constant area blade channels (see Fig. 1), while the higher blade coefficients predicted by Equation [8A], Fig. 3, may only be achieved or superseded with so-called "supersonic blade passages" investigated by (20). In the case of constant area blade passages, ψ_R follows closely the empirical equation (for $M_w > 1$) and ($\beta = 30$ deg)

$$\psi_R = 0.90 [1 - 0.12 (M_w - 1)^{1.5}] \quad [28]$$

as shown (10).

The analysis of the test data determined new loss relations for leakage and blade losses. Introducing the similarity parameters, specific speed, specific diameter and the ratio of the specific diameter of each stage in the newly derived loss relations [25, 27 and 28], the final efficiency equation for two-stage re-entry turbines suitable for high pressure ratios is obtained. The detailed result is shown in Fig. 8, Equations [1B] through [15B]. The essential result of the analysis is summarized in Equation [15B], Fig. 8, which demonstrates overwhelmingly that only five parameters are necessary for determining completely the geometric design parameters and the loss relations of two-stage re-entry turbines. These parameters are: The overall specific speed, the overall specific diameter, the ratio of the stage specific diameters, the relative Mach number and the Reynolds number of the turbine. At this point it has to be mentioned that (10) did not show explicitly the interrelation of the total per cent of admission $\epsilon = (a_1 + a_{11})/\pi D$, and the specific diameter $D_{s, tot}$ as given by Equation [12B], Fig. 8. Equation [12B] was obtained by differentiating the overall efficiency relation Equation [1B], Fig. 8, for negligible blade pumping and disk friction losses.

Using all relations shown in Fig. 8, a final $N_s D_s$ diagram for two-stage re-entry turbines with equal pressure ratios in both stages was constructed and is presented in Fig. 15. This diagram is valid for an overall pressure ratio of 300:1 and a

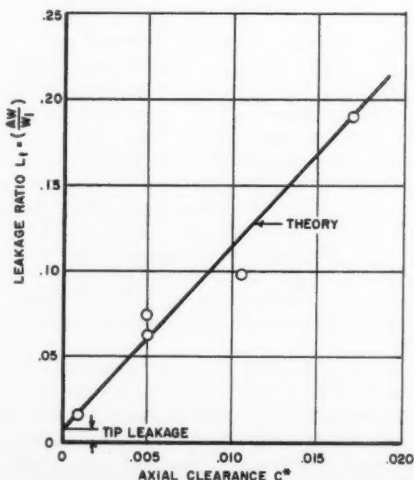


Fig. 12 Static leakage of two-stage single disk turbine $P_r = 300:1$

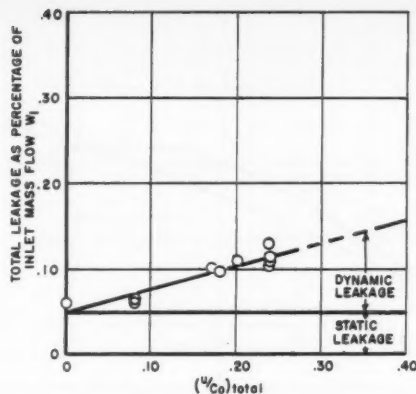


Fig. 13 Measured leakage of two-stage single disk turbine $P_r = 300:1$, clearance $C^* = 0.005$ in.

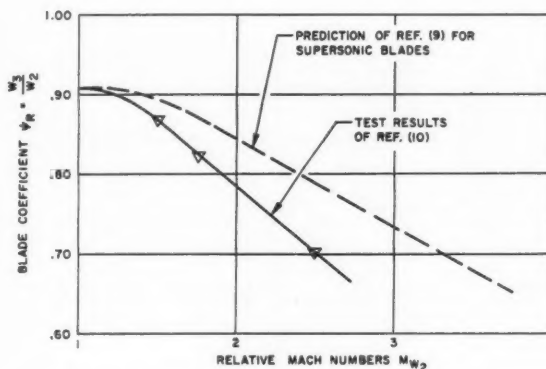


Fig. 14 Mach number relation for $\beta = 30$ deg constant channel blade sections

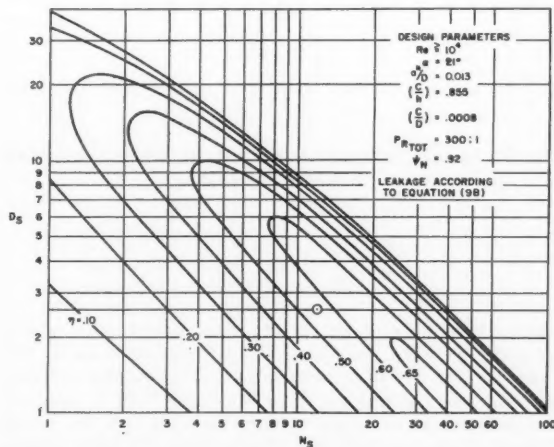


Fig. 15 Final $N_s D_s$ diagram for two-stage re-entry turbines with equal pressure ratio in both stages and 300:1 overall pressure ratio

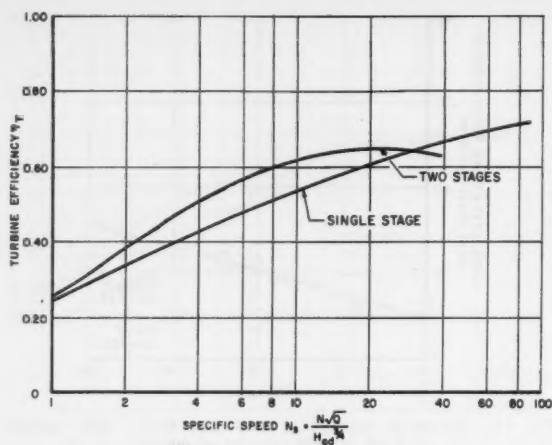


Fig. 16 Comparison of single stage and two-stage re-entry turbines

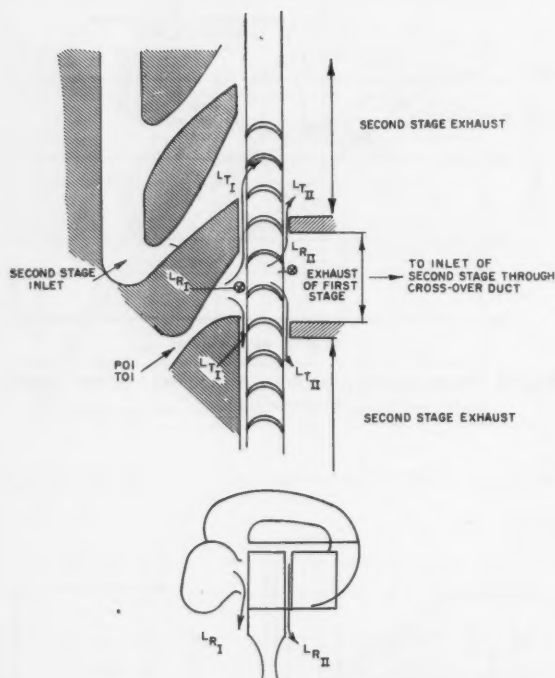


Fig. 17 Leakage paths of two-stage re-entry turbine with parallel flow in both stages

Reynolds number of $Re \geq 10^4$. This is the result of the generalized design point analysis of two-stage re-entry turbines for high overall pressure ratios. The optimum relation of N , and D , illustrated in Fig. 15 is finally used to compare the potential of two-stage re-entry turbines with the potential of a single stage turbine. The optimum efficiency obtainable with both turbine types is plotted in Fig. 16 vs. the specific speed. This diagram is valid for 300:1 pressure ratio and $Re \geq 10^4$. Herein, it is clearly demonstrated that

the two-stage turbine offers superior performance in the low specific speed range from $N_s = 3$ to about 20.

Tests and theory have illustrated that leakage is the most important parameter affecting the performance of two-stage re-entry turbines. In order to decrease the leakage it is proposed to use an arrangement as shown in Fig. 17, where the nozzles of the first stage and second stage are located on the same side of the rotor. This design is called a design with crossover duct for which the leakage paths are indicated in Fig. 17. It can be seen that the leakage occurring at the exhaust of the first stage nozzle is not lost entirely for both stages as in the case of the opposed flow shown in Fig. 7, because this amount of leakage will perform work in the second stage. The energy of the first stage, however, is lost owing to expansion or shock losses when passing through the clearance gap, and owing to mixing losses when joining the nozzle jet of the second stage. Across the rotor of the first stage leakage occurs which did work in the first stage but is lost for the second stage. This amount of leakage consists of tangential and radial components which pass through the axial clearance gap.

Furthermore, it is indicated that the dynamic leakage will perform some work in the case of the parallel flow arrangement, while it appeared to be lost for the previous investigated case (Fig. 7). In summary, it is indicated that a design with crossover duct or parallel flow (shown in Fig. 17) promises higher efficiency than the design with opposed flow (Fig. 7), because some amount of the static and dynamic leakage will do work, whereas the total amount of leakage did no work in the case illustrated by Fig. 7.

A further improvement of the two-stage turbine is suggested by improving the blade passages; that means designing them properly for supersonic flow conditions.

Hydrazine Turbine

The usefulness of the design analysis of two-stage re-entry turbines is finally demonstrated by application of the outlined design concept to high energy propellant accessory power units, using hydrazine with a flame temperature of about 2500 R. The test results of the two-stage turbine tested with nitrogen indicated that a performance of 937 specific hp could be achieved with an axial clearance of 0.005 in., or a specific hp value of 861 for axial clearance of 0.017 in. The design point of the turbine is $u/c = 0.21$. However, preliminary test data of the first hydrazine turbine did not show this performance. Values of only 650 to 700 specific hp were achieved. The reason for this was found to be due to thermal expansion of the housing and nozzle materials; hence, providing large clearances between rotor and first stage nozzle. This resulted in leakage values of about 25-40%. It was also believed that the optimum pressure split is an important parameter in the case of high altitude, high Mach numbers and large leakage flows. In order to determine analytically the optimum pressure split, the previously derived efficiency relations for two-stage re-entry turbines were programed on an IBM machine. Then, the optimum pressure split was evaluated by plotting optimum specific horsepower vs. the pressure ratio of the first stage. These calculations were conducted for several overall pressure ratios, several clearance combinations and several inlet pressure levels. The trend of these calculations is indicated in Figs. 18 and 19.

It has to be mentioned that the optimum pressure split could only be obtained approximately for the low Reynolds number conditions in the second stage, because Reynolds number corrections for $Re \leq 10^3$ are not yet available for high Mach number level, partial admission turbines. Nevertheless, the turbine was modified according to the IBM results, which demanded reduction of the axial clearance and

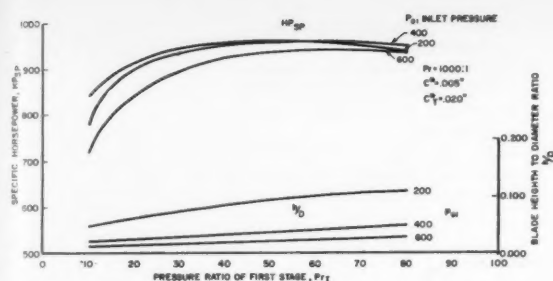


Fig. 18 Horsepower specific vs. pressure ratio of first stage (IBM result)

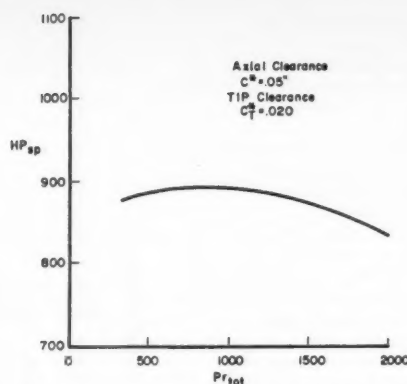


Fig. 19 Horsepower specific vs. overall pressure ratio (IBM result)

the overall pressure ratio in order to decrease the leakage flow. The axial clearance of the first stage and rotor was changed from $C^* = 0.020$ in. to $C^* = 0.005$ in., the tip clearance from $C_T^* = 0.035$ in. to $C_T^* = 0.020$ in. Testing the turbine again, the overall pressure ratio was reduced from 1500:1 to 960:1. The preliminary test data obtained up to date indicate that a specific hp value of 850-900 was achieved as shown in Fig. 20. The continuation of this work and its final results will be discussed in a forthcoming publication.

Conclusions

It is concluded that the generalized design analysis states most precisely the state of the art of single stage and two-stage re-entry turbines. It is demonstrated clearly that the basic criteria of these machines are the specific diameter, the specific speed and the Mach number. For two-stage machines, the pressure split or the ratio of the stage specific diameter is an additional parameter. The optimum analysis revealed that all geometric parameters are functions of these main parameters, as well as the losses stated in the state of the art for two-stage and single stage partial admission turbines. The result of the analysis is presented in general design diagrams which determine the optimum range of the turbines investigated. These diagrams are most useful for solving the design problems of partial admission turbines.

However, it has to be mentioned that these diagrams state only the present state of the art. Further improvement of partial admission turbines will certainly come, and these charts will change to some degree. It is felt by the authors of this paper that definite improvement of this turbine should be possible by more refined analyses of the flow phenomena occurring in the turbine passages. It is suggested that boundary layer and radial equilibrium calculations be conducted for this turbine type—techniques that have been most fruitful for all other high performance axial turbines, axial compressors, and pumps as stated clearly in (1, 2, and 21). Future investigations should also determine the optimum blade passages for supersonic turbines and the design of supersonic nozzles suitable for high pressure ratio turbines. This should include the effect of the rotating cascade upon the nozzle flow at high Mach number conditions.

Acknowledgment

The writers wish to express their appreciation to Dr. O. E. Balje for his suggestions and criticisms during the preparation of this paper. Acknowledgment is also made to the Department of the Navy, Office of Naval Research, which

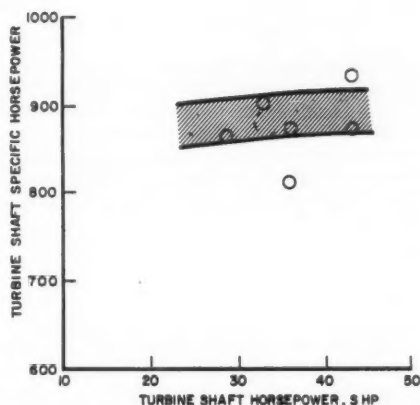


Fig. 20 Test results of two-stage hydrazine turbine

supported the described work under Contract no. NONR 2292(00) in the period from Feb. 1, 1958 through January 30, 1960.

Nomenclature

- A = area, in.²
- A^* = nozzle throat area, in.²
- a = arc of admission, in.
- a^* = cutter diameter
- C = coefficient
- c = absolute velocity or chord length, fps in.
- C_D = dynamic restriction coefficient
- C_F = restriction coefficient
- c_0 = spouting velocity, fps
- C^* = axial clearance, in.
- C_T^* = tip clearance, in.
- D = tip diameter, in., ft
- D_s = specific diameter, $DH_{ad}^{1/4}/\sqrt{\dot{Q}}$
- F = function of ()
- F_1 = leakage function for static conditions
- F_2 = leakage function for total conditions
- f = friction coefficient
- g = gravitational constant, $g = 32.2$ ft per sec²

H_{ad} = adiabatic head, ft
 HP = horsepower
 h = blade height, in.
 K_1 = specific diameter ratio $(D_{s1}/D_{s\ tot})^2$
 K_2 = specific diameter ratio $(D_{s\ II}/D_{s\ tot})^2$
 K_3 = function of $D_{s\ tot}$
 L = losses as % available energy
 L_b = blade pumping loss
 L_d = disk friction loss
 L_{ss} = scavenging loss
 L_t = total leakage loss
 M = Mach number
 N = revolutions per minute, rpm
 N_s = specific speed, $N_1 \sqrt{Q}/H_{ad}^{3/4}$
 P_0 = total pressure, psia
 P_r = pressure ratio
 Re = Reynolds number, $(c \cdot w)/\nu$
 T_0 = total absolute temperature, R
 T = static absolute temperature, R
 t = blade spacing, in.
 u = tip speed, fps
 \dot{w} = mass flow, lb per sec
 z = number of blades
 α = absolute flow angle, deg
 β = blade angle, deg
 γ = specific weight, lb per ft³
 δ = reciprocal of pressure ratio
 ϵ = total per cent of admission $(a_1 + a_{II})/\pi D$
 η = efficiency
 η_T = turbine efficiency
 η_h = hydraulic efficiency
 k = ratio of specific heats
 τ = torque coefficient
 χ = blade density ratio
 ψ = nozzle function
 ψ_N = nozzle coefficient
 ψ_R = blade coefficient

Subscripts

b = blade pumping
 d = disk friction
 f = restriction
 h = hydraulic
 i = ideal
 m = meridional
 N = nozzle
 0 = total conditions
 R = blade
 sc = scavenging
 st = static
 t = turbine
 tot = total
 w = relative
 1 = turbine inlet
 2 = nozzle exhaust, first stage

3 = rotor discharge, first stage
 4 = duct exit
 5 = nozzle exhaust, second stage
 6 = rotor discharge, second stage
 ex = exhaust, second stage
 I = first stage
 II = second stage
 $-$ = average values
 $*$ = nozzle throat conditions

References

- 1 NACA Research Memo., "Aerodynamic Design of Axial Flow Compressors," NACA RME-56B03, vols. I, II and III, Aug. 1956.
- 2 Linhardt, H. D., "Application of Cascade Theories to Axial Flow Pumps," M.E. Thesis, Calif. Instit. of Technology, 1960.
- 3 Stodola, A., "Steam and Gas Turbines," Peter Smith Co., N. Y., 1945.
- 4 Ainley, P. G. and Mathieson, G. C. R., "An Examination of the Flow and Pressure Losses in Blade Rows of Axial Flow Turbines," Aeron. Research Council, London, Tech. Rep. R&N no. 2891, 1955.
- 5 Stanitz, J. D. and Sheldrake, L. J., "Application of a Channel Design Method of High Solidity Cascades and Tests of an Impulse Cascade with 90° of Turning," NACA Rep. 1116, 1953.
- 6 Arnold, D., "Turbine Stress Analyses," Internal Memo., Sundstrand Turbo Co., Denver, Colo., Jan. 1960.
- 7 Balje, O. E., "Accessory Drive Turbines for Aircraft and Missiles," Aeron. Engng. Rev., vol. 15, no. 3, March 1956.
- 8 Stenning, A. H., "Design of Turbines for High Energy Fuels, Low Power Output Applications," Mass. Inst. of Technology, Dynamic Analysis and Control Lab., Rep. no. 79, Sept. 1953.
- 9 Silvern, D. H. and Balje, O. E., "A Study of High Energy Level, Low Power Output Turbines," Sundstrand Turbo Rep. S/TD no. 1196, April 9, 1958.
- 10 Linhardt, H. D., "A Study of High Pressure Ratio Re-entry Turbines," Sundstrand Turbo Rep. S/TD no. 1735, Jan. 1960.
- 11 Cordier, O., "Similarity Conditions for Turbomachines" ("Ähnlichkeitsbedingungen für Strömungsmaschinen,") BWK, Band. 5, 1953, p. 337-340; also VDI-Berichte Bd. 3 1955, p. 85.
- 12 Dickmann, H. E., "Theory of Ducted Propellers" (Beitrag zur Theorie Optimaler Dusenichrauben,) Jahrbuch der Schiffbautechnischen Gesellschaft, 49, Band 1955.
- 13 Buehning, P. G., "On the Behavior of Axial Flow Machines of Extremely High Specific Speed" ("Über das Verhalten von Extrem Schnellläufigen Axialmaschinen,") VDI-Forschungsheft 468, Ausgabe B Band 24, 1958.
- 14 Bowerman, R. E., "The Design of Axial Flow Pumps," ASME, Nov. 1956, Paper no. 55-A-127.
- 15 Balje, O. E., Discussion of "Radial Turbine" paper by Obering, Oberlaender, Proc. of CIMAC Meeting, 1959.
- 16 Pfleiderer, "Turbo-Machines" ("Strömungsmaschinen,") Springer-Verlag, Berlin, 1952.
- 17 Dziallas, R., "Loss and Efficiency Considerations of Pumps" ("Ueber Verluste und Wirkungsgrade bei Kreiselpumpen,") Wasserkraft und Wasserwirtschaft Heft 538 Jahrg. 1943.
- 18 Keenan, J. H., "Reaction Tests of Turbine Nozzles for Supersonic Velocities," ASME Trans., Oct. 1949, vol. 71, no. 7.
- 19 Olson, G., "Partial Admission, Low Aspect Ratios and Supersonic Speeds in Small Turbines," Ph.D. Thesis, Mass. Instit. of Technology, Jan. 1956.
- 20 Boxer, E., Sterrett, J. R. and Wlodarski, J., "Application of Supersonic Vortex Flow Theory to the Design of Supersonic Impulse Compressor or Turbine Blade Sections," NACA RML-52B06, 24 April 1952.
- 21 Hatch, J. E., Giamati, C. C. and Jackson, R. J., "Application of Radial Equilibrium Condition to Axial Flow Turbomachine Design Including Consideration of Change of Entropy with Radius Downstream of Blade Row," NACA RME-54A20, April 1954.

Stresses Owing to Internal Pressure in Solid Propellant Rocket Grains¹

HOWARD B. WILSON Jr.²

Rohm & Haas Co.
Huntsville, Ala.

An analysis was made of the stresses and displacements in an elastic solid propellant grain perforated internally by a star shaped configuration, bonded peripherally to an elastic motor case, and loaded internally by pressure normal to the perforation. The analysis was performed under the assumption of plane strain using conformal mapping and the complex variable method of N. I. Muskhelishvili. The effects on stress concentration at the star tip owing to changes in star tip radius of curvature and web thickness of the grain were studied. The analysis was made specifically for a four-pointed, star shaped internal perforation but can be generalized to an n -pointed configuration.

STRESSES created in solid propellant rocket motor grains by motor operating pressure, volume change, temperature gradients and flight and handling loads are of considerable interest. Many solid propellant grains contain star shaped perforations and particularly high stresses occur at the tips of the star points. In some instances these stresses are great enough to cause cracking of the propellant.

This paper presents a theoretical analysis of the stresses and displacements owing to internal pressure in an elastic solid propellant grain perforated internally with a four-pointed, star shaped configuration and bonded externally to an elastic motor case. The problem is simplified by considering an infinite solid which has a star shaped perforation, and is loaded with uniform pressure normal to the perforation and uniform compression at points infinitely distant from the perforation. The solid is assumed to be in a state of plane strain. The stresses and displacements are calculated along a circle in the solid which corresponds to the external boundary of an actual propellant grain. A method is then devised for determining the thickness and modulus of an elastic case, such that when the case is loaded internally with a stress distribution which closely approximates the stress distribution on the circle in the solid, the resulting dis-

placements at the internal boundary of the case are in close agreement with the displacements on the circle in the solid. Thereby an approximate solution is obtained for the stresses and displacements owing to internal pressure in a case bonded, solid propellant grain.

The analysis is based on the complex variable method of N. I. Muskhelishvili. A summary of the equations of plane elasticity in complex form is given.

Equations of the Plane Theory of Elasticity

The application of complex variable theory in the solution of plane elasticity problems for simply connected regions requires the determination of two functions $\phi(z)$ and $\psi(z)$ of the complex variable z which are analytic in the stressed region and satisfy the boundary value equation (1)³

$$\phi(z) + z\overline{\phi'(z)} + \overline{\psi(z)} = i \int_{s_0}^z [T_x(s) + iT_y(s)] ds \quad [1]$$

where $T_x(s)$ and $T_y(s)$ are the stresses in the x and y directions on the boundary, and the path of integration is along the boundary from an arbitrary fixed point s_0 to a variable point s .⁴

Received Oct. 14, 1960.

¹ This work was sponsored by the Army Ordnance Corps under Contract no. DA-01-021 ORD-5135.

² Scientist, Engineering Research Group; presently Instructor, Theoretical and Applied Mechanics, University of Illinois.

³ Numbers in parentheses indicate References at end of paper.

⁴ In Equation [1] and those which follow, a bar above a function indicates that the function is replaced by its complex conjugate.

The formulas for the stresses and displacements in terms of $\phi(z)$ and $\psi(z)$ are

$$\begin{aligned}\tau_{xx} + \tau_{yy} &= 2[\phi'(z) + \overline{\phi'(z)}] \\ -\tau_{xx} + \tau_{yy} + 2i\tau_{xy} &= 2[\bar{z}\phi''(z) + \psi'(z)] \\ u_x + iu_y &= (1/2\mu)[\kappa\phi(z) - \overline{z\phi'(z)} - \overline{\psi(z)}] \\ &\dots\dots\dots [2]\end{aligned}$$

The constants μ and κ depend on the elastic properties of the material and for plane strain are given by $\kappa = 3-4\nu$ and $\mu = E/2(1 + \nu)$, where ν and E are Poisson's ratio and the modulus of elasticity of the material, respectively.

Consider next a mapping function $z = \omega(\zeta)$ which conformally maps the interior of the unit circle in the ζ -plane onto the stressed region in the z -plane. The unit circle $\zeta = e^{i\theta}$, $0 < \theta < 2\pi$ maps into the boundary of the stressed region, and the curves $|\zeta| = \text{constant}$ and $\arg \zeta = \text{constant}$ map into orthogonal curves defining a curvilinear coordinate system in the z -plane. Let $\phi(\omega(\zeta)) = \phi(\zeta)$ and $\psi(\omega(\zeta)) = \psi(\zeta)$. Then in terms of the transform variable Equations [2] become

$$\begin{aligned}\tau_{\rho\rho} + \tau_{\theta\theta} &= 2\left[\frac{\phi'(\zeta)}{\omega'(\zeta)} + \frac{(\bar{\zeta})_r\phi}{\omega'(\zeta)}\right] \\ -\tau_{\rho\rho} + \tau_{\theta\theta} + 2i\tau_{\rho\theta} &= \frac{2\zeta^2}{\rho^2\omega'(\zeta)}\left[\overline{\omega(\zeta)}\left\{\frac{\phi''(\zeta)}{\omega'(\zeta)} - \right.\right. \\ &\left.\left. \text{and } \frac{\phi'(\zeta)\omega''(\zeta)}{[\omega'(\zeta)]^2}\right\} + \psi'(\zeta)\right] \\ u_\rho + iu_\theta &= \frac{\bar{\zeta}\overline{\omega'(\zeta)}}{2\mu\rho|\omega'(\zeta)|}\left[\kappa\phi(\zeta) - \frac{\omega(\zeta)}{\omega'(\zeta)}\overline{\phi'(\zeta)} - \overline{\psi(\zeta)}\right] \\ &\dots\dots\dots [3]\end{aligned}$$

where $\tau_{\rho\rho}$, $\tau_{\theta\theta}$, $\tau_{\rho\theta}$, u_ρ and u_θ are the stresses and displacements relative to the curvilinear coordinate system in the z -plane, and ρ and θ denote the absolute value of ζ and the argument of ζ , respectively.

Equation [1] can also be expressed in terms of the transform variable. Recalling that the $\omega(\zeta)$ maps $\zeta = e^{i\theta}$, $0 < \theta < 2\pi$, onto the boundary of region in the z -plane and using the notation $\sigma = e^{i\theta}$ gives

$$\phi(\sigma) + \frac{\omega(\sigma)}{\omega'(\sigma)}\overline{\phi'(\sigma)} + \overline{\psi(\sigma)} = H(\sigma) \quad [4]$$

where $H(\sigma)$ is a function which depends on the boundary loading.

If the stressed region in the z -plane which is mapped onto the interior of the unit circle in the ζ -plane is infinite, then

$$A[\sin(\theta_2) - \beta \sin(\theta_1)] - B[\sin(3\theta_2) - \beta \sin(3\theta_1)] - C[\sin(7\theta_2) - \beta \sin(7\theta_1)] - D[\sin(11\theta_2) - \beta \sin(11\theta_1)] = 0 \quad [9]$$

the mapping function may be written in the form

$$z = \omega(\zeta) = \frac{A}{\zeta} + \sum_{n=1}^{\infty} A_n \zeta^n \quad |\zeta| \leq 1$$

For this mapping function, the functions $\phi(\zeta)$ and $\psi(\zeta)$ can

be shown to have series expansions (1) of the form

$$\begin{aligned}\phi(\zeta) &= c_1 \frac{A}{\zeta} + \sum_{n=1}^{\infty} a_n \zeta^n \\ \psi(\zeta) &= (c_2 + ic_3) \frac{A}{\zeta} + \sum_{n=1}^{\infty} b_n \zeta^n \\ &\dots\dots\dots [5]\end{aligned}$$

where

$$\begin{aligned}c_1 &= [\tau_{xx}(\infty) + \tau_{yy}(\infty)]/4 \\ c_2 &= [\tau_{yy}(\infty) - \tau_{xx}(\infty)]/2 \\ c_3 &= \tau_{xy}(\infty)\end{aligned}$$

Determination of the Stresses and Displacements in an Infinite Solid With a Four-Pointed Star Shaped Perforation

The Mapping Transformation

The function which conformally maps the z -plane having a hole with four axes of symmetry onto the region $|\zeta| \geq 1$ in the ζ -plane (2) is of the form

$$z = A\zeta + B/\zeta^3 + C/\zeta^7 + D/\zeta^{11} + E/\zeta^{15} + \dots$$

This transformation is illustrated in Fig. 1. In this paper only a finite number of terms of this equation will be used. The mapping function for a four-pointed star is taken to be

$$z = A\zeta + B/\zeta^3 + C/\zeta^7 + D/\zeta^{11} \quad [6]$$

The coefficients A through D are determined from the following conditions:

- 1 $z = R_s$, which corresponds to the tip of the star point, is mapped onto $\zeta = 1$.
- 2 $z = R_s e^{i\pi/4}$, which corresponds to the tip of the inverse star point, is mapped onto $\zeta = e^{i\pi/4}$.
- 3 The ratio of the width of the star point at two locations is specified.
- 4 The radius of curvature at the tip of the star point is specified.

Condition 1 gives

$$R_s = A + B + C + D \quad [7]$$

Condition 2 gives

$$R_s = A - B + C - D \quad [8]$$

Let the imaginary part of the image in the z -plane of the point $\zeta = e^{i\theta}k$ be denoted by y_k . Then

$$y_k = A \sin \theta_k - B \sin(3\theta_k) - C \sin(7\theta_k) - D \sin(11\theta_k)$$

Let

$$0 < \theta_1 < \theta_2 < \pi/4 \quad \beta = y_2/y_1$$

Then condition 3 gives

The choice of θ_1 , θ_2 and β is arbitrary within the limits that have been specified. For a given choice of θ_1 and θ_2 , the angle δ between opposite sides of the star point is zero when β equals 1 and increases with β .

Since the circle $\zeta = e^{i\theta}$, $0 < \theta < 2\pi$ is mapped onto the star shaped boundary, the radius of curvature at points on

this boundary may be expressed as a function of θ . If the radius of curvature is denoted by r , then

$$r = [(x')^2 + (y')^2]^{3/2} / (x'y'' - y'x'')$$

The primes indicate differentiation with respect to θ . Let R_0 denote the radius of curvature at the tip of the star point. Then condition 4 gives

$$R_0 = \frac{(-A + 3B + 7C + 11D)^2}{(A + 9B + 49C + 121D)} \quad [10]$$

Since Equations [7, 8 and 9] are linear, they may be solved for B , C and D in terms of A . These solutions, when substituted into Equation [10], give a quadratic equation for the determination of A . The two values of A determined from solution of the quadratic are usually real and positive, and in this paper only real positive values of A will be considered. For each value of A , there is a set of B , C , and D values which meet all of the conditions specified above. It has been found that the set corresponding to the smaller value of A frequently gives a mapping function which is not conformal. Therefore the larger value of A is chosen. The coefficients B , C and D , which are all real, are then determined from Equations [7, 8 and 9], and the mapping function is completely determined.

The conditions used to determine the mapping function have been formulated with the primary purpose of reproducing the shape of a practical grain design in the vicinity of the tip of the star point. This results in a rounded off effect at the inverse star point. It has been shown, however, that rounding off the inverse star point within the limits given by the described mapping function has only a small effect on stress in the vicinity of the star tip (3). In order to obtain a better fit at the inverse star point it would be necessary to increase the number of terms in the mapping function and specify additional conditions, such as the radius of curvature at the inverse star point.

Equation [6] defined a function which maps the region exterior to the perforation in the z -plane onto the region $|\zeta| \geq 1$. In some cases it is more convenient to map onto the region $|\zeta| \leq 1$. This mapping function, denoted by $\omega(\zeta)$, is readily determined by replacing ζ by $1/\zeta$ in Equation [6]. Therefore

$$z = \omega(\zeta) = A/\zeta + B\zeta^3 + C\zeta^7 + D\zeta^{11} \quad |\zeta| \leq 1 \quad [11]$$

where the A , B , C and D coefficients are defined previously, gives a conformal transformation of the region exterior to the perforation in the z -plane onto the interior of the unit circle in the ζ -plane.

Solution of the Stress Problem

When there is a uniform normal pressure p_i at the boundary, Equation [1] becomes

$$\phi(z) + z \overline{\phi'(z)} + \overline{\psi(z)} = i \int_{s_0}^s \left[-p_i \frac{dy}{ds} + ip_i \frac{dx}{ds} \right] ds = -p_i z + c$$

It can be seen from Equations [3] that if $\phi(z)$ and $\psi(z)$ are replaced respectively by $\phi(z) + k_1$ and $\psi(z) + k_2$, where k_1 and k_2 are arbitrary constants, the stress formulas are unchanged, and the formula for displacement is changed by a rigid body displacement only. Owing to this arbitrariness in $\phi(z)$ and $\psi(z)$, the constant c may be taken equal to zero without affecting the stress distribution in the solid. In terms of the transform variables, the last equation may be written as

$$\phi(\sigma) + \frac{\omega(\sigma)}{\omega'(\sigma)} \overline{\phi'(\sigma)} + \overline{\psi(\sigma)} = -p_i \omega(\sigma) \quad [12]$$

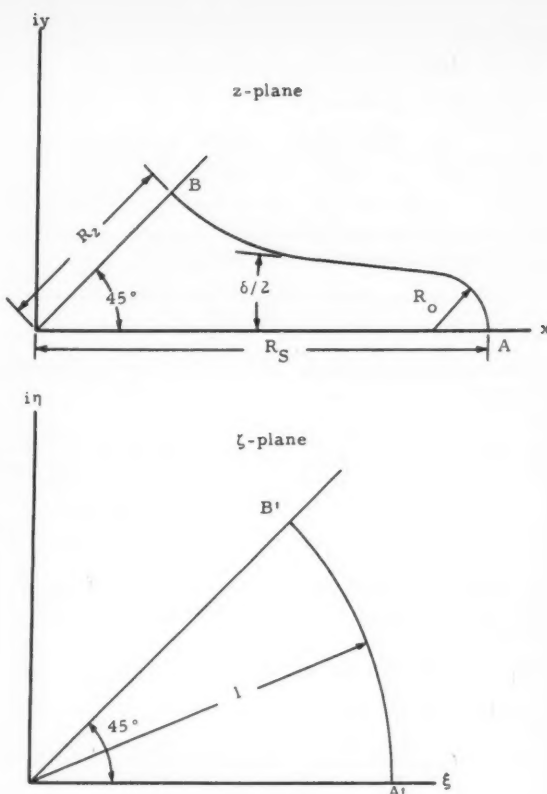


Fig. 1 Conformal mapping of propellant grain with a four-pointed, star shaped geometry onto a circle

Let the stress at infinity be specified such that

$$\tau_{xx}(\infty) = -p_0 \quad \tau_{yy}(\infty) = -p_0 \quad \tau_{xy}(\infty) = 0$$

Equations [5] then become

$$\phi(\zeta) = \frac{-p_0 A}{2\zeta} + \sum_{n=1}^{\infty} a_n \zeta^n \quad [13]$$

$$\psi(\zeta) = \sum_{n=1}^{\infty} b_n \zeta^n \quad [14]$$

Consider next the expansion of $\omega(\zeta)/\omega'(1/\zeta)$ in a series valid for $|\zeta| \geq 1$. The function $\omega(\zeta)$ given by Equation [11] has a pole of order 11 at infinity and $\omega'(1/\zeta)$ has a pole of order 2 at infinity. Since the mapping function is conformal for $|\zeta| \leq 1$, $\omega(\zeta)$ has no zeros for $|\zeta| \leq 1$. Hence $\omega'(1/\zeta)$ has no zeros for $|\zeta| \geq 1$. It follows that $\omega(\zeta)/\omega'(1/\zeta)$ has a pole of order 9 at infinity and therefore has a Laurent expansion valid for $|\zeta| \geq 1$ of the form

$$\frac{\omega(\zeta)}{\omega'(1/\zeta)} = C_9 \zeta^9 + \dots + C_0 + \sum_{n=1}^{\infty} \frac{C_{-n}}{\zeta^n}$$

The coefficients in the series are unique and can be determined by use of partial fractions or division. It is found that

$$\begin{aligned} \frac{\omega(\zeta)}{\omega'(1/\zeta)} &= \frac{A/\zeta + B\zeta^3 + C\zeta^7 + D\zeta^{11}}{-A\zeta^2 + 3B/\zeta^2 + 7C/\zeta^6 + 11D/\zeta^{10}} \\ &= C_9 \zeta^9 + C_8 \zeta^8 + C_7 \zeta^7 + \sum_{n=1}^{\infty} \frac{C_{-4n+1}}{\zeta^{4n-1}} \end{aligned} \quad [15]$$

where

$$\begin{aligned} C_0 &= -D/A \\ C_1 &= -C/A - 3BD/(A)^2 \\ C_2 &= -\frac{B}{A} - \frac{7CD + 3BC}{(A)^2} - \frac{9C^2D}{(A)^3} \\ &\dots\dots\dots [16] \end{aligned}$$

It will be seen later that knowledge of the coefficients of negative powers of ζ is not required. Noting that

$$\frac{\omega(\sigma)}{\omega'(\sigma)} = \frac{\omega(\zeta)}{\omega'(1/\zeta)} \Big|_{\zeta=\sigma}$$

and using Equations [13 and 14], substitution into Equation [12] gives

$$\begin{aligned} \left[-\frac{p_0 A}{2\sigma} + \sum_{n=1}^{\infty} a_n \sigma^n \right] + \left[C_0 \sigma^0 + C_1 \sigma^1 + C_2 \sigma^2 + \sum_{n=1}^{\infty} \frac{C_{-4n+1}}{\sigma^{4n-1}} \right] \left[\frac{p_0 A}{2} \sigma^2 + \sum_{n=1}^{\infty} \frac{n \bar{a}_n}{\sigma^{n-1}} \right] + \\ \left[\sum_{n=1}^{\infty} \frac{b_n}{\sigma^n} \right] = -p_i \left[\frac{A}{\sigma} + B \sigma^3 + C \sigma^7 + D \sigma^{11} \right] \quad [17] \end{aligned}$$

By equating positive powers of σ on both sides of Equation [17], the following system of simultaneous equations is obtained

$$\begin{aligned} a_1 + 9 C_0 \bar{a}_9 + 5 C_1 \bar{a}_5 + C_2 \bar{a}_1 &= 0 \\ a_2 + 8 C_0 \bar{a}_8 + 4 C_1 \bar{a}_4 &= 0 \\ a_3 + 7 C_0 \bar{a}_7 + 3 C_1 \bar{a}_3 &= -p_i \left[B + \left(\frac{p_0}{p_i} \right) \frac{AC_1}{2} \right] = -p_i \alpha_3 \\ a_4 + 6 C_0 \bar{a}_6 + 2 C_1 \bar{a}_2 &= 0 \\ a_5 + 5 C_0 \bar{a}_5 + 1 C_1 \bar{a}_1 &= 0 \\ a_6 + 4 C_0 \bar{a}_4 &= 0 \\ a_7 + 3 C_0 \bar{a}_3 &= -p_i \left[C + \left(\frac{p_0}{p_i} \right) \frac{AC_2}{2} \right] = -p_i \alpha_7 \\ &\dots\dots\dots [18] \end{aligned}$$

$$\begin{aligned} \psi(\zeta) = - \left[p_i A - \frac{p_0 A}{2} \right] \zeta + \left[\frac{p_0 A}{2} C_1 + 3a_3 C_5 + 7a_7 C_9 \right] \frac{1}{\zeta^3} + \left[\frac{p_0 A}{2} C_5 + 3a_5 C_9 \right] \frac{1}{\zeta^7} + \frac{p_0 A C_9}{2} \frac{1}{\zeta^{11}} - \\ \left[A \zeta + \frac{B}{\zeta^3} + \frac{C}{\zeta^7} + \frac{D}{\zeta^{11}} \right] \left[\frac{p_0 A}{2 \zeta^2} + 3a_3 \zeta^2 + 7a_7 \zeta^6 + 11a_{11} \zeta^{10} \right] \\ \left[-\frac{A}{\zeta^3} + 3B \zeta^3 + 7C \zeta^7 + 11D \zeta^{11} \right] \quad [22] \end{aligned}$$

$$\begin{aligned} a_8 + 2 C_0 \bar{a}_2 &= 0 \\ a_9 + 1 C_0 \bar{a}_1 &= 0 \\ a_{10} &= 0 \\ a_{11} &= -p_i \left[D + \left(\frac{p_0}{p_i} \right) \frac{AC_3}{2} \right] = -p_i \alpha_{11} \\ a_n &= 0 \quad \text{for } n \geq 12 \\ &\dots\dots\dots [18] \end{aligned}$$

The solution of this system of equations is found to be

$$\begin{aligned} a_1 = a_2 = a_4 = a_6 = a_8 = a_9 = a_{10} &= 0 \\ a_3 &= \frac{p_i [-\alpha_3 + 7\alpha_7 C_9]}{[1 + 3 C_5 - 21 C_9^2]} \\ a_7 &= \frac{p_i [-\alpha_7 - 3\alpha_7 C_5 + 3\alpha_3 C_9]}{[1 + 3 C_5 - 21 C_9^2]} \\ a_{11} &= -p_i \alpha_{11} \\ a_n &= 0 \quad \text{for } n \geq 12 \\ &\dots\dots\dots [19] \end{aligned}$$

Therefore $\phi(\zeta)$ is uniquely determined and has the form

$$\phi(\zeta) = -p_0 A / 2 \zeta + a_3 \zeta^3 + a_7 \zeta^7 + a_{11} \zeta^{11} \quad [20]$$

where all coefficients of ζ^n are real.

The function $\psi(\zeta)$ must now be determined. The value of $\psi(\zeta)$ on the boundary of the unit circle is given in terms of $\phi(\sigma)$ and $\omega(\sigma)$ by the boundary value Equation [12]. Taking the complex conjugate and transposing gives

$$\psi(\sigma) = -p_i \overline{\omega(\sigma)} - \overline{\phi(\sigma)} - \frac{\overline{\omega(\sigma)} \phi'(\sigma)}{\omega'(\sigma)}$$

From Equation [14], $\psi(\zeta)$ is obviously analytic for $|\zeta| \leq 1$; therefore application of the Cauchy integral formula gives

for $|\zeta| < 1$

$$\begin{aligned} \psi(\zeta) = -\frac{p_i}{2\pi i} \int_{\gamma} \frac{\overline{\omega(\sigma)} d\sigma}{(\sigma - \zeta)} - \frac{1}{2\pi i} \int_{\gamma} \frac{\overline{\phi(\sigma)} d\sigma}{(\sigma - \zeta)} - \\ \frac{1}{2\pi i} \int_{\gamma} \frac{\overline{\omega(\sigma)} \phi'(\sigma) d\sigma}{\omega'(\sigma)(\sigma - \zeta)} \quad [21] \end{aligned}$$

where γ denotes the unit circle and

$$\begin{aligned} \overline{\phi(\sigma)} &= \phi\left(\frac{1}{\sigma}\right) = -\frac{p_0 A}{2} \sigma + \frac{a_3}{\sigma^3} + \frac{a_7}{\sigma^7} + \frac{a_{11}}{\sigma^{11}} \\ \overline{\omega(\sigma)} &= \omega\left(\frac{1}{\sigma}\right) = A \sigma + \frac{B}{\sigma^3} + \frac{C}{\sigma^7} + \frac{D}{\sigma^{11}} \end{aligned}$$

Evaluation of the integrals in Equation [21] gives

Equation [22] may be simplified by noting from Equations [18] that

$$\begin{aligned} \frac{p_0 A}{2} C_1 + 3a_3 C_5 + 7a_7 C_9 &= -a_3 - p_i B \\ \frac{p_0 A}{2} C_5 + 3a_5 C_9 &= -a_7 - p_i C \\ -\frac{p_0 A}{2} C_9 &= -a_{11} - p_i D \end{aligned}$$

Hence $\psi(\zeta)$ may be written as

$$\psi(\zeta) = -p_i \omega\left(\frac{1}{\zeta}\right) - \phi\left(\frac{1}{\zeta}\right) - \frac{\omega(1/\zeta) \phi'(\zeta)}{\omega'(\zeta)} \quad [23]$$

Since $\phi(\zeta)$ and $\psi(\zeta)$ are completely determined, the stresses and displacements relative to the curvilinear coordinate system are easily obtained by direct substitution into Equations [3], and the solution of the problem is complete. These substitutions, though tedious, are straightforward and are not shown here.

Numerical Calculations of the Stresses and Displacements in the Infinite Solid With a Four-Pointed, Star Shaped Perforation

Consider as a numerical example a perforation for which

$$\begin{aligned} R_0/R_s &= 0.085 & R_2/R_s &= 0.42 \\ \theta_1 &= 25 \text{ deg} & \theta_2 &= 30 \text{ deg} & \beta &= 1.0 \end{aligned}$$

In this case it was found that

$$\begin{aligned} A/R_s &= 0.7855 & B/R_s &= 0.2758 \\ C/R_s &= -0.0755 & D/R_s &= 0.0142 \end{aligned}$$

A plot of the boundary of the perforation is shown in Fig. 2. The radius of curvature in the vicinity of the star tip is nearly constant and opposite sides of the star point are parallel near the star tip as required by the condition $\beta = 1$.

For the mapping function that has been specified, calculations were made, using a digital computer, to determine the distribution of stresses and displacements along the boundary of the perforation and along a circle of radius R for which the ratio R/R_s is 2. Two loading conditions were considered: Unit pressure at the perforation boundary with zero stress at infinity, and zero pressure at the perforation boundary with unit compression at infinity. With these results, the effects of arbitrary pressure at the perforation and arbitrary stress at infinity may be obtained by superposition. The circle with $R/R_s = 2$ corresponds to the external boundary of a propellant grain for which the ratio of web thickness to motor diameter is 0.25. The value of Poisson's ratio for the propellant was assumed to be 0.49. Numerical results are shown in Figs. 3 through 7 for the two loading conditions stated. All stresses and displacements are presented in dimensionless form. Stresses are given in the form τ/p , where p denotes either pressure at the perforation boundary or stress at infinity as appropriate. A similar meaning for p holds in the dimensionless displacement quantities. The angle between the bisector of the star point and a radial line drawn to a point on the circle $R/R_s = 2$ is denoted by θ .

In Fig. 5, a positive shear stress on the circle is taken to be one which tends to rotate the propellant interior to the circle in a counterclockwise direction. In Figs. 6 and 7, the positive direction for radial displacement is outward from the star perforation, and positive circumferential displacement is counterclockwise relative to the center of the perforation.

Matching the Stresses and Displacements in a Thin Circular Case With the Stresses and Displacements on a Circle in the Infinite Solid

For the two loading conditions considered the variation of radial stresses and radial displacements on the circle in the solid is very nearly sinusoidal (Figs. 4, 5 and 6). By superposition it follows that this variation will be sinusoidal for any combination of pressure at the perforation and compression at infinity. It can also be seen that the shear stresses on the circle are smaller than the radial stresses, and the circumferential displacements are small compared with the radial displacements. As will be shown, when the solid is loaded simultaneously by pressure at the perforation and by compression at infinity in the proportion of practical interest, the shearing stresses on the circle are of negligible magnitude as compared with the radial stresses. Under these conditions it is possible to closely match the stresses and displacements at the internal surface of a thin circular case with the stresses and displacements on the circle in the solid. This is accomplished by loading a thin ring internally with a sinusoidally varying normal pressure of the same magnitude as the radial stress observed on the circle in the solid, and then adjusting the properties of the ring, so that the radial displacements at the internal surface of the ring and the radial displacements on the corresponding circle in the solid are in close agree-

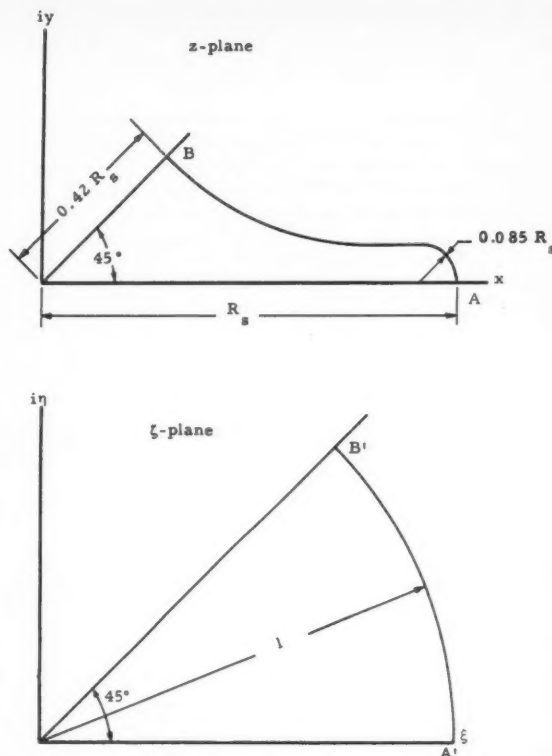


Fig. 2 Numerical example of conformal mapping of propellant grain with a four-pointed, star shaped geometry onto a circle

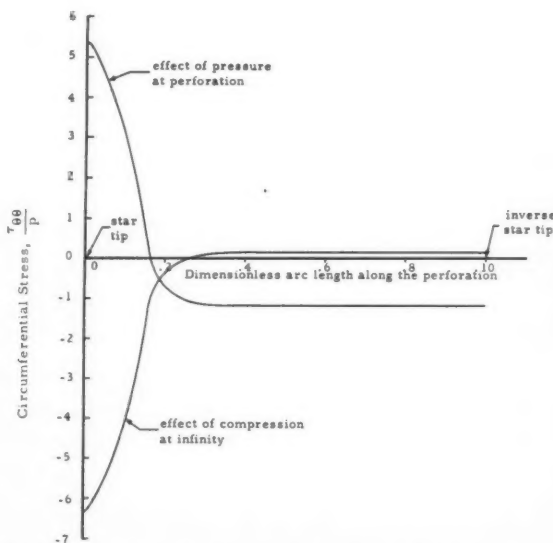


Fig. 3 Circumferential stress along boundary of perforation owing to pressure normal to perforation and to compression at infinity

ment. No attempt is made to match the circumferential displacements or the shearing stresses, since these are negligible in comparison to the radial effects.

Consider a circular ring of internal radius R and external radius R_e . Let the ring be subjected to a zero external pres-

sure and sinusoidally varying internal pressure of the form

$$\tau_{rr} = -\frac{(p_1 + p_2)}{2} - \frac{(p_1 - p_2)}{2} \cos(4\theta)$$

where θ denotes the angle which a radius of the ring makes with a fixed radial line. When θ is equal to 0, τ_{rr} equals $-p_1$, and when θ is equal to $\pi/4$, τ_{rr} equals $-p_2$. The equations for the radial and circumferential displacements and the circumferential stresses at the internal boundary of the ring are found, by application of the general solution for a circular ring (4), to be

$$u_{rr} = \frac{(p_1 + p_2) R(1 + \nu_c)}{2E_c(x^2 - 1)} [1 - 2\nu + x^2] + \frac{(p_1 - p_2) R(1 + \nu_c)}{4E_c(x^2 - 1)^3} \times \frac{[a(x^{14} + x^{12} + x^{10}) + bx^8 + cx^6 + d(x^4 + x^2 + 1)]}{(x^8 + 4x^6 + 10x^4 + 4x^2 + 1)} \times \cos 4\theta \quad [24]$$

$$u_{\theta\theta} = \frac{(p_1 - p_2) R(1 + \nu_c)}{4E_c(x^2 - 1)^3} \times \frac{[e(x^{14} + x^{12} + x^{10}) + fx^8 + gx^6 + h(x^4 + x^2 + 1)]}{(x^8 + 4x^6 + 10x^4 + 4x^2 + 1)} \times \sin 4\theta \quad [25]$$

$$\tau_{\theta\theta} = \frac{(p_1 + p_2)(x^2 + 1)}{2(x^2 - 1)} + \frac{(p_1 - p_2)}{2} \times \left[1 - \frac{2(x^2 + 1)^2(x^4 + 1)^2}{(x^2 - 1)^2(x^8 + 4x^6 + 10x^4 + 4x^2 + 1)} \right] \cos 4\theta \quad [26]$$

where

$$a = \frac{2(9 - 10\nu_c)}{15} \quad b = \frac{2(5 - 2\nu_c)}{3} \quad c = \frac{2(11 - 14\nu_c)}{3} \\ d = \frac{2(7 - 6\nu_c)}{15} \quad e = \frac{4(-3 + 5\nu_c)}{15} \quad f = \frac{4(-7 + \nu_c)}{3} \\ g = \frac{4(5 + \nu_c)}{3} \quad h = \frac{4(1 - 3\nu_c)}{15}$$

$x = R_c/R$ and ν_c and E_c are Poisson's ratio and the modulus of elasticity, respectively, for the ring.

It is convenient to express Equation [24] in dimensionless form as

$$\frac{E_p u_{rr}}{R_s p_i} = \frac{\left(\frac{p_1}{p_i} + \frac{p_2}{p_i}\right) \left(\frac{R}{R_s}\right) (1 + \nu_c)}{2(x^2 - 1) \left(\frac{E_c}{E_p}\right)} [1 - 2\nu_c + x^2] + \frac{\left(\frac{p_1}{p_i} - \frac{p_2}{p_i}\right) \left(\frac{R}{R_s}\right) (1 + \nu_c)}{4(x^2 - 1)^3 \left(\frac{E_c}{E_p}\right)} \frac{[a(x^{14} + x^{12} + x^{10}) + bx^8 + cx^6 + d(x^4 + x^2 + 1)]}{(x^8 + 4x^6 + 10x^4 + 4x^2 + 1)} \cos 4\theta \quad [27]$$

where

$$E_p = \text{propellant modulus} \\ R_s = \text{star point radius} \\ p_i = \text{normal pressure at the boundary of the perforation in the infinite solid}$$

A method may be devised for determining, for any ratio of compressive stress at infinity to pressure at the boundary of the perforation, the thickness and elastic modulus of a circular ring, such that there is exact agreement between radial displacement and radial stress at two points on the circle in the solid, and corresponding points on the internal boundary of the ring. One point considered is on the bisector of the star point and will be called point 1 and will be designated by the subscript 1. The other point is on the bisector of the inverse star point and will be called point 2 and will be designated by the subscript 2. It will be shown that by exactly matching stress and displacement quantities at points 1 and 2, a close match is also obtained at other points along the

boundary of the circle. Calculations will be made for the geometry considered in the previous example.

For an assumed ratio of compressive stress at infinity in the solid to pressure at the boundary of the perforation, dimensionless radial displacements $E_p u_i / R_s p_i$ and $E_p u_2 / R_s p_i$, and dimensionless radial stresses p_1 / p_i and p_2 / p_i may be determined in the solid by use of Figs. 4 and 6. In order for the radial stresses and radial displacements in the ring to agree with those in the solid, it is required in Equation [27]

that for θ equal to 0

$$E_p u_{rr} / R_s p_i = E_p u_1 / R_s p_i$$

and for θ equal to $\pi/4$

$$E_p u_{rr} / R_s p_i = E_p u_2 / R_s p_i$$

for the p_1 / p_i and p_2 / p_i determined previously. For an assumed value of ν_c , this gives two simultaneous equations for the determination of E_c / E_p and x . Elimination of E_c / E_p from these two equations gives a polynomial of degree 14 in x . This polynomial may be solved by successive approximation to determine the value of x nearest to unity. After x is known, E_c / E_p is easily determined by substituting for x in either of the two simultaneous equations and solving for E_c / E_p . By assuming different ratios of compressive stress at infinity to normal pressure at the perforation, various combinations of x and E_c / E_p may be obtained for an assumed

value of ν_c . Figs. 8 through 11 show curves for variation of t/R and E_c / E_p with λ for different combinations of R/R_s and ν_p with ν_c equal to 0.30. The quantity t/R equal to $x - 1$ is the ratio of case thickness to internal case radius, and λ denotes the ratio of stress at infinity in the solid to pressure normal to the boundary of the perforation. For each combination of ν_p and R/R_s , it was found that when λ became sufficiently large the calculated values of t/R and E_c / E_p became complex. These terminal points are indicated at the right end of the curves.

Consider as an example a motor with an aluminum case for which $E_c = 10 \times 10^6$ psi and $\nu_c = 0.30$. Let E_p equal 200 psi, ν_p equal 0.49 and the internal pressure of the motor equal 1000 psi. Referring to Fig. 8 for $E_c / E_p = 5 \times 10^4$, it is found that λ equals 0.9028 and t/R equals 1.42×10^{-2} . Use of Fig. 4 and superposition gives $p_1 / p_i = 0.9104$ and $p_2 / p_i = 0.9288$. Substitution into Equation [26] gives for the maximum stress in the case

$$(\tau_{\theta\theta})_{\max} = p_i [65.35 + 18.04] = 83.39 p_i$$

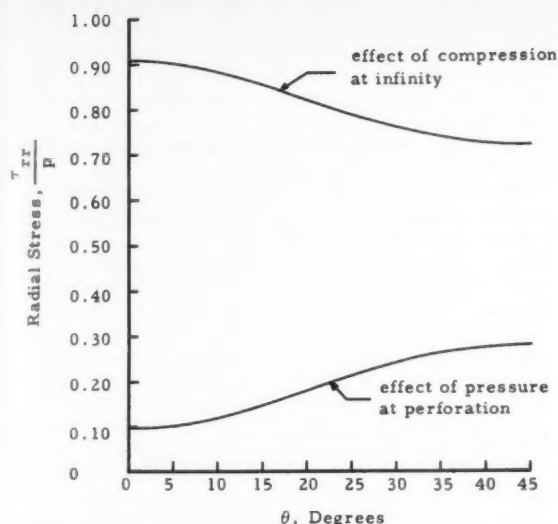


Fig. 4 Compressive radial stress on circle $R/R_s = 2$ owing to pressure normal to perforation and to compression at infinity

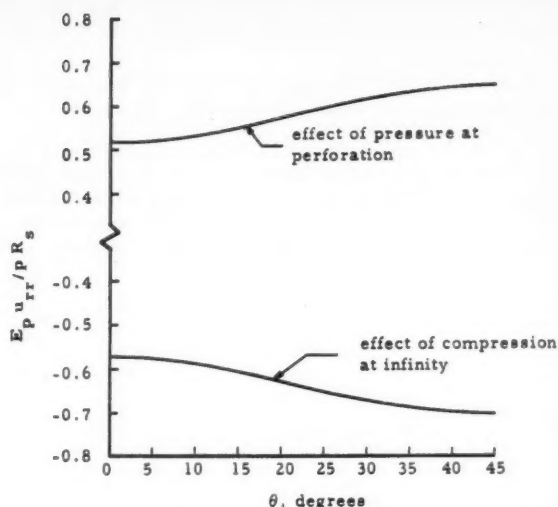


Fig. 6 Radial displacement on circle $R/R_s = 2$ owing to pressure normal to perforation and to compression at infinity ($\nu_p = 0.49$)

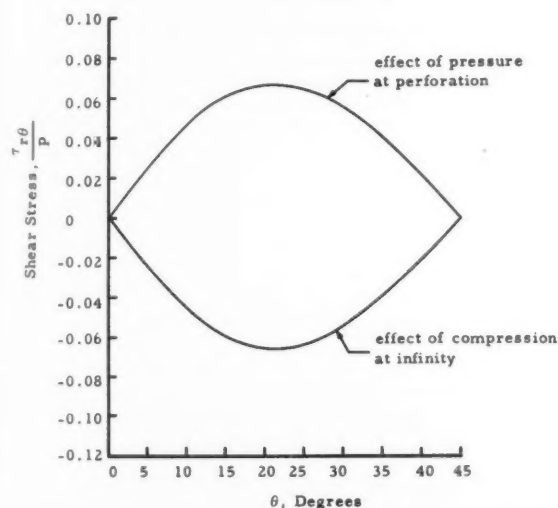


Fig. 5 Shear stress on circle $R/R_s = 2$ owing to pressure normal to perforation and to compression at infinity

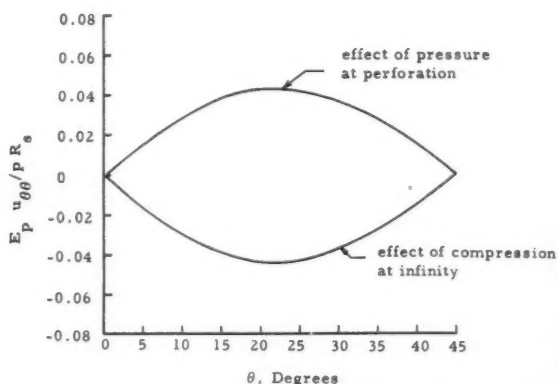


Fig. 7 Circumferential displacement on circle $R/R_s = 2$ owing to pressure normal to perforation and to compression at infinity ($\nu_p = 0.49$)

The value 65.35 represents the effect of the average pressure applied to the inside of the case, and the value 18.04 gives the bending effect of the sinusoidal variation in the internal pressure. The bending stress is 22% of the total stress in this example. For the assumed motor pressure, the maximum stress in the case is 83,400 psi, which is a reasonable design strength for aluminum. By use of Fig. 3 it is also found that the stress at the tip of the star point in the propellant grain is 380 psi compression.

Although there is exact agreement between case and propellant grain displacements and stresses at points 1 and 2, there are small discrepancies at intermediate points along the external boundary of the grain. Since both the radial stresses

and radial displacements on the circle in the solid vary in a nearly sinusoidal manner, there is no significant difference in radial stress and displacement in the grain and in the case. The principal discrepancy is owing to the small shear stresses which exist along the circle in the solid, and owing to the difference in the circumferential displacements in the case and in the solid. Both of these discrepancies are zero at points 1 and 2 and vary almost sinusoidally along the arc of the circle to a maximum halfway between points 1 and 2. It is found by use of Fig. 5 that the maximum shear stress on the circle in the solid is 6 psi when λ equals 0.9028 and the motor pressure is 1000 psi. By use of Fig. 7 and Equation [25], it is also found that the maximum difference in

circumferential displacement in the case and the propellant grain is 0.003 in. for a 4-in. diameter motor. It is believed that both of these quantities are so small as to be negligible.

Effect of Web Thickness and Star Tip Radius of Curvature on Stress at the Star Tip

In order to analyze the effects of web thickness and star tip radius of curvature on stress at the tip of the star point, a stress concentration factor defined by Ordahl and Williams (5) was used. Consider a cylindrical propellant grain with a star shaped internal perforation exposed to arbitrary uni-

form internal and external pressures. Ordahl and Williams defined the stress concentration factor as the ratio of the difference in principal stresses at the star tip to the difference in principal stresses at the inner boundary of a circular cylinder loaded with the same internal and external pressures as the propellant grain, and having an internal radius and an external radius equal respectively to the star point radius and the external radius of the propellant grain.

It can be seen from Figs. 4 and 5 that as the ratio of compression at infinity to pressure at the boundary of the perforation approaches unity, the normal stresses on the circle $R/R_s = 2$ become nearly constant, and the shear stresses are small compared to the normal stresses. It is reasonable, therefore, to expect that the stresses created at the star tip in the solid will differ little from those created at the star tip when the shear stresses on the circle are neglected, and the varying normal stress distribution on the circle is replaced by an average normal pressure. By using an average normal pressure, stress concentration factors were calculated for $R/R_s = 1.5$ and 2.0. These results are shown in Fig. 12.

Note that as R_0 tends to R_s , the internal geometry of the grain becomes a circle, and the stress concentration factor must tend to unity as indicated by the terminal points at the lower ends of the curves.

The stress concentration factors given by the analytical method were found to be approximately 20% greater than those obtained photoelastically by Ordahl and Williams.

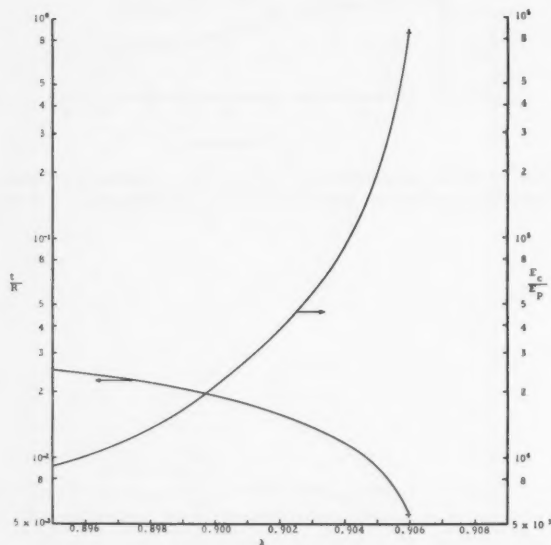


Fig. 8 Variation of case thickness and case modulus with ratio of compression at infinity to pressure at boundary of perforation for $\nu_c = 0.30$, $\nu_p = 0.49$, $R/R_s = 2.0$, $R_0/R_s = 0.085$

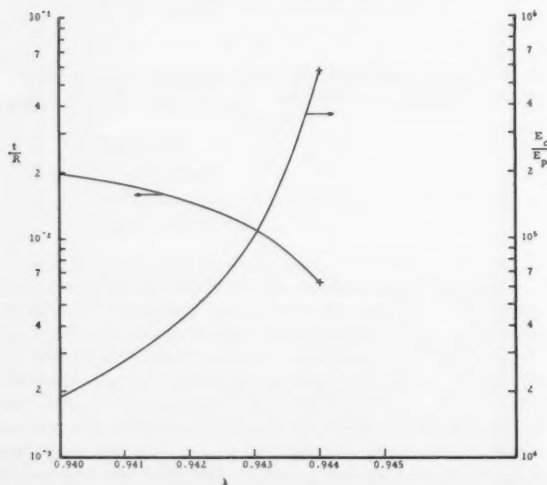


Fig. 9 Variation of case thickness and case modulus with ratio of compression at infinity to pressure at boundary of perforation for $\nu_c = 0.30$, $\nu_p = 0.49$, $R/R_s = 1.5$, $R_0/R_s = 0.085$

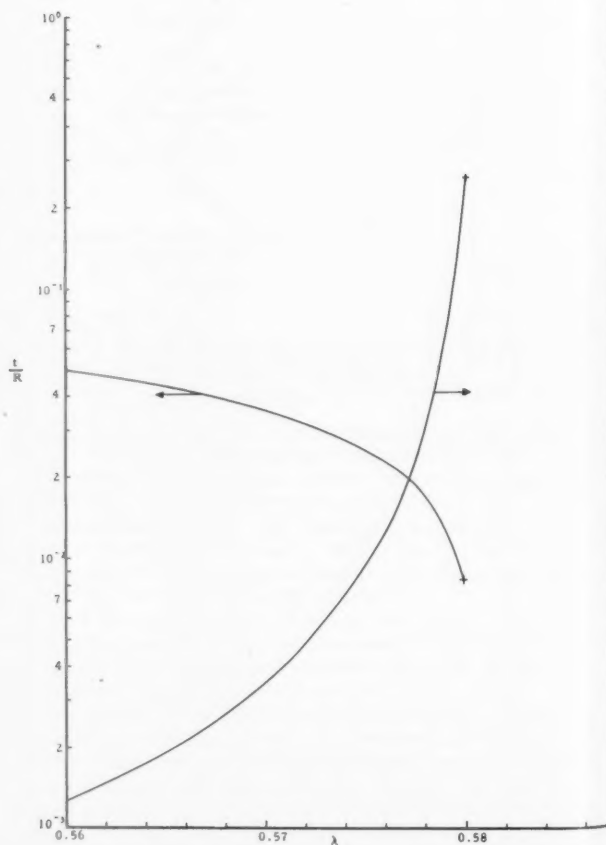


Fig. 10 Variation of case thickness and case modulus with ratio of compression at infinity to pressure at the boundary of the perforation for $\nu_c = 0.30$, $\nu_p = 0.43$, $R/R_s = 2.0$, $R_0/R_s = 0.085$

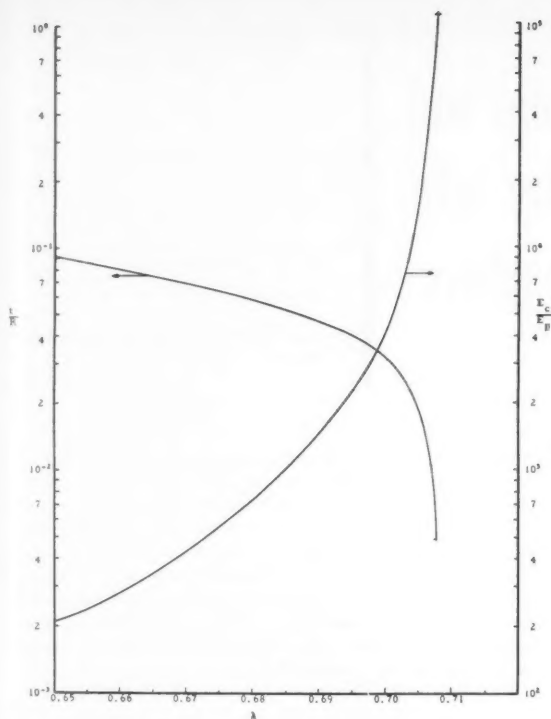


Fig. 11 Variation of case thickness and case modulus with ratio of compression at infinity to pressure at boundary of perforation for $\nu_c = 0.30$, $\nu_p = 0.43$, $R/R_s = 1.5$, $R_o/R_s = 0.085$

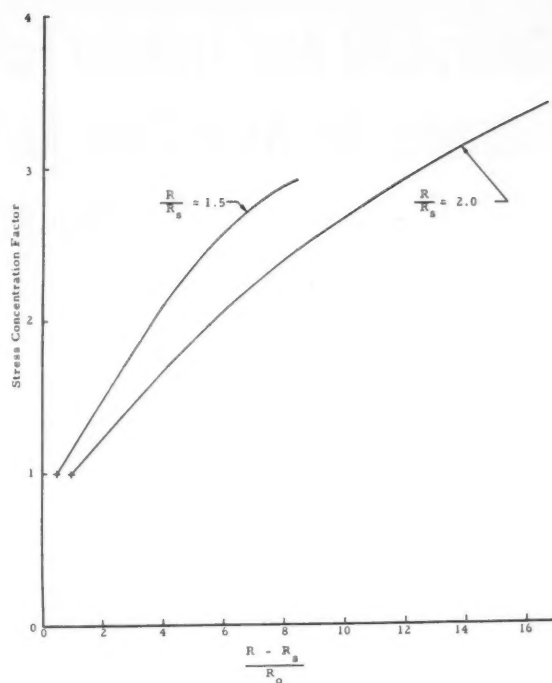


Fig. 12 Variation of stress concentration factor with ratio of web thickness to star tip radius of curvature

Closing Remarks

The approximate solution which has been presented for determining the stresses and displacements in an elastic, case bonded propellant grain with a four-pointed, star shaped internal perforation contained in an elastic motor case is not completely general, because a solution cannot be obtained for arbitrary case dimensions and arbitrary propellant and case elastic properties. If values of ν and E for the case and propellant are assumed, then λ and t/R are uniquely determined. These two quantities then determine the ratio of the maximum stress in the motor case to the internal pressure of the motor. However, as was shown in the numerical example considered, it is possible to obtain ratios of case modulus to propellant modulus, and maximum case stress to case design stress, which compare reasonably with practical values.

It was found that owing to the variation of radial stress exerted on the case by the propellant grain, considerable bending stress can be caused in the case. This may be an im-

portant cause of failure of cases designed on the basis of uniform pressure.

Although only a propellant grain with a four-pointed star geometry was considered, with appropriate changes in the mapping function the analysis can be extended to grains having an arbitrary number of star points (2).

References

- 1 Sokolnikoff, I. S., "Mathematical Theory of Elasticity," McGraw-Hill Book Co., Inc., N. Y., second ed., 1956, pp. 249-327.
- 2 Wilson, H. B. Jr., "Conformal Transformation of a Solid Propellant Grain with a Start-Shaped Internal Perforation Onto an Annulus," ARS JOURNAL, vol. 30, no. 8, Aug. 1960, pp. 780-781.
- 3 Fourny, M. E., "Photoelastic Determination of the Stress Concentration Factor at the Star Point of a Four-Pointed Star-Shaped Rocket Grain," California Institute of Technology, GALCIT SM 60-5, April 1960.
- 4 Muskhelishvili, N. I., "Some Basic Problems of the Mathematical Theory of Elasticity," P. Noordhoff, Ltd., Groningen, Holland, third ed., 1953, pp. 218-223.
- 5 Ordahl, D. D. and Williams, M. L., "Preliminary Photoelastic Design Data for Stresses in Rocket Grains," JET PROPULSION, vol. 27, no. 6, June 1957, pp. 657-662.

Generalized Heat Transfer Formulas and Graphs for Nose Cone Re-Entry Into the Atmosphere¹

R. W. DETRA²
H. HIDALGO³

Avco-Everett Research Laboratory
Everett, Mass.

Utilizing the research results of previously reported investigations of the laminar, turbulent and radiative heat transfer in dissociated air, some generalized formulas for calculating heat transfer are given. Graphs for determining the laminar heat transfer, momentum thickness Reynolds number, and turbulent heat transfer distributions around an axisymmetric body are also given. These heat transfer correlations are valid for velocities between 6000 and 26,000 fps and for altitudes up to 250,000 ft. This range of velocities and altitudes covers the important re-entry regime of practical re-entry trajectories having interest today. In the last section of this report these generalized results are specialized for ICBM nose cone re-entry applications. These formulas and graphs may be found useful for making rapid engineering estimates and preliminary design evaluations of the heating problems associated with re-entry into Earth's atmosphere.

UTILIZING the results of previously reported investigations of the laminar, turbulent and radiative heat transfer in dissociated air, some simple formulas for calculating heat transfer have been obtained. These formulas may be found to be useful for making rapid engineering estimates and preliminary design evaluations of the heating problems associated with nose cone re-entry.

Laminar Heat Transfer

Investigations of the stagnation point heat transfer in dissociated air (1, 2 and 3)⁴ have shown good agreement between experimental results and the theoretical prediction for equilibrium flow given by

$$\dot{q}_s = \frac{0.76}{\sigma^{0.6}} \left\{ (\rho\mu)_{ws}^{0.1} (\rho\mu)_{es}^{0.4} \times \left[1 + (L^{0.5} - 1) \frac{h_{Ds}}{H_s} \right] (H_s - h_{ws}) \sqrt{\left(\frac{du_e}{dx} \right)_s} \right\} \quad [1]$$

Based on a Newtonian velocity gradient at the stagnation point, the gas dynamic charts for equilibrium air (4), the viscosity temperature dependence given by Sutherland, a Lewis number of 1.4 and a Prandtl number of 0.71, the heat transfer rates predicted by Equation [1] can be expressed by the relation

$$\dot{q}_s \sqrt{R} = \dot{q}_s \sqrt{b \cdot \frac{b}{a}} = 865 \left(\frac{V}{10^4} \right)^{3.15} \times \sqrt{\frac{\rho_\infty}{\rho_{SL}}} \frac{H_s - h_w}{H_s - h_{w300} K} \quad [2]$$

Received Sept. 16, 1960.

¹ This work was sponsored by the Air Force Ballistic Missile Division, Air Research and Development Command, United States Air Force, under Contract no. AF 04(645)-18.

² Principal Staff Scientist. Member ARS.

³ Senior Engineer, Avco-Everett Research Laboratory.

⁴ Numbers in parentheses indicate References at end of paper.

This correlation is accurate to 10% over the range of $6000 \leq V \leq 26,000$ fps and $1 \leq \rho_\infty/\rho_{SL} \leq 8 \times 10^{-5}$. Although Equation [2] is based on a Newtonian velocity gradient at the stagnation point, corrections for other stagnation point velocity gradients can be made simply by multiplying Equation [2] by the square root of the velocity gradient ratio (5), as

$$\dot{q}_s = \dot{q}_{s \text{ Newtonian}} \sqrt{\frac{(du_e/dx)_s}{(du_e/dx)_{s \text{ Newtonian}}}}$$

The laminar heat transfer around blunt bodies in dissociated air has been investigated and is reported in (6). Based on the theory presented in (6) laminar form factors, defined by the ratio \dot{q}/\dot{q}_s , have been computed for some typical blunt bodies and are presented in Fig. 1 as a function of the local dimensionless pressure. The parameter defining the body geometry

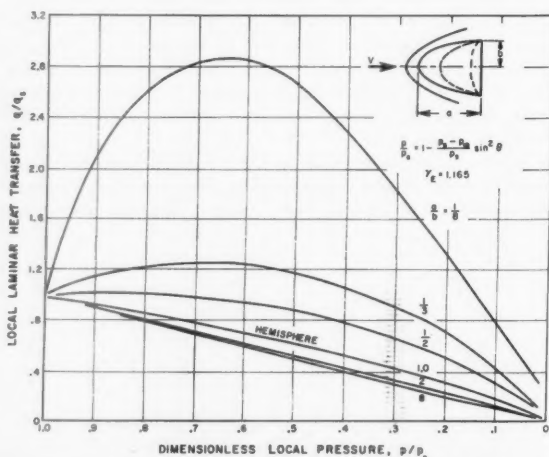


Fig. 1 Effect of geometry and pressure gradients on laminar heat transfer rates

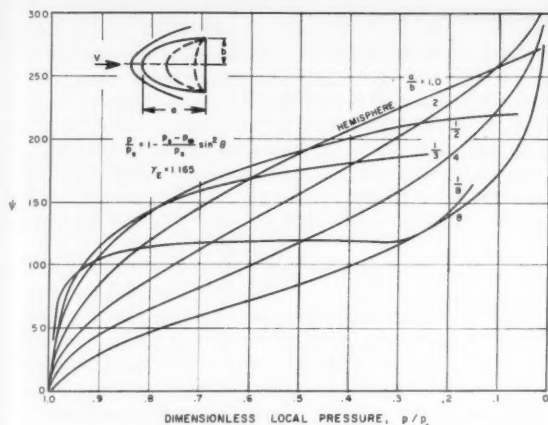


Fig. 2 Effect of geometry on Re_θ

has been taken as the ratio a/b of the major to the minor semiaxis of an ellipsoid of revolution. Low values of a/b represent blunt bodies with large drag values, whereas high values are representative of bodies with low drag. These form factors were computed by using a Newtonian pressure distribution. The stagnation point heat transfer rate given by Equation [2] used in conjunction with the form factors in Fig. 1 makes possible rapid estimations of the laminar heat transfer to typical bodies of revolution.

Transition From Laminar to Turbulent Flow

The current practice for predicting transition from laminar to turbulent flow is to use a Reynolds number Re_θ based on the laminar boundary layer momentum thickness. For a given body shape, the magnitude of Re_θ depends on the position on the body (x/R), and on flight conditions.

Using the numerical solutions of the laminar boundary layer of (1), the momentum thickness θ may be correlated by

$$\theta = \frac{\sqrt{2\xi}}{\rho_\infty u_\infty r} \left[(0.491(1 - 0.090 \beta^{0.4}) \left(\frac{\rho_\infty \mu_\infty}{\rho_w \mu_w} \right)^{0.808} \right] \quad [3]$$

Based on the momentum thickness given by Equation [3] and given flight conditions, the Re_θ may be expressed by

$$Re_\theta = \sqrt{b} \left(\frac{\rho_\infty}{\rho_{SL}} \right)^{0.5076} \left(\frac{V}{10^3} \right)^{0.477} \psi \quad [4]$$

where b is the base radius of the body in inches, and ψ is primarily a function of body geometry. In Fig. 2 values of the function ψ are plotted against the local dimensionless pressure for several values of the parameter a/b for the case of 300 K wall temperature. Use of Equation [4] in conjunction with the results given in Fig. 2 yields an estimation of the momentum thickness Reynolds number on typical nose cone shapes during re-entry. From these results then prediction of transition can be based on a properly chosen transition Reynolds number.

Turbulent Heat Transfer

In (7) it is shown that the local turbulent heat transfer through a highly cooled partially dissociated boundary layer on a blunt body can be expressed by

$$Nu = 0.029 \sigma^{1/3} Re_x^{0.8} [1.037 G(x)^{1/5}] \left[1 + 0.58 \frac{h_{Ds}}{He} \right] \quad [5]$$

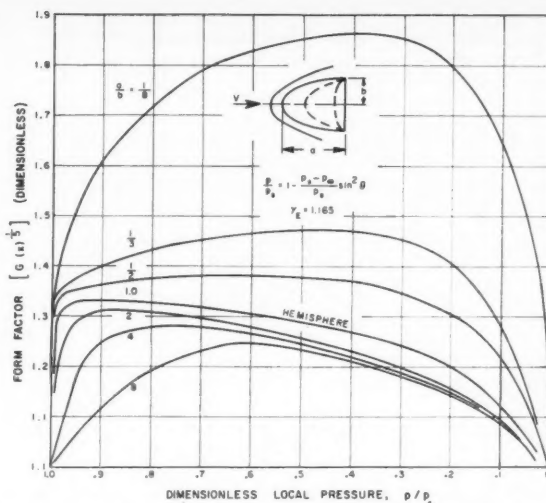


Fig. 3 Effect of geometry and pressure gradients on turbulent heat transfer rates on blunt bodies of revolution

This formula is based on a semiempirical development which relies to a certain extent on experimental data for blunt bodies obtained principally in shock tubes.

The term in the first bracket is the so-called form factor, and represents the contribution of a local pressure gradient and geometry effect to the heat transfer rate. The term $G^{1/5}$ is plotted in Fig. 3 as a function of the local dimensionless pressure on the body for several body shapes. The geometrical parameter a/b used in Fig. 3 is the same as that used for the laminar form factors given in Figs. 1 and 2.

The term in the second bracket is the contribution of the energy of dissociation outside the boundary layer to the heat transfer rates. It depends on both the local pressure and the entropy of the flow external to the boundary layer. The data of (7) indicates a maximum value of $h_{Ds}/He = 0.30$, which gives at most a 17% contribution to the heat transfer rate.

The equation that gives the local heat transfer rates neglecting the form factor and energy of dissociation effects is

$$Nu = 0.029 \sigma^{1/3} Re_x^{0.8} \quad [6]$$

Equation [6] can be correlated as a function of altitude and flight velocity. Using the charts of (4), the Sutherland's law of viscosity,⁶ a Prandtl number $\sigma = 0.71$, a wall temperature of 300 K and a constant ratio of specific heats $\gamma = 1.2$ for the isentropic flow around the body, Equation [6] may be represented by

$$\dot{q} x^{0.2} = 1.346 \times 10^4 \left(\frac{\rho_\infty}{\rho_{SL}} \right)^{0.8} \left(\frac{V}{10^4} \right)^{2.18} \phi \quad [7]$$

where ϕ is a function of the local pressure and is plotted in Fig. 4. This function has a maximum value of 0.261 near the sonic point. Equation [7] reproduces the heat transfer rates of Equation [6] with a maximum error of 5% in the altitude, and velocity range from 40,000 to 200,000 ft and 6000 to 26,000 fps, respectively. At sea level, it yields lower heat transfer rates than the corresponding rates of Equation [6], and the maximum error is 15%. It is important to note that the result expressed by Equation [7] is insensitive to the value of γ used.

⁶ For temperatures that are high in relation to the Sutherland constant, as was assumed in developing Equation [7], the viscosity varies as the one half power of the temperature.

Table 1 $W/C_D A$ and R for $(\dot{q}_{\text{rad}}/\dot{q}_{\text{aero}})_{\text{max}} = 0.10$

$W/C_D A$, psf	R , ft
100	2.82
400	1.03
700	0.68
1000	0.52

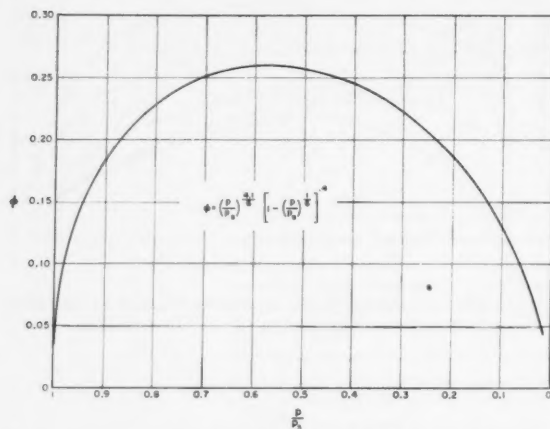


Fig. 4 Function ϕ for the calculation of turbulent heat transfer rates

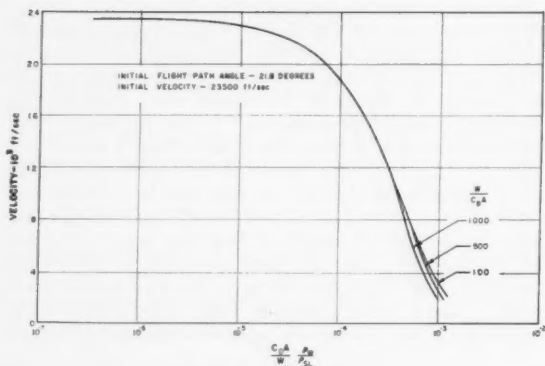


Fig. 5 Generalized hypersonic flight trajectories

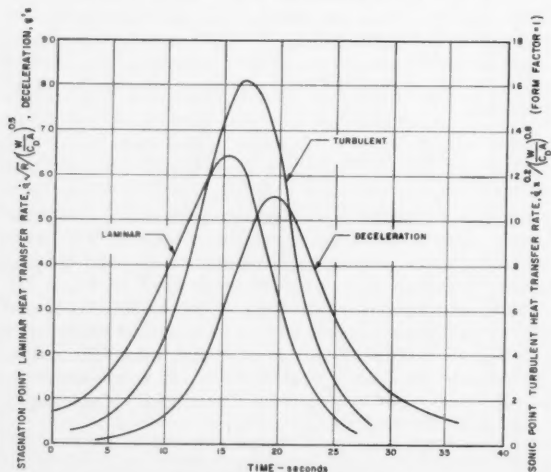


Fig. 6 Generalized heat transfer rates and deceleration for hypersonic re-entry

Radiative Heat Transfer

As an aid to making rapid evaluations of the heat transfer to a body owing to radiation from high temperature air, an engineering equation for predicting the stagnation point radiative heat transfer has been developed. Using the air emissivities given in (8) and the shock wave standoff distances given by Lighthill (9), the expression for the stagnation point radiative heat transfer applicable to the hypersonic ICBM flight re-entry conditions for a surface with zero reflectivity is

$$\frac{\dot{q}_{\text{rad}}}{R} = 10^2 \left(\frac{V}{10^4} \right)^{3.8} \left(\frac{\rho_{\infty}}{\rho_{SL}} \right)^{1.6} \quad [8]$$

With Equations [8 and 2] it can be shown that the stagnation point radiative heat transfer, which is also the maximum radiative heat rate, is small compared with the aerodynamic heat transfer. Eliminating the velocity in terms of the ballistic drag parameter $W/C_D A$ by assuming a straight line trajectory through a single scale height atmosphere, the maximum of the ratio of radiative heat transfer to aerodynamic heat transfer at the stagnation point can be written as

$$\left(\frac{\dot{q}_{\text{rad}}}{\dot{q}_{\text{aero}}} \right)_{\text{max}} = 1.32 \times 10^{-4} R^{1/2} \left(\frac{W}{C_D A} \right)^{1.1} \quad [9]$$

This maximum ratio occurs at a lower altitude than the altitudes for maximum aerodynamic and maximum radiative stagnation point heat transfer rate. Table 1 gives values relating $W/C_D A$ and nose radius R for the case of $(\dot{q}_{\text{rad}}/\dot{q}_{\text{aero}})_{\text{max}} = 0.10$.

The nose radii given in Table 1 vary with $W/C_D A$ in the same general manner as required geometrically to obtain increases in $W/C_D A$ with a fixed gross weight. It should be noted that a surface with a reflectivity different from zero would further decrease the radiative heat transfer. Since the radiative and aerodynamic heat transfer distributions along a re-entry trajectory are similar, the total heat transfer owing to radiation is therefore small compared with the total aerodynamic heat transfer. We conclude then that for preliminary design purposes it is permissible to neglect the stagnation point radiative heating.

Hypersonic Flight Applications

The results given in the preceding sections have been specialized to hypersonic flight re-entry conditions and are presented next.

Analysis based on the assumption of a straight line trajectory suggests that for given initial conditions (velocity and flight path angle), the velocity along the trajectory during re-entry may correlate against the variable $(C_D A/W)(\rho_{\infty}/\rho_{SL})$. Detailed trajectory calculations for an initial flight path angle of 21.8 deg yield the correlation given in Fig. 5. For a given atmospheric model the flight velocity can be obtained as a function of altitude for fixed values of the ballistic drag parameter $W/C_D A$. Although the correlation is not unique at low velocities for all values of $W/C_D A$, the single curve correlation has been found to be satisfactory for describing the trajectories during the major portion of the heating phase of the re-entry.

This suggests a generalized heat transfer rate distribution along the re-entry trajectory. Heat transfer calculations yield the results presented in Fig. 6, where the stagnation point laminar and the turbulent heat transfer rates for all hypersonic flight trajectories with fixed initial conditions (23,500 fps, 21.8 deg) are plotted as a function of time. The sonic point turbulent heat transfer rate has been plotted on Fig. 6 for values of the turbulent form factor of 1. The deceleration encountered along the trajectory which is a function of only the initial trajectory angle has also been plotted on Fig. 6, to show the relative relation between heating and deceleration.

An important consideration in making preliminary design estimates is the maximum heat transfer rate experienced during re-entry. It has been found that the maximum heat transfer rates encountered by a hypersonic nose cone during re-entry from fixed initial conditions of 21.8 deg flight path angle and a velocity of 23,500 fps can be written as follows for the range $100 \leq W/C_{DA} \leq 1000$

Stagnation point

$$(\dot{q}\sqrt{R})_{\max} = 64.2 \left(\frac{W}{C_{DA}} \right)^{0.5} \quad [10]$$

Turbulent heat transfer rate evaluated with sonic point pressure and a form factor of 1:

$$(\dot{q}x^{0.2})_{\max} = 16.2 \left(\frac{W}{C_{DA}} \right)^{0.5} \quad [11]$$

These results are shown plotted in Fig. 7, which includes also a plot of Equation (11) together with a form factor for the hemisphere and the maximum dissociation effect.

Fig. 6 indicates a single time scale is adequate for describing the heating cycle during re-entry for all values of W/C_{DA} . Therefore, the integrated local heat transfer rate should correlate against W/C_{DA} . Calculations of the integrated local heat transfer yield the results

Stagnation point:

$$Q\sqrt{R} = 830 \left(\frac{W}{C_{DA}} \right)^{0.5} \quad [12]$$

Turbulent value at the sonic point with a form factor of 1:

$$Qx^{0.2} = 177.5 \left(\frac{W}{C_{DA}} \right)^{0.5} \quad (13)$$

Comparison of Equations [10 and 12] reveals the stagnation point heating cycle can be considered as a triangular pulse having the peak value given by Equation [10] and time base of 12.9 sec. The corresponding time base for quickly estimating the integrated local turbulent heat transfer is 10.9 sec. For preliminary design purposes the total integrated turbulent heat transfer is sufficiently close to the actual value, considering laminar heat transfer, transition and turbulent heat transfer. At a W/C_{DA} of 300 the error in this approximation is about 5%. At higher values of W/C_{DA} the error becomes smaller because the total heat input increases whereas the laminar contribution remains essentially unchanged.

Nomenclature

- A = reference area for drag coefficient, ft²
 a/b = major semiaxis to minor semiaxis of an ellipsoid of revolution
 b = base radius of re-entry body, in.
 C_D = drag coefficient
 H = total enthalpy
 h = enthalpy
 h_D = average atomic dissociation energy times atom mass fraction in external flow
 L = Lewis number
 Nu = Nusselt number
 P = aerodynamic local pressure
 Q = Total heat transfer per unit area, Btu/ft²
 \dot{q} = Heat transfer rate, Btu/ft² sec
 Re = Reynolds number based on flow conditions external to boundary layer
 R = nose radius at stagnation point, ft
 r = cylindrical radius of body
 u = x-component of velocity
 V = flight velocity, fps
 W = weight, lb
 x = distance along meridian profile of body, ft
 γ = ratio of specific heats
 θ = momentum boundary layer thickness; also angle between longitudinal body axis and the normal to the local tangent to body surface

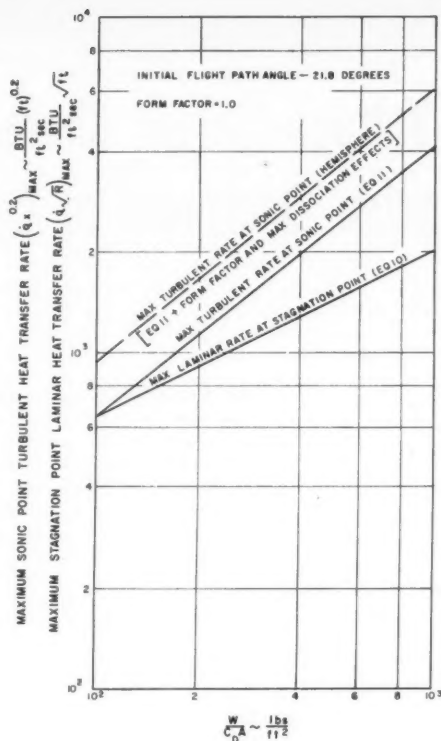


Fig. 7 Maximum heat transfer rates for hypersonic flight

- μ = absolute viscosity
 ρ = mass density
 σ = Prandtl number
 ϕ = pressure function in turbulent heat transfer correlation
 $\xi = \int_0^x \rho w \mu u e r^2 dx$
 $\beta = 2[d \ln u_e / d \ln \xi]$

Subscripts

- e = boundary layer external flow conditions
 s = stagnation point condition
 SL = sea level
 w = wall condition
 ∞ = ambient conditions

References

1. Fay, J. A. and Riddell, F. R., "Stagnation Point Heat Transfer in Dissociated Air," Avco-Everett Research Lab., Everett, Mass., Research Rep. 1, April 1957.
2. Rose, P. H. and Stark, W. I., "Stagnation Point Heat Transfer Measurements in Dissociated Air," Avco-Everett Research Lab., Everett, Mass., Research Rep. 3, April 1957.
3. Rose, P. H. and Riddell, F. R., "An Investigation of Stagnation Point Heat Transfer in Dissociated Air," Avco-Everett Research Lab., Everett, Mass., Research Rep. 7, April 1957.
4. Feldman, S., "Hypersonic Gas Dynamic Charts for Equilibrium Air," Avco-Everett Research Lab., Everett, Mass., Jan. 1957.
5. Probst, R., "Inviscid Flow and Heat Transfer in the Stagnation Point Region of Very Blunt-Nosed Bodies," Avco-Everett Research Lab., Everett, Mass., Jan. 1957.
6. Kemp, H. H., Rose, P. H. and Detra, R. W., "Laminar Heat Transfer Around Blunt Bodies in Dissociated Air," Avco-Everett Research Lab., Everett, Mass., Research Rep. 15, May 1958.
7. Rose, P. H., Probst, R. F. and Adams, M. C., "Turbulent Heat Transfer Through a Highly Cooled Partially Dissociated Boundary Layer," Avco-Everett Research Lab., Everett, Mass., Research Rep. 14, Jan. 1958.
8. Kivel, B. and Bailey, K., "Tables of Radiation from High Temperature Air," Avco-Everett Research Lab., Everett, Mass., Research Rep. 21, Dec. 1957.
9. Lighthill, M. J., "Dynamics of a Dissociating Gas, Part I, Equilibrium Flow," *J. Fluid Mech.*, vol. 2, part I, Jan., 1957, pp. 1-32.

Voltage-Current Characteristics of Tungsten Electrodes in Cesium Vapor¹

L. H. STAUFFER²

General Electric Co.
Schenectady, N. Y.

Experimental data is presented on the voltage-current relationship for tungsten electrodes in pure cesium vapor at pressures in the range of 10^{-6} to 10^{-3} m of mercury. Anode and cathode temperatures ranging from room temperature to over 1500 C are employed. Current-voltage characteristics are presented to illustrate the effect of varying the cesium pressure and the anode temperature. Disruptive breakdown is not observed at the low cesium pressures employed. The voltage-current relationship is smooth up to the point where heating of the electrodes becomes excessive. At the low pressures employed the conduction mechanism is governed entirely by electrode surface phenomena, such as secondary electron emission and contact ionization. Since the mean free path for electron-atom collisions is many gap lengths current carriers can originate only at the electrodes. It is shown that in the pressure range studied the current increases steeply with cesium vapor pressure at all electrode temperatures, regardless of which electrode is heated. When the cesium vapor pressure exceeds 3 to 5 μ , corresponding to a cesium reservoir temperature of 60 to 65 C, a gap between tungsten electrodes will not support potentials in the kilovolt range without excessive power loss

MANY proposed designs for electric propulsion systems make use of one or more electrodes immersed in an alkali metal vapor such as cesium (1,2).³ Electrodes for extraction, acceleration and focusing of cesium ions may be of tungsten, molybdenum or tantalum and often must operate at high temperatures. In the design of such systems a knowledge of the limits governing inter-electrode potentials and potential gradient is essential.

Electrical Conduction in Vacuum

To support electrode potentials of the order of kilovolts, the particle density in the inter-electrode space must approach vacuum conditions. Arcs, sparks or glow discharges are not normally initiated or sustained under these conditions. At pressures of 10^{-3} mm of mercury and higher, electrical discharges are sustained by ionizing collisions in the gap, and by electron and ion bombardment of the electrodes which may in turn contribute secondary electrons or ions to help maintain the discharge. In such discharges the current may rapidly rise to catastrophic magnitudes unless it is limited by the impedance of the circuit. If the pressure is maintained at such a low level that electron-atom collisions in the gap are rare, owing to the low particle density, charge multiplication by ionizing collisions in the gap cannot occur.

To insure against generation of charge carriers in the inter-electrode region, the mean free path for electron-atom collisions must be long compared with the gap length. Since the mean free path for electron-atom collisions is several times the mean free path for atom-atom collisions it is sufficient, for present purposes, to express this criterion in terms of the kinetic theory mean free path. The relation between mean free path and temperature for cesium vapor in equilibrium with its liquid phase is represented by the dashed curve of Fig. 1. This curve was derived by kinetic theory considerations from the vapor pressure-temperature relation (3) shown by the solid curve of Fig. 1. From the mean free path relation it is evident that the criterion for suppression of gas ionization between the electrodes is satisfied for cesium boiler temperatures below 375 K for gaps of a few centimeters in length. This corresponds to cesium vapor pressures below 1 μ (10^{-3} mm of mercury) where the mean free path is many gap lengths.

At pressures below 1 μ , conduction can take place only by the release of charged particles at the electrode surfaces followed by transfer across the gap. Ionization by collisions is precluded by low particle density within the gap. It is, therefore, of interest to briefly examine the possible mechanisms for charge release at the anode and cathode surfaces.

Several processes contribute to the net conduction across a gap between tungsten electrodes in cesium vapor at pressures

Charge Exchange Effects

Several processes contribute to the net conduction across a gap between tungsten electrodes in cesium vapor at pressures

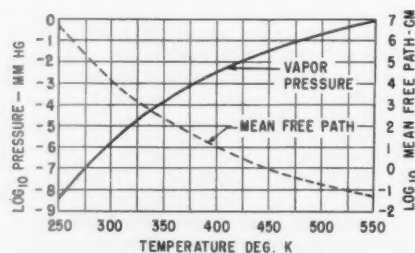


Fig. 1 Temperature dependence of vapor pressure and mean free path of cesium

Presented at the ARS Semi-Annual Meeting, Los Angeles, Calif., May 9-12, 1960.

¹ Work supported by Flight Propulsion Laboratory, General Electric Company.

² Applied Physicist, General Engineering Laboratory.

³ Numbers in parentheses indicate References at end of paper.

below $1\ \mu$. If the cathode is heated it emits electrons which cross the gap and impinge upon the anode surface. Positive ions may be formed by contact ionization at the anode surface, depending on its temperature. These ions cross the gap in the opposite direction, strike the cathode and release secondary electrons which are accelerated toward the anode. The net current is the sum of these three currents. Its magnitude depends upon the energy of impact of ions and electrons corresponding to the potential difference across the gap. It is also affected by both anode and cathode temperatures, and by the cesium vapor pressure which controls the degree to which the electrodes are coated with cesium, thus influencing contact ionization efficiency and secondary electron emission.

To understand the process of current buildup across the inter-electrode space, it is necessary to take into account the more important surface effects at the electrodes.

Cathode Phenomena

Here several effects may be listed.

Thermionic emission: For clean tungsten, molybdenum or tantalum surfaces, electron emission reaches significant levels only at temperatures around 1000 C and above. However, Taylor and Langmuir (4) have shown that the presence of adsorbed cesium on the cathode surface greatly enhances the thermionic emission of electrons. For example, in cesium vapor at $0.1\ \mu$ -pressure, enough cesium is adsorbed on tungsten at 900 K to raise the electron emission to approximately the same level as would be found at 2000 K for clean tungsten. This amounts to an increase of about 10^{12} over the emission of a clean tungsten surface.

Secondary emission owing to positive ion bombardment: The number of electrons released from the cathode by impact of a single positive ion may vary from less than unity to as high as 20 or more, depending upon the type of ion, its energy and the atomic number of the cathode surface material. Bourne, Cloud and Trump (5) have shown that as the energy of the ions increases, the secondary electron emission at first rises steeply and then increases almost linearly with the voltage of the incident ions.

Photoemission: Light, especially in the ultraviolet spectral region, may eject electrons from the cathode by the photoelectric effect. This could play a part in the incipient breakdown process, particularly when the cathode is coated with cesium.

Contact Ionization at the Anode

An atom adsorbed on a metal having a work function higher than the ionization potential of the atom may be evaporated as an ion. It is well known that cesium atoms become ionized in this way when they impinge upon a clean hot tungsten surface (3). At low temperatures the surface becomes partially or completely coated with cesium, and the fraction of incident atoms converted to ions is sharply reduced. As the temperature of the tungsten is increased, a new equilibrium point having a lower surface density of adsorbed atoms is reached. Ultimately a temperature may be reached where the surface density of adsorbed atoms approaches zero. Under this condition the efficiency of the contact ionization process approaches a maximum, and almost all incident atoms are reflected as ions. For example, Taylor and Langmuir (4) have found that, when tungsten is coated with half the number of cesium atoms required for a monolayer, only 1 cesium atom out of 10^6 striking the surface is ionized. When the surface is free of adsorbed cesium, the efficiency of ionization is almost 100%.

There are no other important mechanisms for positive ion production at the anode. However, since the efficiency of contact ionization depends strongly on the cleanliness of the anode surface, the cleanup effect of electron bombardment

may increase positive ion emission. At high current densities and gap voltages, surface cleanup at the anode may, indeed, contribute heavily to current buildup.

Experimental Investigation

Because of the complexity of the inter-electrode conduction mechanism, a theoretical derivation of the current-voltage relationships has not been attempted. It is, therefore, of interest to investigate the relationship experimentally for a range of cesium vapor pressures and electrode temperatures of interest in ion propulsion devices.

Attempts to apply high potentials to a pair of heated electrodes mounted in a bell jar were abandoned because of the difficulty of controlling the cesium pressure in such an enclosure. Also, such arrangements are difficult to outgas. To avoid these difficulties, an electrode arrangement consisting of two flat spiral filaments was adopted. These filaments were sealed in a pyrex glass bulb. A sidearm appendage immersed in a thermostated bath and containing about 1 gm of cesium affords vapor pressure control over the range 10^{-8} mm of mercury to 10^{-1} mm of mercury.

An outstanding advantage of the flat spiral filament form of electrode is that it can be rigorously cleaned at any time by heating to high enough temperature to drive off all contaminants, including adsorbed cesium. Also, the electrode temperature can be determined by calibrating power input or resistance against optical pyrometer readings when the tube is first evacuated. Later temperature determinations are not then affected by blackening of the tube walls by sputtered filament material.

Another advantage of the sealed off tube is that its temperature can be controlled by surrounding it with an oven or a stream of heated air to maintain all parts well above the temperature of the cesium reservoir. Only under these conditions can the vapor pressure in the bulb be found from the reservoir temperature.

While this gap geometry is not ideal, it is believed to be reasonably representative of conditions likely to be met in ion propulsion design. Such an experimental arrangement permits exploratory measurements of electrode current under controlled temperature and pressure conditions over a wide range of applied voltage.

Tube Design

As shown in Fig. 2, two flat tungsten spirals, $\frac{3}{4}$ -in. OD, are formed of 10 turns of 0.025-in. diameter wire. These are supported on 0.060-in. diameter tungsten stems sealed into a 5 in.-diameter pyrex glass bulb. The electrode spacing is 0.25 in. Two guard rings of gold at the ground potential end are provided to take care of surface leakage currents. About a gram of cesium is vacuum distilled into a side arm which is immersed in a thermostated bath to control cesium pressure in the tube. To avoid condensation of cesium on the tube

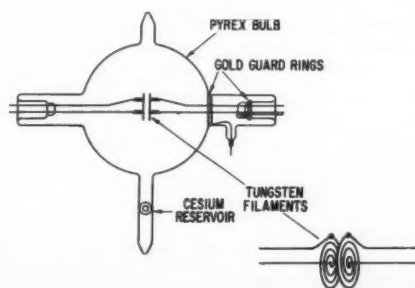


Fig. 2 Tube for current-voltage measurements

walls, it was enclosed in a jacket consisting of two 6-in. diameter glass hemispheres. Heated air was then blown through the intervening space and over the stems. In all experiments the tube was maintained at 95 C or higher, well above the temperature of the cesium reservoir. Thus the cesium pressure could be determined from the temperature of the reservoir by referring to the vapor pressure-temperature relation of Fig. 1.

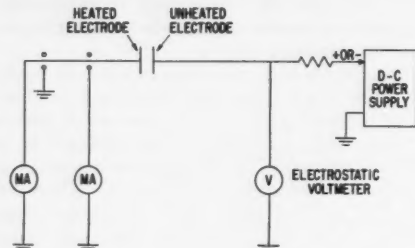


Fig. 3 Circuit for current-voltage measurements

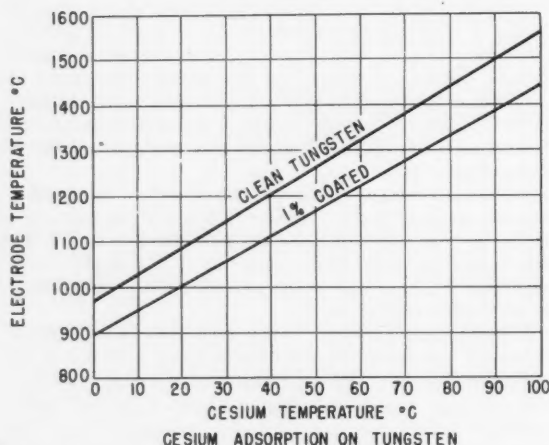


Fig. 4 Temperature for clean and for coated tungsten surfaces

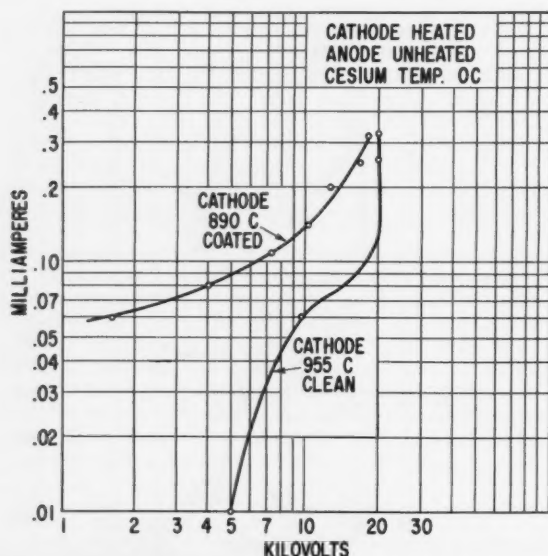


Fig. 5 Current-voltage characteristic for hot cathode with cesium at 0 C

Circuit Arrangements

Fig. 3 shows the circuit arrangement used. A variety of voltmeters, current measuring instruments and series resistors were employed. Their ranges were varied to suit the experimental conditions. The heated electrode was always grounded. The polarity of the ungrounded (unheated) electrode could be changed at will. Because of insulation difficulties, no attempt was made to measure the temperature of this electrode which never attained red heat. Well-filtered d-c power supplies were used except for filament heating, for which 60 cycle a-c was employed.

Current-Voltage Characteristics

Current-voltage characteristics were taken with the heated electrode partially coated with adsorbed cesium and also in the clean condition. Conditions for clean tungsten and for a 1% coating are shown in Fig. 4. The region above the upper line represents conditions under which no cesium is adsorbed on the tungsten surface. Conditions for 1% of a monolayer are represented by the lower line.

Heated Cathode

When only the negative electrode is heated, the primary gap current may be accounted for by simple thermionic emission from the cathode, augmented by secondary electron emission owing to bombardment by ions from the anode. Anode ions can originate from contact ionization when the energy of bombarding electrons from the cathode is sufficient to produce local heating. This heating is augmented by absorption of radiation from the cathode. Fig. 5 illustrates typical current-voltage characteristics for cesium pressures less than 10^{-6} mm Hg, corresponding to a reservoir temperature of 0 C. Higher current at the lower (890 C) electrode temperature is due to enhanced cathode emission caused by adsorbed cesium. At 955 C, the cathode surface is clean, and the emission is characteristic of pure tungsten. Current runaway sets in at about 20 kv.

At a reservoir temperature of 44 C, corresponding to about 10^{-5} mm Hg cesium pressure, current buildup proceeds rapidly in the 20-30 kv region as shown by Fig. 6. Partial coating of the cathode at 1160 deg aids the current growth.

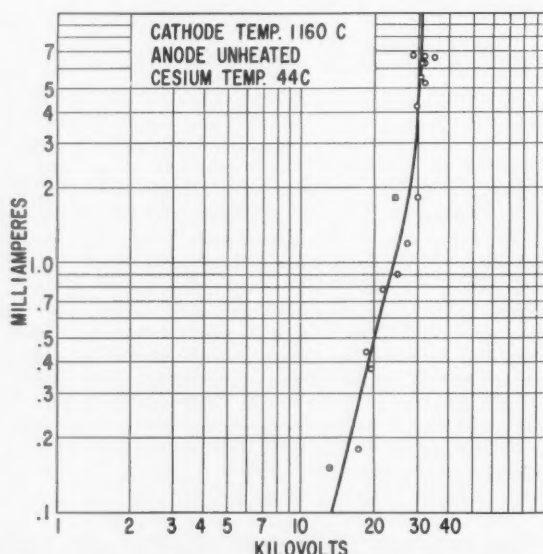


Fig. 6 Current-voltage characteristic for hot cathode with cesium at 44 C

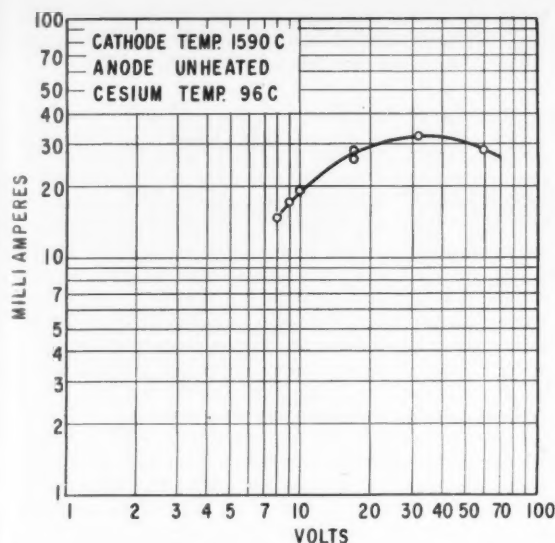


Fig. 7 Current-voltage characteristic for hot cathode with cesium at 96 C

At a reservoir temperature of 96 C, the pressure is about 5×10^{-4} mm Hg or one-half μ . Fig. 7 shows that a potential difference of 30 v produces 30 milliamp of gap current. This corresponds to complete breakdown.

Heated Anode

When the anode is heated, the primary gap current consists of positive ions produced by contact ionization at the hot tungsten surface. Fig. 8 illustrates the current-voltage characteristics for low cesium pressures (17 C reservoir temperature). The upper curve corresponds to an anode temperature of 1010 C, low enough to support a partial coating of cesium, and the lower one corresponds to an anode temperature of 1115 C. This latter temperature is high enough to insure a clean anode surface. The negative slope (decreasing current with increasing voltage) is a striking effect which persists over a wide range of pressure when the anode is heated. A tentative explanation of this lies in the effect of cathode cleanup by ion bombardment on secondary electron emission from its surface. Even at relatively low voltages, positive ions from the anode produce secondary electrons when they strike the cathode. When the cathode is coated with adsorbed cesium, the secondary emission is high, even for ions of a few kilovolts energy. However, as the voltage is raised the ions have enough energy to knock off part of the adsorbed layer. A single ion may remove many atoms depending upon its energy; thus, a new equilibrium is established resulting in a less dense layer and a correspondingly lower yield of secondary electrons for each impinging cesium ion. This causes the net gap current to decrease. Finally, at 10 to 15 kv positive ion bombardment may have almost completely cleaned up the adsorbed layer. This corresponds to a minimum of secondary electron emission, and the gap current falls to a low level. At still higher voltages the secondary emission is from clean tungsten. To account for the steep rise at 20 kv, requires the assumption that the secondary emission characteristic of clean tungsten rises steeply at 20 kv. This is not an unreasonable assumption, since other high atomic number metals, such as gold, exhibit similar characteristics (5).

At a higher cesium pressure corresponding to a reservoir temperature of 50 C, the current-voltage characteristic

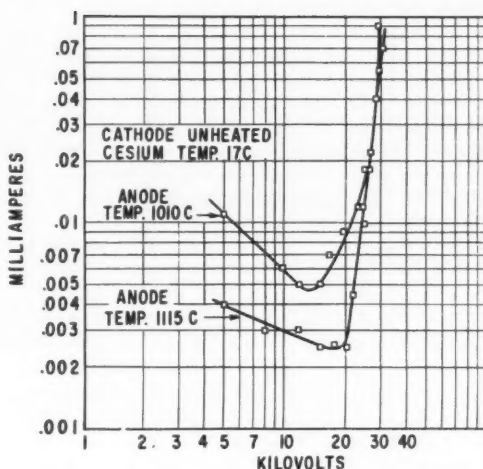


Fig. 8 Current-voltage characteristic for hot anode with cesium at 17 C

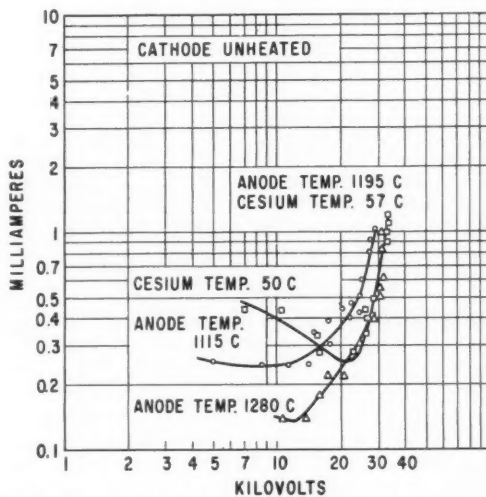


Fig. 9 Current-voltage characteristic for hot anode with cesium at 50 and 57 C

shown by the upper curve of Fig. 9 is obtained. Here, as before, the anode is partially coated, and the slope below 20 kv is negative. However, at a reservoir temperature of 57 C, the negative slope becomes very slight by the lower curve of Fig. 9. Here the higher density of cesium vapor has increased the primary ion current to a level where it begins to obscure the effects of secondary electron emission from the cathode.

When the reservoir temperature reaches 78 C, corresponding to a pressure of 10^{-4} mm of mercury, a steep current buildup sets in below 1 kv. This condition is represented by Fig. 10. Beyond this point high gap voltages cannot be supported.

Effect of Pressure

It is of interest to examine the dependence of current buildup on cesium vapor pressure. At the higher voltages

the current rises almost linearly with gap voltage. The slope of this portion of the curve (conductance) increases with pressure. In Figs. 11 and 12 the gap resistance, at the higher voltages, is plotted against cesium vapor pressure.

With the cathode heated, Fig. 11 shows that the gap resistance falls off steeply at pressures above 10^{-2} μ Hg. This trend is most pronounced when the cathode is free of adsorbed cesium. When the anode is heated the pressure dependence, shown by Fig. 12, is still more pronounced. Points representing anode temperatures low enough to support a partial coating of adsorbed cesium fall on the same curve as points for the higher temperatures corresponding to no adsorbed cesium.

Both of these curves reflect the multiplication of ions and electrons at the electrode surfaces augmented by the presence of adsorbed cesium. For a given electrode temperature the equilibrium surface density of adsorbed cesium depends on the collision rate of cesium atoms with the electrode surface.

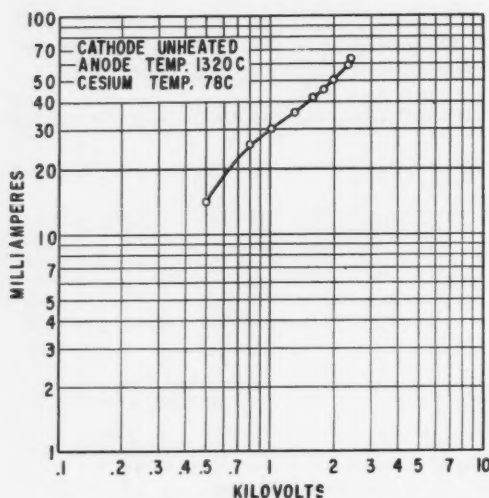


Fig. 10 Current-voltage characteristic for hot anode with cesium at 78 C

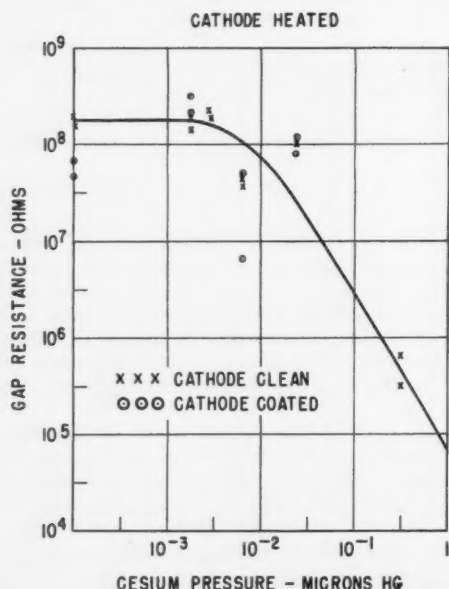


Fig. 11 Effect of cesium pressure on gap resistance with heated cathode

This is, of course, proportional to the vapor pressure. A rapid buildup of current and a corresponding fall in gap resistance with increasing pressure is to be expected.

Conclusions

When high potentials are applied to electrodes in cesium vapor at pressures below 10^{-3} mm Hg the gap current is carried entirely by electrons and positive ions originating at the electrode surfaces. Contact ionization at the anode surface and electron emission by the cathode surface determine the gap current. These processes in turn depend upon the energy of the ions and electrons accelerated across the gap by the applied voltage. Emission processes at the electrodes are strongly influenced by the surface density of adsorbed cesium, which in turn depends on the cesium vapor pressure. This accounts for the strong dependence of the gap current on cesium pressure at all electrode temperatures.

In view of the conduction mechanism described, it may be predicted that the gap current will be a function of the applied voltage, but will be virtually unaffected by the voltage gradient in the gap. Thus short gaps and high voltage gradients may be employed in ion propulsion designs if the total voltage is kept below the limits set by cesium vapor pressure and electrode surface conditions. Field emission at the electrodes must, of course, be suppressed by properly shaping them to avoid high surface gradients.

References

- 1 Stuhlinger, E., "How Useful are Low Thrust Space Vehicles?," *ASTRONAUTICS*, vol. 5, no. 2, Feb. 1960, pp. 24-27, 95-97.
- 2 Forrester, A. T. and Speiser, R. C., "Cesium-Ion Propulsion," *ASTRONAUTICS*, vol. 4, no. 10, Oct. 1959, pp. 34-35, 92-97.
- 3 Taylor, J. B. and Langmuir, I., "Vapor Pressure of Cesium by the Positive Ion Method," *Phys. Rev.*, vol. 51, no. 9, May 1937, pp. 753-760.
- 4 Taylor, J. B. and Langmuir, I., "The Evaporation of Atoms, Ions and Electrons from Cesium Films on Tungsten," *Phys. Rev.*, vol. 44, no. 6, Sept. 1933, pp. 423-458.
- 5 Bourne, H. C., Jr., Cloud, R. W. and Trump, J. G., "Role of Positive Ions in High Voltage Breakdown in Vacuum," *J. Appl. Phys.*, vol. 26, no. 5, May 1955, pp. 596-599.

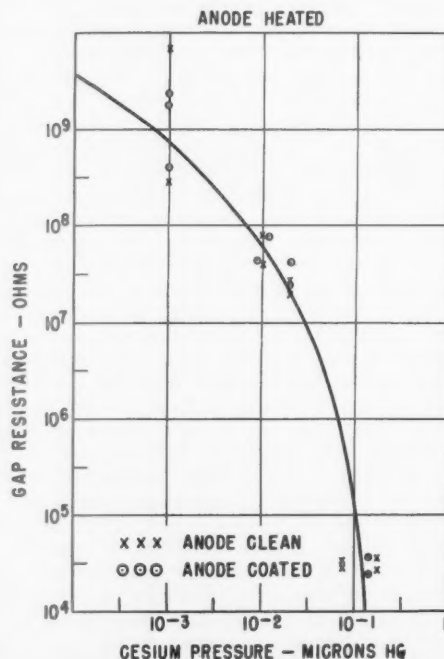


Fig. 12 Effect of cesium pressure on gap resistance with heated anode

Solar Collectors for Use in Thermionic Power Supply Systems in Space

L. D. WING¹

K. E. CAMERON²

The Martin Co.
Baltimore, Md.

The optical aspects of a solar-thermionic power system are described. Various design considerations are presented along with an analytical approach. A modular concept is proposed, and definitions of the problem areas, such as collector fabrication, are followed by an engineering approach to the system design in which a method is presented to decrease the stringent solar alignment tolerance.

THERMIONIC conversion of solar energy to electrical energy is a commonly proposed means of generating secondary power in a space vehicle. The idea hinges on the use of a reflecting collector which concentrates solar energy onto the "hot" surface of a thermionic diode or series of diodes, where the conversion takes place. The heat thus accumulated passes through the converter and is "dumped" into space by the exterior radiating surface of the converter package. The method of energy conversion is not of interest here. Suffice it to note that the temperature on the inner surface of the diode must be very high because the efficiency of the converter is sensitive to the available temperature difference across the two diode plates. It has been found that the most practical form of concentrator which is capable of producing the necessary diode inner plate temperature is a parabolic mirror.

Present thermionic converters have relatively low efficiencies, but systems of the foreseeable future are expected to convert 10% or more of the solar energy entering the converter into usable electric energy. To provide sufficient auxiliary power without exceeding space and weight limitations, it is apparent that energy loss in the collector system must be reduced to an absolute minimum. The purpose of this paper is to discuss what these collector losses are, and to examine means of improving the overall collector efficiency.

Design Considerations

The success of a parabolic solar energy collector is clearly a function of the ingenuity used in manipulating the trade-offs between the following design considerations:

- 1 Total electric power output required.
- 2 Efficiency of the thermionic converter.
- 3 Intensity level of solar energy impinging on converter required to attain (2).³
- 4 Weight and space limitations imposed by the space vehicle (packaging problem, means of positioning the collector and converter relative to the solar radiation and to each other, etc.).
- 5 Vehicle control system solar-seeking capability.
- 6 Allowable misalignment α of the collector axis relative to the impinging solar radiation.
- 7 Efficiency of the collector.

Received Aug. 12, 1960.

¹ Senior Thermal Engineer, Baltimore Div. Member ARS.

² Senior Engineer, Research and Development Dept., Baltimore Div.; now Thermodynamicist, Missile and Space Vehicle Div., General Electric Co., Philadelphia, Pa.

³ Numbers in parentheses indicate References at end of paper.

For the purpose of examining the collector design, the first four items are assumed to be fixed. The use of modules, combining a number of separate collector-converter systems to provide the required electrical output, offers a convenient means of attaining the collector efficiency associated with a noncollapsible mirror. An additional advantage, of course, is the assurance that a single component failure will merely decrease the electrical power instead of cutting it off completely. Justification of the modular approach will become clearer as the collector efficiencies of the best reflectors attainable are examined.

The total required electric power output, combined with the attainable efficiency of the thermionic converter and the minimum practicable diode inner face temperature, defines the optical geometry of each module and the number of modules needed. Module size depends on the space available for storing within the vehicle, the system weight and the mechanical means of positioning the collectors relative to their converters. Remaining design considerations are the overall efficiency of the collector, and the limitations of angular error between the incident solar rays and the parabolic mirror axis (hence, sensitivity demands on the solar positioning system and ability to position the reflector axes relative to some vehicle reference).

One further item is of importance to the optical system. As has been stated, the use of a thermionic converter requires that the solar energy be delivered to the generator cavity at a very high intensity. In order to attain the necessary intensity the solar image reflected from the collector must be extremely small. A large image represents not only a lower intensity of energy within the image, but also the need for a large aperture in the converter face; increasing the size of the aperture results in an increase of energy loss owing to back-radiation, that is, energy reradiated to space from the interior of the converter cavity, back through the aperture. On the other hand, a large aperture decreases the stringency of the alignment of the mirror axes with the incident solar rays (see Fig. 8).

Analysis

In order to estimate the effects of some of the design parameters on the efficiency of the collector system, as well as to understand how the collector is designed, a brief outline of the relevant equations is given. The derivations, chiefly geometric, are considered self-evident (1). A sketch showing the basic geometry of a typical collector (paraboloid of revolution) is shown in Fig. 1.

$$\rho = \frac{2f}{1 + \cos \theta_R} \text{ (general)} \quad [1]$$

$$L = f - \rho \cos \theta_R = \frac{D(1 + \cos \theta_R)}{4 \sin \theta_R} - \frac{D \cot \theta_R}{2} \text{ (general)} \quad [2]$$

$$f = \frac{D(1 + \cos \theta_R)}{4 \sin \theta_R} \text{ (general)} \quad [3]$$

$$S = \frac{\alpha}{57.3} \frac{2\rho - f}{\cos \theta} \text{ (general)} \quad [4]$$

$$d_c = 2f \tan 16' = f/107.3 \quad [5a]$$

$$P/\eta = 0.3861 f^2 (\sin^2 \theta_R - \sin^2 \theta_s) \quad [6a]$$

$$\eta_c = \left[\frac{1 + \cos \theta_R}{2} \right]^2 \quad [7a]$$

Equations [5a through 7a] are applicable when considering the circular solar image.

$$d_a = 0.01862 / \cos \theta_R (1 + \cos \theta_R) \quad [5b]$$

$$P/\eta = I_0 A_R \quad [6b]$$

$$\eta_c = 1 \quad [7b]$$

Equations [5b through 7b] are applicable when considering the aberrated solar image.

Two distinct analytical approaches may be used to design a solar collector system. The first considers the usable energy which lies within the circular solar image. The second considers all energy within the aberrated solar image to be usable. The circular solar image is defined as the image of the sun which has the same diameter as an image reflected from a differentially small, flat mirror placed in the center of the parabolic reflector. The actual or aberrated solar image at the reflector focal plane is a circle of larger diameter than the circular solar image. The difference is owing to the inherent ellipticity of a solar image reflected from any differential area not taken at the paraboloid center; the

greatest ellipticity, of course, arises from differential areas at the paraboloid rim. These ellipticities, when integrated over the entire parabola surface, form a solar image of circular shape having a diameter d_a . The energy within the circular solar image has a constant intensity level, whereas the energy outside decreases with increase in radius until it becomes minimum where the image radius is $d_a/2$ and then vanishes when r is larger than $d_a/2$.

This energy decay is important since near critical misalignment angles obliterate portions of the aberrated solar image. This action will be seen to decrease the total energy delivered to the converter by a factor which is appreciably less than the percentage of area of the aberrated solar image which has failed to fall within the converter aperture. Moreover, the calculated α value which assumes no image loss may be alleviated with only small degradations of the energy delivered to the converter.

Equations [1 through 4] are applicable to either approach, whereas Equations [5a, 6a and 7a] apply only when the circular solar image is considered. Equations [5b, 6b and 7b] replace Equations [5a, 6a and 7a] for the aberrated solar image case.

In general, the circular solar image case would be applicable to the use of a parabolic reflector which concentrates the solar energy on a single thermionic diode. There are two reasons for this: A single diode generator would require the high temperatures associated with the high intensity portion of the image in which the intensity level is constant, and design of a diode of diameter d_c would result in the loss of all energy outside the circular solar image. In addition, any misalignment angle would result in loss from the high intensity portion of the image, which means greater energy loss for smaller values of misalignment angle. The amount of solar energy "wasted" is proportional to the rim angle of the collector (degree of ellipticity of images from differential collector areas). Note that Equations [5a, 6a and 7a] are all functions of θ_R .

If the individual thermionic diodes are placed with their "hot" faces on the inner wall of a "cavity" (converter) having an aperture to permit entry of the concentrated solar energy

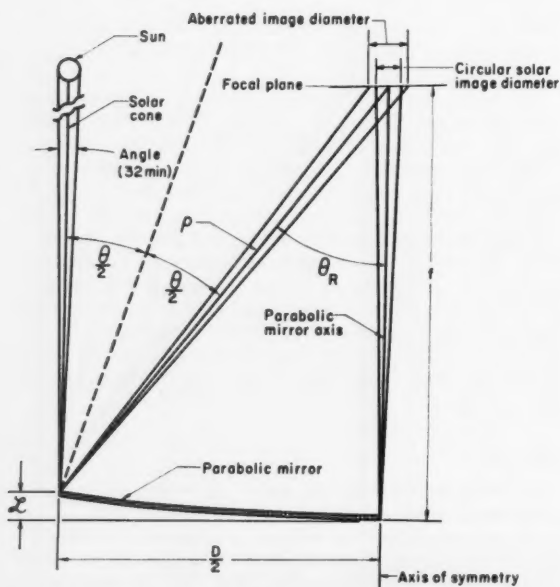


Fig. 1 Geometry of parabolic mirror

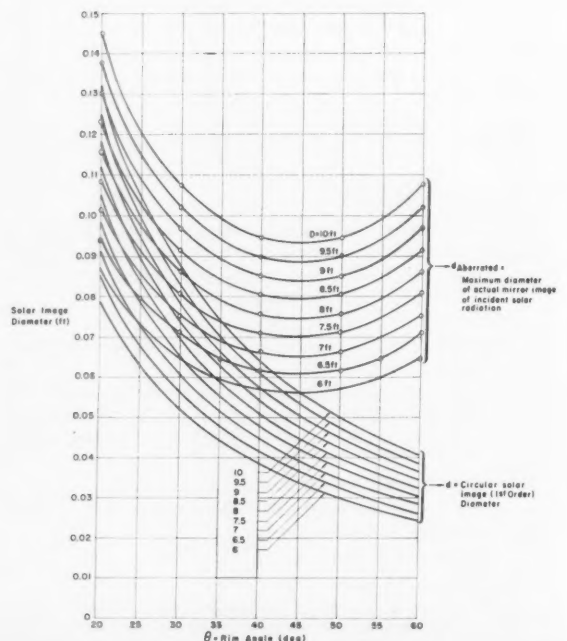


Fig. 2 Solar image diameter vs. rim angle

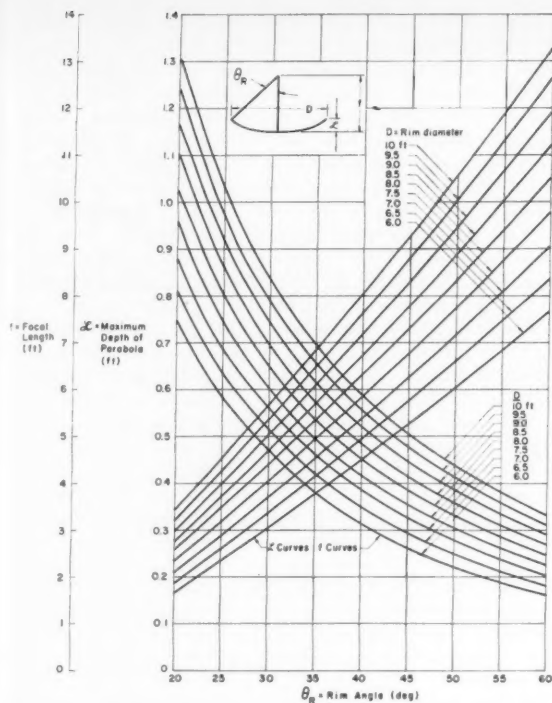


Fig. 3 Geometry relationships of various solar collecting parabolic mirrors

and having highly reflective surfaces on all inner walls (save the diode "hot" faces), then the solar energy is distributed by reflection and reradiation. In this way, the diodes receive a relatively constant intensity of energy, but now *all* energy which enters the cavity aperture (less what is lost owing to back radiation) goes to make up the power input to the converter. Thus, Equations [5b, 6b and 7b] are applicable. These equations are independent of θ_R .

Fig. 2 shows the variation of the circular solar image diameter d_c and the aberrated solar image diameter d_a with rim angle θ_R for a range of collector diameters D . These curves are derived from Equations [5a and 5b]. Fig. 3 gives the reflector focal length f and maximum depth of the parabola L as functions of rim angle for the same range of collector diameters. The data come from the solution of Equations [2 and 3]. Equation [4] is solved, parametrically, in Fig. 4 to yield the relationship between the motion of a point on the solar image relative to a point on the converter aperture resulting from solar misalignment. These data are given as a function of rim angle for the various collector diameters. Fig. 5, from Equation [6b], shows the power delivered to the converter as a function of the reflector efficiency and diameter, applicable to the aberrated solar image. A similar relation for the circular solar image derives from the solution of Equation [6a] and is shown in Fig. 6. The latter figure is plotted as a function of θ_R , since in both Figs. 5 and 6 the efficiency η term does not include energy degradation owing to rim angle aberration.

Fig. 7 is a plot of the concentration efficiency η_c , which is defined as the ratio of power received at the converter aperture to the total power reflected by the collector. This variation is determined from Equation [7a] (circular solar image), and is seen to be independent of all geometric parameters of the collector save the rim angle. When the aberrated image is considered, η_c is unity.

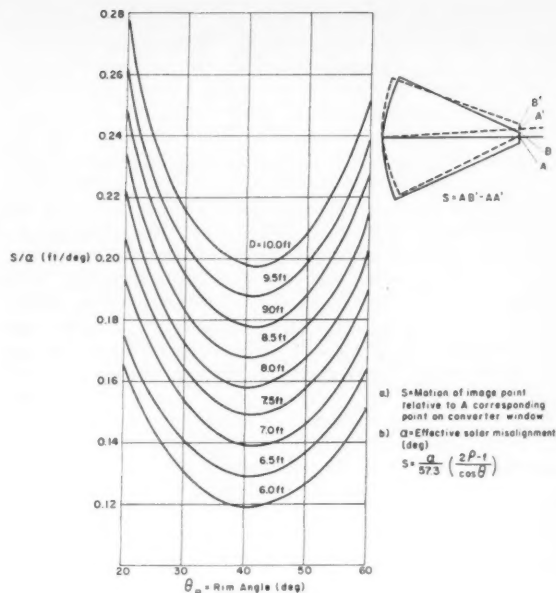


Fig. 4 S/α vs. θ_R for several rim diameters D

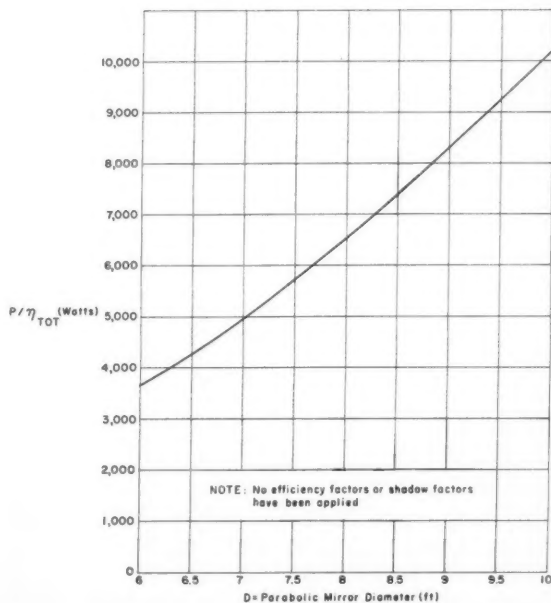


Fig. 5 Power delivered to converter ($d_{\text{aberrated}} < \text{converter aperture}$) vs. parabolic mirror diameter

Discussion

If design is based upon fitting the circular solar image to the converter aperture, the rim angle degradation of energy delivered to the image will be included. The converter aperture diameter is chosen to be larger than the circular solar image diameter to accommodate motion of the image due to angular misalignment of the solar radiation. As we have seen, the aperture diameter depends upon the design of the thermionic converter, which, in turn, depends upon the power available to the converter. Thus, the aperture diameter, the reflector diameter and the rim angle may be

assumed to be fixed for a given design. Then determination of the image diameter (Fig. 2) defines the space on either side of the circular solar image available for the image motion (Fig. 4). Since the converter aperture is larger in diameter than the circular solar image, when α equals 0, it is clear that the assumption of full rim angle degradation of the energy entering the aperture is inaccurate; the energy actually delivered is greater than that indicated by the calculation.

Therefore, it appears more realistic to base the design on the aberrated solar image. In this case, when α equals 0, the entire power (as derived from Fig. 5 with the appropriate η) lies in the aberrated image. If d_a is smaller than aperture diameter, this means that all reflected energy enters the converter cavity. Of course, there will be a smaller distance available for excursions of the image resulting from α . At the same time, if the aberrated image is assumed to move the same distance as the circular solar image, such that none of the circular image escapes the aperture, but a portion of the aberrated image does, then the energy lost from the aberrated image will always be less than the energy loss owing to the rim angle degradation of the circular image. Moreover, the assumption of a circular solar image, of which no portion ever leaves the aperture, yields a power into the converter which is always less than the true value.

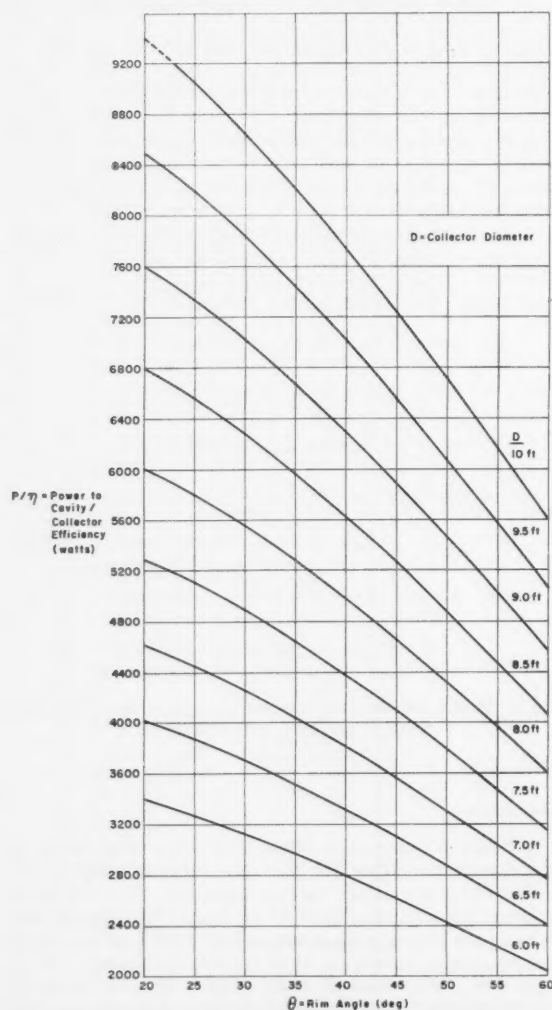


Fig. 6 Power to converter divided by collector efficiency P/η vs. rim angle θ

This is shown in Fig. 11. The two dotted circles represent the converter aperture at $\alpha = 0$ and $\alpha \pm 0$. When α is not equal to 0 the images, both circular and aberrated, move toward the side of the aperture (actually, they both become elliptic as well, but this form change is not shown). In the displaced position, the outer, and least intense, portion of the aberrated image has fallen outside the aperture. This results in the loss of the energy in the horizontally cross hatched image area. The concentric circles which lie outside the circular image represent contours of intensity level—the intensity is highest where the contours are closest together. Note that the portion of “lost” energy occurs for the most part in the lowest intensity level of the image.

The horizontally cross hatched area represents the actual energy lost owing to a given α for the case that considers the aberrated image. However, the calculation which considers only the circular solar image would indicate no loss owing to α , but would have incorporated in it a loss which is represented by the sum of the horizontally and vertically cross hatched areas. Thus, the most accurate method of estimating the power into the converter requires that the aberrated image calculation be used, and the maximum degradation owing to α be determined by subtracting the energy lost owing to α . For this purpose, a good approximation is obtained by assuming a straight line variation of energy intensity with distance from the outer edge of the circular image to the outer edge of the aberrated image, and using this variation in conjunction with the “shadowed” area. The ellipticity of the image must, of course, be accounted for. This can be done graphically using Fig. 4 to determine changes of major axis length and the knowledge that the minor axis is constant. A search of the literature has failed to reveal any attempts at a complete mathematical solution of this problem.

One fact has become eminently clear from the preceding discussion: The efficiency of the solar collector is extremely sensitive to the angular misalignment of the reflector axis with

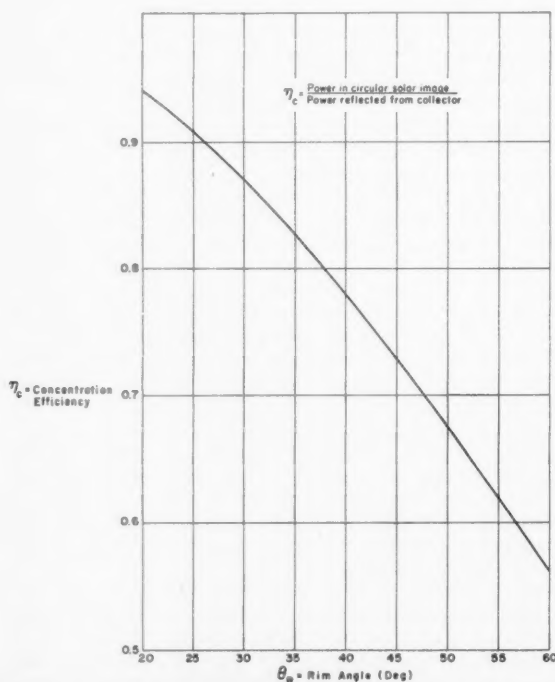


Fig. 7 Concentration efficiency η_c vs. rim angle θ_R applicable when considering circular solar image

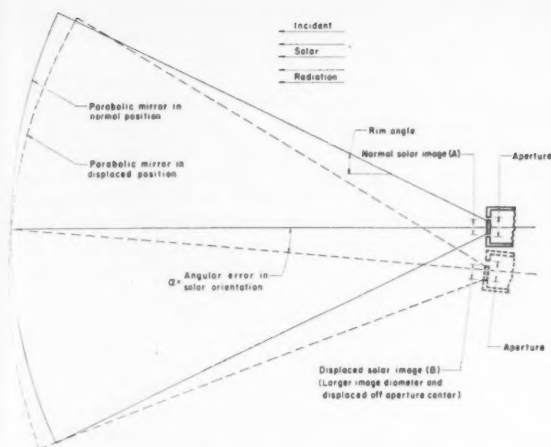


Fig. 8 Effect of solar misalignment with reflector axis

the impinging solar radiation (Fig. 8). Accordingly, a sample calculation was made on a specific collector-converter system. This analysis disclosed that the maximum allowable angular error which would not result in significant degradation of the energy into the converter was approximately 0.1 deg. The stringency of this α tolerance rendered the sample design, which was theoretically adequate, virtually impossible to attain. For convenience, all system errors which result in deformation or displacement of the solar image are reduced to "effective misalignment angles" (α_{eff}), that is, the misalignment angle of impinging solar radiation which would result in the same image variation. Moreover, the 0.1 deg allowable α is, in reality, the allowable α_{eff} .

Therefore, a "budget" was established on the sample design (a 6½-ft diameter collector with a 35 deg rim angle, and a converter aperture diameter which was established by detailed thermionic converter design) in order to determine a practical value of α_{eff} . The values shown reflect the contributions to the effective α which can reasonably be attained by careful design and manufacture

Unfolding mechanism joint slop	0.4 deg
Deflection of support arms	0.2 deg
Mirror surface error (both in manufacture and by thermal deformation)	0.1 deg
Vehicle attitude control system	0.3 deg
Total α_{eff}	1.0 deg

Since the actual α_{eff} differs from the attainable α_{eff} by a factor of 10, it is evident that the sample design cannot do the job. Accordingly, new design features were sought to augment the attainable α_{eff} . The first method investigated involved the use of a converging lens system placed near the converter aperture to diminish the image size, and hence to increase its intensity, and relieve the image motion relative to the aperture with changes in α_{eff} .

While this system was found to be theoretically capable of doing the job, several factors contributed to making it wholly impractical. First, the size of the lenses required resulted in weights which were completely intolerable, particularly since these huge masses had to be attached to the converter which was supported at the end of the unfolding mechanism. Second, in order to avoid exceeding the critical angle, thus blacking out a portion of the energy passing through the lens system by total reflection from the lens surfaces, a series of thin lenses was required. This introduced the complication of optically aligning the lenses such that thermal stresses in the lens support structure would not render the system use-

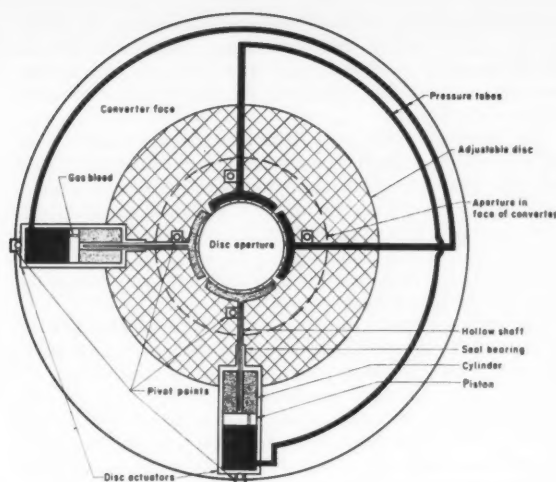


Fig. 9 Aperture positioner, front elevation

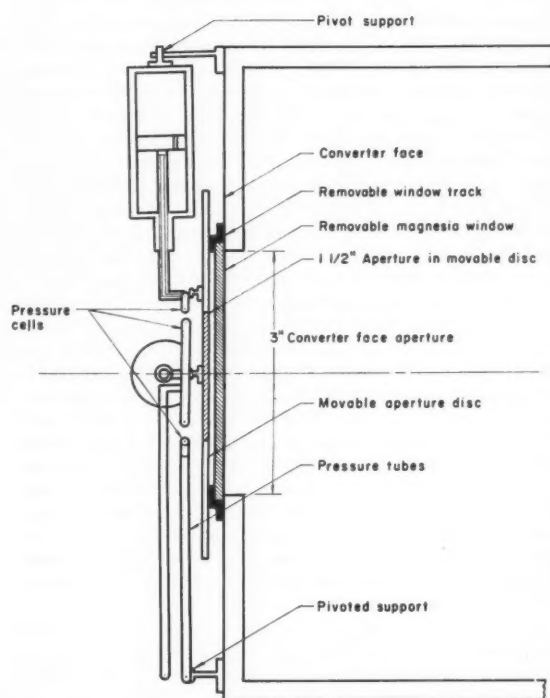


Fig. 10 Aperture positioner, side elevation

less. Further, the first lens (fused silica) was estimated to absorb and reradiate approximately 4% of the energy attempting to pass through it, and each surface of each lens in the system was found (assuming the best coatings) to degrade the energy by about 2%. Thus the energy degradation and the system weight became intolerable and the lens system was discarded.

Automatic aperture positioner

A system of automatic aperture positioning shown in Figs. 9 and 10 was devised to allow the converter aperture (only) to move with the excursions of the solar image arising from solar misalignment. The primary feature of the system is that it permits an appreciable increase in allowable α

without increasing the back radiation from the converter cavity. A secondary, but highly advantageous feature is the fact that the aperture positioner requires no power whatever from the vehicle. Finally the entire weight of the positioner is less than 2 lb.

The aperture positioner consists of a thin movable disk, highly polished (reflective) on both sides, which has a circular hole cut from the center. This hole is the effective converter aperture. Surrounding the hole are four gas filled chambers, each connected by a pressure tube to one end of the actuating cylinders. The gas chambers are attached by pivot joints to the movable disk, and the two cylinders are attached by pivot joints to the converter face.

The dotted circle in Fig. 9 shows the size of the aperture in the face of the converter and marks the locus of positions which the movable disk aperture can assume. When the solar image moves out of the movable disk aperture, the high intensity energy impinges upon the gas chamber (at left of Fig. 9). The gas within this chamber is heated suddenly, causing an intense increase in the pressure in the chamber. This pressure is conveyed to the right-hand chamber of the horizontal cylinder, through the hollow piston shaft, causing a Δ pressure across the piston. As a result, the piston moves to the left to equalize the pressures. When ΔP becomes zero (or a value which is equal to the friction inertia of the system), the piston stops and the disk aperture has been moved to the left to once again contain the solar image. Having so moved, the gas chamber now escapes the solar image and commences to cool by radiation to space. As the temperature decreases, the pressure also decreases, but the rate of change of pressure during the cooling process is much slower than the rate of expansion accompanying the severe heating process. If the pistons were gas tight, that is, if no mass could pass from one side of the system to the other, then the cooling process would merely move the movable disk, and hence, the gas chamber back into the solar image. To prevent this, a tiny gas bleed aperture is provided in the piston.

This results in the following sequence. The solar image moves off center owing to a solar misalignment angle α and falls on the gas chamber. The gas is expanded, pushing the cylinder, perhaps to the left, and moving the disk aperture, and consequently the gas chamber that is fixed to it, until the solar image falls within the disk aperture. The pressure difference across the piston has diminished to near zero, and temporary equilibrium exists. As the gas chamber cools, the gas pressure decreases, but the rate of decrease is sufficiently slow to allow gas to bleed from the far side of the piston back into the gas chamber side through the gas bleed passage. Thus the ΔP remains near zero and the movable disk remains in its displaced position.

Should the solar image be moved to the opposite side, or to the top or bottom, the same process would take place. Also both systems, horizontal and vertical in Fig. 9, can operate simultaneously to correct for diagonal motion of the solar image.

The four gas chambers and the pressure tubes are protected from overheating by using a high melting point material, e.g., tungsten, in the construction. Also, the surfaces are made highly reflective to energy, over the solar band, and as highly emissive within the infrared band as is compatible with the absorptivity requirement. Calculations show that the maximum attainable temperature, assuming that the solar image impinges on the chambers or tubes for an indefinite time period, can be limited to only slightly over 4000 deg R. The piston cylinders are given thermal protection by mirror insulators (not shown in Fig. 9). In addition, a short, reflective cone frustum protects the converter sides during extreme image excursions.

The use of high temperature materials in the tubes, as well as the chambers, has the advantage of permitting the system to work even during extreme excursions of the solar image arising from critical periods of the trajectory, such as the

passage from Earth shadow to full solar exposure. Also, the entire converter face is capable of withstanding the impingement of the solar image during times when the vehicle control system is correcting for solar misalignment.

The sample design utilizing this aperture positioner has demonstrated that a total effective misalignment angle α_{eff} of 1 deg can easily be tolerated. This α_{eff} value can be increased beyond 1 deg by the positioner shown in Fig. 9. However, the upper limit for the sample design has not yet been determined. An additional relaxing of the α_{eff} requirements will result from the application of the same principle to the movement of the entire converter, instead of just a movable aperture disk, although the system weight of such an application will necessarily increase.

It should be noted that the removal of the rim angle degradation by consideration of the aberrated image is a direct result of the ability to move the converter aperture with excursions of solar image. In the initial sample design, only the circular solar image was considered to be delivered to the converter window because the fixed aperture had to include sufficient diameter to accommodate solar image excursions. Once the movable aperture is considered, it becomes possible to accept the aberrated solar image without increasing the aperture diameter (back radiation); hence, no degradation occurs from the 17% (see Fig. 7) of the energy of the aberrated image lying outside the circular solar image.

Vehicle attitude control requirement

Control systems having the capability of aligning a given space vehicle axis within 0.1 deg of the sun are within the reach of present technology. The following data (2) indicate the attitude control tolerance anticipated for presently planned space tasks.

Vehicle task	Attitude control requirement, deg
1 Communications satellite	8
2 Meteorological satellite	1
3 Interplanetary space oriented vehicle	0.005
4 Astronomical satellite	0.0003

The alignment requirements of missions 3 and 4 are such that the solar collector system of α_{eff} would be virtually unaffected by vehicle control, even without the use of the aperture positioner. Of course, the positioner is required to correct for the α_{eff} accruing from all sources other than the attitude control. The optimized design of an aperture control system permits the use of a solar collector-thermionic converter unit in missions 2, 3 or 4. However, mission 1 has such lax control requirements that the use of a solar thermionic power system is impossible without auxiliary collector control. Separate control for the collector modules is complicated and appears to be generally inferior to more stringent control of the entire vehicle since the two control systems, vehicle and collector, would create mutually disturbing torques, and introduce both damping problems and an additional source of system slop. Thus, the use of the solar thermionic auxiliary power source becomes more attractive as the sophistication of space vehicles is advanced.

Collector Mirror Manufacture

Practical methods of manufacturing the collector mirrors have been suggested in the technical literature. Of particular interest is the method described in (3).

As listed in the "budget" table, a reasonable allowable α_{eff} resulting from the collector mirror surface error is 0.1 deg. Since an angular error on the mirror surface contributes approximately a 2 to 1 error in α_{eff} , the 0.1 deg α_{eff} results from an angular error in mirror surface of one-half of 0.1 deg (3 min of arc).

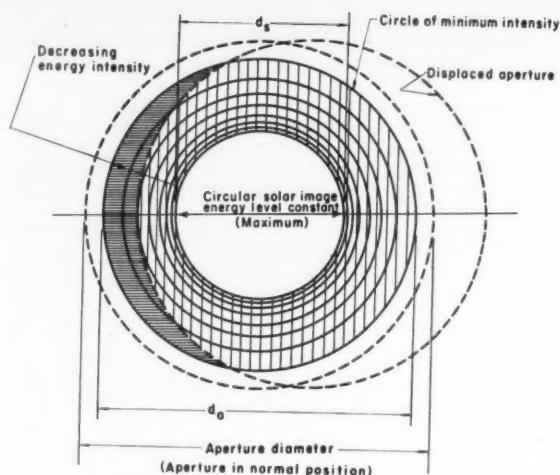


Fig. 11 Effect on energy passing into converter of excursion of image owing to α considering both types of images

The manufacturer of a paraboloid shape is concerned with the distance "off line" of a real surface from a true paraboloid surface per unit length of travel along the surface. Considering a differential element of curved surface length, the angular error allowed by the design "budget" permits an "off line" distance from a true paraboloid, per unit length of travel, equal to the tangent of 0.05 deg, 3 min of arc, or 0.00085 in. per in.

It is necessary to divide this budget realistically between the error introduced by manufacturing and that resulting from deformation of the mirror in space. First, a reasonable level of manufacturing tolerance, one that can be held by the manufacturing process, is defined, and then various means of reducing error resulting from thermal deformation must be examined.

Bearing in mind the allowable mirror design tolerance defined in the preceding discussion, the manufacturing method suggested in (3) has been used to determine whether or not these tolerances can be held. Estimates show that a manufacturing tolerance of 1 wave length distance "off line" per inch of travel can be held. This is equivalent to an error of 2/100,000 in. per in., or less than one fortieth of the budgeted tolerance. The remainder of the 0.1 deg of α_{eff} , then, is available to accommodate the thermal deformation degradation.

Mirror manufacture is divided into three steps: Primary female mold, secondary male mold and tertiary female collector mirror.

Primary female mold: A glass paraboloid of revolution ground and polished to optical accuracy (1 wave length deviation "off line"). A silver coating is evaporated onto the glass under vacuum to provide easy separation of the coating from the glass mold. Then copper is electroplated onto the silver.

Secondary male mold: A dish or igloo built $\frac{1}{4}$ to $\frac{1}{2}$ in. above the primary female mold with epoxy poured into the gap. The epoxy structure is not entirely solid, and has a core which is light yet sufficiently rigid to hold the paraboloid shape of the female mold. The secondary male mold is removed from the female mold, taking the silver and copper electroplate with it.

Tertiary female collector mirror: A thin layer of smooth fiber optic material, similar to Columbia Resin No. 39 which is used in making unbreakable lenses for spectacles, is pressed

onto the male secondary mold with a mandrel. Once the fiber optic material has set, it is parted from the male secondary mold at the silver to male interface. The result is a tertiary female paraboloid shape of optically smooth finish and accurate geometry.

An aluminum coating is then deposited on the tertiary mold under high vacuum conditions to attain the reflectivity values that are necessary to assure the collection efficiency that has been described.

Thermal Deformation

In general, the mirror errors which result from thermal stresses will be of two types: Residual stresses which result from the manufacturing process; thermal stresses arising from the varying conditions of sun and shade or "day and night" in the orbit, earth reflected and radiated energy, and energy radiated or conducted from the converter unit and the parent vehicle. It is probable that the residual stresses will be negligible, provided care is taken in the manufacturing process, but a careful check must be made of the first mirrors manufactured. If significant stresses appear, standard methods of stress relief, using the secondary mold as a control, should be applied.

The "in orbit" thermal stresses can be controlled by thermal insulation of the mirror with respect to the vehicle and the thermionic unit, such that conductive heat transfer is minimized. In addition, the use of special coatings on all surfaces, except the reflecting surface, of the collector structure should be used. These coatings must be selected for the best available combination of absorptivity and emissivity (e.g., low absorptivity in the solar energy band and high emissivity in the lower temperature, infrared band). Finally, a lightweight but stiff backup structure applied to the back of the mirror will decrease the deformations of the reflecting surface.

Radiation Environment

Current data on the intensity levels of both high and low energy radiation in space demonstrates that organic substances, such as Columbia Resin No. 39, may be severely damaged by radiation unless protective measures are taken. Such protection is afforded the collector mirror by incorporating a sufficient thickness of the aluminum coating to act as an effective shield. The aluminum thickness required will, of course, vary from vehicle to vehicle, depending upon the radiation intensity levels and the duration of operation within the danger regions (e.g., Van Allen belt) anticipated for each mission.

Conclusions

The modular concept of solar collector design results in an improved overall efficiency for thermionic conversion from solar to electrical energy. The ability to add or subtract module units yields a flexibility in power output, which permits the use of a single system design for a wide range of missions. While the module system requires rigid parabolic mirrors of very high optical quality, the manufacturing demands can be met without resort to any significant changes in the established techniques.

The use of an automatic aperture positioner decreases the attitude control system accuracy requirements to a presently attainable level.

The nonfolding mirrors provide a high concentration of thermal energy with a minimum system size. Thus, an additional decrease in attitude control requirements is achieved, since the overall system moment of inertia is decreased. In addition, the solar image aberration from support structure deformations arising from control system loads and thermal stresses is minimized by compactness of design.

Acknowledgment

The authors wish to express their appreciation to Dr. W. L. Hyde, Assistant Director of Research, American Optical Co., for his helpful suggestions on reflector manufacturing techniques.

Nomenclature

- A_R = projected area of reflector, ft²
 D = diameter of the parabolic mirror, ft
 d_c = diameter of the circular solar image, ft
 d_a = diameter of the aberrated solar image, ft
 f = focal length of the mirror, ft
 L = maximum depth of the parabolic mirror, ft
 P = power delivered at the solar image, w
 S = maximum motion (relative to center of circular solar image) of a point in focal plane reflecting from mirror rim owing to α , ft
 α = angular error between incident solar radiation and paraboloid axis, deg

- β = solar cone angle, 32 min
 θ_S = angle between paraboloid axis and line connecting center of solar image with outside of shadow cast on mirror by the converter, deg
 θ_R = mirror rim angle, deg (see Fig. 1)
 η = efficiency of collector system, not including rim angle error included in Equation [6a]
 η_c = concentration efficiency, ratio of power received at converter aperture to total power reflected by parabolic mirror
 I_0 = intensity of solar energy at vehicle location relative to sun, 130 w/ft² in vicinity of Earth, w/ft²

References

- 1 Hiester, N. K., Tiets, T. E., Loh, E., Duwes, P., "Theoretical Considerations on Performance Characteristics of Solar Furnaces," *JET PROPULSION*, vol. 27, no. 5, May 1957, pp. 507-513, 546.
- 2 Lewis, C., "U. S. Space Effort Matures in Dual Patterns," *Aviation Week*, March 7, 1960, p. 111.
- 3 Haas, G., "Filmed Surfaces for Reflecting Optics," *J. Optical Soc. Amer.*, vol. 45, no. 11, Nov. 1955, p. 945.

Linearized Magnetogasdynamic Channel Flow With Axial Symmetry

F. EDWARD EHLERS¹

Boeing Scientific Research
Laboratories
Seattle, Wash.

The equations for the axisymmetric flow of a conducting gas through a cylindrical channel in a magnetic field are linearized under the assumption of small magnetic Reynolds number and small values of the magnetic interaction parameter. Solutions for subsonic and supersonic flow are found by means of Laplace and Fourier integral transforms, and simple approximations are derived for the axial and wall perturbation velocities and the velocity profiles far downstream of the magnetic field sources. Some numerical calculations are given for subsonic flow through the magnetic field produced by a circular current loop concentric to the channel cross section. As a result of the imposed field, the flow is accelerated through the field near the channel axis and decelerated near the wall. No numerical calculations are given for supersonic flow, but the properties of the flow are discussed.

WHEN a conducting gas flows through a tube in the presence of a magnetic field, the resulting induced currents exert forces on the gas. As a consequence, the dynamics equations for the flow are coupled to Maxwell's equations. In the subsequent analysis we shall treat the conducting gas as a continuum, neglecting such phenomena as the spiralling of electrons about the lines of magnetic induction, the related "Hall effect," and charge separation. We shall assume the walls of the channel to be nonmagnetic and nonconducting.

To linearize the magnetogasdynamics equations we assume, first, that the magnetic Reynolds number is small. Another parameter associated with the flow, called the interaction parameter, is the ratio of the magnitude of the body forces

produced by the imposed magnetic field and of the inertial force. If this quantity also is assumed to be small, then the equations are linearized by expanding the flow variables, such as density and velocity, in power series of this parameter. In the following, the linearized equations for the first approximation are solved for both subsonic and supersonic steady flow through a cylindrical channel. Numerical calculations are given for subsonic flow and for the magnetic field produced by a single current loop whose axis coincides with the axis of the cylindrical channel.

Equations of Motion for the Flow of a Conducting Gas in a Magnetic Field

On the basis of the preceding discussion, the equations of motion for the steady flow of a conducting gas and for the

Received Aug. 25, 1960.

¹Staff Scientist, Mathematics Research Laboratory. Member ARS.

magnetic and electric fields are:

Continuity

$$\nabla \cdot \hat{\rho} \hat{V} = 0 \quad [1]$$

Momentum

$$\hat{\rho} \hat{V} \cdot \nabla \hat{V} = \hat{J} \times \hat{B} - \nabla \hat{p} \quad [2]$$

Energy

$$\hat{T} \hat{\rho} \hat{V} \cdot \nabla \hat{s} = \hat{J} \cdot \hat{J} / \sigma \quad [3]$$

Maxwell's equations

$$\hat{J} = \sigma(\hat{E} + \hat{V} \times \hat{B}) \quad [4]$$

$$\nabla \times \hat{E} = 0 \quad [5]$$

$$\nabla \times \hat{B} / \mu = \hat{J} \quad [6]$$

$$\nabla \cdot \hat{B} = 0 \quad [7]$$

where

$\hat{\rho}$ = density of gas

\hat{V} = velocity

\hat{T} = temperature

\hat{p} = pressure

\hat{s} = entropy per unit mass

The electromagnetic quantities \hat{E} , \hat{B} and \hat{J} are, respectively, the electric field intensity, the magnetic induction and the current density. The electrical properties of the gas are represented by the conductivity σ and the magnetic permeability μ .

Equations [1 through 7] provide seven relations for eight variables. An additional relation is obtained by assuming that the gas behaves like an ideal gas. Then the entropy is related to the pressure and density by

$$\begin{aligned} \hat{s}/c_v &= \log(\hat{p}/\hat{\rho}^\gamma) \\ &= \log \hat{p} - \gamma \log \hat{\rho} \end{aligned} \quad [8]$$

where c_v is the specific heat at constant volume, and γ is the ratio of specific heat at constant pressure to c_v .

Let us introduce the following dimensionless variables into Eqs. [1 through 8]

$$\begin{aligned} \hat{E} &= b_0 u_0 E & \hat{B} &= b_0 B \\ \hat{J} &= \sigma b_0 u_0 J & \hat{\rho} &= \rho_0 \rho \\ \nabla &\rightarrow \nabla/r_1 & \hat{s} &= c_s s \\ \hat{V} &= u_0 V & c_p &= (\hat{p} - p_0)/(\frac{1}{2} \rho_0 u_0^2) \end{aligned} \quad [9]$$

The quantities u_0 , ρ_0 and p_0 are, respectively, the velocity, density and pressure at infinity where the flow is undisturbed, and b_0 is the magnitude of the magnetic induction at some particular reference point chosen for convenience. Since we are concerned primarily with the flow in a cylindrical tube, we have used the radius of the tube as the characteristic length. The choice of $b_0 u_0$ for normalizing the electric field implies that it arises principally from the induction due to the motion of the conducting gas in the magnetic field. The quantities ρ_0 and a_0 are the density and velocity of sound for the gas undisturbed by the magnetic and electric fields. Equations [1 through 8] become, after eliminating p and J

$$\nabla \cdot \rho V = 0 \quad [10]$$

$$\rho V \cdot \nabla V + \rho a_s^2 \nabla s / \gamma M^2 + a_s^2 \nabla \rho / M^2 = m(E \times B) + m(V \times B) \times B \quad [11]$$

$$V \cdot \nabla s = \gamma(\gamma - 1) M^2 m [E \cdot E + 2E \cdot (V \times B) + (V \times B) \cdot (\nabla \times B)] / \rho a_s^2 \quad [12]$$

$$\nabla \times E = 0 \quad \nabla \times B = r_m (E + V \times B) \quad [13]$$

$$\nabla c_p / 2 = \rho a_s^2 \nabla s / \gamma M^2 + a_s^2 \nabla \rho / M^2 \quad [14]$$

where

$$m = \sigma b_0^2 r_1 / \rho_0 u_0$$

M = Mach number of undisturbed stream

a_s = dimensionless velocity of sound in gas

Linearization of the Equations for the Steady Axially Symmetric Flow of a Conducting Gas in a Magnetic Field

For the following analysis, we shall assume a steady flow of a conducting gas in a cylindrical tube in the presence of a steady axially symmetric magnetic field, with the conductivity so small that the induced magnetic field is small compared with the imposed field. Therefore, we can expand the electromagnetic field quantities in powers of the magnetic Reynolds number. Since we are applying a static magnetic field only, then the first term in the expansion for the electric field is of the first order in the magnetic Reynolds number. We also shall assume that the parameter

$$m = \sigma b_0^2 r_1 / \rho_0 u_0$$

which may be interpreted as the ratio of the electric body force to the inertial force, is small. Therefore, we note from Equations [11 and 12] that only the imposed magnetic field plays a role in the first approximation in m and the magnetic Reynolds number of the flow variables.

With the preceding considerations, the equations of motion of the steady flow of a gas of small conductivity in a cylindrical tube in an axially symmetric magnetic field take the form

$$(\rho u)_x + (\rho v)_r + \rho v/r = 0 \quad [15]$$

$$\rho u u_x + \rho v u_r + a_s^2 \rho_x / M^2 + a_s^2 s_x / \gamma M^2 = m B_2 (v B_1 - u B_2) \quad [16]$$

$$\rho u v_x + \rho v v_r + a_s^2 \rho_r / M^2 + a_s^2 s_r / \gamma M^2 = -m B_1 (v B_1 - u B_2) \quad [17]$$

$$u s_x + v s_r = M^2 m (v B_1 - u B_2)^2 \gamma (\gamma - 1) / \rho a_s^2 \quad [18]$$

where B_1 and B_2 are the x and r components of the imposed magnetic induction and are therefore known functions of x and r . If we assume $m \ll 1$, and the gas at $x = -\infty$ to be at uniform velocity in the x direction, then, under a magnetic field that vanishes at $x = -\infty$, the variables of the flow can be expanded about the undisturbed state $\rho = a_s = u = 1$ and $v = 0$ in powers of the parameter m . In this way the following linear equations for the first approximation result

$$u_{1x} + \rho_{1x} + v_{1r} + v_1/r = 0 \quad [19]$$

$$M^2 u_{1x} + \rho_{1x} + s_{1x} / \gamma = -M^2 B_2^2 \quad [20]$$

$$M^2 v_{1x} + \rho_{1r} + s_{1r} / \gamma = M^2 B_1 B_2 \quad [21]$$

$$s_{1x} = \gamma(\gamma - 1) M^2 B_2^2 \quad [22]$$

Since for an axially symmetric field $B_2 = 0$ and $v = 0$ on the axis $r = 0$, the flow along the center streamline is isentropic. We note also that the entropy s_1 can be found to a first approximation in m by integrating Equation [22]. Thus

$$s_1 = \gamma(\gamma - 1) M^2 \int_{-\infty}^x B_2^2(\xi, r) d\xi \quad [23]$$

where we assumed the flow to be in the positive x direction and $s_1 = 0$ at $x = -\infty$. Similarly, the density is obtained by integrating Equation [19]

$$\rho_1 = -u_1 - \int_{-\infty}^x (v_{1r} + v_1/r) dx \quad [24]$$

Eliminating s_1 and ρ_1 from Equation [20] by Equations [23 and 24] yields

$$u_1 = \frac{1}{M^2 - 1} \int_{-\infty}^x (v_{1r} + v_1/r) dx - \frac{\gamma M^2}{M^2 - 1} \int_{-\infty}^x B_2^2 dx \quad [25]$$

Since u_1 and ρ_1 are expressed as integrals involving the radial component of the velocity v_1 , it seems advantageous to find the single differential equation for v_1 . Differentiating Equation [20] with respect to r and Equation [21] with respect to x , then subtracting and eliminating u_1 by Equation [25] lead to

$$v_{1rr} + v_{1r}/r - v_1/r^2 - (M^2 - 1)v_{1xz} = F(x, r) \quad [26]$$

where

$$F(x, r) = [(1 - M^2) + \gamma M^2](B_2^2)_r + (1 - M^2)(B_1 B_2)_x \quad [27]$$

is a known function of x and r .

General Solution for the Linearized Subsonic Flow of a Conducting Gas Through a Cylindrical Tube in a Magnetic Field

We shall now find the solution of Equation [26] for the flow of a conducting gas through a cylindrical tube under an axially symmetric magnetic field. To solve the differential equation we first apply the Fourier transform in x . This yields the ordinary differential equation

$$\bar{v}_{1rr} + \bar{v}_{1r}/r - (\alpha^2 \beta^2 + 1/r^2)\bar{v}_1 = \bar{F}(\alpha, r)$$

where

$$\bar{v}_1 = (1/\sqrt{2\pi}) \int_{-\infty}^{\infty} e^{i\alpha x} v_1(x, r) dx$$

and

$$\beta^2 = 1 - M_\infty^2$$

The general solution to \bar{v}_1 which vanishes at $r = 0$ and satisfies the boundary condition $\bar{v}_1 = 0$ at the wall $r = 1$ is

$$v_1 = \int_0^1 \eta \bar{F}(\alpha, \eta) [I_1(\alpha\beta\eta)K_1(\alpha\beta) - I_1(\alpha\beta)K_1(\alpha\beta\eta)] I_1(\alpha\beta r) d\eta / I_1(\alpha\beta) + \int_0^r \eta \bar{F}(\alpha, \eta) [I_1(\alpha\beta r)K_1(\alpha\beta\eta) - I_1(\alpha\beta\eta)K_1(\alpha\beta r)] d\eta \quad [28]$$

where $I_1(z)$ and $K_1(z)$ are the Bessel functions of imaginary argument, following the notation of Watson (4).² For convenience in evaluating the inverse transforms, we take a portion of the first integral and add it to the second and obtain

$$v_1 = \int_r^1 \eta \bar{F}(\alpha, \eta) I_1(\alpha\beta r) [I_1(\alpha\beta\eta)K_1(\alpha\beta) - I_1(\alpha\beta)K_1(\alpha\beta\eta)] d\eta / I_1(\alpha\beta) + \int_0^r \eta \bar{F}(\alpha, \eta) I_1(\alpha\beta\eta) [I_1(\alpha\beta r)K_1(\alpha\beta) - I_1(\alpha\beta)K_1(\alpha\beta r)] d\eta / I_1(\alpha\beta) \quad [29]$$

Since the function $F(x, r)$ and not its transformation is known, the solution for v_1 is expressed in convolution integrals of the form

$$v_1 = (1/\sqrt{2\pi}) \int_r^1 \eta \int_{-\infty}^{\infty} [\partial F(\xi, \eta) / \partial \xi] G_0(x - \xi, r, \eta) d\xi d\eta + (1/\sqrt{2\pi}) \int_0^r \eta \int_{-\infty}^{\infty} [\partial F(\xi, \eta) / \partial \xi] G_0(x - \xi, \eta, r) d\xi d\eta \quad [30]$$

where

$$G_0(x, \eta, r) = \lim_{c \rightarrow 0} (1/\sqrt{2\pi}) \int_{ic-\infty}^{ic+\infty} \times \frac{e^{-ipx/\beta} I_1(\rho\eta) [I_1(pr)K_1(p) - I_1(p)K_1(pr)] dp}{-ipI_1(p)}$$

Evaluating the integral by the method of residues yields

$$G_0(x, \eta, r) = -\sqrt{\pi/2} \left[\eta(r - 1/r) + \pi \sum_{n=1}^{\infty} \frac{e^{-anx/\beta} J_1(a_n\eta) Y_1(a_n) J_1(a_nr)}{a_n J_0(a_n)} \right]$$

for $x \geq 0, r > \eta$

$$\int_{-\infty}^x v_{1r} \Big|_{r=1} dx = \int_0^1 \int_{-\infty}^x \eta^2 F(\xi, \eta) d\xi d\eta + \frac{\pi}{2} \sum_{n=1}^{\infty} \int_0^1 \int_0^{\infty} \eta [F(x - \tau, \eta) - F(x + \tau, \eta)] e^{-an\tau/\beta} J_1(a_n\eta) Y_1(a_n) d\tau d\eta \quad [31]$$

² Numbers in parentheses indicate References at end of paper.

$$G_0(x, \eta, r) = (\sqrt{\pi/2}) \pi \sum_{n=1}^{\infty} \frac{e^{-anx/\beta} J_1(a_n\eta) Y_1(a_n) J_1(a_nr)}{a_n J_0(a_n)}$$

for $x < 0, r > \eta$

where a_n is the n th root of the Bessel function $J_1(z)$.

Wall Velocity and Pressure for Subsonic Flow

When $r = 1$, then $v_z = 0$; the tangential perturbation component at the wall, from Equation [25], becomes

$$u_1 = - \int_{-\infty}^x v_{1r} d\xi / \beta^2 + \gamma M^2 \int_{-\infty}^x B_2^2 d\xi / \beta^2 \quad [32]$$

The relation for the pressure coefficient obtained by linearizing Equation [14] may be written

$$\nabla c_p / 2 = (m/M^2)(\nabla s_1 / \gamma + \nabla \rho_1) \quad [33]$$

Eliminating ρ_1 and s_1 from Equation [20] by the x component of Equations [33 and 22] leads to the following equation for the pressure coefficient

$$c_p = -2m \left[u_1 + \int_{-\infty}^x B_2^2 d\xi \right] \quad [34]$$

The first term is the usual linearized theory relation for the pressure coefficient; the second term may be referred to as the "magnetic pressure."

To find u_1 for $r = 1$, we need v_{1r} . Differentiating Equation [30] with respect to r and setting $r = 1$ yield

$$v_{1r} \Big|_{r=1} = (1/\sqrt{2\pi}) \int_0^1 \int_{-\infty}^{\infty} \eta F_{\xi}(\xi, \eta) G_1(x - \xi, \eta) d\xi d\eta \quad [35]$$

where for x smaller than zero

$$G_1(x, \eta) = -\sqrt{\pi^3/2} \sum_{n=1}^{\infty} e^{-anx/\beta} J_1(a_n\eta) Y_1(a_n) \quad [36]$$

and for x larger than zero

$$G_1(x, \eta) = \sqrt{2\pi} \left[\eta + \frac{\pi}{2} \sum_{n=1}^{\infty} e^{-anx/\beta} J_1(a_n\eta) Y_1(a_n) \right] \quad [37]$$

Substituting Equations [36 and 37] into Equation [35] yields, after some algebraic manipulation and integration

In a subsequent section we shall consider the flow through a magnetic field produced by a circular loop of current around the tube at the origin. For this field $F(x, r)$ is an even function and vanishes at x equals $\pm\infty$. The series gives the largest contribution near $\tau = 0$ for which the bracketed equation vanishes. For $x = 0$, the second term in Equation [38] vanishes identically. It appears that, except for rather moderate values of x , the contributions of the series can be neglected. Since the a_n are zeros of $J_1(a)$, they are quite large ($a_1 = 3.8317$), and the terms of the series become rapidly small with increasing n for fixed τ . Neglecting the series term is equivalent to approximating $G_1(x, \eta)$ by the step function

$$\begin{aligned} G_1(x, \eta) &= 0 & x < 0 \\ G_1(x, \eta) &= \sqrt{2\pi\eta} & x \geq 0 \end{aligned} \quad \dots [39]$$

With this approximation, the wall perturbation velocity from Equation [32, 39 and 27] becomes

$$u_1 = - \int_{-\infty}^x B_2^2 d\xi + 2(1 + \gamma M^2/\beta^2) \times \int_{-\infty}^x \int_0^1 \eta B_2^2 d\eta d\xi - \int_0^1 \eta^2 B_1 B_2 d\eta \quad [40]$$

where B_2 in the first integral is evaluated at $r = 1$, and B_1 and B_2 in the third integral are evaluated at x . This equation is a good approximation for any magnetic field which vanishes at x equals $\pm\infty$. However, Equation [40] gives the exact linearized value of u_1 for $x = 0$ and $x = \infty$, since the terms we neglected vanish identically at these points when $F(x, r)$ is an even function of x and is zero at $x = \pm\infty$.

Velocity Profile at $x = +\infty$

At $x = \infty$, the vertical velocity vanishes and the coefficient of pressure is constant over the cross section. The velocity distribution across the tube at $x = \infty$ can be found without making use of the solution for v_1 . To this end we multiply Equation [34] by rdr and integrate. Thus

$$\int_0^1 c_p r dr / 2m = - \int_0^1 u_1 r dr - \int_0^1 \int_{-\infty}^x B_2^2 dx r dr \quad [41]$$

To eliminate $\int_0^1 u_1 r dr$ we make use of Equation [25]. Integrating $\int_0^1 v_1 r dr$ by parts and applying the condition $v_1 = 0$ at $r = 0$ and 1, we find that terms involving v_1 in Equation [25] vanish. Thus Equation [41] becomes

$$\int_0^1 c_p r dr / 2m = -(1 + \gamma M^2/\beta^2) \int_0^1 \int_{-\infty}^x B_2^2 dx r dr$$

This equation gives the average coefficient of pressure at any cross section x . For $x = \infty$, the coefficient of pressure is constant and therefore

$$c_p / 2m = -2(1 + \gamma M^2/\beta^2) \int_0^1 \int_{-\infty}^{\infty} B_2^2 dx r dr \quad [42]$$

Substituting for the coefficient of pressure in Equation [34] we obtain the following equation for the distribution of velocity across the tube at $x = \infty$

$$u_1 = 2(1 + \gamma M^2/\beta^2) \int_0^1 \int_{-\infty}^{\infty} B_2^2 dx r dr - \int_{-\infty}^{\infty} B_2^2 dx \quad [43]$$

This result agrees with Equation [40] for $x = +\infty$ and $r = 1$, and is valid for any magnetic field which vanishes at $x = \pm\infty$. Since the assumption of either subsonic or supersonic flow was not made in the derivation, the equation holds for both subsonic and supersonic flow.

We note that the quantity $1 + \gamma M^2/\beta^2$ is negative for $M > 1$ and positive for $M < 1$. Hence there is a drop in pressure when the gas flows subsonically through the tube and a rise in pressure when the flow is supersonic. The

density profile at $x = \infty$ can be found by combining Equations [24 and 25] to be

$$\rho_1 = -M^2 u_1 - \gamma M^2 \int_{-\infty}^{\infty} B_2^2 dx \quad [44]$$

Thus a rise in velocity causes a proportionate decrease in density. By means of Equation [23] we find that at $x = +\infty$

$$\rho_1 = -M^2 u_1 - s_1/(\gamma - 1) \quad [45]$$

or using Equations [42 and 43]

$$\rho_1 = M^2 c_{p\infty} / 2m - s_1(\infty, r) / \gamma$$

For subsonic Mach numbers, this is always negative. The density profile has the same general shape as the velocity profile, differing only in translation and scale.

Velocity Distribution along the Axis of the Tube, Subsonic Flow

Since in the limit as $r \rightarrow 0$

$$(v_1/r)_{r=0} = (\partial v_1 / \partial r)_{r=0}$$

the axial velocity from Equation [25] becomes

$$u_1)_{r=0} = -(2/\beta^2) \int_{-\infty}^x (v_1/r)_{r=0} dx \quad [46]$$

Differentiating Equation [30] with respect to r and setting $r = 0$ lead to

$$(v_1/r)_{r=0} = (1/\sqrt{2\pi}) \int_{-\infty}^{\infty} \int_0^1 \times [\eta \partial F(\xi, \eta) / \partial \xi] G_2(x - \xi, \eta) d\eta d\xi \quad [47]$$

where for x larger than zero

$$G_2(x, \eta) = \sqrt{\pi/2} \left[(\eta - 1/\eta) - \pi \sum_{n=1}^{\infty} e^{a_n x / \beta} J_1(a_n \eta) Y_1(a_n) / 2J_0(a_n) \right] \quad [48]$$

and for x smaller than zero

$$G_2(x, \eta) = (\pi\sqrt{\pi/2}) \sum_{n=1}^{\infty} e^{a_n x / \beta} J_1(a_n \eta) Y_1(a_n) / 2J_0(a_n) \quad [49]$$

Applying the same arguments as for the wall velocity distribution, we approximate $G_2(x, \eta)$ by

$$G_2(x, \eta) = 0$$

for $x < 0$, and

$$G_2(x, \eta) = \sqrt{\pi/2} (\eta - 1/\eta)$$

for $x > 0$. Substituting into Equation [47] we find that

$$(v_1/r)_{r=0} \cong \frac{1}{2} \int_0^1 (\eta^2 - 1) F(x, \eta) d\eta$$

Expressed in terms of the magnetic field components, this becomes, after integration of one of the integrals by parts

$$(v_1/r)_{r=0} \cong -(\beta^2 + \gamma M^2) \int_0^1 \eta B_2^2 d\eta + \frac{\beta^2}{2} \int_0^1 (B_1 B_2)_z (\eta^2 - 1) d\eta$$

From this, the perturbation velocity on the axis is

$$u_1)_{r=0} \cong - \int_0^1 B_1 B_2 (\eta^2 - 1) d\eta + 2 \left(\frac{\beta^2 + \gamma M^2}{\beta^2} \right) \int_0^1 \int_{-\infty}^x \eta B_2^2 d\xi d\eta \quad [50]$$

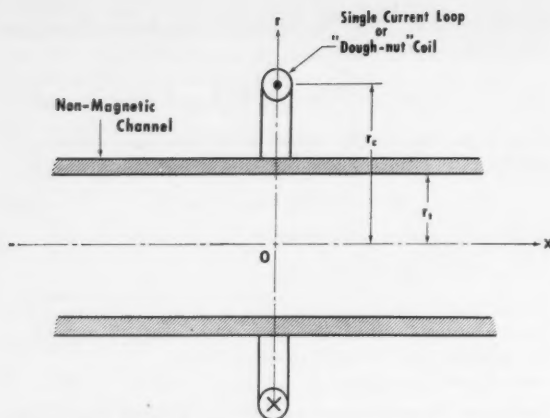


Fig. 1 Circular current loop and cylindrical channel

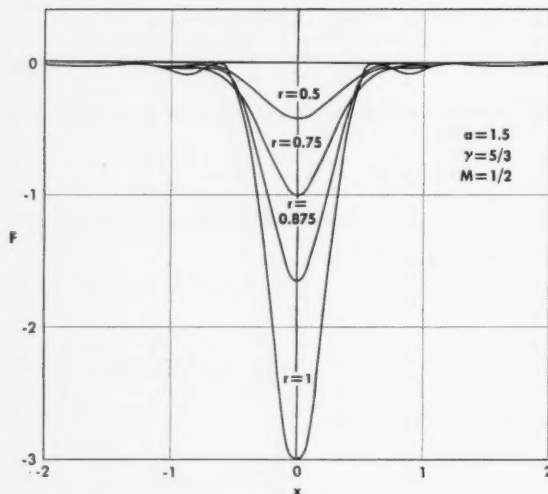


Fig. 2 The function $F(x, r)$ for a subsonic Mach number of $M = 0.5$ and $\gamma = 5/3$

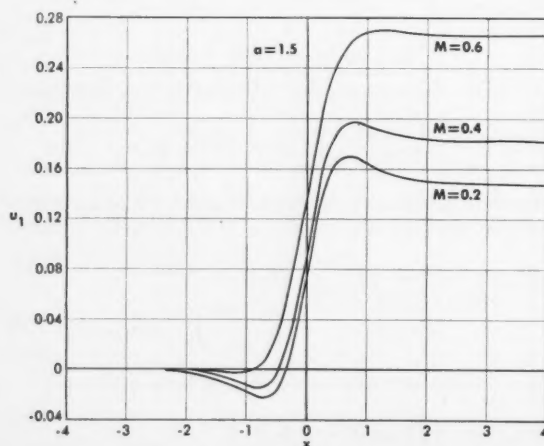


Fig. 3 Distribution of axial perturbation velocity, $a = 1.5$, $\gamma = 5/3$

Velocity and Pressure Along the Wall and Along the Axis for the Magnetic Field of a Single Circular Current Loop

For a numerical example using the preceding theory, we shall consider now the magnetic field induced by a single circular current loop which lies in the plane through $x = 0$ normal to the axis of the channel (see Fig. 1). (This magnetic field may be approximated quite well in the laboratory by a "doughnut"-type coil.) The components of the magnetic induction are derived on p. 270 of Smythe (3). Normalized to the magnitude of the field at $x = r = 0$ and expressed in terms of our variables, the relations become

$$B_1 = \frac{a}{\pi \sqrt{(a+r)^2 + x^2}} \left[K(k) + \frac{a^2 - r^2 - x^2}{(a-r)^2 + x^2} E(k) \right]$$

$$B_2 = \frac{ax}{\pi r \sqrt{(a+r)^2 + x^2}} \left[-K(k) + \frac{a^2 + r^2 + x^2}{(a-r)^2 + x^2} E(k) \right] \quad [51]$$

where

$$k^2 = 4ar / [(a+r)^2 + x^2]$$

The function $F(x, r)$ computed by Equation [27] using the field components in Equation [51] is shown in Fig. 2 for $M = 0.5$.

The integrals involving the magnetic field components used to find the perturbation velocity and pressure coefficient must be evaluated numerically. Using Equations [40 and 50] for the perturbation velocity along the wall and along the axis with the relations for B_1 and B_2 from Equation [51], we obtain the results in Figs. 3 and 4. For these calculations, the ratio of specific heats $\gamma = 5/3$, and the ratio of loop radius to channel radius is chosen as $a = 1.5$. The greatest change in the velocity along the wall and along the axis occurs in the small range of x within one radius of both sides of the current loop. The gas along the axis is accelerated through the field while the gas along the wall is decelerated.

The pressure coefficient along the wall is shown in Fig. 5 for $\gamma = 5/3$, $M = 0.2, 0.4$ and 0.6 , and for $a = 1.5$. We note that the curves are quite different from the velocity distribution. This is attributed to the magnetic pressure term

$$\int_{-\infty}^x B_2^2 d\xi$$

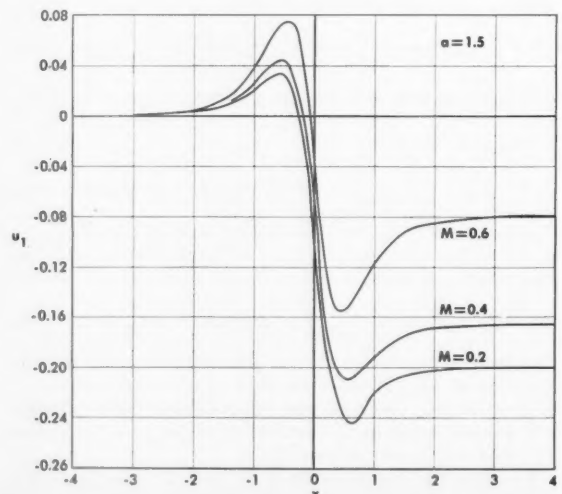


Fig. 4 Distribution of wall perturbation velocity, $a = 1.5$, $\gamma = 5/3$

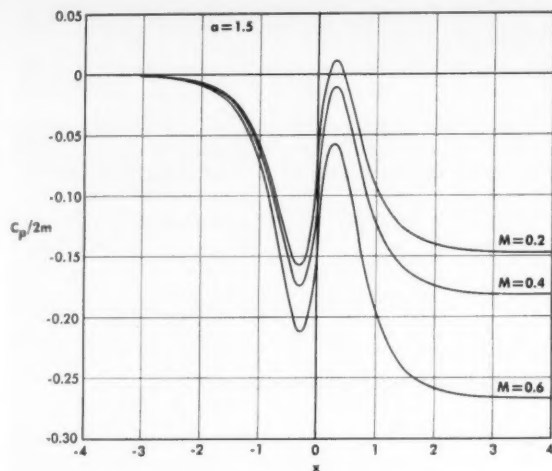


Fig. 5 Distribution of pressure coefficient along wall, $a = 1.5$, $\gamma = 5/3$

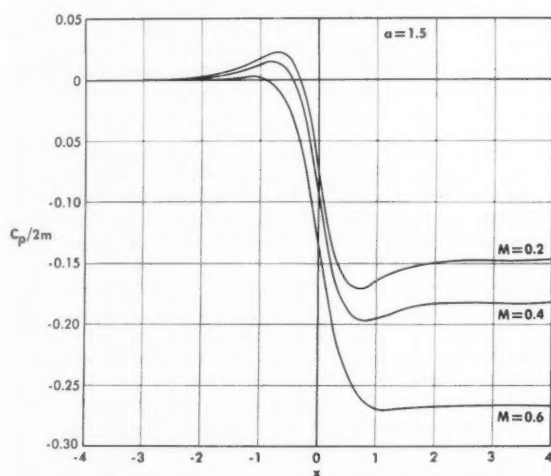


Fig. 6 Distribution of pressure coefficient along the axis, $a = 1.5$, $\gamma = 5/3$

The pressure coefficient along the axis is shown for the same parameter values in Fig. 6. Since B_2 is zero along the axis, the pressure coefficient is proportional to $-u_1$.

Perturbation Velocity, Density and Entropy Profiles Far Downstream of a Single Current Loop

The perturbation velocity profile across the channel far downstream is found by integrating numerically Equation [43] with the field components given by Equation [51].

The results of the computations are shown in Fig. 7 for a Mach number of 0.4 and for $a = 1.2, 1.5, 2.0$ and 4. The profile shape for all the values of a is nearly parabolic.

The density and entropy profiles at $x = \infty$ have the same form as the velocity profile, differing only in a scale factor and translation. The entropy profiles at $x = -2, -1$ and 0 are shown in Fig. 8. Note the different scale factors on the curves. The entropy profile at $x = \infty$ is simply double the curve for $x = 0$. The perturbation density profiles at $x = \infty$ for $M = 0.2$ are shown in Fig. 9 for $a = 1.2, 1.5, 2.0$ and 4.

MARCH 1961

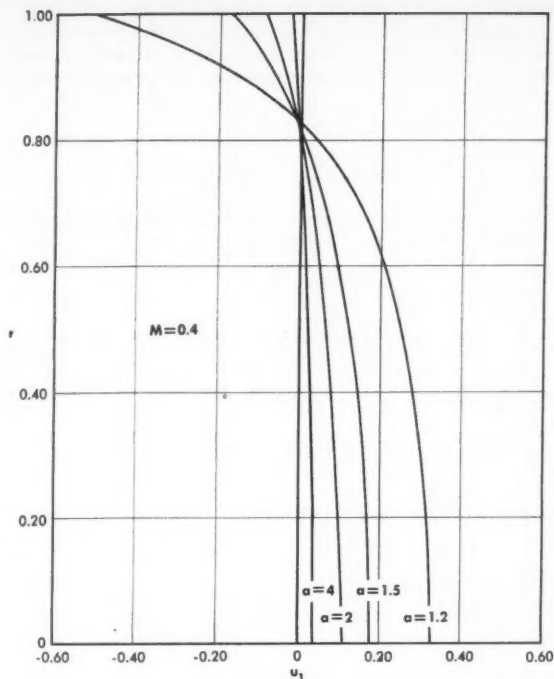


Fig. 7 Perturbation velocity profiles far downstream of the current loop, $M = 0.4$, $\gamma = 5/3$

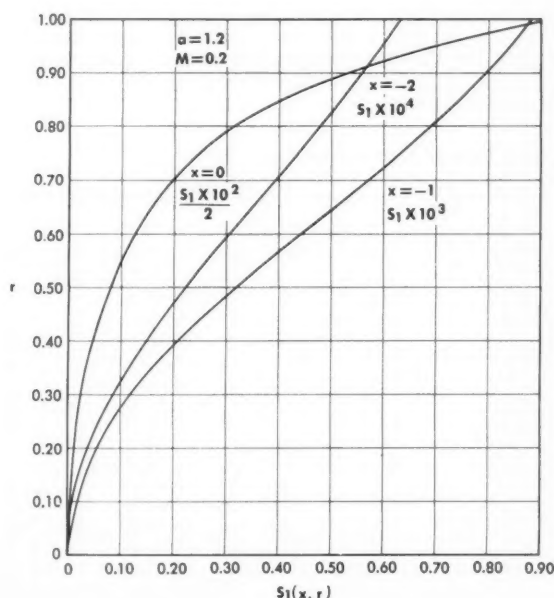


Fig. 8 Dimensionless entropy profiles for $M = 0.2$, $\gamma = 5/3$, $a = 1.2$ and $x = -2, -1$ and 0 (note scale factor for each curve)

General Solution for the Linearized Supersonic Flow of a Conducting Gas in a Cylindrical Tube in a Magnetic Field

When the flow is supersonic, the differential equation for the vertical velocity v_1 differs only in the sign of $\beta^2 = 1 - M_\infty^2$. If $\delta = \sqrt{M_\infty^2 - 1}$ is introduced, and the two-sided Laplace

transform in x is applied, the resulting ordinary differential equation in r has the same form as that for the Fourier transform for subsonic flow. Therefore, since the boundary conditions are the same as for subsonic flow, the Laplace transform for v_1 can be written down immediately as Equation [28 or 29] with

$$v_1 = \alpha \int_{-\infty}^{\infty} e^{-\alpha x} v_1(x) dx$$

The solution for v_1 can be expressed as a sum of convolution integrals. Define the function $G_s(x, r, \eta)$ by

$$G_s(x, r, \eta) = \frac{1}{2\pi i} \int_{\gamma-i\infty}^{\gamma+i\infty} \times \frac{e^{px/\delta} I_1(p\eta) [K_1(p) I_1(pr) - I_1(p) K_1(pr)] dp}{p I_1(p)} \quad [52]$$

and the function $H_1(x, r, \eta)$ by

$$H_1(x, r, \eta) = \frac{1}{2\pi i} \int_{\gamma-i\infty}^{\gamma+i\infty} e^{px/\delta} I_1(p\eta) K_1(pr) dp/p \quad [53]$$

Then the solution for v_1 becomes

$$v_1 = \int_0^1 \int_{-\infty}^{\lambda+\delta(\eta-1)} G_s(x-\xi, r, \eta) \eta F_\xi(\xi, \eta) d\xi d\eta - \int_0^r \int_{\lambda+\delta(\eta-1)}^{\mu+\delta(\eta-1)} H_1(x-\xi, r, \eta) \eta F_\xi(\xi, \eta) d\xi d\eta - \int_r^1 \left[\int_{-\infty}^{\lambda-\delta(\eta-1)} H_1(x-\xi, r, \eta) \eta F_\xi(\xi, \eta) d\xi - \int_{-\infty}^{\lambda+\delta(\eta-1)} H_1(x-\xi, r, \eta) n F_\xi(\xi, \eta) d\xi \right] d\eta$$

where

$$\lambda = x + \delta(r-1)$$

$$\mu = x - \delta(r-1)$$

In this form the disturbances of the magnetic field are summed up over the entire region up stream of the two Mach lines through the point x, r .

Wall Velocity in Supersonic Flow

Following an analysis very similar to that for subsonic flow,

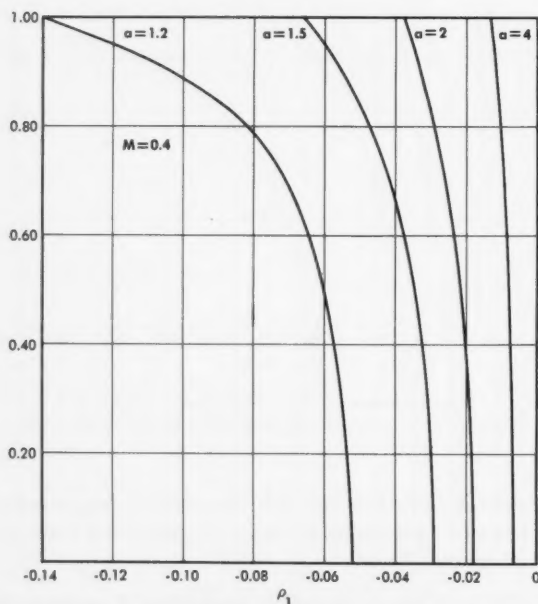


Fig. 9 Perturbation density profiles at $x = \infty$ for $a = 1.2, 1.5$ and 4 , and $M = 0.4$

we find that the tangential perturbation velocity on the wall is given by

$$u_1 = (1/\delta^2) \int_{-\infty}^x v_1 dx - (\gamma M^2/\delta^2) \int_{-\infty}^x B_2^2 dx$$

The Laplace transform for v_{1r} at $r = 1$ is identical in form to the Fourier transform for v_{1r} in subsonic flow, and the solution for v_{1r} can be expressed by the convolution integral

$$v_{1r}|_{r=1} = \int_0^1 \eta \int_{-\infty}^{x+\delta(\eta-1)} F_\xi(\xi, \eta) G_s(x-\xi, \eta) d\xi d\eta$$

where

$$G_s(x, \eta) = \frac{1}{2\pi i} \int_{\gamma-i\infty}^{\gamma+i\infty} \frac{e^{px/\delta} I_1(p\eta)}{p I_1(p)} dp$$

Using the calculus of residues we obtain

$$G_s(x, \eta) = \eta + 2 \sum_{n=1}^{\infty} \cos(a_n x/\delta) J_1(a_n \eta)/a_n J_0(a_n) \quad [54]$$

where a_n is the n th zero of $J_1(z)$.

In (1) a detailed study of the singularities of $G_s(x, \eta)$ was made by approximating the Bessel functions by the first term in their asymptotic expansions and then summing the resulting Fourier series. It was found that $G_s(x, \eta)$ has logarithmic singularities along certain of the Mach lines $\mu_1 = x - \delta(\eta-1)$ and $\lambda_1 = x + \delta(\eta-1)$ and a finite step discontinuity across others. The signs of the singularities are indicated graphically in Fig. 10. The plus sign on a Mach line, for instance, indicates that the contribution to u_1 from the convolution integral across the singularity has the same sign as $F_\xi(\xi, \eta)$. The function $G_s(x, \eta)$ is not singular on Mach lines which have no signs. The result of the finite step discontinuities yields integrals over certain triangles defined by the axis and two Mach lines of opposite families. The signs of the contribution of $F_\xi(\xi, \eta)$ to u_1 in these regions are indicated in the appropriate triangles in Fig. 10. For supersonic flow, the function $F_\xi(\xi, \eta)$ for the magnetic field due to the single current loop has more changes in sign than for subsonic flow (compare Figs. 2 and 11). Because of the properties of $G_s(x, \eta)$, it appears that the perturbation velocity along the wall is oscillatory. This type of behavior was found in the calculation for supersonic flow by Hains, Yoler and Ehlers (2) using the method of characteristics applied to the nonlinear equations for small magnetic Reynolds number.

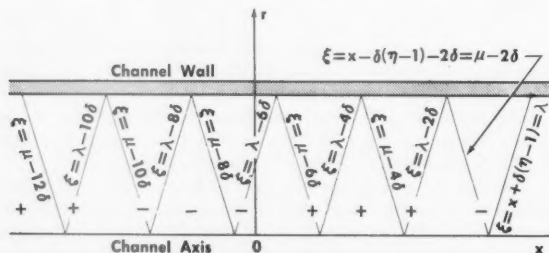


Fig. 10 Sketch indicating signs of logarithmic singularities of kernel functions on Mach lines and signs of some integrals contributing to perturbation velocity u_1 on wall

Axial Velocity Distribution for Supersonic Flow

When the flow is supersonic, the perturbation velocity on the axis of the tube is given by Equation [46] with β^2 replaced by $-\delta^2$. To find v_r for $r = 0$ we consider Equation [29] with β replaced by δ as its Laplace transform. Applying the convolution integral to the resulting equation, we obtain

$$v_{1r}|_{r=0} = \int_0^1 \eta \int_0^{x+\delta(\eta-2)} F_\xi(\xi, \eta) H_2(x - \xi, \eta) d\xi d\eta - \int_0^1 \int_{x+\delta(\eta-2)}^{x-\delta\eta} F_\xi(\xi, \eta) (x - \xi) d\xi d\eta / 2\sqrt{(x - \xi)^2 - \delta^2\eta^2}$$

where

$$H_2(x, \eta) = 1/2(\eta - 1/\eta) - (\pi/2) \sum_{n=1}^{\infty} \cos(a_n x / \delta) J_1(a_n \eta) Y_1(a_n) / J_0(a_n) \quad [55]$$

In (1), the singularities of $H_2(x, \eta)$ were analyzed in some detail by a procedure similar to that applied to $G_4(x, \eta)$. The function $H_2(x, \eta)$ was found to have infinite square root singularities when certain Mach lines $x \pm \delta\eta$ are approached from one side and finite singularities from the other side. These singularities are illustrated in Fig. 12. A plus sign, for example, on one side of a Mach line indicates that the infinite singularity approached from that side contributes to v_1 a quantity which has the same sign as $F(\xi, \eta)$. We note that the axial perturbation velocity with $F(\xi, \eta)$ in Fig. 11 has the same oscillatory behavior as the wall velocity.

Conclusion

The magnetohydrodynamic equations for the axial-symmetric flow of a conducting gas through a cylindrical channel were linearized under the assumption of small magnetic Reynolds number and small magnetic interaction parameter. It was assumed that the flow in the channel is uniform at infinity upstream, and the magnetic field vanishes at infinity both downstream and upstream of the magnetic field sources.

For axial-symmetric fields, the flow along the axis is isentropic. To a first approximation in the interaction parameter, the entropy of the gas is obtained from a simple integration of the square of the radial component of the magnetic field.

For a single current loop and subsonic flow, the axial and wall perturbation velocity distributions were calculated. Most of the influence of the magnetic field is found in the vicinity of the current loop. Along the wall the velocity is first slightly accelerated, and then decelerated very rapidly in the neighborhood of the current loop. Far downstream on the wall the velocity asymptotically approaches a value less than the upstream initial velocity. On the other hand, the axial velocity decreases slightly, then in the neighborhood of the coil increases rapidly to a downstream value which is greater than the initial undisturbed velocity. For the streamlines in the neighborhood of the axis, the gas is accelerated in passing through the field, whereas for streamlines near the wall, the gas is decelerated. The effect of the magnetic field, then, is to deflect the stream from the wall toward the axis. Since the radial velocity vanishes far downstream of the current loop, there results a shear flow in which the velocity decreases and the entropy increases as we move from the axis to the wall of the channel. The resulting velocity, density and entropy profiles are somewhat parabolic in shape.

Since the linearized supersonic flow is more difficult to compute from the solution than the linearized subsonic flow, only the singularities of the kernel functions for the convolution integrals of the axial and wall perturbation velocities were investigated. Although the kernel functions become infinite along certain Mach lines, the resulting perturbation velocities are finite. The signs of the kernel function indicate an oscillatory variation along the tube for the axial and wall velocity distributions in supersonic flow.

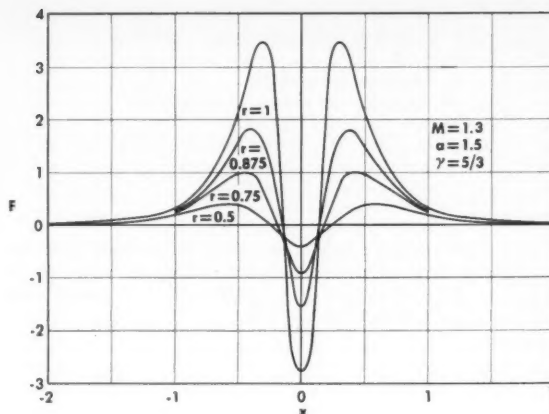


Fig. 11 The function $F(x, r)$ for $M = 1.3$ and $\gamma = 5/3$

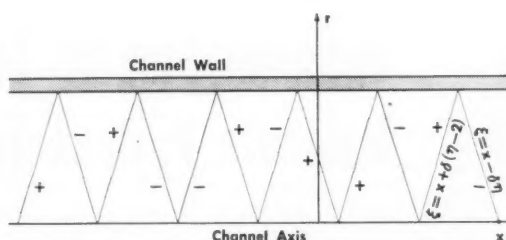


Fig. 12 Sketch indicating signs of infinite square root singularities of kernel function on Mach lines; e.g., a positive sign to right of a Mach line indicates sign of singularity as Mach line is approached from right

Nomenclature

a	= ratio of current loop radius to channel radius
a_n	= n th zero of Bessel function, $J_1(z)$
a_s	= normalized velocity of sound
b_0	= reference value of magnetic induction
B	= normalized magnetic induction vector
B_1, B_2	= axial and radial components of B
c_p	= $(\hat{p} - p_0) / (1/2 \rho_0 u_0^2)$, coefficient of pressure
c_v	= specific heat at constant volume
E	= normalized electric field vector
$F(x, r)$	= linearized body forces resulting from applied magnetic field, Equation [27]
$G_0(x, \eta, r)$	= Equation [31]
$G_1(x, \eta)$	= Equation [36 and 37]
$G_2(x, \eta)$	= Equation [48 and 49]
$G_3(x, \eta, r)$	= Equation [52]
$G_4(x, \eta)$	= Equation [54]
$H_2(x, \eta)$	= Equation [55]
$H_1(x, \eta, r)$	= Equation [53]
J	= normalized current density vector
k^2	= $4ar / [(a + r)^2 + x^2]$
M	= u_0 / a_0 , Mach number of undisturbed flow
m	= $\sigma b_0^2 r / \rho_0 u_0$, magnetic interaction parameter
p	= pressure
R	= gas constant
r_t	= channel radius
s	= normalized entropy
T	= temperature
u, v	= normalized axial and radial velocity components
V	= normalized velocity vector
x, r	= axial and radial coordinates, respectively
α	= Fourier or Laplace transform variable
β	= $\sqrt{1 - M^2}$

γ	= ratio of specific heat at constant pressure to specific heat at constant volume
δ	= $\sqrt{M^2 - 1}$
μ	= magnetic permeability
ξ, η	= running axial and radial coordinates
λ	= $x + \delta(r - 1)$, Mach line
μ	= $x - \delta(r - 1)$, Mach line
λ_1	= $x + \delta(\eta - 1)$, Mach line
μ_1	= $x - \delta(\eta - 1)$, Mach line
ρ	= normalized mass density of gas
σ	= electrical conductivity of the gas
0	= denotes variable evaluated for undisturbed stream conditions except where otherwise indicated
1, 2, 3, ..	= denote order of approximation in m except where otherwise indicated

(\wedge) = dimensional quantity

References

- 1 Ehlers, F. E., "The Linearized Solution for the Flow of a Conducting Gas through a Cylindrical Channel under the Influence of a Magnetic Field," Boeing Scientific Research Laboratories, Seattle, Wash., Document D1-82-0009, March 1960.
- 2 Hains, F. D., Yoler, Y. A. and Ehlers, F. E., "Axially Symmetric Hydromagnetic Channel Flow," Boeing Scientific Research Laboratories, Seattle, Wash., Document D1-82-0025; also in "Dynamics of Conducting Gases," edited by Cambel, A. B. and Fenn, J. B., Proc. Third Biennial Gas Dynamics Symposium, Northwestern Univ. Press, Evanston, Ill. 1960.
- 3 Smythe, W. R., "Static and Dynamic Electricity," McGraw-Hill Book Co., Inc., N. Y., 1950.
- 4 Watson, G. N., "The Theory of Bessel Functions," second edition University Press, Cambridge, England, 1958.

Optimum Staging Technique to Maximize Payload Total Energy

EDGAR R. COBB¹

Thiokol Chemical Corp.
Huntsville, Ala.

The Lagrangian multiplier method was used to derive a technique to minimize a missile gross takeoff weight with the payload total energy per unit weight as a constraint. The resulting equations are presented as a closed form solution and are applicable to a general case where different mass ratios, specific impulses, attitude angles and initial thrust to weight ratios are inherent in missile stages. An example showing the comparison of the total energy constraint optimization technique with the velocity constraint optimization technique is included. From the results of this example, it appears that the energy constraint approach need only be considered for small missiles where the altitude is significant with respect to the velocity.

PREVIOUS optimization studies and techniques (1-8)² have been based on the payload velocity constraint to minimize gross takeoff weight, or on the reciprocal problem, to maximize payload velocity with a gross takeoff weight constraint. This paper presents a method to minimize gross takeoff weight for a general case with the payload package weight known and the total energy imparted to the payload as a constraint. The resulting equations are general in that different specific impulses, mass fractions, initial thrust to weight ratios and average attitude angles can be input for each stage.

The gross takeoff weight of an N stage missile can be expressed as

$$W_T = W_{PL} + \sum_{n=1}^N W_{MO_n} \\ = W_{PL}(\lambda_1)(\lambda_2) \dots (\lambda_N) \quad [1]$$

The stage ratio λ_n is constrained by the payload energy equation

Received Aug. 8, 1960.

¹ Redstone Division; presently Associate Engineer at Texaco Experiment Incorporated, Richmond, Va. Member ARS.

² Numbers in parentheses indicate References at end of paper.

$$\Phi = -\frac{E_T}{W_{PL}} + \frac{V^2}{2g} + h = 0 \quad [2]$$

where

V = burnout velocity

$$= g \sum_{n=1}^N I_{spn} \ln \left[\frac{\lambda_n}{\lambda_n(1 - \mu_n) + \mu_n} \right] - g \sum_{n=1}^N \sin \Psi_n t_n$$

h = burnout altitude

$$= \sum_{n=1}^N (V_1 + \dots + V_{n-1}) \sin \Psi_n t_n + \sum_{n=1}^N (g t_n I_{spn} \sin \Psi_n) \times \\ \left[1 - \frac{\ln \frac{\lambda_n}{\lambda_n(1 - \mu_n) + \mu_n}}{\frac{(\lambda_n - 1)\mu_n}{\lambda_n(1 - \mu_n) + \mu_n}} \right] - \sum_{n=1}^N \frac{g \sin^2 \Psi_n t_n^2}{2}$$

$$t_n = \frac{\mu_n(\lambda_n - 1) I_{spn}}{(\lambda_n) a_{0n}}$$

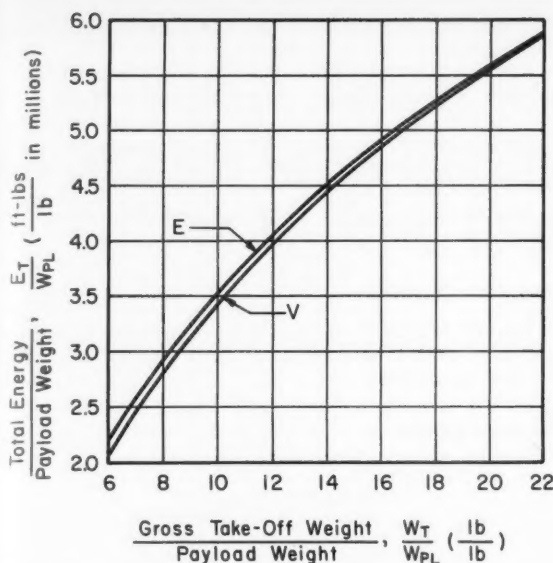


Fig. 1 Variation of total energy/payload weight, with gross take-off weight/payload weight, for optimum staging

The gross takeoff weight W_T will be at a minimum when $dW_T/d(\lambda_n) = 0$ subject to the payload energy constraint. The problem can be readily solved by use of Lagrangian multipliers. The Lagrange multiplier method enables the problem to be written as

$$\frac{\partial W_T}{\partial(\lambda_n)} + \eta \frac{\partial \Phi}{\partial(\lambda_n)} = 0 \quad [3]$$

The solution of Equation [3] results in the following set of equations

$$\frac{\mu_n I_{spn} \sin \Psi_n}{a_{0n}(\lambda_n)} \left\{ [V + g(t_{n+1} \sin \Psi_{n+1} + \dots + t_N \sin \Psi_N)] \times \left[\frac{a_{0n}}{\sin \Psi_n} \frac{\lambda_n}{\lambda_n(1 - \mu_n) + \mu_n} - 1 \right] + V_1 + \dots + V_n \right\} = -\frac{W_T}{\eta} = \text{constant} \quad [4]$$

where

η = Lagrange multiplier

$V = V_1 + V_2 + \dots + V_n + \dots + V_N$

$$V_n = g I_{spn} \ln \left[\frac{\lambda_n}{\lambda_n(1 - \mu_n) + \mu_n} \right] - g t_n \sin \Psi_n$$

Equations [4 and 2] form a set of $N + 1$ transcendental equations with $N + 1$ unknowns and must be solved for λ by an iterative process. The minimum gross takeoff weight can then be found by Equation [1].

If the terms resulting from the altitude component are neglected, Equation [4] can be written as

$$\frac{\mu_n I_{spn}}{\lambda_n} \left[\frac{\lambda_n}{\lambda_n(1 - \mu_n) + \mu_n} - \frac{\sin \Psi_n}{a_{0n}} \right] = \text{constant} \quad [5]$$

which was obtained by Weisbord (7) using the following definitions

$$\mu_n = 1 - \epsilon_n$$

Figs. 1, 2 and 3 show the comparison of the energy constraint Equation [4], curve E, with the velocity constraint Equation [5], curve V. The data were calculated for a typi-

cal two-stage solid propellant missile with the following assumed parameters

$$\begin{aligned} \mu_1 &= 0.90 \\ \mu_2 &= 0.89 \\ a_{01} &= a_{02} = 3 \\ I_{sp1} &= 255 \text{ lb-sec per lb} \\ I_{sp2} &= 285 \text{ lb-sec per lb} \\ \sin \Psi_1 &= 0.80 \\ \sin \Psi_2 &= 0.60 \end{aligned}$$

The variation of total energy to payload weight ratio E_T/W_{PL} , with optimized gross takeoff weight to payload weight ratio W_T/W_{PL} , is shown in Fig. 1. A larger value of E_T/W_{PL} for any given W_T/W_{PL} is obtained by using the energy constraint relations rather than the velocity constraint relations to determine missile staging. Approximately a 1% difference is noted by the two optimization techniques.

Fig. 2 shows the change in E_T/W_{PL} with missile staging for a constant W_T/W_{PL} . The first-stage ratio λ_1 is plotted as the independent variable, since for a two-stage system and a given W_T/W_{PL} , selection of either λ_1 or λ_2 will determine the missile staging. The maximum total energy to payload weight ratios are predicted by the energy constraint Equation [4]. The points designated V on the curves were established by the velocity constraint Equation [5].

Fig. 3 shows the second-stage ratio λ_2 as a function of first-stage ratio λ_1 for optimum staging. With any given value of W_T/W_{PL} , λ_{1E} is greater than λ_{1V} and λ_{2E} is smaller than λ_{2V} , where the subscripts E and V refer to the energy constraint technique and the velocity constraint technique, respectively. This results from the fact that $\partial h/\partial \lambda_1$ is greater than $\partial h/\partial \lambda_2$. Hence, when altitude terms are not neglected, as they are in Equation [5], the results of a change in the first-

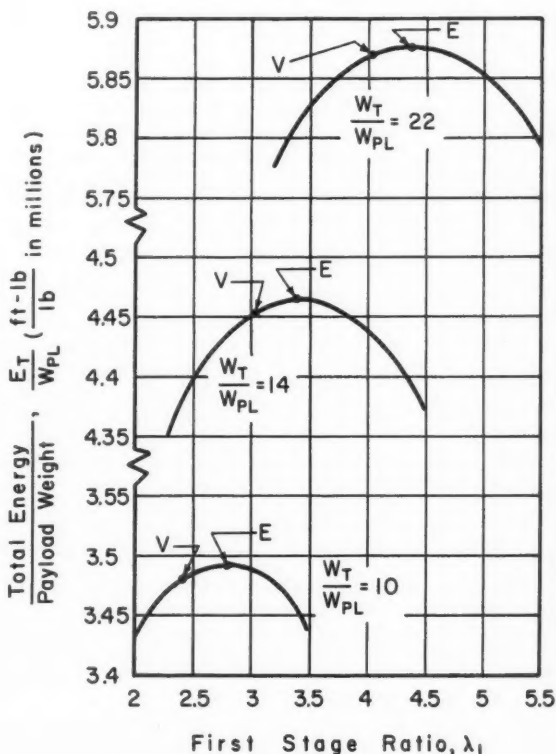


Fig. 2 Variation of total energy/payload weight, with first-stage ratio for constant gross takeoff weight/payload weight

stage ratio cause a greater change in potential energy than would an equivalent change in the second-stage ratio.

Although the energy constraint technique is more complex because of the altitude terms, it appears that the total work done relative to a payload should be considered in some cases rather than only the payload velocity component. This reasoning becomes more apparent with small stage ratios, where the potential energy component becomes significant with respect to the kinetic energy component. For larger stage ratios, the percent of total energy owing to the altitude term

decreases, and the curves in Figs. 1 and 3 appear to approach each other.

The fact that the mass fraction of a rocket motor is some function of initial thrust to weight ratio and absolute motor size restricts the use of only one optimization technique. Other factors such as economics, flight path and system complexity must be considered. Fig. 2 shows the flatness of the E_T/W_{PL} ratio as a function of missile staging; hence, only a slight penalty is realized for nonoptimum designs near the maximum.

Acknowledgment

The author acknowledges the support and suggestions furnished by Messrs. R. H. Wall and R. H. Sforzini of Thiokol Chemical Corporation.

Nomenclature

n	= stage number
W_{RO_n}	= weight of nth stage rocket
W_{f_n}	= weight of propellant in nth stage motor
W_{MO_n}	= weight of nth stage motor
W_{PL}	= weight of payload package
a_{0n}	= initial thrust to weight ratio of nth stage
I_{sp_n}	= average specific impulse of nth stage
Ψ_n	= average thrust attitude angle with horizontal of nth stage
t_n	= burning time of nth stage
λ_n	= $W_{RO_n}/(W_{RO_n} - W_{MO_n})$, stage ratio
μ_n	= W_{f_n}/W_{MO_n} , mass fraction

References

- 1 Goldsmith, M., "On the Optimization of Two Stage Rockets," *JET PROPULSION*, vol. 27, no. 4, April 1957, p. 415.
- 2 Schurmann, E. E. H., "Optimum Staging Technique for Multi-staged Rocket Vehicles," *JET PROPULSION*, vol. 27, no. 8, Aug. 1957, pp. 863-865.
- 3 Michelson, I., "Ultimate Design of High Altitude Sounding Rockets," *JET PROPULSION*, vol. 27, no. 10, Oct. 1957, pp. 1107-1108.
- 4 Ten Dyke, R. P., "Computation of Rocket Step Weights to Minimize Initial Gross Weight," *JET PROPULSION*, vol. 28, no. 5, May 1958, pp. 338-340.
- 5 Subotowicz, M., "The Optimization of the N-Step Rocket with Different Construction Parameters and Propellant Specific Impulses in Each Stage," *JET PROPULSION*, vol. 28, no. 7, July 1958, pp. 460-463.
- 6 Hall, H. H. and Zambelli, E. D., "On the Optimization of Multi-stage Rockets," *JET PROPULSION*, vol. 28, no. 7, July 1958, pp. 463-465.
- 7 Weisbord, L., "Optimum Staging Techniques," *JET PROPULSION*, vol. 29, no. 6, June 1959, pp. 445-446.
- 8 Builder, C. H., "General Solution for Optimization of Staging of Multi-Staged Boost Vehicles," *ARS JOURNAL*, vol. 29, no. 7, July 1959, pp. 497-499.

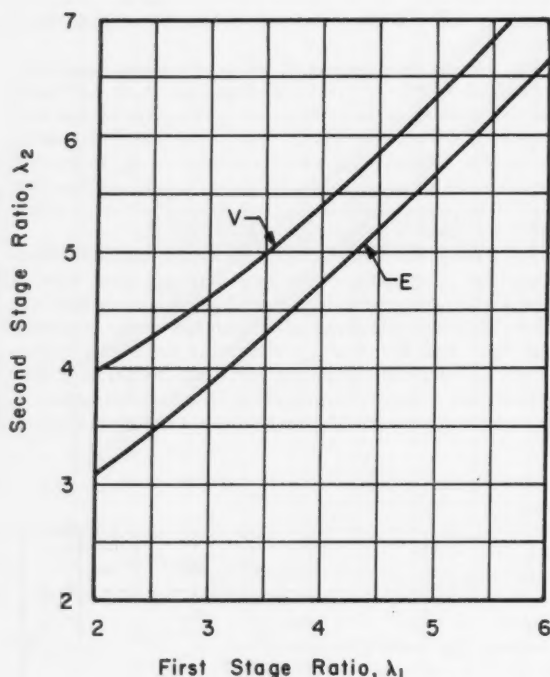


Fig. 3 First-stage, ratio vs. second-stage ratio for optimum staging

Characteristic Velocity Requirements for Impulsive Thrust Transfers Between Non Co-Planar Circular Orbits

L. RIDER¹

Convair-Astronautics
San Diego, Calif.

The characteristic velocity requirements for several types of impulsive thrust transfers between non co-planar and noncongruent circular orbits are determined. An analysis is made of four types of two- or three-impulse transfers which provide energy economy over a Hohmann-type transfer with plane change at apogee. All possible initial and final circular orbits described in the same sense and with relative inclination between the orbital planes of 90 deg or less are examined. Each transfer type is found to provide significant transfer energy economy in certain regions of the configuration space, defined by the ratio of inner to outer circular orbital radii σ and the relative angle of intersection between the orbital planes i .

A CONSIDERABLE part of the synthesis of a procedure to accomplish orbital rendezvous involves tradeoffs among energy, time and ballistic error sensitivity. Hence, having a reasonably precise description of minimum energy transfers between arbitrary orbits is not only of interest in itself but contributes to the derivation of an effective rendezvous procedure.

Rendezvous procedures being developed for use in the near future, restricted because of payload capabilities, generally involve launch or injection of the rendezvous vehicle with near minimum required plane changes. In a later time period, with the anticipated use of more effective methods of propulsion and with the necessity of providing logistic and maintenance support for satellite systems deployed in more than one orbit, such "co-orbital" rendezvous may need to be supplemented by more general procedures.

The co-planar problem of minimum energy impulsive orbital transfer has been treated fairly extensively (1-24).²

The non co-planar problem is only now in the process of investigation, as shown by the fewer and more recent references (25-34). The method of distributing the plane change of a Hohmann-type transfer between non co-planar circular orbits appeared first in (25) where it was applied to transfer to a "24-hr" orbit. Reference (29) provides a more general application of the same method. In (26 and 28) there is an analysis of the special case of the non co-planar bi-elliptic transfer when initial and final circular orbits are the same size. The analysis of (30) indicates the improvement possible by distributing the plane change of this transfer. The general problem of minimum energy transfer between non co-planar elliptic orbits of small relative inclination is discussed (27), and a first-order solution for the case of small eccentricities or small relative inclination is indicated (33). In (34) it is demonstrated that the optimal orientation providing the minimum energy transfer is such that initial, transfer and final orbits are co-planar. Analysis of transfer between a circular orbit and a point not located in the orbital plane is given (31). The investigation of two-impulse transfers between non co-planar circular and elliptic orbits is made

in (32), where numerical results are given for specific configurations, and the effect of variation of the elliptic orbit geometry and orientation is presented.

The contribution of the present paper is threefold: First, the non co-planar bi-elliptic transfer with single and distributed plane changes is generalized by considering initial and final circular orbits of different radii. Second, a non co-planar three-impulse Hohmann transfer is introduced, and is characterized by having velocity applications not located on the line of intersection of initial and final orbital planes. Third, a comparison is made of transfer energy requirements for the several types of two- and three-impulsive thrust apsidal transfers between non co-planar and noncongruent circular orbits about the same force center. The ideal energy required for the transfer in terms of a characteristic velocity is compared with the energy required for a "modified Hohmann" transfer between the same orbits. All possible initial and final circular orbits with the same rotational sense and with relative inclination between orbital planes of 90 deg or less are examined, and the general area of applicability of particular transfer types determined. The evaluation criterion is minimal characteristic velocity for the transfer. The use of the resulting information will be analogous to the application of the Hohmann transfer between co-planar circular orbits for providing a lower bound on two-impulse transfer energy requirement.

Assumptions for the analysis are that the gravitational force acting on the transfer vehicle is due only to a central inverse square field, that transfer vehicle mass is negligible compared with central mass, and that changes in vehicle velocity can be approximated by instantaneous velocity increments.

Transfers Between Co-Planar Circular Orbits

A brief examination of some of the minimum energy transfers between co-planar circular orbits will serve to provide an introduction to the treatment, later, of the non co-planar case, as well as to make the notation of the present paper more familiar.

Two-Impulse Transfer

Lawden (4) has shown that the minimum energy two-impulse transfer is a Hohmann transfer which requires a tan-

Received Sept. 6, 1960.

¹Senior Research Engineer, Preliminary Design Group; now Member of the Technical Staff, Aerospace Corp., Los Angeles, Calif. Member ARS.

²Numbers in parentheses indicate References at end of paper.

gential application of velocity of sufficient magnitude to allow the vehicle to ascend ballistically to the desired orbital altitude. At apogee of the transfer ellipse, a second velocity increment is applied, again tangential to and in the direction of the vehicle velocity, and of magnitude equal to the difference between apogee velocity and the velocity in a circular orbit at that altitude.

If the ratio of radial distance from the force center of inner to outer circular orbit is expressed as σ , the characteristic velocity requirement for the transfer, ratioed to circular velocity in the inner orbit, can be expressed as

$$\frac{V_{CH}}{V_{C_0}} = (1 - \sigma) \sqrt{\frac{2}{1 + \sigma}} + \sqrt{\sigma} - 1 \quad [1]$$

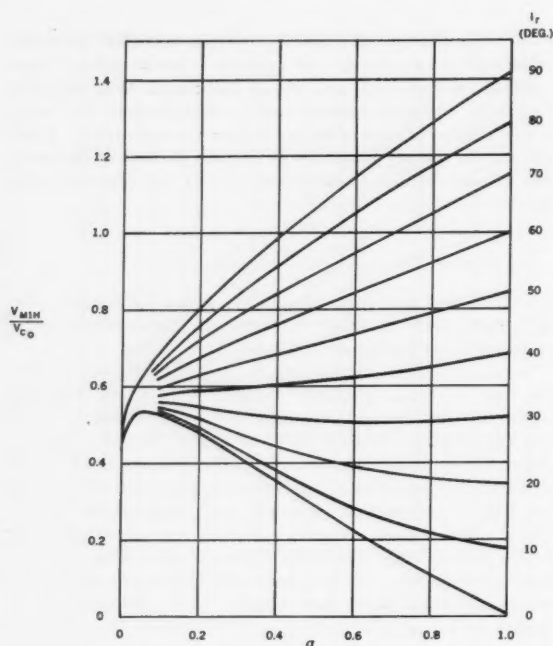


Fig. 1 "Mod-1 Hohmann" transfer velocity requirement

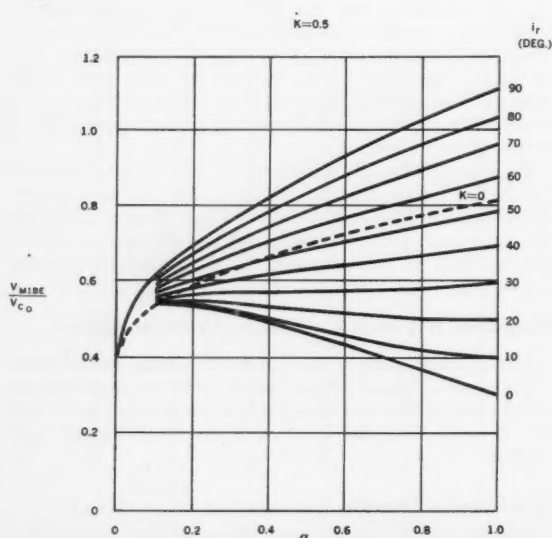


Fig. 2 "Mod-1 bi-elliptic" transfer velocity requirement

This is illustrated in Fig. 1, by the curve for $i_r = 0$. It has been shown that the velocity requirement maximizes for $\sigma = 0.064$, which is equivalent to an outer orbit radial distance approximately 15.58 greater than the inner orbital radial distance.

Three-Impulse Transfer

Ehrlicke (8), Hoelker and Silber (10) and Shternfeld (16) have independently devised a "bi-elliptic" three-impulse transfer which provides energy savings over the Hohmann transfer for certain ranges of σ . The "bi-elliptic" transfer which provides the energy savings is characterized by a transfer apogee at a radial distance larger than that of the outer circular orbit.

All velocity increments are applied horizontally and in the plane of the initial and final orbits. If we consider transfer sense from inner to outer circular orbits, the first velocity increment is of sufficient magnitude to place the apogee of the transfer ellipse at a specified altitude. The second velocity increment, applied at this apogee position, modifies the character of the transfer ellipse, so as to cause perigee to occur at the radial distance of the final circular orbit. The third velocity increment (retro) reduces the transfer perigee velocity to circular velocity.

The characteristic velocity requirement for this three-impulse maneuver is given by

$$\frac{V_{CH}}{V_{C_0}} = \sqrt{\frac{2}{1 + \sigma_A}} - 1 + \sqrt{2\sigma_A} \times \left[\sqrt{\frac{\sigma_A}{\sigma - \sigma_A}} - \sqrt{\frac{\sigma_A}{1 + \sigma_A}} \right] + \sqrt{\sigma} \left[\sqrt{\frac{2\sigma}{\sigma + \sigma_A}} - 1 \right] \quad [2]$$

where as before the ratio of inner to outer circular radial distance is given by σ , and where the ratio of inner circular to transfer apogee radial distance is given by σ_A . The curve $K = 0.5$, $i_r = 0$, of Fig. 2 illustrates the velocity requirement for the transfer if the transfer apogee distance is placed at twice the radial distance of the outer circular orbit ($K = \sigma_A/\sigma$). The curve $K = 0$ provides the velocity requirement if the transfer apogee position is at infinity, i.e., $\sigma_A = 0$.

The analysis of (10) indicates that any bi-elliptic transfer, with $\sigma_A < \sigma$, requires less velocity than the Hohmann transfer for $\sigma < 0.064$, that the bi-elliptic is conditionally superior to the Hohmann for $0.064 \leq \sigma \leq 0.084$, and that the bi-elliptic is inferior to the Hohmann transfer for $\sigma > 0.084$.

Transfers Between Non Co-Planar Circular orbits

Our method for synthesizing several two- and three-impulse transfers between non co-planar circular orbits which are to be representative of the near minimum energy transfer between such orbits, will be more "experimental" than analytic. This is necessitated by the present lack of analytical techniques for describing the minimum energy transfer between orbits with given orientation.

Although the method for synthesizing the transfers will be somewhat arbitrary, it is expected that adherence to the following three a posteriori synthesizing principles will provide transfers with the near minimum energy character

1 For the special case of zero relative inclination between initial and final circular orbits, all acceptable synthesized transfers must reduce to either a Hohmann or a bi-elliptic transfer.

2 The larger part of the plane changing impulse must occur at that part of the transfer path where vehicle velocity in the transfer orbit is near minimum.

3 Each acceptable synthesized transfer must provide a region in the i_r - σ configuration space where it is more economical than the "modified Hohmann" transfer to be discussed.

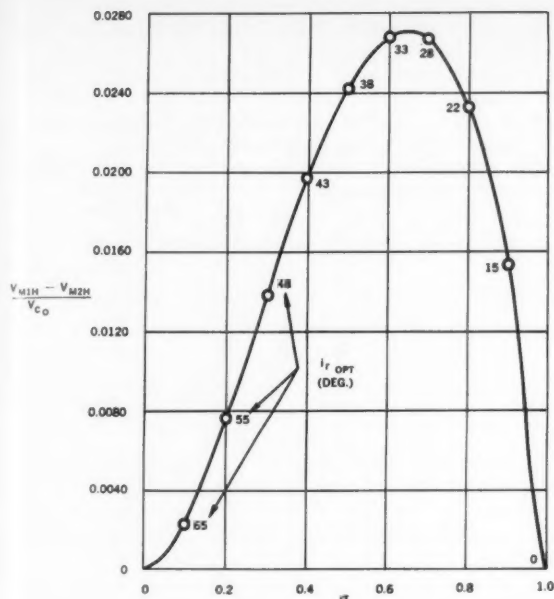


Fig. 3 Maximum velocity savings using "Mod-2 Hohmann" transfer

Two-Impulse Transfers

The "Mod-1 Hohmann" transfer

Perhaps the most natural generalization to the non coplanar case is found in the adaptation of the Hohmann transfer to provide the required non coplanar transfer. The Hohmann transfer is modified by incorporating a non coplanar velocity component at the apogee of the transfer ellipse. At this position, at the outer circular radial distance, vehicle velocity is simultaneously raised to circular velocity and rotated through the required relative inclination. Both velocity increments of the "Mod-1 Hohmann" transfer are applied at the line of intersection of initial and final orbital planes.

The characteristic velocity requirement for such a maneuver is given by

$$\frac{V_{M1H}}{V_{C0}} = (k_1 - k_2)^{1/2} + (k_3 - k_4 \cos i_r)^{1/2} \quad [3]$$

where

$$\begin{aligned} k_1 &= (3 + \sigma)/(1 + \sigma) & k_2 &= \sqrt{8/(1 + \sigma)} \\ k_3 &= (1 + 3\sigma)/(1 + \sigma) & k &= \sqrt{8\sigma^3/(1 + \sigma)} \end{aligned} \quad [4]$$

Fig. 1 illustrates the velocity requirement.

The "Mod-2 Hohmann" transfer

There exists a modification that can be made to the Hohmann transfer which will satisfy the three synthesizing principles, that is, to distribute the plane change between the two velocity increments, rather than accomplish it entirely at the outer increment as is characterized by the "Mod-1 Hohmann" transfer. The "Mod-2 Hohmann" transfer was first devised by Transue (25) and applied to the ascent to a "24 hr" orbit, where for a relative inclination change of $i_r = 30$ deg it was found that a velocity savings of 79 fps could be realized.

The characteristic velocity requirement for the "Mod-2

$i_{r OPT}$ = TOTAL PLANE CHANGE ALLOWING MAXIMUM VELOCITY SAVINGS

i_1 = PARTIAL PLANE CHANGE AT THE TRANSFER PERIGEE

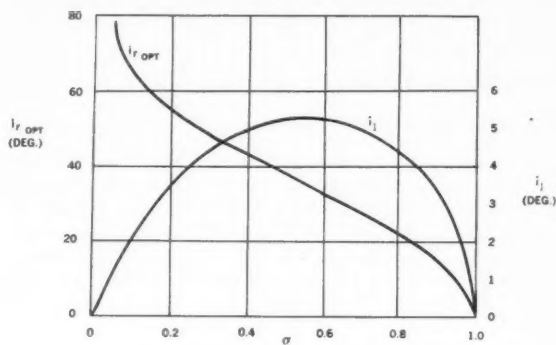


Fig. 4 Variation of $i_{r OPT}$ and i_1 with σ

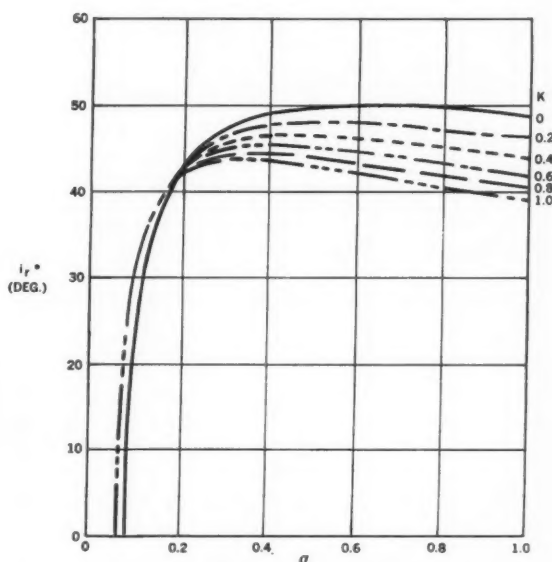


Fig. 5 Minimum relative inclination at which "Mod-1 bi-elliptic" provides savings

Hohmann" transfer is given by

$$\frac{V_{M2H}}{V_{C0}} = [k_1 - k_2 \cos i_1]^{1/2} + [k_3 - k_4 \cos (i_r - i_1)]^{1/2} \quad [5]$$

where k_i are defined as in the "Mod-1 Hohmann" case, and where the partial plane change i_1 associated with the velocity increment at the inner circular orbit satisfies the optimizing constraint

$$\begin{aligned} k_2^2 k_3 \sin^2 i_1 - k_1 k_4^2 \sin^2 (i_r - i_1) + \\ k_2 k_1^2 \sin^2 (i_r - i_1) \cos i_1 - \\ k_2^2 k_4 \sin^2 i_1 \cos (i_r - i_1) = 0 \end{aligned} \quad [6]$$

The "Mod-2 Hohmann" transfer provides velocity economy over the "Mod-1 Hohmann" transfer in the entire $i_r - \sigma$ configuration space. For the maximum velocity savings, however, there is a particular i_r , call it $i_{r OPT}$, associated with each σ . Fig. 3 illustrates the maximum velocity savings. It can be seen that the maximum economy occurs for $\sigma \approx 0.65$ and $i_{r OPT} \approx 30$ deg. Considering an inner circular orbit at 100 nautical miles altitude and an outer circular orbit at ap-

proximately 2020 nautical miles, with a relative inclination between the two of 30 deg, a savings of approximately 690 fps will result. Fig. 4 shows the magnitude of the partial plane change at the inner orbit for the conditions of maximum velocity indicated in Fig. 3.

Three-Impulse Transfers

The "Mod-1 bi-elliptic" transfer

For every σ and i_r a unique "modified bi-elliptic" transfer is determined when we specify the radial distance of apogee of the transfer ellipse at which the entire plane change be accomplished. We will be concerned only with those "modified bi-elliptic" transfers for which the position of the apogee is at a radial distance greater than that of the outer circular orbit; hence, choice of K where $0 \leq K \leq 1$, and $\sigma_A = K\sigma$ completely specifies the transfer for given σ and i_r .

In terms of this notation, $K = 1$ implies transfer apogee at outer circular radial distance, and the "Mod-1 bi-elliptic" transfer degenerates into the "Mod-1 Hohmann" transfer

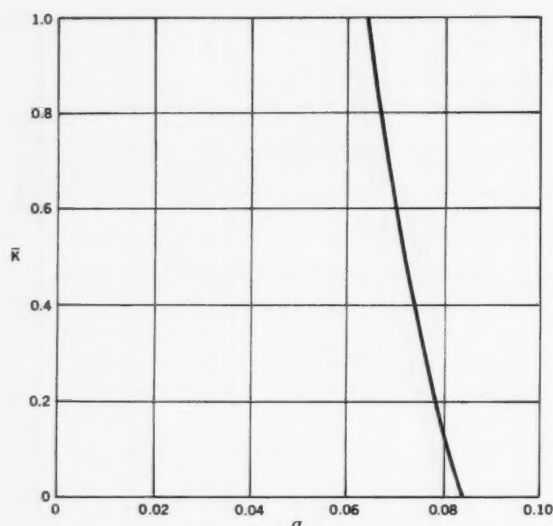


Fig. 6 K vs. σ for $i_r^* = 0$

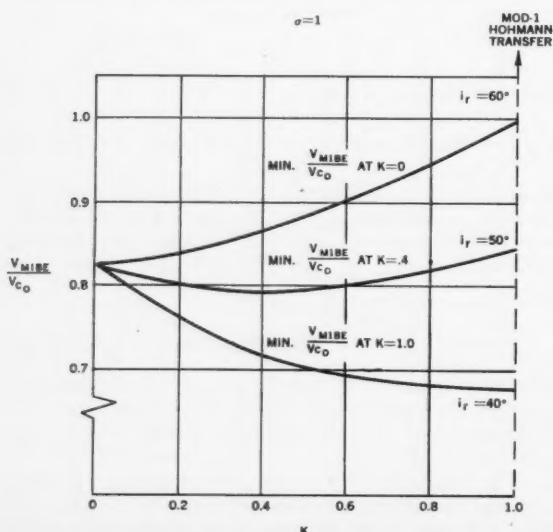


Fig. 7 Example of K dependence on i_r for minimum V_{MIBE}/V_{C0}

with relative inclination change accomplished at the outer circular orbit radial distance.

At the other extreme, $K = 0$ describes an escape to infinity and subsequent return to the appropriate radial distance determined by σ . In this case relative inclination change is accomplished with no expenditure of energy.

The characteristic velocity requirement for the "Mod-1 bi-elliptic" transfer is given by

$$\frac{V_{MIBE}}{V_{C0}} = (l_1 - l_2)^{1/2} + (l_3 - l_4 \cos i_r)^{1/2} + (l_5 - l_6)^{1/2} \quad [7]$$

where

$$\begin{aligned} l_1 &= \frac{3 + \sigma_A}{1 + \sigma_A} & l_2 &= \sqrt{\frac{8}{1 + \sigma_A}} \\ l_3 &= \frac{2(2\sigma_A + \sigma + 1)\sigma_A^2}{(1 + \sigma_A)(\sigma + \sigma_A)} & l_4 &= \frac{4\sigma_A^2}{\sqrt{(1 + \sigma_A)(\sigma + \sigma_A)}} \\ l_5 &= \frac{(3\sigma + \sigma_A)\sigma}{\sigma + \sigma_A} & l_6 &= \sqrt{\frac{8\sigma^3}{\sigma + \sigma_A}} \end{aligned} \quad [8]$$

Fig. 2 illustrates the velocity requirement for $K = 0$ and $K = 0.5$.

A comparison of "Mod-1 bi-elliptic" and "Mod-1 Hohmann" transfers from a minimum energy standpoint can be made as follows:

For $0 \leq \sigma < 0.0642$ the "Mod-1 bi-elliptic" transfer provides the most economical method of transfer, independent of the relative inclination (i_r) between initial and final orbits.

For all $\sigma \geq 0.0642$, there is a value of i_r^* which is a function of K —call it i_r^* —such that for all $i_r > i_r^*(K)$, a transfer velocity savings can be effected by using a "Mod-1 bi-elliptic" rather than a "Mod-1 Hohmann" transfer. For $i_r < i_r^*(K)$, the "Mod-1 Hohmann" transfer is more economical. i_r^* vs. σ for various K is shown in Fig. 5.

For any particular σ in the range $0.0642 < \sigma < 0.0838$, there is a unique $K \neq 0$, call it \bar{K} , such that $i_r^*(\bar{K}) = 0$ hence any "Mod-1 bi-elliptic" transfer characterized by $0 \leq K < \bar{K}$ will be more economical for all i_r . \bar{K} vs. σ is shown in Fig. 6.

For $0.0838 \leq \sigma \leq \sim 0.2$ and for $i_r > i_r^*(K)$ (i.e., those conditions for which the "Mod-1 bi-elliptic" transfer is more economical), the smaller the value of K (i.e., the greater the radial distance of the transfer apogee), the larger will be the transfer energy savings.

For σ approximately equal to 0.2, $i_r^*(K)$ is independent of K and approximately equal to 42 deg. This implies the interesting result that for $i_r \approx 42$ deg and $\sigma \approx 0.2$, the velocity required for the transfer is approximately the same for all $0 \leq K \leq 1$.

For $\sim 0.2 < \sigma \leq 1$, as can be seen from Fig. 5, the character of the variation of i_r^* with K reverses, and as K increases i_r^* decreases. For all $i_r > i_r^*$, however, no general observation can be made concerning the value of K associated with the most economical transfer. This is illustrated in Fig. 7 for the case of $\sigma = 1$. In this illustration it can be seen that K corresponding to the minimum energy transfer may be equal to zero, 1, or any intermediate value depending upon relative inclination i_r .

The maximum economy of the "Mod-1 bi-elliptic" over the "Mod-1 Hohmann" transfer illustrated in Fig. 8 for various relative inclination i_r . Since the majority of points plotted in this figure involve vehicle escape and subsequent return—a rather impractical method of transfer—the energy savings of a "Mod-1 bi-elliptic" transfer with $K = 0.5$ is shown in Fig. 9. Again, $K = 0.5$ implies transfer apogee at twice the radial distance of the outer circular orbit.

The "Mod-2 bi-elliptic" transfer

Since the distribution of the plane change in the "Mod-2 Hohmann" transfer provided velocity savings over the

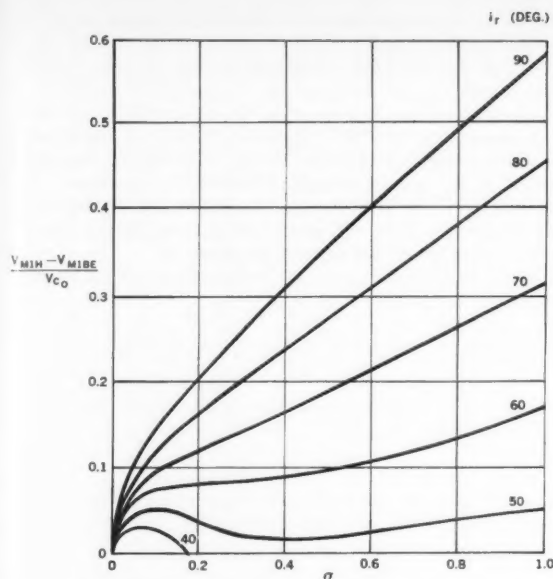


Fig. 8 Maximum velocity savings using "Mod-1 bi-elliptic" transfer

"Mod-1 Hohmann" transfer, one might expect that distributing the plane change of the "Mod-1 bi-elliptic" will also provide a velocity economy. Such is found to be the case.

The characteristic velocity requirement for the "Mod-2 bi-elliptic" transfer is given by

$$\frac{VM_{2BE}}{V_{C_0}} = (l_1 - l_2 \cos i_1)^{1/2} + (l_3 - l_4 \cos i_2)^{1/2} + (l_5 - l_6 \cos i_3)^{1/2} \quad [9]$$

where l_i are defined as in the previous case. The values of the partial plane changes i_1 , i_2 and i_3 which provide the minimum transfer characteristic velocity requirement for given values of σ , σ_A and i_r , must satisfy the set of equations

$$\begin{aligned} i_r - (i_1 + i_2 + i_3) &= 0 \\ l_2(\sin i_1)(l_3 - l_4 \cos i_2)^{1/2} - l_4(\sin i_2)(l_1 - l_2 \cos i_1)^{1/2} &= 0 \\ l_4(\sin i_2)(l_5 - l_6 \cos i_3)^{1/2} - l_6(\sin i_3)(l_3 - l_4 \cos i_2)^{1/2} &= 0 \end{aligned} \quad [10]$$

which can be derived using Lagrange's method of multipliers. Each of the partial plane changes is accomplished on the line of intersection of initial and final orbital planes, and simultaneously with each of the coplanar velocity applications that would be required in a co-planar bi-elliptic transfer with the same σ and σ_A .

The maximum velocity savings of this transfer over the "Mod-1 bi-elliptic" transfer is illustrated in Fig. 10. The relative inclinations at which such maximum economy occurs is shown in Fig. 11. In Fig. 12, the characteristic velocity economy of the "Mod-2 bi-elliptic" over the "Mod-1 Hohmann" is shown for $K = 0.5$ for various i_r and σ . It should be noted that for $K = 1$, the "Mod-2 bi-elliptic" degenerates into the "Mod-2 Hohmann" transfer.

The "Mod-3 Hohmann" transfer

It can be recalled that the "Mod-2 Hohmann" transfer distributed the plane change of the "Mod-1 Hohmann" transfer which was characterized by total relative inclination change accomplished at transfer apogee. There exists a modification of the "Mod-2 Hohmann" transfer which will convert it from a two-impulse to a three-impulse transfer and satisfy the three synthesizing principles. Unlike any of the preceding transfers which were examined, the "Mod-3 Hohmann" transfer is

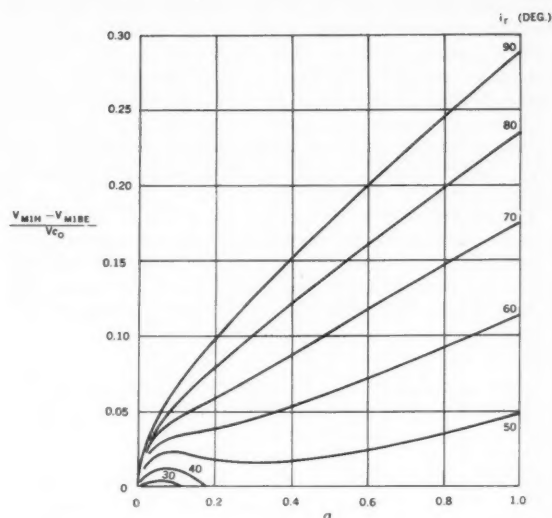


Fig. 9 Velocity savings using "Mod-1 bi-elliptic" transfer with $K = 0.5$

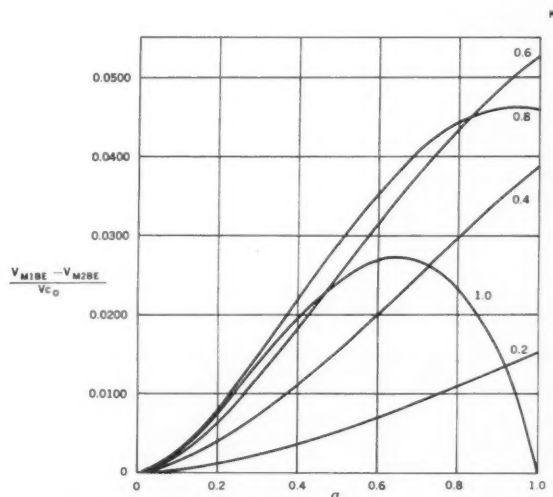


Fig. 10 Maximum economy of "Mod-2 bi-elliptic" over "Mod-1 bi-elliptic"

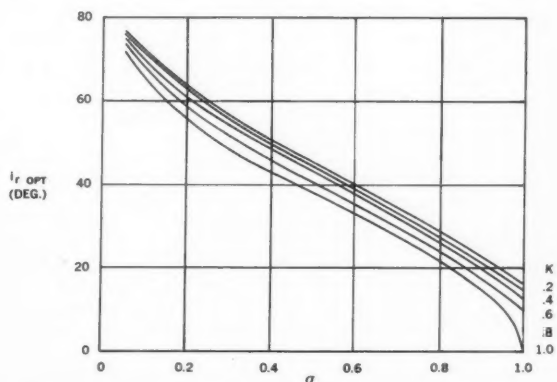


Fig. 11 Relative inclination for maximum economy condition of Fig. 10

characterized by velocity increments, none of which are applied on the intersection of initial and final orbital planes.

Considering the sense of transfer to be from inner to outer circular orbit, the first and third velocity increments are of similar character to the velocity increments of the "Mod-2 Hohmann" transfer. Both are applied horizontally at the transfer apsides, and a plane change is incorporated in each. The first increment is of sufficient magnitude to place transfer apogee at the radial distance of the desired outer final circular orbit, and the third velocity increment also raises transfer apogee velocity to circular velocity.

The second velocity increment will occur at some intermediate point of the ascent ellipse and will change only the direction of the velocity at that point. The transfer velocity magnitude and elevation with respect to the horizontal will be preserved. The magnitude of the plane change at the

second velocity application is calculated so as to move the perigee of the transfer ellipse from the initial orbital plane and place it in the final desired orbital plane, thereby ensuring that transfer apogee will occur in the desired orbital plane.

The trace of the maneuver on the geocentric sphere is illustrated in Fig. 13. Part of the characteristic velocity savings of this maneuver over the "Mod-1 Hohmann" maneuver occurs at the second velocity increment application. The fact that the velocity in the transfer ellipse at this point is not in a horizontal plane will allow a relative inclination change to be made with smaller velocity requirement.

The characteristic velocity requirement for the total maneuver is given by

$$\frac{V_{MSH}}{V_{c_0}} = (k_1 - k_2 \cos i_1)^{1/2} + k_3(1 - \cos i_2)^{1/2} + (k_3 - k_4 \cos i_3)^{1/2} \quad [11]$$

where k_1, k_2, k_3 and k_4 are defined as in the "Mod-1 Hohmann" case and where

$$k_3 = [(1 + \sigma) + (1 - \sigma) \cos \theta] / \sqrt{1 + \sigma} \quad [12]$$

i_1, i_2 and i_3 are the partial plane changes measured on a geocentric sphere, and must satisfy the geometric constraints

$$i_3 = \arcsin [\sin A \sin (\theta - B) / \sin \theta]$$

$$i_2 = \arccos \left[\frac{\cos i_3 \cos A + \sin i_3 \sin A \cos \theta \cos (\theta - B)}{1 - \sin i_3 \sin A \sin \theta \sin (\theta - B)} \right] \quad [13]$$

where

$$A = \arccos [\cos i_r \cos i + \sin i_r \sin i \cos \Omega]$$

$$B = \arcsin [(\sin \Omega \sin i_r) / A]$$

For given values of σ, i_r and $\Omega \leq 45$ deg, a computer program was devised which provided the values of θ, i_1, i_2 and i_3 that minimized the characteristic velocity requirement. The lower bound of these relative minimums was found to occur at $\Omega = 0$ (at which point the "Mod-3 Hohmann" degenerates into the "Mod-2 Hohmann's transfer"). Hence, for the Ω range considered, the "Mod-2 Hohmann" provides a lower bound for the "Mod-3 Hohmann" transfer velocity requirement.

As Ω increases from zero, the characteristic velocity required for the transfer increases, and at some small value of Ω the velocity requirement equals that of the "Mod 1 Hohmann" transfer. The values of Ω at which this occurs do not exceed approximately 15 deg for combinations of $i_r \geq 10$ deg and $\sigma \leq 0.9$. This does provide some flexibility as far as time of injection into final orbit is concerned, but not as much flexibility as provided by the "Modified bi-elliptic" transfers with adjustable K values.

Conclusions

A major purpose of the preceding analysis was to enable choice (based on velocity requirement) of a particular transfer type given a point or a region in the configuration space. This can be conveniently accomplished if we consider not the fps velocity economy of the transfer types, but rather the ratio of such velocity savings to the characteristic velocity requirement of the "Mod-1 Hohmann" transfer at that point of the configuration space. This is shown in Fig. 14.

The shaded area of the figure indicates that region of the configuration space where the transfer types investigated provide less than a 5% economy in transfer velocity over the "Mod-1 Hohmann" transfer.

The teardrop shaped region indicating "Mod-2 Hohmann" transfer and best "Mod-3 Hohmann" transfer performance provides a minimum velocity economy of 5%. Maximum economy of 7.5% occurs at $\sigma = 0.6$ and $i_r = 17.5$ deg.

At higher i_r , the 5, 10 and 20% contours of the "Modified bi-elliptic" transfers appear. It can be seen that better than a 20% savings can be achieved for i_r and σ combinations in the vicinity of 80-90 deg and 0.8-1.0, respectively.

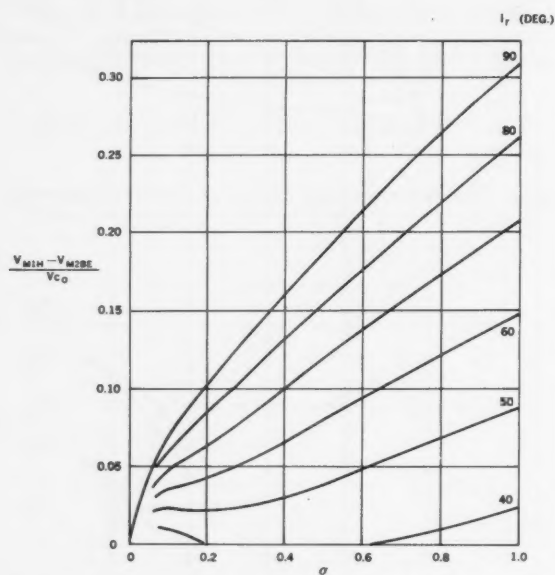


Fig. 12 Velocity savings using "Mod-2 bi-elliptic" transfer with $K = 0.5$

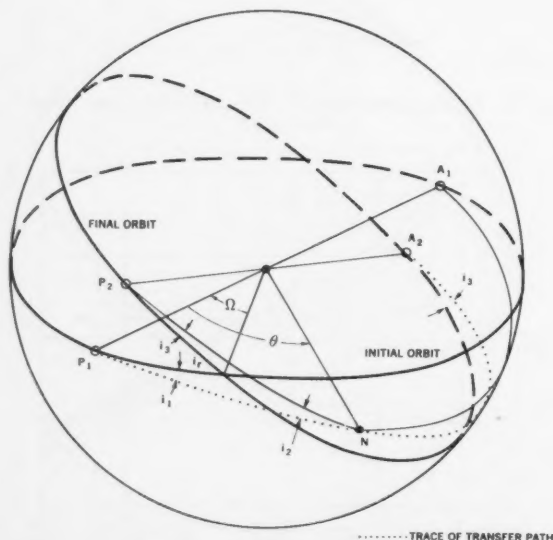


Fig. 13 Trace of "Mod-3 Hohmann" transfer on geocentric sphere

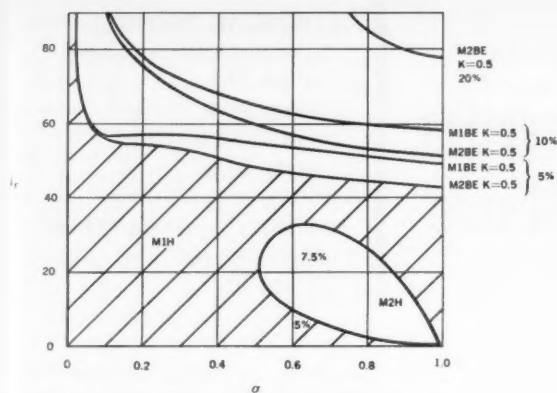


Fig. 14 Choice of transfer type

Acknowledgment

The writer wishes to express his gratitude to W. D. Davis of the Preliminary Design Group, who provided the computer programming for the required numerical data.

Nomenclature

r	= radial distance from force center to point of interest
V	= scalar velocity
V_{CH}	= characteristic velocity requirement
i_r	= relative inclination between orbital planes
σ	= r_0/r_1
σ_A	= r_0/r_A
k, K, l	= auxiliary parameters defined in text
Ω, θ	= geometric parameters defined in Fig. 13

Subscripts

0	= inner circular orbit
1	= outer circular orbit
A	= apogee of transfer ellipse
C	= circular
M1H	= Mod-1 Hohmann
M2H	= Mod-2 Hohmann
M3H	= Mod-3 Hohmann
M1BE	= Mod-1 bi-elliptic
M2BE	= Mod-2 bi-elliptic

References

Co-Planar

- 1 Lawden, D. F., "Entry Into Circular Orbits," *J. Brit. Interplanet. Soc.*, vol. 10, no. 1, Jan. 1951, pp. 5-17.

- 2 Lawden, D. F., "The Determination of Minimal Orbits," *J. Brit. Interplanet. Soc.*, vol. 11, no. 5, Sept. 1952.
- 3 Lawden, D. F., "Orbital Transfer via Tangential Ellipse," *J. Brit. Interplanet. Soc.*, vol. 11, no. 6, Nov. 1952, pp. 278-289.
- 4 Lawden, D. F., "Inter-Orbital Transfer of a Rocket," *J. Brit. Interplanet. Soc.*, Annual Rep. 1952, pp. 321-333.
- 5 Lawden, D. F., "Escape to Infinity From Circular Orbits," *J. Brit. Interplanet. Soc.*, vol. 12, no. 2, March 1953, pp. 68-71.
- 6 Lawden, D. F., "Transfer Between Circular Orbits," *JET PROPULSION*, vol. 26, no. 7, July 1956, pp. 555-558.
- 7 Vargo, L. G., "Criteria for Orbital Entry," *JET PROPULSION*, vol. 28, no. 1, Jan. 1958, pp. 54-55.
- 8 Ehrlicke, K. A., "Interplanetary Mission Profiles," Convair Astronautics, San Diego, Calif., Internal Rep. no. AZM-023, April 1958.
- 9 Vargo, L. G., "Optimal Transfer Between Two Co-Planar Terminals in a Gravitational Field," AAS, Western Regional Meeting, no. 58-20, Aug. 1958.
- 10 Hoelker, R. F. and Silber, R., "The Bi-Elliptic Transfer Between Circular Co-Planar Orbits," Army Ballistic Missile Agency, Redstone Arsenal, Ala., DA Tech. Memo no. 2-59, Jan. 1959.
- 11 Silber, R. and Horner, J. M., "Two Problems of Impulse Minimization Between Co-Planar Orbits," Army Ballistic Missile Agency, Redstone Arsenal, Ala., DA Tech. Memo no. 23-59, Feb. 1959.
- 12 Munick, H., "An Optimal Transfer Path From an Elliptic Orbit to a Higher Energy Circular Orbit," *ARS JOURNAL*, vol. 29, no. 6, June 1959, pp. 449-451.
- 13 Munick, H., McGill R. and Taylor, G. E., "Minimization of Characteristic Velocity for Transfer Between Arbitrary Terminals in an Inverse Square Field Using Two Impulses," *ARS Preprint* no. 959-59, Nov. 1959.
- 14 Edelbaum, T. N., "Some Extensions of the Hohmann Transfer Maneuver," *ARS JOURNAL*, vol. 29, no. 11, Nov. 1959, pp. 864-865.
- 15 Smith, G. C., "The Calculation of Minimal Orbits," *Astronautica Acta*, vol. V, fasc. 5, 1959, p. 253.
- 16 Shternfeld, A., "Soviet Space Science," Basic Books Inc., N. Y., 1959, pp. 100-111.
- 17 Ting, L., "Optimum Orbital Transfer by Two Impulses," Polytechnic Institute of Brooklyn, N. Y., PIBAL Rep. no. 536, Jan. 1960.
- 18 DeBra, D. B. and Gundel, B. H., "Circularization of Elliptic Orbits," AAS, 6th National Meeting, Jan. 1960, Preprint no. 60-36.
- 19 Leitmann, G., "Establishment of a Circular Satellite Orbit by Double Impulse," *J. Brit. Interplanet. Soc.*, vol. 17, no. 7, Jan.-Feb. 1960, pp. 194-198.
- 20 Rider, L., "Ascent From Inner Circular to Outer Co-Planar Elliptic Orbits," *ARS JOURNAL*, vol. 30, no. 3, March 1960, pp. 254-258.
- 21 Horner, J. M., "Optimum Orbital Transfer," Submitted to 1960 ARS Chrysler Corp. Undergraduate Competition, June 1960.
- 22 Ting, L., "Optimum Orbital Transfer by Several Impulses," Polytechnic Institute of Brooklyn, N. Y., PIBAL Rep. no. 608, June 1960.
- 23 Leitmann, G., "Note on Establishments of a Circular Satellite Orbit by Double Impulse," *J. Brit. Interplanet. Soc.*, vol. 17, no. 10, July-Aug. 1960, pp. 358-359.
- 24 Munick, H., McGill, R. and Taylor, G. E., "Analytic Solutions to Several Optimum Orbit Transfer Problems," 11th IAF Congress, Stockholm, Aug. 1960.

Non Co-Planar

- 25 Transue, J. R., "Optimum Change of Orbit Plane," Convair Astronautics, San Diego, Calif., Internal Rep. no. CA-P-2, Jan., 1959.
- 26 Rider, L., "Characteristic Velocity for Changing the Inclination of a Circular Orbit to the Equator," *ARS JOURNAL*, vol. 29, no. 1, Jan. 1959, pp. 48-49.
- 27 Lawden, D. F., "Interplanetary Rocket Trajectories," in "Advances in Space Science," vol. 1, Academic Press, Inc., N. Y., 1959, pp. 1-52.
- 28 De Bra, D. B., "Orbital Plane-Change Maneuver," *Astron. Sci. Rev.*, vol. 1, no. 4, Oct.-Dec. 1959, p. 19.
- 29 Horner, J. M. and Silber, R., "Impulse Minimization for Hohmann Transfer Between Inclined Circular Orbits of Different Radii," Army Ballistic Missile Agency, Redstone Arsenal, Ala., DA Tech. Rep. no. 70-59, Dec.
- 30 Edelbaum, T. N., "Propulsion Requirements for Controllable Satellites," *ARS Preprint* no. 1228-60, May 1960.
- 31 Wolfe, J. F. and De Bra, D., "Two Maneuver Ascents to Circular Orbits," *J. Astron. Sci.*, vol. VII, no. 2, Summer 1960, pp. 47-48.
- 32 Brunk, W. E., "Transfer Between Non Co-Planar Orbits With Minimum Velocity Requirements," AAS, Western National Meeting, Aug. 1960, no. 60-69.
- 33 Long, R. S., "Transfer Between Non Co-Planar Elliptical Orbits," *Astronautica Acta*, vol. VI, fasc. 2-3, 1960, pp. 167-178.
- 34 Ting, L., "Optimum Orbital Transfer by Impulses," *ARS JOURNAL*, vol. 30, no. 11, Nov. 1960, pp. 1013-1018.

Probability of Satellite Interception by an Air Launched Pre-Guided Missile¹

EDGAR M. JACOBS²

Caywood-Schiller, Associates
Chicago, Ill.

GEORGE W.
MORGENTHAUER³

The Martin Co.
Denver, Colo.

ROBERT A. SEBASTIAN⁴

Caywood-Schiller, Associates
Chicago, Ill.

The following note develops a simple computational model containing the timing, operational and mechanistic error parameters expected to be present in attempts at satellite interception utilizing an aircraft launched, pre-guided missile. Such a model will introduce simplifying approximations, but its value lies in its ability to measure the relative importance of the various errors and to determine where improvement will be most rewarding. The approximations introduced are believed to be consistent with the precision of present instrument accuracies.

Satellite Interception

IN OCTOBER 1959, The U. S. Air Force launched a ballistic missile from a B-47 bomber cruising at 35,000 ft. The missile ascended in a near vertical flight and is reported to have come within a few miles of the satellite Explorer VI. [Some newspapers indicated a 4-mile miss (1),⁵ although other sources do not support this.]

The main steps envisioned in such a satellite interception are:

The satellite is initially detected and tracked by ground based equipment and its orbit is predicted.

The predicted orbit is used to determine where and when the interception is to take place; here, a circular orbit is assumed.

A missile-bearing aircraft is directed to a launch point in space time.

An automatic signal initiates the launch of the interceptor missile.

The missile is inertially guided during powered flight; then it is in free-fall flight to the interception point.

The interception takes place at or near the missile apogee.

The errors associated with each of these steps will be integrated by the model to provide an estimate of the likelihood that the missile comes within a specified distance R of the satellite.

The Geometry of Interception

Let a Cartesian coordinate system be set up at the *predicted intercept point* Q at altitude h above the surface of Earth. (See Fig. 1.)

In Fig. 1 the z -axis is vertical and the y -axis is tangent to the satellite orbit at Q . The x -axis is perpendicular to both the z -axis and the y -axis, and plane ρ is the xz -plane. Positive directions on the axes are shown. The heading of the carrier aircraft with respect to the plane ρ is θ . The dotted line indicates the missile's path.

The missile is launched at point P and is inertially guided during powered flight to the point of burnout C . This guided

flight consists of: A short horizontal path for a distance of r ft, from P to P' ; a pitchup at P' ; an essentially vertical powered flight for a distance c from P' to C . The missile is then in a vertical free-fall flight from C to its apogee, which it is to attain when the satellite pierces plane ρ .

It may be advantageous to aim to make the apogee of the missile occur at a point A , above Q , i.e., at the point $(0, 0, a)$, rather than $(0, 0, 0)$. Then the missile will remain in a given spherical neighborhood of Q for a longer period of time.

The coordinates of the points P , P' , A and C are

$$P': (0, 0, -z')$$

$$P: (-r \cos \theta, -r \sin \theta, -z')$$

$$C: (0, 0, c - z')$$

$$A: (0, 0, a)$$

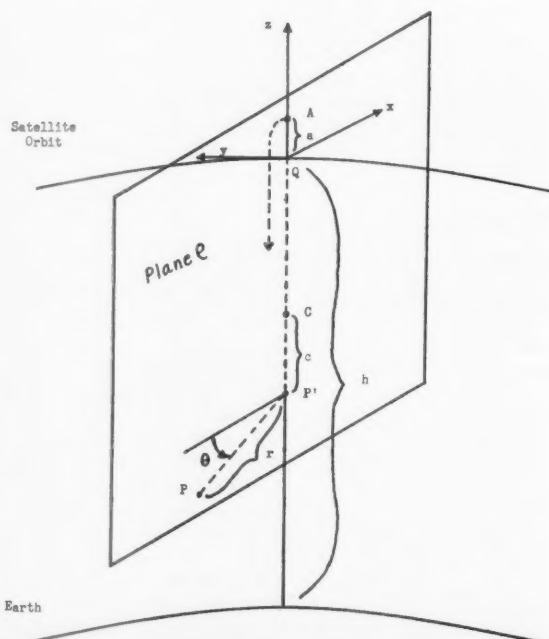


Fig. 1 Geometry of the tactical situation

Received Sept. 29, 1960.

¹ This study was performed by Caywood-Schiller, Associates, for the Weapons Guidance Laboratory, WADC, under Air Force contract AF 33-616-6275.

² Senior Operations Analyst.

³ Manager, Operations Research Dept.

⁴ Senior Operations Analyst.

⁵ Numbers in parentheses indicate References at end of paper.

Sources of Error

In order to reflect mission inaccuracies in the calculated probabilities, a complete listing of aircraft, operational and satellite position parameter errors must be made.

Tracking radars determine satellite position and velocity with some error. In the local rectangular Cartesian coordinate system at Q , the satellite is imagined to be at point $(0, -y_s, 0)$. The errors in the predicted future position of the satellite owing to these tracking errors and owing to orbit perturbations, increase with increasing prediction time. The satellite is predicted to pierce plane ρ at point $Q(0, 0, 0)$, at time t_s sec from the time of position fix. The velocity is estimated to be V_s .

The point of piercing of plane ρ is actually $\Delta x_s, 0, \Delta z_s$,⁶ and the actual velocity is $V_s + \Delta V_s$; the time required to pierce plane ρ is $t_s + \Delta t_s$. The actual velocity and actual altitude are dependent, i.e., ΔV_s and Δz_s are dependent random variables, which follow the laws of orbital motion. Also $\Delta t_s, \Delta y_s$ and ΔV_s are dependent. For circular orbits

$$V_s^2 = \frac{\mu}{R_0 + h}$$

$$\Delta V_s = \frac{-\mu \Delta z_s}{2V_s(R_0 + h)^2}$$

where

R_0 = radius of Earth

Δh = Δz_s , error in orbital altitude

μ = Earth's gravitational constant

But

$$y_s \doteq V_s t_s$$

hence

$$\Delta y_s \doteq V_s \Delta t_s + t_s \Delta V_s$$

Thus also $\Delta y_s, \Delta t_s$ and Δz_s are dependent. In the first-order error analysis which follows, some of these errors are treated as independent because available estimates of their magnitudes are imprecise and do not warrant great sophistication of treatment.

The aircraft is to fly with a heading of θ in a horizontal direction (with a vertical velocity component of zero). The missile is to be launched at the point $P: (-r \cos \theta, -r \sin \theta, -z')$, at t_1 sec before the satellite is scheduled to pierce plane ρ . Actually, the heading of the aircraft is $\theta + \Delta \theta$, and the vertical velocity component is $\Delta V_{A/C}$. Owing to navigation errors the aircraft launches the missile at the point $(-r \cos \theta + \Delta x', -r \sin \theta + \Delta y', -z' + \Delta z')$. Moreover, owing to computer lags, relays sticking, etc., the missile is actually launched $t_1 + \Delta t_1$ sec before the satellite is scheduled to pierce plane ρ .

The missile, when launched, is supposed to travel a horizontal distance of r ft, pitch up, travel in a vertically powered flight a distance of c ft, and then proceed in a free-fall flight to A . The time from launch to burnout is to be t_m sec, after which time the velocity is entirely in the vertical direction and is V_m .⁷ However, the missile actually travels $r + \Delta r$ ft

⁶ The signs of $\Delta x_s, \Delta z_s$ and all subsequent error terms may be either + or -.

⁷ V_m is the velocity calculated to carry the missile from C to its apogee at A , a distance of $z' + a - c$. In general

$$V_m = \sqrt{2\mu \left(\frac{1}{R_0 + h_0} - \frac{1}{R_0 + h_m} \right)}$$

where h_0 and h_m are burnout and maximum altitudes, respectively.

⁸ The error terms $\Delta r, \Delta c, \Delta t_m$ and ΔV_m are generally not independent; however, their relationships are complex. An approximation to the dependence of $\Delta c, \Delta t_m$ and ΔV_m is

$$\Delta c \doteq \left(\frac{V_m \Delta t_m + t_m \Delta V_m}{K} \right)$$

horizontally and $c + \Delta c$ ft vertically; it has a burning time of $t_m + \Delta t_m$ sec, and has a burnout velocity of $V_m + \Delta V_m$.⁸ At burnout the inclination from the vertical of the missile velocity vector is equivalent to $\Delta \alpha_x$ mils in the x -direction and $\Delta \alpha_y$ mils in the y -direction.

Earth's rotation and Earth's oblateness will both have an effect on the trajectory of the missile. However, these two effects are completely predictable (2), and hence are ignored in this study.

Table 1 summarizes in symbol form the estimated and actual values of the parameters just mentioned.

Probability of Interception Formula

Suppose that at time $t = 0$, the satellite actually pierces the plane ρ . It is useful to think of the orbit as locally rectilinear over a flat Earth. Thus for time t , shortly before or after the instant when the satellite actually pierces plane ρ (t positive or negative), the approximate coordinates of the location of the missile and satellite are⁹

Satellite:

$$\begin{aligned} X_s &\doteq \Delta x_s \\ Y_s &\doteq t(V_s + \Delta V_s) \\ Z_s &\doteq \Delta z_s \end{aligned} \quad \dots \dots \dots [1]$$

Missile:

$$\begin{aligned} X_m &\doteq \Delta x' + [(r + \Delta r) \cos(\theta + \Delta \theta) - r \cos \theta] + \\ &\quad [(V_m + \Delta V_m) \sin \Delta \alpha_x][t_f + Kc/V_m + \Delta t_1 + \Delta t_s - t] \\ &\doteq \Delta x' + (\cos \theta) \Delta r - (r \sin \theta) \Delta \theta + \\ &\quad V_m[t_f + Kc/V_m - t] \Delta \alpha_x \\ Y_m &\doteq \Delta y' + [(r + \Delta r) \sin(\theta + \Delta \theta) - r \sin \theta] + \\ &\quad [(V_m + \Delta V_m) \sin \Delta \alpha_y][t_f + Kc/V_m + \Delta t_1 + \Delta t_s - t] \\ &\doteq \Delta y' + (\sin \theta) \Delta r + (r \cos \theta) \Delta \theta + \\ &\quad V_m[t_f + Kc/V_m - t] \Delta \alpha_y \\ Z_m &\doteq a + \Delta z' + \Delta c + t_f \Delta V_m + [t_m + t_f] \Delta V_{A/C} - \\ &\quad (1/2)g(t + \Delta t_s + \Delta t_1)^2 \end{aligned} \quad \dots \dots \dots [2]$$

where g is gravitational acceleration at orbital altitude (neglect differential gravity effects), and where t_f is free-fall time (sometimes approximated by V_m/g). Actually, neglecting oblateness perturbations

$$t_f = \sqrt{\frac{h_m + R_0}{2\mu}} \int_{h_0 + R_0}^{h_m + R_0} \sqrt{\frac{h}{h_m + R_0 - h}} dh$$

where h_0 and h_m are burnout and maximum altitudes, respectively. This is easily integrated by using the substitution $h = x^2$, to give

$$\begin{aligned} t_f &= \sqrt{\frac{2(R_0 + h_m)}{\mu}} \left[\frac{\sqrt{R_0 + h_0}}{2} \sqrt{h_m - h_0} + \right. \\ &\quad \left. \frac{\pi}{4} (R_0 + h_m) - \frac{(R_0 + h_m)}{2} \arcsin \sqrt{\frac{R_0 + h_0}{R_0 + h_m}} \right] \end{aligned}$$

where $1/K$ is the fraction of burnout velocity V_m , which characterizes the average speed during the vertical powered ascent. $1/K$ is available from testing and missile design data. If ΔV_m and Δt_m were considered strongly dependent, and rocket propulsion behavior were found more important than random atmospheric and aerodynamic effects, we could replace Δt_m and Δc by a factor times ΔV_m . For simplicity we treat Δc and ΔV_m as independent.

⁹ Since the error terms are small compared with the quantities themselves, the products of errors have been neglected; also the approximations $\cos \Delta \alpha_x \doteq 1$, and $\sin \Delta \alpha_x \doteq \Delta \alpha_x$ have been used

Equations [2] could obviously include other terms in X_m and Y_m to account for wind bias, error in aircraft horizontal velocity imparted to the missile, etc. These could instead be combined into $\Delta x'$, etc.

Thus, the relative distance components in the x , y and z directions as functions of t are

$$\begin{aligned}\Delta \bar{x} &= \Delta x' - \Delta x_s + (\cos \theta) \Delta r - (r \sin \theta) \Delta \theta + \\ &\quad V_m [t_f + Kc/V_m - t] \Delta \alpha_x \\ \Delta \bar{y} &= \Delta y' - t(V_s + \Delta V_s) + (\sin \theta) \Delta r + (r \cos \theta) \Delta \theta + \\ &\quad V_m [t_f + Kc/V_m - t] \Delta \alpha_y \\ \Delta \bar{z} &= a + \Delta z' - \Delta z_s + \Delta c + t_f \Delta V_m + [t_m + t_f] \Delta V_{A/C} - \\ &\quad (1/2)g(t + \Delta t_s + \Delta t_1)^2 \quad [3]\end{aligned}$$

The time t_c at which the distance between missile and satellite is a minimum, is found by minimizing the function

$$\Delta^2(t) = \Delta \bar{x}^2 + \Delta \bar{y}^2 + \Delta \bar{z}^2 \quad [4]$$

However, this leads to a cubic equation in t_c which is cumbersome to solve.

A good approximation to t_c is obtained by noting that near the predicted intercept point the satellite speed, about 24,000 fps, is very much greater than that of the missile near its apogee. Hence for some small increment of time about t_c , the values of $\Delta \bar{x}$ and $\Delta \bar{z}$ are almost constant while $\Delta \bar{y}$ is varying rapidly. An attractive value of t to use in this range may then be that value for which $\Delta \bar{y} = 0$. Thus $\Delta \bar{x}$ and $\Delta \bar{z}$ will be computed in the plane, parallel to plane ρ , through the point on the satellite orbit at which $Y_m = Y_s$.

Setting $\Delta \bar{y} = Y_m - Y_s = 0$ gives, to first order error terms

$$t_c \doteq \frac{\Delta y'}{V_s} + \frac{(\sin \theta)}{V_s} \Delta r + \frac{(r \cos \theta)}{V_s} \Delta \theta + \left[\frac{V_m}{V_s} t_f + \frac{Kc}{V_s} \right] \Delta \alpha_y \quad [5]$$

Assuming Equation [5] for t_c , then $\Delta \bar{y} = 0$ and $\Delta \bar{x}$ and $\Delta \bar{z}$, to first order error terms, are

$$\begin{aligned}\Delta \bar{x} &\doteq \Delta x' - \Delta x_s + (\cos \theta) \Delta r - \\ &\quad (r \sin \theta) \Delta \theta + [V_m t_f + Kc] \Delta \alpha_x \quad [6]\end{aligned}$$

$$\Delta \bar{z} \doteq a + \Delta z' - \Delta z_s + \Delta c + t_f \Delta V_m + [t_m + t_f] \Delta V_{A/C} -$$

$$(1/2g) \left[\frac{\Delta y'}{V_s} + \frac{(\sin \theta)}{V_s} \Delta r + \frac{(r \cos \theta)}{V_s} \Delta \theta + \left(\frac{V_m}{V_s} t_f + \frac{Kc}{V_s} \right) \Delta \alpha_y + \Delta t_s + \Delta t_1 \right]^2 \quad [7]$$

Assume that $\Delta x'$, Δx_s , Δr , $\Delta \theta$ and $\Delta \alpha_x$, are independent random variables having normal distributions with zero mean values and variances $\sigma^2_{\Delta x'}$, $\sigma^2_{\Delta x_s}$, $\sigma^2_{\Delta r}$, $\sigma^2_{\Delta \theta}$ and $\sigma^2_{\Delta \alpha_x}$, respectively. (These variances may be estimated from design and operational test data.) Then $\Delta \bar{x}$ is normally distributed with mean value and variance given by Equations [8 and 9], respectively

$$E(\Delta \bar{x}) = 0 \quad [8]$$

$$\begin{aligned}\text{Var}(\Delta \bar{x}) &= \sigma^2_{\Delta x'} + \sigma^2_{\Delta x_s} + (\cos^2 \theta) \sigma^2_{\Delta r} + \\ &\quad (r^2 \sin^2 \theta) \sigma^2_{\Delta \theta} + [V_m t_f + Kc]^2 \sigma^2_{\Delta \alpha_x} \quad [9]\end{aligned}$$

$$\text{Var}(\Delta \bar{z}) = \sigma^2_{\Delta a} + \sigma^2_{\Delta z_s} + \sigma^2_{\Delta c} + t_f^2 \sigma^2_{\Delta V_m} + (t_m + t_f)^2 \sigma^2_{\Delta V_{A/C}} + \frac{g^2}{2} \left[\frac{\sigma^2_{\Delta y'}}{V_s^2} + \left(\frac{\sin \theta}{V_s} \right)^2 \sigma^2_{\Delta r} + \right.$$

$$\left. \left(\frac{r \cos \theta}{V_s} \right)^2 \sigma^2_{\Delta \theta} + \left(\frac{V_m t_f}{V_s} + \frac{Kc}{V_s} \right)^2 \sigma^2_{\Delta \alpha_y} + \sigma^2_{\Delta t_s} + \sigma^2_{\Delta t_1} \right] \quad [11]$$

Table 1 List of important parameters and errors

Parameter	Estimated value	Actual value
Position of satellite when piercing plane ρ	(0, 0, 0)	(Δx_s , 0, Δz_s)
Velocity of satellite at plane ρ	V_s	$V_s + \Delta V_s$
Time required for satellite to travel from initial position to plane ρ	t_s	$t_s + \Delta t_s$
Heading of aircraft (w.r.t. plane ρ)	θ	$\theta + \Delta \theta$
Launch point, P	($-r \cos \theta$, $-r \sin \theta$, $-z'$)	($-r \cos \theta + \Delta x'$, $-r \sin \theta + \Delta y'$, $-z' + \Delta z'$)
Launch time of missile (given in seconds before the satellite scheduled to pierce plane ρ)	t_1	$t_1 + \Delta t_1$
Vertical component of aircraft velocity	0	$\Delta V_{A/C}$
Horizontal distance traveled by missile before pitchup	r	$r + \Delta r$
Vertical distance missile travels to burnout after pitchup	c	$c + \Delta c$
Burning time of missile	t_m	$t_m + \Delta t_m$
Velocity of missile at burnout	V_m	$V_m + \Delta V_m$
Missile velocity vector inclination from the vertical in the x -direction (after burnout)	0	$\Delta \alpha_x$
Missile velocity vector inclination from the vertical in the y -direction (after burnout)	0	$\Delta \alpha_y$

The variate $\Delta \bar{z}$ is a difference between a linear combination of (assumed) normal variates and a χ^2 -type variate (square of a normal deviate) with 1 deg of freedom (3). The mean value and variance of $\Delta \bar{z}$ are given by Equations [10 and 11], respectively, if we assume that the random variables in $\Delta \bar{z}$ are independent, and $\Delta z'$, Δz_s , Δc , ΔV_m , $\Delta \alpha_y$ and $\Delta V_{A/C}$ have zero means.

$$\begin{aligned}E(\Delta \bar{z}) &= a - \frac{g}{2V_s^2} [\sigma^2_{\Delta y'} + (\sin^2 \theta) \sigma^2_{\Delta r} + (r^2 \cos^2 \theta) \sigma^2_{\Delta \theta} + \\ &\quad (V_m t_f + Kc)^2 \sigma^2_{\Delta \alpha_y} + V_s^2 \sigma^2_{\Delta t_s} + V_s^2 \sigma^2_{\Delta t_1}] \quad [10]\end{aligned}$$

If $f(\Delta\bar{x}, \Delta\bar{z})$ is the joint density function for $\Delta\bar{x}$ and $\Delta\bar{z}$, then the probability that the missile will pass within a distance R of the satellite is

$$P(R) = \iint_{\{\Delta\bar{x}^2 + \Delta\bar{z}^2 \leq R^2\}} f(\Delta\bar{x}, \Delta\bar{z}) d\Delta\bar{x} d\Delta\bar{z} \quad [12]$$

Simple Closed Form Solution

It is possible to simplify $\Delta\bar{z}$ by replacing the χ^2 variate term with its mean value, i.e., include a fixed bias for $\Delta\bar{z}$ owing to the timing errors. This is a good approximation because the χ^2 term is the square of first-order errors, is divided by V_s^2 , and so should be small compared with the rest of the terms. Then for this new variate $\Delta\bar{Z}$

$$\Delta\bar{Z} = \Delta z' - \Delta z_s + \Delta c + t_f \Delta V_m + (t_m + t_f) \Delta V_{A/C} + E(\Delta\bar{z}) \quad [13]$$

$$E(\Delta\bar{Z}) = E(\Delta\bar{z}) \quad [14]$$

$$\text{Var}(\Delta\bar{Z}) = \sigma^2_{\Delta z'} + \sigma^2_{\Delta z_s} + \sigma^2_{\Delta c} + t_f^2 \sigma^2_{\Delta V_m} + (t_m + t_f)^2 \sigma^2_{\Delta V_{A/C}} \quad [15]$$

As can be seen from Equations [6 and 7], $\Delta\bar{x}$ and $\Delta\bar{z}$ contain some of the same error inputs, e.g., Δr , $\Delta\theta$, etc., and are not statistically independent. However, the simplified error variable $\Delta\bar{Z}$ defined in Equation [13] has replaced these common error inputs with a constant. Independence of $\Delta\bar{x}$ and $\Delta\bar{Z}$ may then be assumed.

At the time that the missile and satellite both have the same y -coordinate ($Y_m = Y_s$), the probability that the missile will be within distance R of the satellite may now be approximated by

$$P(R) = \frac{1}{2\pi\sigma_{\Delta\bar{x}}\sigma_{\Delta\bar{Z}}} \iint_{\{\Delta\bar{x}^2 + \Delta\bar{z}^2 \leq R^2\}} \exp \left\{ -\frac{1}{2} \left[\frac{\Delta\bar{x}^2}{\sigma_{\Delta\bar{x}}^2} + \frac{[\Delta\bar{Z} - E(\Delta\bar{z})]^2}{\sigma_{\Delta\bar{Z}}^2} \right] \right\} d\Delta\bar{x} d\Delta\bar{Z} \quad [16]$$

This integral is the probability mass under an offset elliptic normal surface and over a circle of radius R at the origin. Integrals of this type have been studied at the Rand Corp., at the National Bureau of Standards, and elsewhere. [See (4) for a summary.] Moreover, in a paper presented to the Operations Research Society in May 1960, DiDonato and Jarnagin of the U. S. Naval Weapons Lab. have described a method for the high speed numerical evaluation of the integral of any elliptical Gaussian distribution over an offset ellipse or circle, by a digital computer. There is evidence that such integrals may be approximated by replacing the circular region of integration by a square region of equal area. This square would then have a side equal to $R\sqrt{\pi}$. Thus

$$P(R) = \left[\frac{1}{\sqrt{2\pi}\sigma_{\Delta\bar{x}}} \int_{-R\sqrt{\pi}/2}^{R\sqrt{\pi}/2} e^{-\frac{1}{2} \left(\frac{\Delta\bar{x}}{\sigma_{\Delta\bar{x}}} \right)^2} d\Delta\bar{x} \right] \left[\frac{1}{\sqrt{2\pi}\sigma_{\Delta\bar{Z}}} \int_{-R\sqrt{\pi}/2}^{R\sqrt{\pi}/2} e^{-\frac{1}{2} \left[\frac{\Delta\bar{Z} - E(\Delta\bar{z})}{\sigma_{\Delta\bar{Z}}} \right]^2} d\Delta\bar{Z} \right] \\ = \Phi \left(\frac{R\sqrt{\pi}}{2\sigma_{\Delta\bar{x}}} \right) \Phi \left(\frac{R\sqrt{\pi} - E(\Delta\bar{z})}{2\sigma_{\Delta\bar{Z}}} \right) \quad [17]$$

where

$$\Phi(W) = \frac{1}{\sqrt{2\pi}} \int_{-W}^W e^{-\frac{u^2}{2}} du$$

More Detailed Solution

A more accurate evaluation of the integral in Equation [12] requires the detailed determination of the probability distribution of $\Delta\bar{z}$.

Let u and v (which correspond to normal and χ^2 -type variates respectively) be defined as

$$u = a + \Delta z' - \Delta z_s + \Delta c + t_f \Delta V_m + (t_m + t_f) \Delta V_{A/C} \quad [18]$$

$$v = \frac{\Delta y'}{V_s} + \frac{(\sin \theta)}{V_s} \Delta r + \frac{(r \cos \theta)}{V_s} \Delta \theta +$$

$$\left[\frac{V_m}{V_s} t_f + \frac{Kc}{V_s} \right] \Delta \alpha + \Delta t_s + \Delta t_i \quad [19]$$

Also let

$$\sigma_1^2 = \text{Var}(u) \quad \sigma_2^2 = \text{Var}(v)$$

Then it is readily observed that $\Delta\bar{z} = u - (g/2)v^2$, and by our earlier assumptions u and v are independent.

The distribution function of $\Delta\bar{z}$, denoted by $F_{\Delta\bar{z}}$, is difficult to obtain in mathematically closed form, but this function

may be obtained numerically using the following technique

$$F_{\Delta\bar{z}}(\xi) = P(u - (g/2)v^2 < \xi) = \int_{-\infty}^{\xi} g(\Delta\bar{z}) d\Delta\bar{z} = \sum_{i=-\infty}^{\infty} P(s_i - \Delta s < u < s_i + \Delta s) P[-(g/2)v^2 < \xi - s_i] \quad [20]$$

where $g(\Delta\bar{z})$ is the density function of $\Delta\bar{z}$, and $s_n = \xi$.

Standard statistical procedures may be used to tabulate the two factors in this summation as

$$P(s - \Delta s < u < s + \Delta s) = P \left[\frac{s - \Delta s}{\sigma_1} < \frac{u}{\sigma_1} < \frac{s + \Delta s}{\sigma_1} \right] \quad [21]$$

$$P \left(\frac{gv^2}{2} > s - \xi \right) = P \left[\frac{v^2}{\sigma_2^2} = \chi^2 > \frac{2(s - \xi)}{g\sigma_2^2} \right] \quad [22]$$

These expressions may be found in the standard normal and χ^2 tables, respectively.

Assuming independence, the bivariate probability distribution of $\Delta\bar{x}$ and $\Delta\bar{z}$ may then be obtained by multiplication of their individual distributions, and the numerical evaluation of the integral in Equation [12] may be completed as

$$P(R) = \frac{1}{\sqrt{2\pi}\sigma_{\Delta\bar{x}}} \iint_{\{\Delta\bar{x}^2 + \Delta\bar{z}^2 \leq R^2\}} \exp \left\{ -\frac{\Delta\bar{x}^2}{2\sigma_{\Delta\bar{x}}^2} \right\} g(\Delta\bar{z}) d\Delta\bar{x} d\Delta\bar{z} \quad [23]$$

where $g(\Delta z)$ is the density function of Δz . It may be obtained from $F_{\Delta z}(\xi)$, the cumulative, by a differencing process. For example

$$2\epsilon g(\Delta z) = \sum_{i=-\infty}^n P\left(\frac{s_i - \Delta s}{\sigma_1} < \frac{u}{\sigma_1} < \frac{s_i + \Delta s}{\sigma_1}\right) \left\{ P\left[\chi^2 > 2 \frac{(s_i - \Delta z - \epsilon)}{g\sigma_2^2}\right] - P\left[\chi^2 > 2 \frac{(s_i - \Delta z + \epsilon)}{g\sigma_2^2}\right] \right\} \quad [24]$$

where ϵ is a small quantity.

Numerical Example

Formula [17] will now be used to calculate $P(2)$, the probability of coming within 2 nautical miles of a satellite in a circular orbit at 150 nautical miles. Hypothetical values of the parameters and standard deviations of the parameter errors are given in Tables 2 and 3.

Table 2 Parameters

$V_s = 4.17$ n.m./sec	$V_m = 1.21$ n.m./sec
$\theta = 0$	$z' = 145$ n.m.
$r = 2$ n.m.	$R = 2$ n.m.
$c = 50$ n.m.	$h = 150$ n.m.
$t_m = 30$ sec	$K = 2$
$g = 0.00486$ n.m./sec ²	$t_f = 242.3$ sec

Table 3 Standard deviations of parameter errors

$\sigma_{\Delta x_s} = 1$ n.m.	$\sigma_{\Delta t_s} = 1$ sec
$\sigma_{\Delta s_s} = 1$ n.m.	$\sigma_{\Delta V_{A/C}} = 0.005$ n.m./sec
$\sigma_{\Delta t_s} = 0.5$ sec	$\sigma_{\Delta r} = 0.02$ n.m.
$\sigma_{\Delta \theta} = 0.0005$ radian	$\sigma_{\Delta V_m} = 0.0005$ n.m./sec
$\sigma_{\Delta x'} = 0.5$ n.m.	$\sigma_{\Delta c} = 0.04$ n.m.
$\sigma_{\Delta y'} = 0.5$ n.m.	$\sigma_{\Delta \alpha_s} = 0.0005$ radian
$\sigma_{\Delta s'} = 0.2$ n.m.	$\sigma_{\Delta \alpha_y} = 0.0005$ radian

Thus, from Equation [9]

$$\text{Var}(\Delta x) = \sigma_{\Delta x}^2 = 1.289 \text{ n.m.}^2$$

and from Equation [15]

$$\text{Var}(\Delta Z) = \sigma_{\Delta z}^2 = 1.072 \text{ n.m.}^2$$

From Equation [17] it can be seen that for given values of R , $\sigma_{\Delta x}$ and $\sigma_{\Delta z}$ the maximum value of $P(R)$ occurs when $E(\Delta z) = 0$. In this example, therefore, the value of a that maximizes $P(R)$ is 19 ft.

For this value of a

$$P(2) = 0.80$$

This value of a is found by setting $E(\Delta z) = 0$ in Equation [10]. Actually, V_m , which appears in $E(\Delta z) = 0$, is a function of a , and so a must be determined recursively between $E(\Delta z) = 0$ and the expression for V_m . However, a is generally small because the missile must not go past point Q too fast. Hence, V_m is relatively insensitive to it. We may neglect a in V_m , or estimate it, and then proceed to use V_m in $E(\Delta z) = 0$ to find an improved estimate of a .

References

- 1 Carroll, G., "ALBM-Feather in Our Cap," *The Chicago American*, Oct. 19, 1959.
- 2 Roberson, R. E., "Vertical Ballistic Trajectories Over an Oblate Earth," *JET PROPULSION*, vol. 28, no. 5, May 1958.
- 3 Mood, A., "Introduction to the Theory of Statistics," McGraw-Hill Book Co., Inc., N. Y., 1950.
- 4 Morgenthaler, G. W., "Some Target Coverage Problems," *The Martin Co.*, Denver Colo., Rep. P-59-69, Sept. 1959.

Alignment of an Inertial Autonavigator

L. R. McMURRAY¹

Autonetics Div., North American Aviation, Inc., Downey, Calif.

The advantages of inertial navigation are numerous, and inertial autonavigators provide guidance for many aerospace vehicles. However, before the autonavigator can provide useful information, it must go through a process of alignment. The purpose of this paper is to define the concept of alignment, discuss how it may be accomplished and discuss some of the problems encountered which limit the accuracy of alignment.

The general theory of alignment is given in the first section of the paper; a specific example of an Earth-based, locally level autonavigator is described, to illustrate the theory, in the second section. It is shown how to align this model autonavigator, and in particular it is shown how the alignment of the autonavigator platform can be achieved automatically by a gyrocompassing technique. The effect of several component bias error sources on the accuracy of the example autonavigator's platform alignment is also discussed. In both sections the emphasis is on the mathematical and physical concepts of alignment rather than on the engineering aspects.

Received Jan. 14, 1960.

¹ Senior Research Engineer.

General Theory

AN INERTIAL autonavigator is an instrument which measures the nongravitational inertial acceleration acting on it, and solves a second-order vector differential equation to determine its position vector and its velocity vector (1-4).² As in solving any differential equation, the initial conditions must be known in order to obtain a particular solution. In an inertial autonavigator the initial conditions are the initial physical quantities of position, velocity, and platform orientation of the autonavigator. The process of inserting the initial position and velocity into the autonavigator computer and placing the platform in the desired orientation, is called autonavigator alignment.³

All of the required initial conditions are associated with the basic differential equation that the autonavigator solves. This is a well-known equation of physical mechanics

$$\ddot{\bar{A}}_m + \bar{g} = \ddot{\bar{R}} + \dot{\bar{\omega}} \times \bar{R} + 2\dot{\bar{\omega}} \times \dot{\bar{R}} + \bar{\omega} \times (\bar{\omega} \times \bar{R}) \quad [1]$$

where

- \bar{A}_m = measured inertial acceleration
- \bar{g} = acceleration owing to mass attraction
- \bar{R} = position vector in platform coordinate system S
- $\dot{\bar{R}}$ = velocity vector in S
- $\ddot{\bar{R}}$ = acceleration vector in S
- $\bar{\omega}$ = angular velocity of platform relative to inertial coordinate system.

It is necessary to compute \bar{g} and add it to the left-hand side of Equation [1], as the accelerometers measure only the nongravitational inertial forces acting on the autonavigator. In general \bar{g} is computed from a relationship $\bar{g} = \bar{g}(\bar{R})$.

Consider Equation [1] from a scalar component viewpoint. There are three independent scalar components of \bar{A}_m : $A_{m,1}(t)$, $A_{m,2}(t)$ and $A_{m,3}(t)$. The three components of \bar{g} are completely determined by \bar{R} . On the right-hand side of Equation [1] there are six scalar quantities: $R_1(t)$, $R_2(t)$, $R_3(t)$, $\omega_1(t)$, $\omega_2(t)$ and $\omega_3(t)$. Hence some rule must be prescribed so that only three of the six scalar quantities are independent. Stated more generally, all six scalar quantities must be related to three independent parameters. Once the rule has been prescribed, the remaining three quantities are determined from the solution of Equation [1]. Thus the first of the initial conditions needed for autonavigator alignment are the required initial condition of the three scalar quantities to be determined from Equation [1]. Alignment for this phase is achieved by storing the initial values in the computer memory.

Since a vector has both magnitude and direction, Equation [1] must also be considered from a coordinate system orientation viewpoint. The computer must keep track of the orientation of the platform coordinate system relative to the inertial coordinate system, say by direction cosines. The initial values of the inertial and platform system orientations are the remaining initial values required for the autonavigator alignment.

The two coordinate systems associated with Equation [1] will now be defined in detail and discussed. The first coordinate system is the inertial coordinate system XYZ . This system is defined here as a right-handed rectangular Cartesian coordinate system, with its origin at the center of Earth and its orientation a prescribed arbitrary constant relative to the "fixed" stars. The origin should have been placed at the center of the sun, since the center of Earth is rotating in inertial space, but the center of Earth location of the origin is

much more convenient, and the effect of this error on the autonavigator is small. Hence this error will be neglected.

The second coordinate system is a platform coordinate system xyz . This system is defined here as a right-handed rectangular Cartesian coordinate system with its origin at the center of Earth. The orientation of the system is some convenient prescribed orientation fixed relative to the physical platform; i.e., the xyz system is thought of as being embedded in the physical platform.

Two items should be pointed out concerning the choice of coordinate systems described. First, the choice of the center of Earth as the origin of the coordinate system is motivated by the assumption that the autonavigator is in an Earth bound vehicle. Many computations, e.g., $\bar{g} = \bar{g}(\bar{R})$, are greatly simplified if this choice of origin and vehicle trajectory are used. For other vehicle trajectories, other origins and coordinate systems might be used in addition to the ones described.

It should also be pointed out that additional coordinate systems could be introduced for various reasons, even for an Earth bound vehicle. However they would be in addition to the basic minimum set of coordinate systems (5, 6).

As stated earlier, the orientation of both coordinate systems must be known all of the time. The present orientation consists of the initial orientation plus the change in orientation. In the inertial system there is no change. In the platform coordinate system the change may be prespecified or may be determined as part of the solution of Equation [1]. In either case the change can be determined by monitoring the precessing signals sent to the gyros from the computer. Hence the orientation of the two coordinate systems can be determined if their initial orientations are known.

Also as stated earlier, it is these initial orientations that form the remainder of the initial conditions needed for the alignment. Hence let us examine these initial conditions. The initial orientation of the inertial coordinate system is the arbitrary but prescribed orientation of the system itself. The initial orientation of the platform coordinate system can be determined by one of two methods. These two methods will now be discussed.

The first method is to place the autonavigator in a known environment and monitor certain signals. These signals are used to determine the arbitrary initial conditions and the changes that occurred during the test to give final conditions at the end of the test. These final conditions then become initial conditions for the operational phase immediately following the test. One of the biggest disadvantages of this method is lack of control over certain initial conditions.

The second method is to prescribe the initial platform orientation and then place the platform in that orientation. For certain initial conditions, the platform alignment can be accomplished automatically by optical methods or by inserting servo loops in the mechanization during the alignment period. An example of a servo loop method known as leveling and gyrocompassing is given.

Let us review the operation of autonavigator alignment. Prior to the alignment period at least two coordinate systems are prescribed. Also certain quantities of Equation [1] are prescribed, including the rule giving \bar{g} as a function of \bar{R} . During the alignment period, the initial scalar values of the remaining quantities of the right-hand side of Equation [1] are determined and inserted in the computer memory. Alignment is completed by either determining the orientation of the platform or by placing the platform in a desired orientation.

Example 1

Up to this point the discussion has purposely been very general, so that the basic theoretical aspects could be discussed without being restricted to a special example. At this point, however, it is helpful to introduce an example to illustrate the theory. The autonavigator will first be described,

² Numbers in parentheses indicate References at end of paper.

³ The term "autonavigator alignment" is sometimes used to refer just to the process of placing the platform in the desired orientation, but the broader definition given will be used in this paper.

and then it will be shown that the platform orientation part of the autonavigator alignment can be achieved automatically by servo loops.

The desired platform coordinate system orientation is defined as follows: The $+z$ -axis lies along the radius vector from the center of Earth. The x -axis lies in the plane defined by the z -axis and Earth's spin axis, with the North Pole having a $+x$ value. The y -axis completes the coordinate system. Fig. 1 shows this coordinate system and why the x -axis is referred to as the north pointing axis and the y -axis the west pointing axis.

The physical platform is to be parallel to the xy plane of the desired platform coordinate system. Since the physical platform is tangent to Earth, this system is sometimes called a locally level platform. Two level accelerometers lie along the x and y platform axes, respectively (see Fig. 2). The lack of a z accelerometer will be justified later. The gyros are placed on the platform such that there will be one input axis along each of the platform axes (see Fig. 2).

A spherical homogeneous Earth is assumed so that $\bar{g} = -g\hat{z}$. The trajectory has been restricted to move on the surface of Earth, so that $\bar{R} = R_0\hat{z} \equiv \bar{a}$, and $g_z = g$. Then the only z component of acceleration is g plus centripetal acceleration. Since this can be completely determined by the computer there is no need for a z accelerometer.

Under these restrictions, Equation [1] becomes

$$A_{mz} = -a(\omega_x^2 + \omega_y^2) + g \quad [2]$$

$$A_{mx} = a(\dot{\omega}_y + \omega_x\omega_z) \quad [3]$$

$$A_{my} = a(-\dot{\omega}_x + \omega_y\omega_z) \quad [4]$$

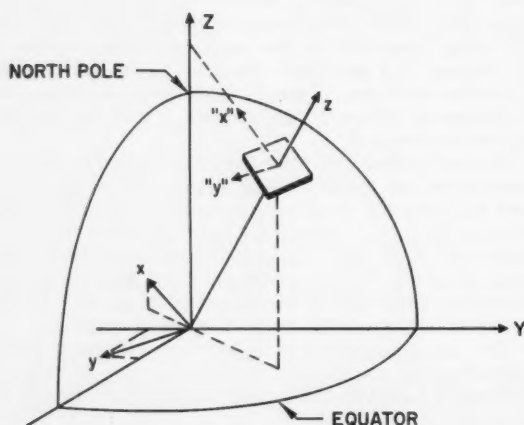


Fig. 1 Example autonavigator platform orientation

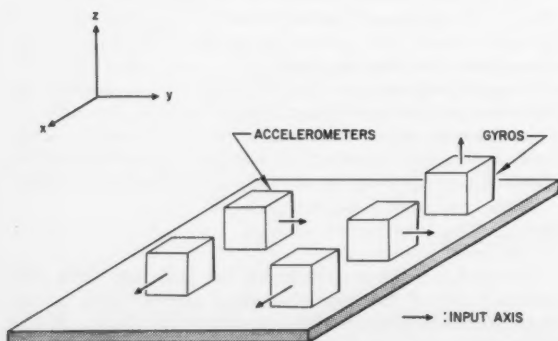


Fig. 2 Example autonavigator component orientation

Since the x -axis is to point north at all times, there is a relationship between ω_x and ω_z

$$\omega_x = \omega_z \tan \lambda \quad [5]$$

where λ is the latitude. Thus for the example autonavigator, Equation [1] has two independent scalar quantities A_{mx} and A_{my} , and two quantities to be determined ω_x and ω_y with the parameter λ . Equation [2] is not mechanized, since there is no need to do so.

Now the scalar components of \bar{R} have been completely specified in the platform coordinate system as $(0, 0, a)$. Hence the orientation of the platform coordinate system is sufficient to determine \bar{R} . Expressing \bar{R} in the Earth-fixed coordinate system and converting to longitude L and latitude λ gives

$$\lambda(t) = \int_0^t \omega_y(\tau) d\tau + \lambda_0 \quad [6]$$

$$L(t) = \int_0^t \omega_x(\tau) \sec \lambda d\tau + L_0 - \Omega t \quad [7]$$

where Ω is Earth rotation rate in inertial space of 15 deg per sidereal hr (or 15.041 deg per hr).

Equations [3 through 6] are necessary to describe the proper platform orientation to be maintained. Equation [7] is needed if longitude information is desired. The velocity vector mechanizations are not given here but can easily be determined.

Equations [3 through 7] are taken to be the autonavigator equations. The initial scalar quantities needed for alignment are ω_{x0} , ω_{y0} and $\omega_{z0} = \omega_{x0} \tan \lambda_0$. Concerning the initial orientation information the two quantities, λ_0 and L_0 are needed and are used instead of direction cosines, as previously suggested in the discussion on general theory. The desired initial orientation of the platform has been prescribed. The initial orientation of the inertial system is immaterial in this example.

Let us now assume that the autonavigator is at rest relative to Earth. Then $\omega_{x0} = \Omega \cos \lambda_0$, $\omega_{y0} = 0$ and $\omega_{z0} = \Omega \sin \lambda_0$.

Since the platform orientation has been explicitly prescribed, it is necessary to use the second method of orientating the platform; i.e., the platform is placed in orientation locally level with the x -axis pointing north. Placing the platform in the desired orientation is accomplished in two steps. The platform is first aligned "by eye" near the desired orientation. The second step depends on the equipment available. Mounting mirrors on the platform plus an external autocollimator and an orientation reference is one procedure. Another procedure is possible using the components of the autonavigator to automatically align the platform. The latter is denoted as leveling and gyrocompassing and will now be discussed.

Let us consider what would happen to the accelerometer outputs if the platform is not aligned exactly as desired. If the platform is not exactly level, then A_{mx} is not equal to $a\omega_{x0}\omega_{z0}$ and A_{my} is not equal to 0 as desired, since the accelerometers will detect a component of the autonavigator support vertical thrust. If there is an azimuth misalignment, say the x -axis is pointing ϕ_x radians (a small angle) to the west of north, then the x gyro would have to be precessed at the rate

$$\Omega \cos \lambda_0 \cos \phi_x \approx \Omega \cos \lambda_0$$

and the y gyro would have to be precessed at the rate

$$-\Omega \cos \lambda_0 \sin \phi_x \approx -\phi_x \Omega \cos \lambda_0$$

to maintain the platform level. Since the gyros are not precessed at this rate, the platform will precess relative to the local level, mainly about the y -axis, at a rate proportional to the azimuth misalignment. This precession will be detected, mainly by the x accelerometer, as a nonlevel condition.

Thus one would suppose that the accelerometer outputs can be used to servo the platform to the desired orientation.

This supposition is correct as will be shown. Let ϕ_x , ϕ_y and ϕ_z be the positive angular rotations of the platform from the desired orientation. Then using small angle approximations, the accelerations detected by the x and y accelerometers resulting from misorientation are $-g\phi_y$ and $+g\phi_x$, respectively. Again using small angle approximations, the drift rate of the platform about the y -axis induced by azimuth misorientation is $\phi_x\Omega \cos \lambda_0$.

Consider the interconnected accelerometers and gyros as shown in Fig. 3. The solid lines are electrical connections, and the dashed lines are connections arising from the physics of the situation. The change in gyro orientation is the integral of the precessing signal, and hence gyros are shown as integrators. The K_1 and K_4 gains are for velocity servo loops. The K_2 and K_5 gains are to decrease the effective radius of Earth and quicken the response of the system. The K_3 gain is used to correct misorientation in azimuth. The drift rates induced by a nonlevel platform do not affect the final conclusion to be given, and hence they have been omitted to simplify the figure.

Let us determine the time response of ϕ_x , ϕ_y and ϕ_z owing to an initial misorientation ϕ_{x0} , ϕ_{y0} and ϕ_{z0} , which results from the coarse orientation of the platform. This response can be determined from Laplace transform theory or from differential equations theory, and it can easily be shown that all three angles approach zero as desired for an appropriate set of gain constants. For our purposes the following simple argument can be used. Assume that appropriate K_i have been chosen so that the system is a stable one. Assume further that the angles approach some finite constant value, called steady-state values and denoted by a double s subscript. Then the integrators of Fig. 3 have a "net" input of zero. Hence

$$0 = a\Delta\omega_y(K_3/a) \quad \therefore \dot{\phi}_x = 0$$

$$0 = +a\Delta\omega_z[(1 + K_2)/a] \quad \therefore \dot{\phi}_z = 0$$

$$0 = a\Delta\omega_y[(1 + K_2)/a] + \phi_{xss}\Omega \cos \lambda_0 \quad \therefore \dot{\phi}_y = 0$$

This implies

$$0 = -g\phi_{yss} \quad \therefore \Delta\omega_y = 0$$

$$0 = g\phi_{xss} \quad \therefore \Delta\omega_z = 0$$

$$0 = \phi_{xss}\Omega \cos \lambda_0 \quad \therefore \Delta\omega_y = 0$$

Therefore $\phi_{xss} = \phi_{yss} = \phi_{zss} = 0$, and it is concluded that a coarse orientation "by eye" followed by the servo loop shown in Fig. 3 will, if given sufficient time, automatically align the platform of the example autonavigator.

This servo procedure of aligning an autonavigator platform is called leveling and gyrocompassing. The leveling term naturally refers to ϕ_x and ϕ_y going to zero. The term Foucault gyrocompass was used for a gyro so constrained that it could be used as a compass. Owing to similarity of the Foucault gyrocompass and the loop described, the term gyrocompassing has been extended to this method of aligning the platform.

Example 2

The autonavigator described assumed perfect components. In reality the components do not function perfectly, and the result is deterioration of accuracy in the alignment; see (1-3). Let us consider the effect of bias errors in the components on the platform alignment.

Let the bias errors in the x and y accelerometers be denoted by ∇_x and ∇_y , respectively, and let the bias drift rates of the x , y and z gyros be ϵ_x , ϵ_y and ϵ_z , respectively. Let us use the same basic servo loop of the preceding example, only now the nonlevel induced drift rate $-\phi_x\Omega \sin \lambda_0$ about the y -axis is important and has been included. The exact servo loop with the bias error sources included is shown in Fig. 4.

Again one can use Laplace transform theory to obtain the transient response of the platform (see Appendix); however,

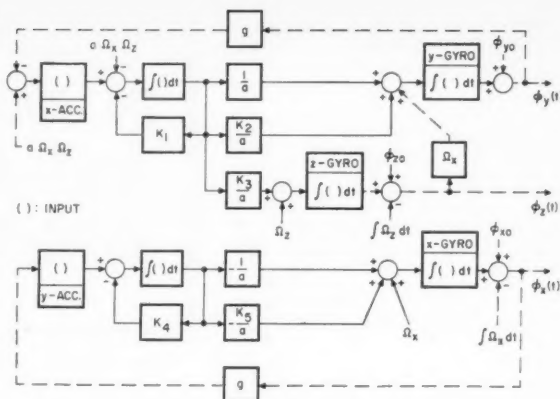


Fig. 3 Level and gyrocompass alignment of platform for no error sources

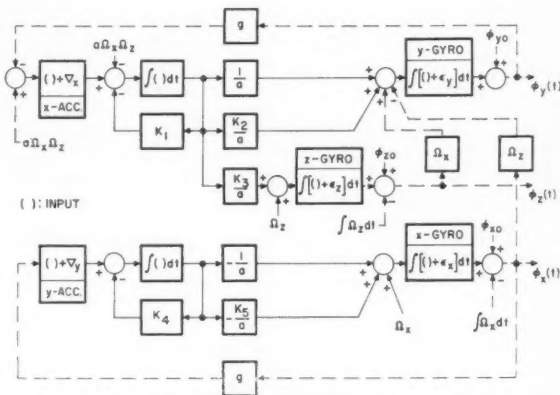


Fig. 4 Level and gyrocompass alignment of platform with bias error sources

let us proceed as before. It is assumed that the misorientation angles ϕ_x , ϕ_y and ϕ_z have reached a finite constant value. Then

$$0 = K_3\Delta\omega_{yss} + \epsilon_z$$

$$0 = +(1 + K_5)\Delta\omega_{zss} + \epsilon_x$$

$$0 = \phi_{xss}\Omega \cos \lambda_0 + (1 + K_2)\Delta\omega_{yss} + \epsilon_y - \phi_{xss}\Omega \sin \lambda_0$$

$$0 = -g\phi_{yss} + \nabla_x - aK_1\Delta\omega_{yss}$$

$$0 = g\phi_{xss} + \nabla_y - aK_4\Delta\omega_{zss}$$

hence

$$\Delta\omega_{yss} = -\epsilon_z/K_3$$

$$\Delta\omega_{zss} = -\epsilon_x/(1 + K_5)$$

$$\phi_{xss} = -\nabla_y/g + K_4/(1 + K_5) \cdot a/g \cdot \epsilon_x$$

$$\phi_{yss} = +\nabla_x/g + K_1/K_3 \cdot a/g \cdot \epsilon_z$$

$$\phi_{zss} = \frac{-\epsilon_y}{\Omega \cos \lambda_0} + \frac{1 + K_2}{K_3} \cdot \frac{\epsilon_x}{\Omega \cos \lambda_0} +$$

$$\frac{aK_4 \tan \lambda_0}{g(1 + K_5)} \epsilon_z - \frac{\tan \lambda_0}{g} \nabla_y$$

If these were the only error sources, then the values of $\Delta\omega_{zss}$ and $\Delta\omega_{yss}$ could be observed and compensations made to eliminate ϵ_z and ϵ_x as error sources. However, since the effect of ϵ_z and ϵ_x on ϕ_i is very small, no compensation will be made. To obtain a feeling for the magnitude of the misorien-

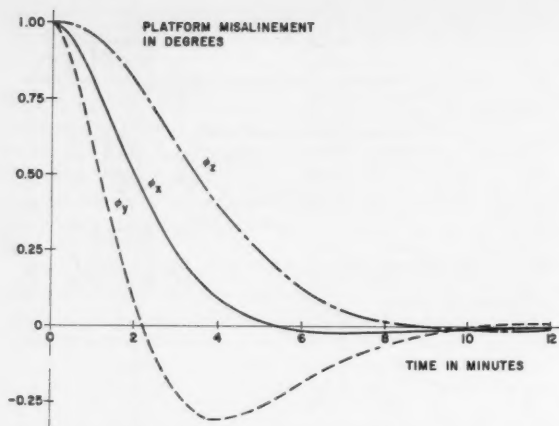


Fig. 5 Transient response of platform

tation angles relative to the bias error sources, let

$$\begin{aligned} \lambda_0 &= 45 \text{ deg} & K_4 &= 0.02 \text{ sec}^{-1} \\ K_1 &= 0.03 \text{ sec}^{-1} & K_5 &= 100 \\ K_2 &= 232 & \nabla_x &= \nabla_y = 0.0001g \\ K_3 &= 20,000 & \epsilon_x &= \epsilon_y = \epsilon_z = 0.001 \text{ deg/hr} \end{aligned}$$

The K values were chosen to give the system a time constant of about 100 sec. The initial transient response dies out in about 12 min to leave the following steady-state platform mis-orientation angles

$$\begin{aligned} \phi_{xss} &\doteq -\nabla_y/g \doteq -20 \text{ sec} \\ \phi_{yss} &\doteq \nabla_x/g \doteq 20 \text{ sec} \\ \phi_{zss} &\doteq -\epsilon_y/\Omega \cos \lambda_0 - (\tan \lambda_0/g)\nabla_y \doteq -39 \text{ sec} \end{aligned}$$

It should be noted, however, that for the gyrocompassing technique the value of ϕ_{zss} is inversely proportional to $\Omega \cos \lambda$. For $\lambda = 45 \text{ deg}$ as in the foregoing computation, the value of ϕ_{zss} is small, but as λ approaches 90 deg , ϕ_{zss} approaches infinity. Thus the gyrocompassing technique cannot be used near the polar regions owing to the presence of noise, e.g., bias errors in the system.

We conclude by reviewing the alignment procedure of the autonavigator examples. First the orientations of both co-

ordinate systems were prescribed. The quantities to be solved for by the computer were the platform rotation rate in inertial space $\dot{\omega}$, and position in longitude L and latitude λ . The initial scalar quantities ω_{x0} and ω_{y0} were determined from the initial latitude λ_0 . Two additional initial conditions which were needed were the scalar quantity ω_{z0} , which in this case was zero, and the initial longitude L_0 . The remaining part of the alignment, that of placing the platform in its proper orientation, was accomplished in two steps. The first step was a coarse orientation "by eye," and the second and final step was automatic orientation using leveling and gyrocompassing servo loops. For a perfect autonavigator, the steady-state orientation of the platform was the exact desired orientation. For an autonavigator with bias errors in the accelerometers and gyro drift rates, the steady-state orientation of the platform was a slight offset from the desired orientation.

Appendix

The transient response of the platform to the leveling and gyrocompassing servo loops is of importance, as well as the steady-state response. The transient response of the platform misalignment angles for the alignment shown in Fig. 4 have been calculated and are shown in Fig. 5. It was assumed that the misalignment angles after the coarse alignment were 1 deg about each axis, and that the gain constants and instrument bias errors had the values specified earlier. The instrument errors do affect the transient response, but only to the extent of a few tens of seconds of arc. Thus it is only near the steady-state condition that they have an appreciable percentage effect on the response. Near the steady-state condition the instrument errors become the predominant terms, and the misalignment angles approach the values given in the text.

References

- 1 Duncan, D. B., "Analysis of an Inertial Guidance System," *JET PROPULSION*, vol. 28, no. 2, Feb. 1958, p. 111.
- 2 Klass, P. J., "Inertial Guidance," *Aviation Wk.*, special report, vol. 64, nos. 1-4, 1956.
- 3 O'Donnell, C. F., "Inertial Navigation," *J. Franklin Inst.*, vol. 266, no. 4, Oct., 1958, p. 257, and vol. 266, no. 5, Nov. 1958, p. 373.
- 4 Slater, J. M. and Duncan, D. B., "Inertial Navigation," *Aeron. Engng. Rev.*, vol. 15, no. 1, Jan. 1956, p. 49.
- 5 Slater, J. M., "Choice of Coordinate Systems in Inertial Navigation," *Navigation*, vol. 5, no. 2, June 1956, p. 58.
- 6 Wrigley, W., Woodbury, R. B. and Hovorkal J., "Inertial Guidance," *Aeron. Engng. Rev.*, vol. 16, no. 10, Oct., 1957, p. 59.

Effect of Geometrical Libration on the Damped Motion of an Earth Satellite

L. N. ROWELL¹ and
M. C. SMITH²

The Rand Corp.
Santa Monica, Calif.

Satellites stabilized by the gravitational gradient are sensitive to disturbing torques arising from many sources. One example is the geometrical libration occurring whenever the orbit is not circular. The motion due to this source can be reduced about the pitch axis by a reaction wheel whose speed is controlled by either the pitch angular rate measured by a rate gyroscope or by the pitch angle measured by a horizon scanner. In each of these possible mechanizations there results an error in pitch which is a function of eccentricity of the orbit. Another possible mechanization described here makes use of a combination of rate gyro and horizon scanner to control the reaction wheel speed. In this case the error in pitch is a function of system tuning and not the accuracy at which the orbit has been achieved.

ONE APPROACH to closed loop stabilization of satellite vehicles makes use of reaction wheels and Earth's gravitational gradient (1 through 7).³ The gravitational gradient system is inherently stable but is sensitive to disturbing torques. The present discussion is limited to the effect of geometrical libration on the damped motion of a satellite about its pitch axis.

In the stabilizing systems discussed here, only angular motion about the pitch axis of the satellite is considered. In the first example the angular rate about the pitch axis, which includes the rotation of the satellite about its own pitch axes plus the orbital motion of the vehicle, is measured by a rate gyro. The control voltage on the reaction wheel motor is made proportional to the measured angular rate. In the second example the displacement from the vertical is measured by means of a horizon scanner. A signal proportional to this displacement activates the reaction wheel. In the third example the sensors are combined to give a torque wheel signal which combines the information obtained from the gyroscope and the horizon scanner.

In the systems discussed, stabilization about the other two axes, roll and yaw, is obtained by a similar system, i.e., by a gyro aligned with its sensitive axis in the roll direction, and a reaction wheel with its spin axis aligned in the yaw direction. The signal from the roll gyro is the input to the yaw reaction wheel. Because of coupling between the angular momentum of the yaw wheel and the orbital motion, damping in roll results.

Equations of Motion

Both the equations of motion about the center of mass and the equations of orbital motion must be considered.

The vector differential equation of orbital motion of a point mass moving under only the influence of an inverse square law central force field is

$$\frac{d^2 \vec{r}}{dt^2} = -\frac{\mu \vec{r}}{r^3} \quad [1]$$

The solutions of this equation yield

$$r = \frac{a(1 - e^2)}{1 + e \cos v} \quad [2]$$

and

$$r^2 \dot{v} = h = \text{constant} \quad [3]$$

where

- r = distance of satellite from center of force, function of semimajor axis of orbit
- a = semimajor axis of orbit
- e = eccentricity of orbit
- v = true anomaly of vehicle in its orbit
- $r^2 \dot{v}$ = angular momentum,

The total angular acceleration of the vehicle about its pitch axis is found to be (1)

$$I_y(\ddot{\alpha} + \ddot{v}) + \frac{3\mu}{r^3} (I_x - I_z) \cos \alpha \sin \alpha + T_D = 0 \quad [4]$$

where

- α = angular displacement about pitch axis
- I_x, I_y, I_z = principal moments of inertia about roll, pitch and yaw axis, respectively
- μ = proportional to gravitational attraction of central force field
- T_D = internally or externally generated torques

It is necessary to replace \ddot{v} in Equation [4] by an expression involving time. This is most easily accomplished by first expressing \ddot{v} as a function of r , \dot{r} and \dot{v} as follows: The time derivative of Equation [3] gives

$$\ddot{v} = -\frac{2\dot{r}\dot{v}}{r^3} = -\frac{2\dot{r}\dot{v}}{r} \quad [5]$$

By expressing r , \dot{r} and \dot{v} in terms of the orbital elements a and e and the eccentric anomaly E , Equation [5] becomes (see Appendix)

$$\ddot{v} = -2en^2 \sqrt{1 - e^2} \frac{\sin E}{(1 - e \cos E)^4} \quad [6]$$

Received Oct. 13, 1960.

¹ Mathematician, Engineering Div.

² Physical Scientist, Engineering Div.

³ Numbers in parentheses indicate References at end of paper.

where n is the mean angular rate of the satellite in its orbit.

Proceeding under the assumption that e is small (approximately 0.01 or less), terms involving e^2 are neglected; then

$$\ddot{\theta} \approx -2en^2 \sin E(1 + 4e \cos E) \quad [7]$$

Using Equation [7], Equation [4] may now be written

$$I_s \ddot{\alpha} + 3n^2(I_s - I_x)(1 + 3e \cos E) \sin \alpha \cos \alpha + T_D \approx 2I_y en^2 \sin E(1 + 4e \cos E) \quad [8]$$

Assuming α to be small, Equation [8] becomes

$$I_s \ddot{\alpha} + 3n^2(I_s - I_x)\alpha + T_D \approx 2I_y en^2 \sin E \quad [9]$$

if e^2 terms are neglected.

By using Kepler's equation and again neglecting e^2 terms, Equation [9] may be written

$$I_s \ddot{\alpha} + 3n^2(I_s - I_x)\alpha + T_D \approx 2I_y en^2 \sin nt \quad [10]$$

The Laplace transform of Equation [10], assuming zero initial conditions, is

$$[I_s s^2 + 3n^2(I_s - I_x)]\alpha(s) + T_D(s) = 2en^2 I_y \frac{n}{s^2 + n^2} \quad [11]$$

Rate Gyro Pitch Damping

The damping torque obtained from the pitch gyro reaction wheel system is of the form

$$T_D(s) = K_G K_W K \frac{s}{s + 1/T} (s\alpha + s\dot{\alpha}) \quad [12]$$

where $K/(sT + 1)$ is the performance function, and K_G and K_W are, respectively, the gains of the gyro and the reaction wheel.

Ideally the orbital rate term should be removed, since it only serves to disturb the system. Mean orbital rate is the only quantity which is easily available and if added will remove most of the orbital rate term. Hence Equation [12] becomes

$$T_D(s) = K_G K_W K \frac{s(s\alpha + s\dot{\alpha} - n/s)}{s + 1/T} \quad [13]$$

where n is the mean angular rate in the orbit.

By combining Equations [36 and 38] and neglecting e^2 terms

$$\dot{\alpha} \approx n(1 + 2e \cos E) \quad [14]$$

Again using Kepler's equation, neglecting e^2 terms and assuming zero initial conditions, the Laplace transform of Equation is

$$s\dot{\alpha} - \frac{n}{s} = 2en \left(\frac{s}{s^2 + n^2} \right) \quad [15]$$

The final form of Equation [13] is now

$$T_D(s) = K_G K_W K \frac{s}{s + 1/T} \left[s\alpha + 2en \left(\frac{s}{s^2 + n^2} \right) \right] \quad [16]$$

Inserting Equation [16] into Equation [11] and rearranging terms gives

$$\alpha(s) = -2enk \times$$

$$\frac{s^2 - (n^2/k)s - n^2/kT}{(s^2 + n^2)[s^2 + (k + 1/T)s^2 + 3n^2k_1s + 3n^2k_1/T]} \quad [17]$$

where

$$k = \frac{K_G K_W K}{I_y} \quad k_1 = \frac{I_x - I_s}{I_y}$$

The parameters of Equation [17] were assigned the following typical numerical values

$$\begin{aligned} k &= 6 \text{ per hr} \\ k_1 &= 0.78 \\ T &= \frac{1}{2} \text{ hr} \\ n &= 4 \text{ radians per hr} \\ I_y &= 5000 \text{ slug ft}^2 \end{aligned}$$

By introducing these numerical values into Equation [17] and then factoring the cubic term, the following equation results

$$\alpha(s) = -48e \frac{s^2 - 2.667s - 8}{(s + 5.881)(s^2 + 16)[(s + 1.56)^2 + 16.657]} \quad [18]$$

The inverse Laplace transform of $\alpha(s)$ gives

$$\alpha(t) = e[-3.456 \sin(4t + 1.634) - 1.135e^{-5.881t} - 4.560e^{-1.56t} \sin(4.081t - 1.548)] \quad [19]$$

where e is the eccentricity of the orbit. The angle α will be in radians for t in hr.

Horizon Scanner Pitch Damping

If a horizon scanner is used as the vertical references about the pitch axis, some advantages are gained. This instrument is sensitive to the displacement of the vehicle from the vertical and not to the total angular velocity in inertial space. The output of the horizon scanner is connected to the magnetic field of d-c electric motor (pitch reaction wheel). Assuming that there are no d-c components in the horizon scanner output, the system equation is

$$\left[s^2 + ks + \frac{3(I_s - I_x)}{I_y} n^2 \right] \alpha(s) = \frac{2en^2}{s^2 + n^2} \quad [20]$$

Introducing the same system parameters as before, and taking the inverse Laplace transform of Equation [20] gives

$$\alpha(t) = e[0.99 \sin(4t - 0.841) + 0.74e^{-3t} \sin(5.3t + 1.678)] \quad [21]$$

It is evident from a comparison of Equations [19 and 21] that the amplitude of the undamped oscillatory term owing to the geometrical libration is 0.3 as large using horizon scanner sensor as using the gyro sensor. Also, it is evident that to get an amplitude of displacement from the vertical of 0.1 deg, the accuracy of the determination of the vertical by the horizon scanner, an orbit of eccentricity $e = 0.0005$ is necessary if the gyro sensor is used, and $e = 0.002$ if a horizon scanner sensor is used.

Horizon Scanner—Gyroscopic Pitch Damping

According to Equations [19 and 21], the systems considered have the common difficulty that there is an undamped oscillation about the pitch axis directly proportional to the eccentricity of the orbit. This oscillation is not a serious fault as long as the eccentricity of the orbit can be established to within acceptable limits. By removing the dependence of the satellite vertical indication on the eccentricity of the orbit, less severe accuracy requirements would be demanded of the ascent guidance of the rocket. A torque wheel signal which is a combination of the information obtained from the gyroscope and the horizon scanner can remove the dependence of the vertical indication on the eccentricity of the orbit.

In Fig. 1 is the functional block diagram of the pitch damping system in which information is obtained from both the gyroscope and horizon scanner. The torque added by the

reaction wheel to the torque balance of the satellite is seen from Fig. 1 to be

$$T_D(s) = K_W s \left[-K_G \left(s\alpha + sv + \frac{U_G}{s} \right) + K_{HS} \left(s + \frac{1}{T_L} \right) \left(\alpha + \frac{U_{HS}}{s} \right) \right] \quad [22]$$

where K_W , K_G and K_{HS} are the gains of the reaction wheel, the sensing gyro and the horizon scanner, respectively. The constants U_G and U_{HS} are the uncertainties in the gyro drift rate and horizon scanner offset, respectively. For small angle approximations and small eccentricities, the Laplace transform of Equation [4], neglecting initial conditions, can be written as

$$I_y s^2 (\alpha + v) + 3n^2 (I_z - I_x) \alpha + T_D(s) = 0 \quad [23]$$

Equations [22 and 23] are combined to give

$$[I_y + K_W (K_{HS} - K_G)] s^2 \alpha + [I_y - K_W K_G] s^2 v + \left[\frac{K_W K_{HS}}{T_L} s + 3n^2 (I_z - I_x) \right] \alpha + K_W K_{HS} \left(s + \frac{1}{T_L} \right) U_{HS} - K_W K_{HS} U_G = 0 \quad [24]$$

Then by choosing the gains K_W and K_G so that $K_W K_G$ is equal to I_y , the contribution of the true anomaly would disappear from Equation [24]. The gains of the horizon scanner and gyro can be adjusted, so as to change the frequency of oscillation of the satellite, but for the present discussion, assume that they are equal. Then Equation [24] can be written as

$$\alpha(s) = \frac{\Delta s^2 v + U_G - (s + 1/T_L) U_{HS}}{s^2 + \frac{s}{T_L} + 3n^2 \left(\frac{I_z - I_x}{I_y} \right)} \quad [25]$$

where

$$\Delta = - \frac{I_y - K_W K_G}{I_y}$$

is a tuning error and the initial conditions have been omitted.

Since the uncertainty terms of Equation [24] are damped in the time domain, only the effect of a tuning error need be considered. Thus, Equations [15 and 25] are combined to give

$$\alpha(s) = \frac{\Delta \left(n + 2en \frac{s^2}{s^2 + n^2} \right)}{s^2 + \frac{s}{T_L} + 3n^2 \left(\frac{I_z - I_x}{I_y} \right)} \quad [26]$$

For critical damping $1/T_L = 12.24$ per hr. The displacement in the vertical indication arising from this source is periodic and is found to be

$$\alpha(t) = \Delta [-0.599e \sin(4t - 1.158) + (4 + 5.604e)t e^{-6.12t} - 0.549e e^{-6.12t}] \quad [27]$$

For a 0.1% error in tuning and an e of 0.001

$$\alpha(t) = (-0.599 \times 10^{-6}) \sin(4t - 1.158) + (4.006 \times 10^{-3}) t e^{-6.12t} - (0.549 \times 10^{-6}) e^{-6.12t} \quad [28]$$

and the amplitude of the oscillation is approximately 0.12 sec.

Reaction Wheel Speed

The wheel speed is obtained from Equation [22], where

$$T_D(s) = sH(s) \quad [29]$$

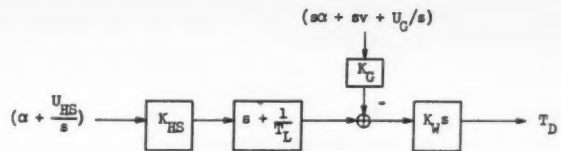


Fig. 1 Pitch damping system

The quantity $H(s)$ is the angular momentum of the wheel. Consider only the input to the wheel from the orbital motion. This causes the angular momentum of the wheel to be

$$H(s) = -K_W K_G \left(\frac{n}{s} + 2en \frac{s}{s^2 + n^2} \right) \quad [30]$$

or taking the inverse Laplace transform and dividing by I_W

$$\omega(t) = \frac{-K_W K_G}{I_W} (n + 2en \cos nt) \quad [31]$$

For I_W equal to 0.05 slug ft², the first term on the left gives

$$\omega(\max) = -1060 \text{ rpm} \quad [32]$$

The wheel speeds arising from the second term of Equation [31] and the other terms of Equation [29] are all smaller than Equation [32]; hence, a wheel of 0.05 slug ft² moment of inertia should be satisfactory.

Conclusions

From a comparison of Equations [19, 21 and 28], it is evident that a combination of the sensing devices will effectively remove the forced error in pitch which is caused by the geometrical libration. This is achieved by accurate tuning and not by depending on orbits having extremely small eccentricities, as is the case when the horizon sensor or gyro sensor is used separately.

Appendix

The angular momentum of a body moving under only the influence of an inverse square law central force field is

$$r^2 \dot{\psi} = \sqrt{\mu a (1 - e^2)} = h \quad [33]$$

where

r = distance of body from center of force
 v = true anomaly of body in its orbit (8)

From Equation [33], the angular acceleration of the body in its orbit is

$$\ddot{v} = -2\dot{r}\dot{\psi}/r \quad [34]$$

This angular acceleration may be expressed in terms of a , e and the eccentric anomaly E by using the equations of orbital motion.

According to Kepler's third law

$$n = \sqrt{\mu/a^3} \quad [35]$$

and Equation [33] becomes

$$\dot{v} = \frac{na^2}{r^2} \sqrt{1 - e^2} \quad [36]$$

where n is the mean angular rate of the body in its orbit.

Using Equation [36] and the time derivative of Equation [2], Equation [34] becomes

$$\ddot{v} = -\frac{2}{r^3} n^2 a^3 e \sin v \quad [37]$$

Now, if r and $\sin v$ are replaced according to

$$r = a(1 - e \cos E) \quad [38]$$

$$\sin v = \frac{\sqrt{1 - e^2} \sin E}{1 + e \cos E} \quad [39]$$

respectively, then

$$\ddot{v} = -2en^2 \sqrt{1 - e^2} \frac{\sin E}{(1 - e \cos E)^4} \quad [40]$$

References

- 1 Roberson, R. E., "Attitude Control of Satellites and Space Vehicles," "Advances in Space Science," vol. II, Academic Press, Inc., N. Y., 1960, p. 351.
- 2 Stocker, T. A. J. and Vachino, R. F., "The Two-Dimensional Librations of a Dumbbell-Shaped Satellite in a Uniform Gravitational Field," American Astronautical Society, Proc. Western Regional Meeting, Palo Alto, Calif., Aug. 1958.
- 3 Klemperer, W. B. and Baker, R. M. L., Jr., "Satellite Librations," *Astronautica Acta*, vol. 3, 1957, p. 16.
- 4 Davis, W. R., "Determination of a Unique Altitude for an Earth Satellite," American Astronautical Society, Proc. IV Annual Meeting, N. Y., Jan. 1958.
- 5 Schindler, G. M., "On Satellite Librations," *ARS JOURNAL*, vol. 29, no. 5, May 1959, p. 368.
- 6 Haussermann, W., "An Attitude Control System for Space Vehicles," *ARS JOURNAL*, vol. 29, no. 3, March 1959, p. 203.
- 7 Smart, W. M., "Celestial Mechanics," Longman's Green and Co., N. Y., 1953.
- 8 Moulton, F. R., "Differential Equations," Dover Publications, Inc., N. Y., 1958.

Variables That Are Determinate for Any Orbit¹

ROBERT R. NEWTON²

The Johns Hopkins University
Silver Spring, Md.

The rectangular components of the angular momentum vector and of the "eccentricity vector" form a set of six variables that specify the geometry of any orbit. Only five of these are independent for a given orbit, but there is no particular one that can be eliminated for all orbits, without indeterminacy. The time derivatives of these variables, and important transformations involving them, are presented, using both longitude and argument of the latitude as the additional variable needed. Finally, a method of handling phase of the motion is suggested.

IT IS well known that the familiar set of orbit elements, namely, a , e , i , ω , Ω and σ , become indeterminate for certain values. This indeterminacy is reflected in the fact that the equations for the time derivatives of the elements (1)³ contain singularities at $e = 0$ and 1, and at $i = 0$.

In order to remove the singularity at $e = 0$, it is customary to replace the elements e and ω by⁴ $e \sin \omega$ and $e \cos \omega$, using the argument of the latitude as the angle variable and the time of a nodal crossing to fix the phase of the motion in the orbit.

When e is not too near zero, one can replace ω by the longitude of perigee, and use longitude as the angle variable (2). However, when e is also small, this fails.

The coordinate system described in this paper originated in the desire to find a system to handle the case of small eccentricity and small inclination. It turns out that the system is capable of handling any orbit without indeterminacy, even when making the transition from bound to unbound orbits. That is, the singularity at $e = 1$ is also avoided. The cost

of avoiding all singularities turns out to be the use of a redundant variable.

In discussing the variables, it is convenient to divide them into two classes. The first class, which we shall call "geometric variables," fixes the orbit. In the familiar set, this class consists of a , e , i , ω and Ω . The second class fixes the phase of the motion in the orbit. In the familiar set, this consists of a single element σ , which we shall call the phase variable.

Geometric Variables

For the set of geometric variables, we use the rectangular components of the angular momentum vector⁵ \mathbf{P} and of the "eccentricity vector" \mathbf{e} . By \mathbf{e} , we mean a vector whose magnitude is e , and which is directed from the origin toward the position of perigee. When e is small, the direction of \mathbf{e} is not well defined, but its rectangular components nevertheless remain well defined, so that the variables used are well defined under all circumstances.

\mathbf{P} and \mathbf{e} have altogether six components. Of these, only five are independent, because of the relation

$$\mathbf{P} \cdot \mathbf{e} \equiv 0 \quad [1]$$

⁵ A boldface symbol is used to denote a vector, and the corresponding italic symbol to denote the magnitude of the vector.

Received Nov. 9, 1960.

¹ This work was supported by the Department of the Navy, Bureau of Naval Weapons, under Contract NOrd 7386.

² Supervisor, Space Research and Analysis Group, Applied Physics Laboratory. Member ARS.

³ Numbers in parentheses indicate References at end of paper.

⁴ These variables were apparently first used by Lagrange [see (1), p. 421].

However, none of the six variables can be eliminated for all orbits. For example, if we eliminated P_z , the z -component of \mathbf{P} , the remaining variables would fail for an equatorial orbit. Thus, in setting up a program to handle any orbit, it is convenient to retain all six geometric variables. Equation [1] is then useful as an integral of the equations of motion, which is independent of any other integrals, such as the energy integral, that may exist.

The relations connecting \mathbf{P} , \mathbf{e} , and the conventional elements are obvious, e is the magnitude of \mathbf{e} , and a is given by

$$a = P^2/(1 - e^2) \quad [2]$$

for a proper choice of units. i is given by

$$\cos i = P_z/P \quad [3]$$

whereas ω and Ω are found by solving the equations

$$\begin{aligned} e_x &= e(\cos \omega \cos \Omega - \sin \omega \cos i \sin \Omega) \\ e_y &= e(\cos \omega \sin \Omega + \sin \omega \cos i \cos \Omega) \\ e_z &= e \sin \omega \sin i \end{aligned} \quad [4]$$

The components of \mathbf{P} are

$$\begin{aligned} P_x &= P \sin i \sin \Omega \\ P_y &= -P \sin i \cos \Omega \\ P_z &= P \cos i \end{aligned} \quad [5]$$

In finding the time derivatives $\dot{\mathbf{P}}$ and $\dot{\mathbf{e}}$, it is convenient to use three unit vectors, \mathbf{P}_0 in the direction of \mathbf{P} , \mathbf{r}_0 in the direction of \mathbf{r} , and \mathbf{f}_0 defined by

$$\mathbf{f}_0 = \mathbf{P}_0 \times \mathbf{r}_0 \quad [6]$$

\mathbf{f}_0 is in the direction of increasing anomaly. The derivative $\dot{\mathbf{e}}$, for an arbitrary perturbing acceleration vector \mathbf{F} , is found from the derivatives⁶

$$\begin{aligned} d\mathbf{e}/dt &= (P \sin f)(\mathbf{F} \cdot \mathbf{r}_0) + (r/P)(2 \cos f + e + e \cos^2 f)(\mathbf{F} \cdot \mathbf{f}_0) \\ di/dt &= (r \cos \varphi/P)(\mathbf{F} \cdot \mathbf{P}_0) \\ d\omega/dt &= -(P \cos f/e)(\mathbf{F} \cdot \mathbf{r}_0) + \\ &\quad (r \sin f/Pe)(2 + e \cos f)(\mathbf{F} \cdot \mathbf{f}_0) - (r \sin \varphi/P \tan i)(\mathbf{F} \cdot \mathbf{P}_0) \\ d\Omega/dt &= (r \sin \varphi/P \sin i)(\mathbf{F} \cdot \mathbf{P}_0) \end{aligned} \quad [7]$$

In these, f is the true anomaly and φ is $\omega + f$, the argument of the latitude.

It is easiest to start with the simplest component, namely e_z . Differentiating e_z from Equation [4], and substituting from Equation [7], we readily find

$$\dot{e}_z = -(P \sin i \cos \varphi)(\mathbf{F} \cdot \mathbf{r}_0) + P^{-1}[r \sin i \sin \varphi (2 + e \cos f) + re \sin i \sin \omega](\mathbf{F} \cdot \mathbf{f}_0) - (er \sin f \cos i/P)(\mathbf{F} \cdot \mathbf{P}_0)$$

In this, $r \sin i \sin \varphi = r \sin \theta = z$, where θ is the latitude. $e \sin i \sin \omega$ is e_z itself. $er \sin f$ is the magnitude of $\mathbf{e} \times \mathbf{r}$, a vector whose direction coincides with that of \mathbf{P} , and which hence makes the angle i with the z -axis. Thus, $er \sin f \cos i$ is $(\mathbf{e} \times \mathbf{r})_z$. Finally, $\sin i \cos \varphi$ can be identified as the z -component of \mathbf{f}_0 .

Thus, we have identified the coefficients in \dot{e}_z with the products of scalars by the z -components of certain vectors. This suggests for $\dot{\mathbf{e}}$ the form

$$\dot{\mathbf{e}} = -(P\mathbf{f}_0)(\mathbf{F} \cdot \mathbf{r}_0) + P^{-1}[\mathbf{r}(2 + e \cos f) + re](\mathbf{F} \cdot \mathbf{f}_0) - P^{-1}(\mathbf{e} \times \mathbf{r})(\mathbf{F} \cdot \mathbf{P}_0) \quad [8]$$

which can be verified by the procedure used to get \dot{e}_z .

$\dot{\mathbf{P}}$ is well known to be

$$\dot{\mathbf{P}} = \mathbf{r} \times \mathbf{F} \quad [9]$$

Except for the term $e \cos f$, Equations [8 and 9] involve only the vectors \mathbf{r} , \mathbf{e} and \mathbf{P} . $e \cos f$, and $e \sin f$, which will be needed later, are to be calculated from

$$e \cos f = \mathbf{e} \cdot \mathbf{r}_0 \quad e \sin f = \mathbf{e} \times \mathbf{r}_0 \cdot \mathbf{P}_0 \quad [10]$$

Angle Variables and Elimination of the Time

The three angle variables most commonly used are f , φ or longitude λ . None of these is well defined for all orbits. However, either φ or λ is well defined for all orbits, so we shall not consider further the use of f as an angle variable.

For both choices of angle variable, the time derivatives and the explicit methods of transforming in either direction between rectangular coordinates and the variables \mathbf{P} , \mathbf{e} are needed. These relations involve only standard results, but the sequence of relations needed may not be obvious.

φ as angle variable

The value of $\dot{\varphi}$ is

$$\dot{\varphi} = (P/r^2)[1 - (r^3/P^2)(\cot i \sin \varphi)(\mathbf{F} \cdot \mathbf{P}_0)] \quad [11]$$

Given \mathbf{r} , \mathbf{p} , where \mathbf{p} is the linear momentum vector, to find \mathbf{P} , \mathbf{e} , φ , first use

$$\mathbf{P} = \mathbf{r} \times \mathbf{p} \quad [12]$$

whence P , \mathbf{P}_0 and i can be found. To find \mathbf{e} , first compute

$$e \sin f = P(\mathbf{r}_0 \cdot \mathbf{p}), \quad e \cos f = (P^2/r) - 1 \quad [13]$$

Then

$$\mathbf{e} = (e \cos f)\mathbf{r}_0 - (e \sin f)\mathbf{f}_0 \quad [14]$$

Finally, φ is found from

$$\begin{aligned} \sin \varphi &= zP/r\sqrt{P_x^2 + P_y^2} \\ \cos \varphi &= (\mathbf{P} \times \mathbf{r})_z/r\sqrt{P_x^2 + P_y^2} \end{aligned} \quad [15]$$

Given \mathbf{P} , \mathbf{e} , φ , to find \mathbf{r} , \mathbf{p} , first find $\sin i$, $\cos i$, $\sin \Omega$, $\cos \Omega$, from the components of \mathbf{P} given in Equations [5]. From these, and $\sin \varphi$, $\cos \varphi$, calculate the components of \mathbf{r}_0

$$\begin{aligned} r_{0,x} &= \cos \varphi \cos \Omega - \sin \varphi \cos i \sin \Omega \\ r_{0,y} &= \cos \varphi \sin \Omega + \sin \varphi \cos i \cos \Omega \\ r_{0,z} &= \sin \varphi \sin i \end{aligned} \quad [16]$$

Next, calculate $e \cos f$ and $e \sin f$ from Equations [10], and

finally calculate \mathbf{r} and \mathbf{p} from

$$\begin{aligned} \mathbf{r} &= [P^2/(1 + e \cos f)]\mathbf{r}_0 \\ \mathbf{p} &= (e \sin f/P)\mathbf{r}_0 + (P/r)\mathbf{f}_0 \end{aligned} \quad [17]$$

As an alternate to calculating $e \cos f$ and $e \sin f$ from Equations [10], we can use

$$\begin{aligned} h &= e \sin \omega = e_z/\sin i \\ l &= e \cos \omega = (e_y P_z - e_z P_y)/\sqrt{P_x^2 + P_y^2} \\ e \sin f &= l \sin \varphi - h \cos \varphi \\ e \cos f &= l \cos \varphi + h \sin \varphi \end{aligned} \quad [18]$$

⁶ These are given in (1), pp. 404-5. We have changed the forms slightly to facilitate expression in terms of the present orbit elements, and to avoid the subtraction of nearly equal quantities.

λ as angle variable

The value of $\dot{\lambda}$ is

$$\dot{\lambda} = P_x/r^2 \cos^2 \theta \quad [19]$$

Given \mathbf{r} , \mathbf{p} , to find \mathbf{P} , \mathbf{e} , λ , use Equations [12, 13 and 14] to find \mathbf{P} and \mathbf{e} ; $\sin \lambda$ and $\cos \lambda$ are found from

$$\sin \lambda = y/\sqrt{x^2 + y^2} \quad \cos \lambda = x/\sqrt{x^2 + y^2} \quad [20]$$

Given \mathbf{P} , \mathbf{e} , λ , to find \mathbf{r} , \mathbf{p} , find $\tan \theta$ from

$$\tan \theta = -(P_x \cos \lambda + P_y \sin \lambda)/P_z \quad [21]$$

whence $\sin \theta$ and $\cos \theta$ can be found using trigonometric identities. Then find r_0 from

$$\begin{aligned} r_{0,x} &= \cos \theta \cos \lambda \\ r_{0,y} &= \cos \theta \sin \lambda \\ r_{0,z} &= \sin \theta \end{aligned} \quad [22]$$

and find $e \cos f$, $e \sin f$, and t_0 from Equations [10 and 6]. \mathbf{r} and \mathbf{p} are then found from Equations [17].

When the perturbing acceleration \mathbf{F} does not involve the time explicitly, the time can of course be eliminated from Equations [8 and 9] upon division by $\dot{\varphi}$ or $\dot{\lambda}$, as the case may be. Singularities now appear, not only because the definitions of φ and λ are undetermined for some orbits, but also because φ and λ do not increase without limit for unbound orbits. However, there still may be an advantage, at least in the numerical integration of bound orbits, to using an angle variable instead of time as the independent variable. When this is done, the only transcendental functions needed are

$$\begin{aligned} dT/d\varphi = & -(\Delta_\varphi/\dot{\varphi}) + (r^2/P^4)\{(P_x^2 + P_y^2)[(P^2 + PP_x + P_x^2)/(P + P_x)] \times \\ & (P + P_x) \cdot \Delta \mathbf{P} + P_x^3[(P_x + P_{xi}) \Delta P_x + (P_y + P_{yi}) \Delta P_y] - r_0 P_x (r/P^2)(P_{xi}^2 + P_{yi}^2)[(r/P_x^2) + (r_0/P_x^2)] \times \\ & \{[(P_x + P_{xi}) \Delta P_x + (P_y + P_{yi}) \Delta P_y][\sqrt{P_x^2 + P_y^2} + \sqrt{P_{xi}^2 + P_{yi}^2}]^{-1} + \\ & (e_y \Delta P_x + P_{xi} \Delta e_y - e_x \Delta P_y - P_{yi} \Delta e_x) \cos \varphi + [P_x \Delta e_x + e_x (P + P_x)^{-1} (P + P_x) \cdot \Delta \mathbf{P}] \sin \varphi\} \quad [24] \end{aligned}$$

Finally

$$\begin{aligned} (dT/d\lambda) = & (r^2 \cos^2 \theta/P_x^2) \Delta P_x + P_{xi}[(r \cos \theta/P_x) + (r_0 \cos \theta_0/P_{xi})]\{(r \cos \theta/P_x^2 P_x)[(P_x + P_{xi}) \Delta P_x + \\ & (P_y + P_{yi}) \Delta P_y + (P_x + P_{xi}) \Delta P_x] - P_x^2 (r \cos \theta/P_x^2 P_x)(r_0 \cos \theta_0/P_{xi}^2 P_{xi})[\cos \lambda (P_x \Delta e_x + \\ & e_{xi} \Delta P_x - P_x \Delta e_x - e_{xi} \Delta P_x) + \sin \lambda (P_x \Delta e_y + e_{yi} \Delta P_x - P_y \Delta e_x - e_{yi} \Delta P_y) + \\ & [(P_x/\cos \theta) + (P_{xi}/\cos \theta_0)]^{-1}[(P_x + P_{xi}) \Delta P_x + [(P_x + P_{xi}) \cos \lambda + (P_y + P_{yi}) \sin \lambda][\Delta P_x \cos \lambda + \Delta P_y \sin \lambda]]\} \quad [25] \end{aligned}$$

functions of the independent variable. With bound orbits, the values needed can be specified in advance and stored in the memory, instead of being computed in the course of the integration.

Phase Variables

When time is used as the independent variable, the phase variable is either φ , or λ , the initial values of φ and λ . When an angle is used as independent variable, the phase variable is t , the value of time at the angle value used to start the inte-

gration. One can keep track of phase by integrating Equations [11 or 19] or their reciprocals, keeping φ_i , λ_i or t_i constant. Alternatively, one may use the procedure analogous to the use of $d\sigma/dt$, that is, computing the derivatives of φ_i , λ_i or t_i , and integrating.

Both methods have disadvantages. If Equations [11 or 19] are used, the integration must be done with great accuracy, because the derivatives are large even for an unperturbed orbit. In the other method, the derivatives are proportional to the perturbation, but may contain oscillations [(1), p. 421] which grow in amplitude with time and hence are difficult to integrate.

A third procedure has the disadvantage of using more complicated derivatives than the other two, but may be worth exploring. We shall illustrate it using an angle as independent variable. An analogous procedure exists when using time. Let α denote the angle variable. Let $t_0(\alpha)$ denote that function which time is of α for the unperturbed orbit. Define $T(\alpha)$ by

$$T(\alpha) = t(\alpha) - t_0(\alpha) \quad [23]$$

where $t(\alpha)$ is time on the actual orbit. Then $T(\alpha)$ is proportional to the time, and oscillations in $dT/d\alpha$ seem to be bounded. However, we have not explored the properties of $dT/d\alpha$ thoroughly, and it may prove to have the same disadvantage as $d\sigma/dt$.

To write $dT/d\varphi$, let Equation [11] be written in the form

$$\dot{\varphi} = (P/r^2)(1 + \Delta_\varphi)$$

which defines Δ_φ . Then

In both Equations [24 and 25], a subscript i refers to an initial value, and $\Delta P_x = P_x - P_{xi}$, etc. If Equations [24 and 25] are used in numerical integration, the dependent variables should be ΔP_x , Δe_x , etc., instead of P_x , e_x , etc. The derivation of Equations [24 and 25] is straightforward, though tedious, so we present no details.

References

- 1 Moulton, F. R., "Introduction to Celestial Mechanics," 2nd ed., The MacMillan Co., N. Y., 1914.
- 2 Kozai, Y., "The Motion of a Close Earth Satellite," *Astron. J.*, vol. 64, no. 1274, Nov. 1959, pp. 367-377.

Technical Notes

Heat Release Rate, Temperature and Pressure in Solid Rocket Instability¹

F. T. McCLURE,² R. W. HART³ and J. F. BIRD⁴

Applied Physics Laboratory,

The Johns Hopkins University, Silver Spring, Md.

ACOUSTIC instability in solid propellant motors is the phenomenon which occurs when the combustion of the propellant supplies energy to the acoustic field in one or more of the resonant modes to the rocket cavity. In previous papers (1,2)⁵ we have stressed that, if the burning zone at the propellant surface is very thin compared to the wave length of the sound field, it is most convenient to represent the acoustic properties of this zone as a surface having a specific acoustic admittance Y of the form

$$Y = -(\bar{v}/\bar{P})[(\mu/\epsilon) - (1/\gamma)] \quad [1]$$

In this expression

- \bar{v} = steady-state velocity of the gases leaving the combustion zone
- \bar{P} = steady-state pressure
- γ = specific heat ratio of the gases
- μ/ϵ = response function of the propellant, namely the ratio of the fractional increment of mass flow rate to the fractional increment of pressure

The real part of the admittance has properties similar to resistance in electrical circuits. If it is positive the surface attenuates, while if it is negative the surface amplifies. Since \bar{v} and \bar{P} are both positive quantities it is clear the surface will amplify only if the real part of $\mu/\epsilon > 1/\gamma$. The response function, μ/ϵ , depends intimately on the structure of the burning zone of the propellant. It has been analyzed for one model of this zone and found to be a rather complicated function of a number of parameters needed to completely characterize the propellant (1). The examination of individual parameters is complicated by the fact that the nature of the dependence seems to differ from one domain in the parameter field to another, and it is difficult to determine which domain best represents typical propellants. However, one general property does come out of the analysis, namely that the response function tends to have a broad maximum as a function of frequency in the acoustic region. In addition this maximum generally exceeds $1/\gamma$. As a consequence, broad frequency response is expected in agreement with most experimental experience.

The factor \bar{v}/\bar{P} is not, however, dependent on the structure of the burning zone. Its appearance requires only that this zone be thin compared to the wave length, which is generally quite a safe assumption. Assuming that the necessary cri-

terion on μ/ϵ has been met, increasing \bar{v}/\bar{P} increases the amplification, and vice versa. In particular, if we are operating in the neighborhood of a broad maximum in the real part of μ/ϵ the amplification (per unit surface) will be essentially proportional to \bar{v}/\bar{P} .

Since this factor is dependent on so few assumptions its behavior may have rather general significance, and this does not seem to have been adequately stressed previously. Note that we may rewrite it as follows

$$\bar{v}/\bar{P} = \bar{m}/\bar{p}\bar{P} = (\bar{m}/\bar{P}^2)(RT_f/M) \quad [2]$$

where

- \bar{m} = mass rate of burning per unit surface (solid density \times linear burning rate)
- R = gas constant
- T_f = flame temperature
- M = molecular weight of the propellant gases

The quantity $\bar{m}RT_f/M$ is a direct measure of the heat release rate so that we find agreement with the general experimental observation that acoustic instability is more severe in propellants of high rate of heat release (3-6).

Noting that raising the propellant temperature increases the burning rate for fixed pressure, we see that equation [2] is consistent with the frequent observation that instability is also more severe at higher temperatures (3,6). It should be noted, however, that propellant temperature is a sensitive parameter in the response function, and, in fact, in many parameter domains has the reverse of the above dependence (1). This may account for the observation that, with some propellants, instability is observed to be greater at either temperature extreme (3,6).

With respect to the dependence on pressure we will remember that the rate of burning of propellants increases less than proportional to pressure so that we can expect instability to be more severe at lower pressures (3,5,6).

We must recognize that in this phenomenon one is balancing gains against losses and there are a variety of losses in a rocket motor with different dependence on the operational conditions, so that complete generality cannot be achieved by examining one factor in the gain function alone. It is encouraging, however, that the admittance concept has inherently in its makeup the very generalizations which have been arrived at over many years of experimental investigation.

A word might here be said about the function of additives, such as aluminum, which suppress instability. They may act either by increasing the losses in the system or by decreasing the propellant amplification. Consider the use of aluminum. Small amounts of aluminum powder generally increase both the rate of burning and the flame temperature. Thus if the general efficacy of aluminum is due to its presence in the surface zone (as is rather commonly believed) then it must have an effect on the response function, which in turn would mean that it must modify the structure of the burning zone in a significant manner.

In closing we should like to mention that it appears that many of the results of the excellent experiments of Brownlee

Received Aug. 26, 1960.

¹ This research supported by the Bureau of Naval Weapons, Department of the Navy, under NOrd 7386.

² Chairman, Research Center.

³ Supervisor, Theoretical Study Group, Research Center.

⁴ Physicist, Theoretical Study Group, Research Center.

⁵ Numbers in parentheses indicate References at end of paper.

EDITOR'S NOTE: The Technical Notes and Technical Comments sections of ARS JOURNAL are open to short manuscripts describing new developments or offering comments on papers previously published. Such manuscripts are usually published without editorial review within a few months of the date of receipt. Requirements as to style are the same as for regular contributions (see masthead page).

and Marble (6) can be interpreted by examination of the gain-loss balance along these same lines. Significant information as to the nature of the important loss mechanisms appears to be imbedded in these results, and a summary of the analysis will be offered for publication shortly.

References

- 1 Hart, R. W. and McClure, F. T., "Combustion Instability: Acoustic Interaction With a Burning Propellant Surface," *J. Chem. Phys.*, vol. 30, 1959, pp. 1501-1514; see also: Bird, J. F., Haar, L., Hart, R. W. and McClure, F. T., "Effect of Solid Propellant Compressibility on Combustion Instability," *J. Chem. Phys.*, vol. 32, 1960, pp. 1423-1429.
- 2 McClure, F. T., Hart, R. W. and Bird, J. F., "Acoustic Resonance in Solid Propellant Rockets," *J. Appl. Phys.*, vol. 31, 1960, pp. 884-896; see

also (by these authors): "Solid Propellant Rocket Motors as Acoustic Oscillators," in the ARS series "Progress in Astronautics and Rocketry—Vol. I: Solid Propellant Rocket Research," Academic Press, N. Y., 1960, pp. 295-358; also (by these authors): "Acoustic Instability in Solid Fuel Rockets," *ARS JOURNAL*, vol. 30, no. 9, pp. 908-910.

3 Angelus, T. A., Berl, W. G., Green, L., Jr., Hart, R. W., Landsbaum, R. W., McClure, F. T., Price, E. W., Shuey, H. M. and Summerfield, M., "A General Review of Acoustic Instability in Solid Propellant Rockets," Proc. Eighth International Combustion Symposium, Pasadena, Calif., Aug. 28-Sept. 2, 1960.

4 See, for example, Green, L., Jr., "Some Effects of Oxidizer Concentration and Particle Size on Resonance Burning of Composite Solid Propellants," *JET PROPULSION*, vol. 28, 1958, pp. 159-164.

5 Price, E. W., "Analysis of Results of Combustion Instability Research on Solid Propellants," ARS Preprint 1068-60, 1960.

6 See, for example, Brownlee, W. G. and Marble, F. E., "An Experimental Investigation of Unstable Combustion in Solid Propellant Rocket Motors," ARS Preprint 1067A-60, 1960.

Advanced Uncooled Nozzle for Solid Propellant Rocket

CHUK-CHING MA¹

Rocketdyne Div., North American Aviation, Inc.
Canoga Park, Calif.

This paper is concerned with the advanced design of an uncooled nozzle for a solid propellant rocket. The results of analytical studies, which include various advanced uncooled nozzle designs based on the requirements of a hypothetical second stage rocket engine, are presented. However, the nozzle design concept thus developed is applicable to any rocket engine. Among the five possible schemes investigated, the most promising appears to be a design involving a nozzle made of resin-bonded refractory-grade silica or other vitreous materials, the upper part (throat region) inwardly covered with a layer of graphite which in turn is coated with zirconium oxide. Molybdenum containing 0.5 per cent titanium alloy is used as an outer surface covering for the entire nozzle. Based on a concept of the efficient use of a combination of several materials each of which serves a particular function, the above design for the construction of an uncooled nozzle is believed to be completely novel and results in a nozzle weight which is much lower than that of a conventional fluid-cooled or uncooled nozzle of comparable thrust rating and expansion ratio.

Nozzle Design Concept

THE RELATIVELY recent interest in the attainment of high performance of a solid propellant rocket has emphasized the improvements that can be gained by the reduction of inert component weight. The nozzle is one of the major components of any rocket engine; therefore, it is highly important to direct design effort toward its weight reduction. The nozzle design concept presented here makes the most efficient use of a combination of materials to develop a lightweight uncooled nozzle.

Conventional uncooled nozzles consist of high temperature resistant, low thermal conductivity materials to serve as a thermal barrier, surrounded by another material to provide a heat sink and the necessary structural strength. An example is the nozzle for the third stage Vanguard motor which uses a flame-sprayed aluminum oxide coating, as a thermal barrier, on a steel forging which serves simultaneously as a heat sink and as a carrier for the applied load. Because all carbon

steels and alloy steels have only moderate heat capacity, a sizable thickness of this material is required to absorb the heat passing through the thermal barrier over the period of firing so that the temperature rise produced does not exceed mechanical strength requirements. In addition, because of the high density of steels, the weight of the resultant nozzle is often higher than any other component of the propulsion system. Obviously, the weight could be reduced by using a material having high heat capacity, high thermal conductivity and low density to serve as a heat sink and another material having high tensile strength-to-weight ratio to provide strength at elevated temperatures.

There are many substances which will absorb more heat per lb than carbon steels or alloy steels. The use of graphite both as a heat sink and as the nozzle structural material was first investigated (Scheme 2, Table 1), since it retains and, in fact, increases its strength up to 4700 F (1)² and has a mean specific heat of 0.47 Btu/lb/deg F over this temperature range. An interior coating of zirconium oxide (Rokide Z) was used as a thermal barrier to minimize the heat transferred from the gas stream to the graphite wall. The weight of this nozzle is fairly low in comparison with a Rokide-Z-insulated metal nozzle (Scheme 5, Table 1). However, there is no assurance that this design is workable because graphite currently available may not be resistant enough to vibration and shock by itself. The next logical approach is to wrap the graphite wall externally with a suitable high strength material, so that the graphite serves solely as a heat sink instead of performing the dual duties mentioned in the foregoing (Scheme 3, Table 1). Molybdenum containing 0.5-per cent titanium was selected for this purpose because it has the best tensile strength-to-weight ratio and other favorable characteristics. The use of tungsten and tungsten-rhenium alloy as the wrapping material was also investigated, but the gain due to graphite weight reduction (due to higher allowable graphite wall temperature) is more than offset by the much higher metal weight required. The resultant weight in this alternate design (Scheme 3) is approximately 30 per cent higher than that of an unwrapped nozzle, but is substantially lower than that of a conventional Rokide-Z-insulated metal nozzle. The third alternative is to wrap only the throat and the area in its vicinity with high strength metal (molybdenum containing 0.5 per cent titanium; Scheme 4, Table 1). The weight of the nozzle based on this scheme is only 3 per cent higher than that of the bare graphite nozzle, but the former may suffer the same disadvantage of the latter, i.e., the possibility of fracture of the graphite skirt.

A further investigation was devoted to finding a nonbrittle substance which could serve both as a thermal barrier and a heat sink by having the combined favorable properties of low density, low thermal conductivity and moderately high heat capacity. Resin bonded silica or other vitreous materials

Received Aug. 30, 1960.

¹ Senior Technical Specialist, Rocketdyne; Lecturer in Engineering, University of California.

² Numbers in parentheses indicate References at end of paper.

Table 1 Nozzle inert weight comparisons

Scheme number	Wall structure	Requirements				Nozzle inert weight, lb	Relative ^a weight, ratio
		Astrolite, lb	Graphite, lb	Rokide Z, lb	Molybdenum, lb		
1	This nozzle is made of a molybdenum-wrapped Astrolite wall with a graphite insert, which is coated on the inside with Rokide Z.	28.0	7.5	4.5	12.5	52.5	1.0
2	This nozzle is made of graphite coated internally with Rokide Z.	0	45.6	13.7	0	59.3	1.13
3	This nozzle is made of graphite wrapped externally with molybdenum and coated with Rokide Z.	0	49.0	24.5	12.0	76.5	1.46
4	Same as Scheme No. 2 except the graphite is partially wrapped with molybdenum	0	40.0	15.3	5.4	60.7	1.16
5	This nozzle is made of molybdenum sheet insulated internally with Rokide Z.	0	0	93.6	25.9	119.5	2.28

^a The relative weight ratio is the ratio of the inert weight of the nozzles of the various schemes relative to the inert weight of the nozzle of Scheme 1.

fall in this category. They have heat capacities approximately twice as high as that of any heat resistant alloy, have thermal conductivities in the range of 0.15 Btu/hr/ft/deg F, and weigh only one-fifth as much as ordinary steel. Molybdenum or other heat-resistant alloys must be used in conjunction with this kind of material to provide structural strength. The use of a metal-wrapped, resin bonded silica nozzle should, therefore, result in a substantial weight saving. However, the resin bonded silica has the disadvantage of ablating over the time of burning, which would gradually increase the nozzle throat area and drastically change the thrust of a solid propellant rocket engine. To overcome this shortcoming, the resin bonded silica is lined internally with zirconium - oxide - coated graphite in the region of the throat. As ablation downstream of the throat will only change the area ratio slightly, and can therefore be tolerated, it is only necessary to provide a graphite lining and in the vicinity of the nozzle throat. The resultant nozzle inert weight in this design is not only substantially lower than that of the conventional uncooled nozzle, but also considerably less than that of any other scheme as indicated in Table 1.

From the above comparisons, the advanced uncooled nozzle—based on the design concept of making efficient use of the individual favorable characteristics of several known materials to fabricate a composite nozzle wall—is shown to have considerable merit. If the feasibility of the uncooled nozzle thus developed can be further substantiated by actual tests, this design concept can advance the state-of-art considerably.

Nozzle Description

Uncooled nozzles of five different designs have been evaluated and their inert weights are tabulated in Table 1. The inert weight of the nozzle designed under Scheme 1 is the lowest among the five. In this section, this nozzle is described in more detail.

The nozzle of Scheme 1 consists of a basic frame made of refractory grade siliceous material containing approximately 95 per cent silica. There are a number of siliceous materials under different trade names available. The use of Astrolite, a phenolic bonded refractory grade silica containing approximately 96 per cent SiO_2 , is assumed to illustrate the nozzle design concept. Because the phenolic resin in the Astrolite gradually vaporizes or burns off when the operating temperature exceeds 600 F, it is necessary to provide additional thickness to compensate for the ablation of the Astrolite surface exposed to the gas flame. Based on information obtained from the manufacturer, an extra layer of 0.12 to 0.15 in. is quite enough for a firing period of 1 to 1.5 min.

The Astrolite body is wrapped with molybdenum containing 0.5 per cent titanium alloy which provides structural strength at elevated temperatures. The temperature of the molybdenum-Astrolite boundary is limited to about 1800 F. This is accompanied by adjusting the thickness of the Astrolite layer. Molybdenum containing 0.5 per cent titanium alloy instead of pure molybdenum is used as it has higher tensile strength at elevated temperatures. Calculations have also been made for using tungsten, tungsten-rhenium alloy and fiber glass instead of molybdenum alloy, but the resultant inert weight of nozzles wrapped with any one of the former materials is higher.

In order to avoid ablation in the throat region, a graphite insert is used. The inside surface of the graphite is coated with flame-sprayed Rokide Z (zirconium oxide) to serve as a thermal barrier. The thickness of the Rokide Z coating is so

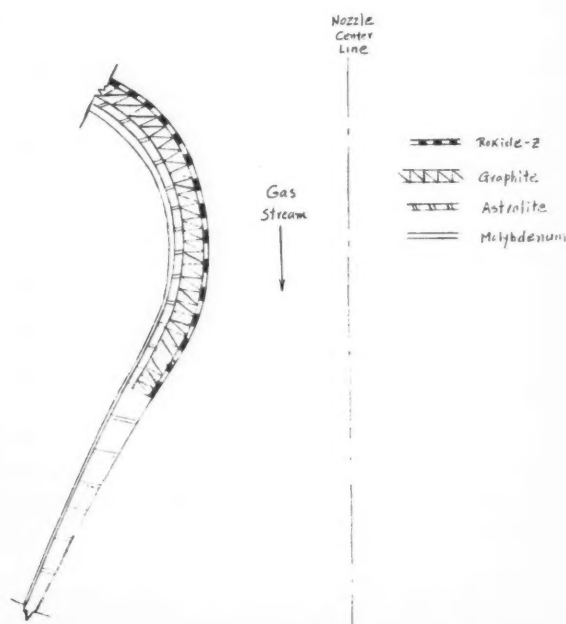


Fig. 1 Uncooled nozzle wall structure

designed that the inside surface temperature will be about 500 deg F below the melting point of zirconium oxide (mp approximately 4700 F) at the end of the firing period. The thickness of both the graphite and zirconium oxide layers is adjusted so that the temperature at the graphite-Astrolite boundary is always at least 200 F below the melting point of silica (mp approximately 3100 F).

The nozzle as described above is sketched schematically in Fig. 1 showing the design of the throat region and lower sections of the nozzle.

Results

Nozzle wall thickness and inert weight estimates for various design schemes require stress and heat transfer calculations. In the present study, conventional graphical techniques, empirical equations and numerical methods, all of which have the singular advantage of giving rapid approximation with an accuracy in the range of ± 20 per cent, are used for hand calculations. These methods may not be accurate enough for actual hardware designs, but they are good enough for evaluation studies involving comparisons of different designs. The details of these methods are given in (2-4).

The results are based on the requirements of a hypothetical second-stage rocket engine. For calculating purposes, the sea level thrust under optimum expansion is assumed to be 50,000 lb, and the firing period is assumed to be 1 min. The results are given in Table 1.

Conclusion

As a result of this study, it is concluded that an advanced uncooled nozzle utilizing several layers of different materials

to form the nozzle wall has the following favorable characteristics:

1. It results in the efficient use of several materials, each of which has certain favorable physical, mechanical and chemical properties, for the fabrication of an uncooled nozzle which can stand the prevailing severe thermal and pressure conditions.

2. It utilizes the best possible combination of metallic and nonmetallic materials to attain the goal of developing a high performance and lightweight nozzle.

3. The fabrication technique for this nozzle is only slightly more complicated than that of a conventional uncooled nozzle.

The principal area of technological uncertainty is the reliability of the recently developed resin bonded refractory grade siliceous materials. Whether these materials can conform to the claims of the manufacturers remains to be seen and requires experimental evaluations.

Acknowledgments

The author wishes to thank Charles Morse, Frank Hunter Jr. and several members of the technical staff of Rocketdyne for their assistance.

References

- 1 "Reactor Handbook," vol. 1, "Materials," 2nd edition, Intersci. Publ. New York, 1960.
- 2 McAdams, W. H., "Heat Transmission," McGraw-Hill, New York, 1954.
- 3 Bartz, D. R.: "A Simple Equation for Rapid Estimation of Rocket Nozzle Convective Heat Transfer Coefficients," *JET PROPULSION*, Jan. 1957.
- 4 Grover, J. H. and Holter, W. H., "Solution of the Transient Heat Conduction Equation for an Insulated Infinite Metal Slab," *JET PROPULSION*, Dec. 1957.

Stagnation Point Radiative Transfer

H. KENNET¹ and S. L. STRACK²

Boeing Airplane Co., Seattle, Wash.

IT IS well known that during superorbital re-entry into Earth's atmosphere the temperatures encountered in the stagnation region of the re-entering vehicle may well exceed 10,000 K. In this temperature range, the highly compressed air in the shock layer enveloping the vehicle will radiate thermally to an appreciable degree. This radiation heat flux would, under such conditions, be several times the usual aerodynamic heat flux, as was calculated by Meyerott (1)³ for a circumlunar vehicle, and by Kivel (2) for a Martian probe.

These calculations were only approximate, however, in view of the highly complicated formulation of the exact radiation transfer problem [see Lighthill (3)]. Basically, the approximations used in (1 and 2) were to replace the stagnation point region by an infinite slab at a uniform temperature T_s and density ρ_s , whose thickness δ is the shock standoff distance. The radiative flux q_0 into the nose is then given in this idealized situation by

$$q_0 = (\epsilon'\delta)\sigma T_s^4 \quad [1]$$

where σ is the Stefan-Boltzmann constant and ϵ' the emissivity per unit length is a known tabulated function of the temperature and density (2).

Received Sept. 12, 1960.

¹ Research Specialist, Flight Technology Dept., Aero-Space Div.

² Research Specialist, Structures Technology Dept., Aero-Space Div.

Numbers in parentheses indicate References at end of paper.

When the product $(\epsilon'\delta)$, herein called the effective emissivity, becomes unity, the black-body limit is reached. Obviously the radiation from the gas cannot exceed this black-body limit, and consequently the solution usually advocated is to replace $(\epsilon'\delta)$ by unity whenever this product exceeds unity. The statement is made in the literature (2) that when $(\epsilon'\delta)$ is equal to 1 the value of the radiation heat flux q_0 as predicted by Equation [1] is approximately 20% higher than the actual value of this heat flux. It is the intent of this note to show that in reality the heat flux q_0 as predicted by Equation [1] overestimates the actual heat flux by approximately 80%. A modification to Equation [1] is consequently given (see Eq. [8]) which improves the accuracy considerably.

The problem will be restricted to the case of a nonscattering medium. The shock wave is assumed to have unit transmissivity, so that it does not reflect any of the radiation impinging on it. The body surface is assumed to have unit emissivity and in addition it is assumed to be highly cooled (i.e., $T_w \leq 3000$ K).

Under these conditions the radiation flux q_k at any point \mathbf{x} in space is given as an integral over all frequencies ν and over all source points \mathbf{x}' (4)

$$q_k(\mathbf{x}) = - \int_0^\infty d\nu \iiint_{-\infty}^\infty \rho(\mathbf{x})\mu_\nu(\mathbf{x})B_\nu(\mathbf{x}') \times \frac{1}{r^3} e^{-\int_0^r \rho(r')\mu_\nu(r')dr'} dx_1' dx_2' dx_3' \quad [2]$$

Here

ρ = density

μ_ν = mass absorption coefficient in the frequency range $(\nu, \nu + d\nu)$

$r = \mathbf{x} - \mathbf{x}'$, distance from the source point to the field point

B_ν = Planck function, given in terms of Planck's and Boltzmann's constants h and k , and the speed of light c

$$B_\nu = \frac{2h\nu^3}{c^2} \cdot \frac{1}{e^{h\nu/RT} - 1} \quad [3]$$

In the temperature range $2000 \text{ K} < T < 20,000 \text{ K}$ it is possible to employ a frequency averaged absorption coefficient, in the following manner [see (4)]

$$\bar{\rho\mu} = \frac{\int_0^\infty \rho\mu_\nu B_\nu d\nu}{\int_0^\infty B_\nu d\nu} = \frac{\int_0^\infty \rho\mu_\nu B_\nu d\nu}{(\sigma T^4/\pi)} \quad [4]$$

where the integration of the denominator can be found in any text which covers black-body radiation [see Sommerfeld (5)].

To make the mathematics tractable, a spherical nose shape was chosen. Since radiation effects will become important only at very large hypersonic Mach numbers, of the order of 30 or 40, we take the shock shape to be concentric with the body. The geometry is shown in Fig. 1, where all the pertinent lengths and angles have been indicated. The most suitable coordinate system, a spherical one, with (r, θ, φ) as coordinates was utilized, where the angle φ (not shown in sketch) is an azimuth angle measured in a plane perpendicular to the plane of the paper. The radiation heat flux q_0 at point "0" is found by forming the dot product of \mathbf{q}_R and \mathbf{n} . The air within the cap is assumed to be at a uniform temperature T_s and density ρ_s .

When this is done and use is made of the frequency averaged absorption coefficient, the following expression is obtained

$$q_0 = \frac{\sigma T_s^4}{\pi} \int_0^{\pi/2} \int_0^{r_s(\theta)} \int_0^{2\pi} \frac{\bar{\rho\mu} e^{-\bar{\rho\mu} r}}{r^2} d\varphi dr \sin \theta \cos \theta d\theta \quad [5]$$

where $r_s(\theta)$, the distance from point "0" to the shock, is given by

$$r_s(\theta) = R[\sqrt{\cos^2 \theta + 2(\delta/R) + (\delta/R)^2} - \cos \theta] \quad [6]$$

In order to carry out the integration, use is made of E_n , the integro-exponential function of order n , defined by [see Kourganoff (6)]

$$E_n(\lambda) = \int_1^\infty \frac{e^{-\lambda x}}{x^n} dx \quad [7]$$

in terms of which Equation [5] can be integrated exactly to give the result

$$q_0 = \sigma T_s^4 \left\{ 1 - 2 \left(1 + \frac{\alpha}{2} \right)^2 \left[E_3(\bar{\rho\mu}\delta) - \frac{1}{1 + 2/\alpha} E_3 \left(\bar{\rho\mu}\delta \sqrt{1 + \frac{2}{\alpha}} \right) \right] + \frac{1}{2} \left(\frac{\alpha}{\bar{\rho\mu}\delta} \right)^2 \left[(1 + \bar{\rho\mu}\delta) e^{-\bar{\rho\mu}\delta} - \left(1 + \bar{\rho\mu}\delta \sqrt{1 + \frac{2}{\alpha}} \right) e^{-\bar{\rho\mu}\delta \sqrt{1 + \frac{2}{\alpha}}} \right] \right\} \quad [8]$$

where the ratio (δ/R) has been designated by α .

From hypersonic flow theory, α is proportional to the inverse of the shock wave density ratio ρ_s/ρ_∞ , and hence will range in value from $1/0$ to $1/\infty$ for those Mach numbers and altitudes at which the thermal radiation of air becomes important.

The results of Equation [8] can be reduced to the special case of an infinite slab by letting

$$\alpha = \delta/R = 0 \quad [9]$$

since for a slab the radius of curvature R becomes infinite. When this is done, we find that for this special case

$$\lim_{\alpha \rightarrow 0} q_0 = \sigma T_s^4 [1 - 2E_3(\bar{\rho\mu}\delta)] \quad [10]$$

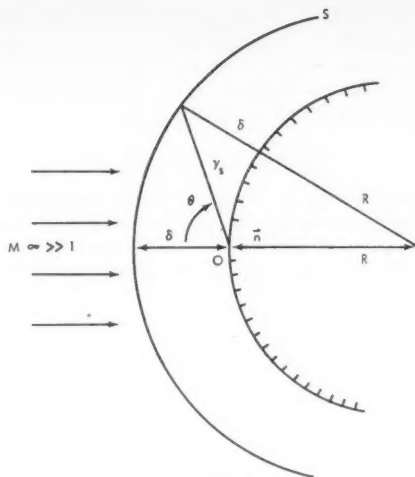


Fig. 1 Spherical cap geometry

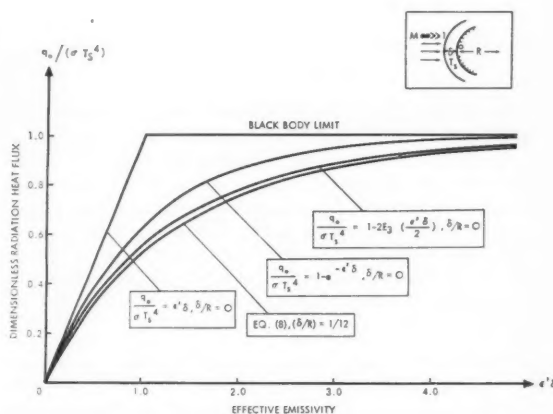


Fig. 2 Exact and approximate behavior of stagnation point radiation flux with the effective emissivity

which is identical with the result obtained by Goulard and Goulard (7) along somewhat different lines.

Utilizing the series expansion for $E_3(\lambda)$

$$E_3(\lambda) = 1/2 - \lambda + \mathcal{O}(\lambda^2 \ln \lambda) \quad [11]$$

it is found that for $\bar{\rho\mu}\delta \ll 1$, Equation [10] reduces to

$$\lim_{\alpha \rightarrow 0} q_0 \cong (2\bar{\rho\mu})\delta\sigma T_s^4, \quad \bar{\rho\mu}\delta \ll 1 \quad [12]$$

By comparing Equations [1 and 12] we identify the frequency averaged absorption coefficient $\bar{\rho\mu}$ as $(\epsilon'/2)$, where ϵ' , it will be recalled, is the emissivity per unit length. This conforms to the definition of ϵ' as given by Meyerott (1) and Kivel (2).

In Fig. 2, the ratio $(q_0/\sigma T_s^4)$, as given by Equation [1, 8 and 10], is plotted against the effective emissivity. For the curved shock layer, a value of $\alpha = 1/12$ was chosen, which cor-

responds to a flight speed of approximately 30,000 fps at an altitude of 36,000 ft. It can be seen that for this particular case the maximum deviation of the slab approximation from the result for the curved shock layer is of the order of 7%.

In conclusion it is interesting to note that the result

$$q_0 = \sigma T_s^4(1 - e^{-\epsilon^0}) \quad [13]$$

obtained by dividing the infinite slab into infinitesimal slabs, each having an absorptivity per unit length equal to its emissivity per unit length, and then integrating over the width of the slab, approximates the correct result to within 20%.

Calibration of Hypersonic High Temperature Wind Tunnels

S. E. NEICE¹ and R. W. RUTOWSKI²

Lockheed Aircraft Corp., Missiles and Space Div.,
Sunnyvale, Calif.

Methods for calibrating hypersonic high temperature wind tunnels, using measured reservoir and stagnation point quantities, along with a Mollier diagram for equilibrium air, are described. Three methods are discussed for the determining of the equilibrium state of the reservoir and stagnation region using different combinations of measured pressure, density and heat transfer rates. Methods for the determination of free stream properties, corresponding to the established reservoir and stagnation conditions are presented.

HYPERSONIC high enthalpy wind tunnels, where air is the testing medium, present unique calibration problems. There are two principal features of the flow in such high enthalpy wind tunnels which make calibration and meaningful interpretation of test results difficult: Air at high temperatures is far from a perfect gas; and dissociation of gas in the high temperature reservoir results in a nonequilibrium free stream (frozen flow) in the test section.

Real gas effects for equilibrium air have been evaluated by Feldman (1).³ Nonequilibrium effects, as regards atomic recombinations of partially dissociated air, have been considered by Bray (2). An important conclusion of Bray's investigations is that stagnation point properties are not greatly affected by nonequilibrium in the free stream. In the range in which most facilities operate, nonequilibrium involves dissociated oxygen combined with a relatively small amount of dissociated nitrogen. Under these conditions only about 25% of the total mixture is frozen. Stagnation pressures and heat transfer rates would, according to Bray, be only slightly affected. In many cases this effect could be neglected.

The charts and graphs of (1), particularly the Mollier diagram, suggest that equilibrium free stream properties could be accurately determined by a combined graphical and iterative procedure, which would make use of measured reservoir properties and properties at the stagnation point of a spherical-nosed model in the test section. The free stream properties, determined in this manner, would not correspond to the existing nonequilibrium free stream conditions, since

References

- 1 Meyerott, R. E., "Radiation Heat Transfer to Hypersonic Vehicles," Third AGARD Combustion and Propulsion Panel Colloquium, Palermo, Sicily, March 17-21, 1958.
- 2 Kivel, B., "Radiation from Hot Air and Stagnation Heating," Avco-Everett Research Laboratory, Everett, Mass., RR 79, Oct. 1959.
- 3 Lighthill, M. J., "Dynamics of a Dissociating Gas. Part 2: Quasi-Equilibrium Theory," *J. Fluid Mech.*, vol. 8, no. 2, June 1960.
- 4 Magee, J. L. and Hirschfelder, J. O., "Thermal Radiation Phenomena," in "Blast Wave," University of California, Los Alamos Scientific Laboratory Rep. no. LA-2000, chap. III.
- 5 Sommerfeld, A., "Thermodynamics and Statistical Mechanics," Academic Press, Inc., N. Y., 1956, p. 151.
- 6 Kourganoff, V., "Basic Methods in Transfer Problems," Oxford, at the Clarendon Press, 1952 Appendix 1, p. 253.
- 7 Goulard, R. and Goulard, M., "One Dimensional Energy Transfer in Radiant Media," *Int. J. Heat and Mass Transfer*, vol. 1, no. 1, June 1960.

most free stream properties are sizably altered by relatively small amounts of "freezing." What would be established, however, is an "effective equilibrium free stream corresponding to the equilibrium stagnation point flow." Measured stagnation point quantities, such as heat transfer rates, would be appropriate to this equilibrium free stream. Such data would be applied to a full-scale body which does travel through an equilibrium medium. Defining the "effective equilibrium free stream" would appear, therefore, to be the appropriate calibration method whenever stagnation properties are considered. It is the purpose of this note to describe certain methods of calibration which make use of the relatively conservative stagnation point properties, pressure and heat transfer rate, certain reservoir properties, and the Mollier diagram for equilibrium air.

Determination of Reservoir and Stagnation Point Properties

Method 1: Using reservoir pressure and density and stagnation point heat transfer rates

This method is particularly applicable to the spark heated type of tunnel. The reservoir density is known, since the dimensions and initial conditions in the arc chamber are known. The reservoir pressure and stagnation point heat rate are measured quantities. Hence, all reservoir properties can be determined, and the reservoir enthalpy also applies to the stagnation point. With this stagnation enthalpy known, we need one other stagnation point property. This can be accomplished from the measured stagnation point heat rate using the expression for the stagnation heat rate as given by Fay and Riddell (3).

$$q_s = 0.94 (\rho_w \mu_w)^{0.1} (\rho_s \mu_s)^{0.4} [1 + (L^{0.52} - 1)(h_D/h_s)] \times (h_s - h_w)(dV_s/dx)^{1/2} \quad [1]$$

where

$$(dV_s/dx)_s = \frac{1}{r} [2(p_s - p_1)/\rho_s]^{1/2} \quad [2]$$

At hypersonic speeds, $p_1 \ll p_s$, and hence Equation [2] can be written as

$$(dV_s/dx)_s = \frac{1}{r} (2p_s/\rho_s)^{1/2} \quad [3]$$

The unknown quantities in Equations [1 and 3] concern only the stagnation properties, if the typical cold wall case is considered. Equations [1 and 3] can be combined, for simplicity of explanation, into the following functional form

$$q_s = q_s(p_s, \rho_s, \mu_s) \quad [4]$$

The stagnation condition can now be evaluated by successive approximations, since each of the unknown stagnation

Received Sept. 6, 1960.

¹ Research Specialist, Gas Dynamics Department. Member ARS.

² Staff Scientist, Gas Dynamics Department.

³ Numbers in parentheses indicate References at end of paper.

quantities, shown in Equation [4], are interrelated. The procedure is to choose a succession of points along the known stagnation enthalpy line and apply the stagnation values at each point to determine the corresponding stagnation heat rate. The point which agrees with the measured heat rate will be the appropriate stagnation condition. The coefficient of viscosity can be evaluated by using Sutherland's expression, including the modification for dissociation effects as evaluated by Hansen (4).

Method II: Using measured reservoir density and pressure, and stagnation pressure

This method may be applied in a manner similar to the previous method, but considerably more simply, since it establishes the stagnation point conditions without an iteration procedure. The measured reservoir pressure and density establish the reservoir condition. The intersection on the Mollier diagram of the reservoir enthalpy and the measured stagnation pressure establishes the stagnation condition.

Method III: Shock tunnel adoption of method II

This method, applicable to shock tunnel operation, is different only in the way the reservoir condition is established. In shock tunnel operation the reservoir is formed by the reflection of the shock wave from the downstream end of the shock tube. From a known initial tube pressure, and the measured velocity of the shock wave just prior to reflection, all reservoir conditions can be evaluated from the Rankine-Hugoniot relationships. Solutions to these are presented graphically in (1). The measured stagnation pressure along with the reservoir (stagnation) enthalpy, establish the stagnation condition.

Determination of the Free Stream Conditions

General method

With established conditions in the reservoir and at the stagnation point, we may now proceed to evaluate the equilibrium free stream condition with the aid of a Mollier diagram. A schematic drawing of a Mollier diagram is shown in Fig. 1 to illustrate the procedure. Reservoir and stagnation conditions are indicated. The free stream, condition 1, lies somewhere along the constant entropy line S_1 . The condition behind the normal shock, condition 2, with an exception which will be discussed later, lies along the constant entropy line S_2 close to the stagnation condition.

A convenient method of solution is to use the conservation of mass, momentum and energy across a normal shock, as expressed in the following equations

$$\bar{V}_2/\bar{V}_1 = \rho_1/\rho_2 \quad [5]$$

$$\bar{p}_2 = \bar{p}_1 + {}_1\bar{p}\bar{V}_1^2[1 - \bar{V}_2/\bar{V}_1] \quad [6]$$

$$\bar{h}_2 = \bar{h}_1 + (\bar{V}_1^2/2)[1 - (\bar{V}_2/\bar{V}_1)^2] \quad [7]$$

Determination of the correct free stream condition from these equations involves a method of successive approximations.

Using \bar{v}_2/\bar{v}_1 as the independent parameter, solve Equation [5, 6 and 7] for a chosen series of free stream points a_1, b_1, c_1 which lie along the reservoir entropy line \bar{S}_r (Fig. 1). A series of points behind the normal shock a_2, b_2, c_2 will be determined which will establish a locus of points crossing the entropy line \bar{S}_n . The correct condition 2 will, of course, be the intersection of this locus and \bar{S}_n .

Approximation for hypersonic low-density flows

When low density hypersonic flow is established in the test section, the assumption of an inviscid isentropic region behind the shock wave no longer holds true. This phenomenon has been demonstrated theoretically and experimentally (5,6,7). The flow process between the shock wave and the stagnation point is similar to that through a well-developed boundary

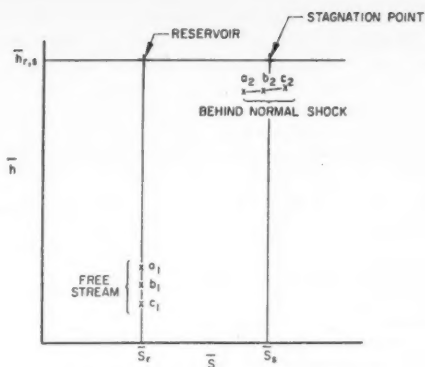


Fig. 1 Schematic Mollier diagram

layer and is neither isentropic nor isoenergetic. For hypersonic flows, however, the difference between conditions behind the shock and the stagnation point is very small. If it is assumed that these two conditions are identical, Equations [5, 6 and 7] can be solved directly for the free stream condition.

Approximation for large expansions

When large expansions from the reservoir to the free stream condition are used, the general method tends to break down. This occurs because the value of the free stream enthalpy h_1 is on the order of the possible error in the evaluation of the stagnation enthalpy h_r . Equation [7] cannot be used unless the errors in any one term are small compared to each of the other terms. In this case, an alternative procedure described by Farmer (8) must be used.

For very large expansions, with resultant high Mach numbers, it is especially true that

$$\bar{p}_1 \ll \bar{p}_2 \quad \bar{V}_2 \ll \bar{V}_1 \quad [8]$$

Therefore, if \bar{p}_1 and \bar{V}_2 are neglected, Equation [6] assumes the form

$$\bar{V}_1^2 \cong \bar{p}_2/\bar{p}_1 \quad [9]$$

It is also true that

$$h_1 \ll (\bar{V}_1^2/2)[1 - (\bar{V}_2/\bar{V}_1)^2] \quad [10]$$

so that Equation [7] can be written as

$$\bar{V}_1^2 \cong 2\bar{h}_r \quad [11]$$

Combining Equation [9 and 11] we obtain

$$\bar{p}_1 \cong 2\bar{h}_r/\bar{p}_2 \quad [12]$$

Equations [11 and 12] permit the evaluation of the free stream velocity and density from the known values of stagnation enthalpy and stagnation pressure. The remaining free stream conditions can be determined on the Mollier diagram from the intersection of the known reservoir entropy and free stream density.

Concluding Remarks

Certain of the procedures discussed here have been applied to the calibration of the Lockheed 3-in. shock tunnel, and are currently being applied to the Lockheed spark heated tunnel. It is felt that such methods involve errors which are within the accuracy of the measured quantities. The flow in some

high enthalpy wind tunnels is undoubtedly frozen to some degree. It should be noted again that a small amount of "freezing" will not appreciably influence stagnation point results. The influence of free stream nonequilibrium on properties along slender bodies or thin wing shapes, however, has not been clearly established as yet, so that interpretation of test data obtained under such conditions must be done with caution.

Nomenclature

h = enthalpy
 \bar{h} = normalized enthalpy, h/RT_0
 L = Lewis number
 p = pressure
 \bar{p} = normalized pressure, p/p_0
 q = heat transfer rate
 r = effective radius of curvature at stagnation point
 R = gas constant
 S = entropy
 \bar{S} = normalized enthalpy, S/R
 T = temperature
 V = velocity
 \bar{V} = normalized velocity, $V/\sqrt{RT_0}$
 x = distance around body for stagnation point
 ρ = density
 $\bar{\rho}$ = normalized density, ρ/ρ_0
 μ = coefficient of viscosity

Subscripts

1 = free stream condition
 2 = condition behind normal shock
 D = dissociation
 e = external flow just outside boundary layer
 0 = standard atmosphere
 r = reservoir
 s = stagnation point
 w = wall condition

References

- 1 Feldman, S., "Hypersonic Gas Dynamic Charts for Equilibrium Air," Avco Res. Lab., Everett, Mass., 1957.
- 2 Bray, K. N. C., "Atomic Recombination in a Hypersonic Wind-Tunnel Nozzle," *J. Fluid Mech.*, vol. 6, Pt. 1, 1959, pp. 1-32.
- 3 Fay, J. A. and Riddell, F. R., "Theory of Stagnation Point Heat Transfer in Dissociated Air," *J. Aeron. Sci.*, vol. 25, no. 2, 1958, pp. 73-85.
- 4 Hansen, C. F., "Approximations for the Thermodynamic and Transport Properties of High Temperature Air," NACA TN 4150, 1958.
- 5 Adama, M. C. and Probstein, R. F., "On the Validity of Continuum Theory for Satellite and Hypersonic Flight Problems at Altitude," *J. Propulsion*, vol. 28, no. 2, Feb. 1958, pp. 86-89.
- 6 Hoshizaki, H., "Shock-Generated Vorticity Effects at Low Reynolds Numbers," Lockheed Missiles and Space Div., Sunnyvale, Calif., LMSD-48379, vol. 1, 1959.
- 7 Neice, S. E., Rutowski, R. W. and Chan, K. K., "Stagnation Point Heat Transfer Measurements in Hypersonic Low Density Flow," *J. Aero/Space Sci.*, vol. 27, no. 5, 1960, pp. 387-389.
- 8 Farmer, A. V., "A Probe for Determining Flow Conditions in a Short-Duration Hypersonic Stream," Lockheed Missiles and Space Division, Sunnyvale, Calif., LMSD 49705, 1959.

Calculation of C^* for Highly Dissociated Propellant Combustion Products

L. J. GORDON¹

Aerojet-General Corp., Sacramento, Calif.

A method of calculation of theoretical C^* values, which is accurate, conservative of calculational effort, and which remains valid for the general nonisentropic flow case, is presented.

IT IS convenient in both theoretical and experimental propellant evaluation, to separate performance values into two parameters C^* and C_F such that

$$I_s = C^* \cdot C_F / g \quad [1]$$

Formulas for theoretical calculation of these parameters for a simple gas are well known. Altman and Carter² show, however, that for combustion gases which are extensively dissociated, C^* can only be calculated accurately from its definition

$$C^* = P_c \cdot A_t / \dot{m} \quad [2]$$

and the continuity equation $\dot{m} = \rho u A_t$. [3]

Throat conditions may be obtained by a stepwise process which determines the expansion pressure at which (ρu) is a maximum, and hence at which A_t is a minimum.

Altman and Carter present a good approximate method of calculation of C^* and C_F using two different values of $\bar{\gamma}$ (one averaged for the chamber throat region, and another averaged over the entire expansion process), but it has become modern

practice with large digital computers to calculate C^* via the stepwise determination of $(\rho u)_{\max}$, although this is a fairly time-consuming process. A procedure for calculating C^* which is somewhat more involved than that of Altman and Carter, which yields values of C^* as accurate as those obtained via $(\rho u)_{\max}$, and is conservative of calculational effort is presented.

Using the normal gas composition iterative process and entropy or enthalpy search routine, calculate for two arbitrarily chosen pressures, say $P_1 = 0.6P_c$ and $P_2 = 0.5P_c$, along the assumed (not necessarily isentropic) flow path the set of values: $P_1, T_1, H_1, \rho_1, u_1$ and $P_2, T_2, H_2, \rho_2, u_2$. Define three parameters K_1, K_2 and c from

$$(P_1/P_2)^{(K_1-1)/K_1} = T_1/T_2 \quad [4]$$

$$P_1/P_2 = (\rho_1/\rho_2)^{K_1} \quad [5]$$

$$(H_1 - H_2)/(T_1 - T_2) = c \quad [6]$$

For any other pressure in the vicinity of P_1 and P_2 , the values of T, ρ and u along the chosen path are then given by

$$T = T_1(P/P_1)^{(K_1-1)/K_1} \quad [7]$$

$$\rho = \rho_1(P/P_1)^{1/K_1} \quad [8]$$

$$u^2 = u_1^2 - 2gc(T - T_1) \quad [9]$$

The throat pressure is that at which (ρu) and hence $\ln(\rho u)$ is a maximum; therefore

$$\frac{d(\ln \rho u)}{dP} = \frac{1}{\rho} \frac{d\rho}{dP} + \frac{1}{u} \frac{du}{dP} = 0 \quad [10]$$

$$\frac{1}{\rho} \frac{d\rho}{dP} = -\frac{1}{u} \frac{du}{dP} \quad [11]$$

$$\frac{1}{\rho} \frac{d\rho}{dP} = -\frac{1}{u} \frac{du}{dT} \cdot \frac{dT}{dP} \quad [12]$$

The derivatives of Equation [12] can be obtained from Equations [7, 8 and 9]. Substitution of these derivatives

Received Oct. 7, 1960.

¹ Senior Engineer, Thermodynamics Section, Solid Rocket Research Div. Member ARS.

² Lewis, B., Pease, R. N. and Taylor, H. S., Editors, "Combustion Processes," vol. II of "High Speed Aerodynamics and Jet Propulsion," Princeton University Press, Princeton, 1956, chap. 2 (by D. Altman and J. M. Carter).

into Equation [12] and rearrangement yields

$$\left[\frac{u_1^2}{gcT_1} + 2 \right] \frac{K_1}{K_2(K_1 - 1)} = \left[\frac{2K_1}{K_2(K_1 - 1)} + 1 \right] \left(\frac{P}{P_1} \right)^{\frac{K_1 - 1}{K_1}} \quad [13]$$

Equation [13] can be solved numerically for $P_t = P$, and Equations [8 and 9] may then be solved for the desired $(\rho u)_{\max}$. If the equilibrium gas composition at the throat is desired, Equation [7] may be solved for $T_t = T$, and then the equilibrium gas composition at T_t and P_t may be calculated.

This procedure is found to be useful even where there are large changes in \bar{M} such as might occur from condensation of a vapor during the expansion. The procedure fails, however, if a liquid-solid phase change is predicted in the throat region.

The values of C^* calculated by this method agree within three significant figures with values calculated via $(\rho u)_{\max}$. In the latter method, it is found that because of the nature of the ρu vs. P curve, it generally takes five or more determinations of ρu along the flow path to determine $\rho u_{(\max)}$. In the method described here one needs to employ the iterative process to determine equilibrium gas composition, the most time-consuming portion of shifting equilibrium flow calculations, only twice to determine the throat conditions.

It is interesting to show a numerical example of the difference between K_1 and K_2 and the variance of \bar{M} with P for a highly dissociated gas. For a liquid oxygen/hydrocarbon mixture ratio of 3.0, the calculated P - T - \bar{M} values are shown in Table 1.

Values of K_1 , K_2 , etc., are found to be

$$\begin{aligned} K_1 &= 1.094 \\ K_2 &= 1.127 \\ C^* &= 5806 \text{ fps} \\ I_s &= 297.0 \\ C_F &= 1.645 \end{aligned}$$

An average $\bar{\gamma}$ for the same propellant, calculated from the

Table 1 Change in molecular weight for shifting equilibrium expansion

	P , psia	T , R	M
Chamber	1000	6662	24.55
Throat	578	6352	24.92
Exhaust	14.7	4716	27.18

chamber-exhaust pressure-temperature values is found to be

$$\bar{\gamma} = 1.089.$$

Using this $\bar{\gamma}$ in the usual formulas yields values of C^* and C_F different from those given in the foregoing and produces a discrepancy in the I_s - C_F - C^* relationship.

It is useful to realize that the procedure described here does not imply that the throat velocity is sonic, since this is true only for isentropic flow. When desired, the procedure can be used to calculate the sonic velocity from its primary definition $a^2 = (dP/d\rho)_s$.

Nomenclature

A_t	= throat area
a	= acoustic velocity
C^*	= characteristic exhaust velocity
C_F	= thrust coefficient
c	= parameter as defined by Equation [6]
g	= gravitational constant
I_s	= propellant specific impulse
K_1	= parameter as defined by Equation [4]
K_2	= parameter as defined by Equation [5]
\dot{m}	= mass flow rate
P_s	= combustion chamber pressure
S	= entropy
u	= gas velocity
γ	= isentropic flow coefficient
ρ	= gas density

Entrance Effects in the High Temperature Heat Transfer From Dissociated Gases¹

P. BRO² and S. STEINBERG³

Avco Research and Advanced Development Div.,
Wilmington, Mass.

Convective heat transfer rates have been measured from a dissociated gas mixture containing H_2 , H , H_2O , CO , HCl , etc., at approximately 6500 F and 1 atm to the walls of a pipe in the gas entrance region at Reynolds numbers of 3360 to 7720. It was found that the standard correlation for fully developed, turbulent-pipe flow predicted the heat transfer rate within 20 per cent in regions as close as approximately 8 diameters from the inlet. Considerably higher heat transfer rates were obtained farther upstream.

IN THE selection of refractory materials for rocket engine applications, it is necessary to consider the susceptibility of these materials to chemical attack by corrosive rocket ex-

hausts from a thermodynamic as well as from a kinetic point of view. At sufficiently high temperatures the rates of gas/solid corrosion reactions may be assumed to be controlled by the rate of mass transfer across the boundary layer at the reacting surface. However, a problem is presented by the geometry of the usual rocket engine systems since no satisfactory, empirical correlations are available for the rate of mass transfer in dissociated gases in the nozzle entrance regions of the rocket engines. In our studies of the surface chemistry of rocket engines, we have based our analysis of the gas/solid reaction kinetics in entrance regions on experimentally determined heat transfer rates. The corresponding mass transfer rates were estimated by means of the analogy between turbulent heat and mass transfer. It is believed that experimental data on entrance effects in the high temperature heat transfer in dissociated gases are of general interest, and we present some of our results in the section which follows.

Experimental Procedure

The corrosive gases were heated to temperatures of 6000 to 7000 F at approximately one atm in a plasma generator similar to one described in the literature,⁴ and the hot gases were thermally equilibrated before they entered the test section shown in Fig. 1. The test section was composed of three

Received Sept. 6, 1960.

¹ This work was performed for the U. S. Air Force under contract AF04(647)-258.

² Asst. Section Chief, Physical Chemistry Section.

³ Senior Scientist, Physical Chemistry Section.

⁴ John, R. R. and Bade, W. L., ARS JOURNAL, vol. 29, 1959, p. 523.

⁵ T. Munson, unpublished results.

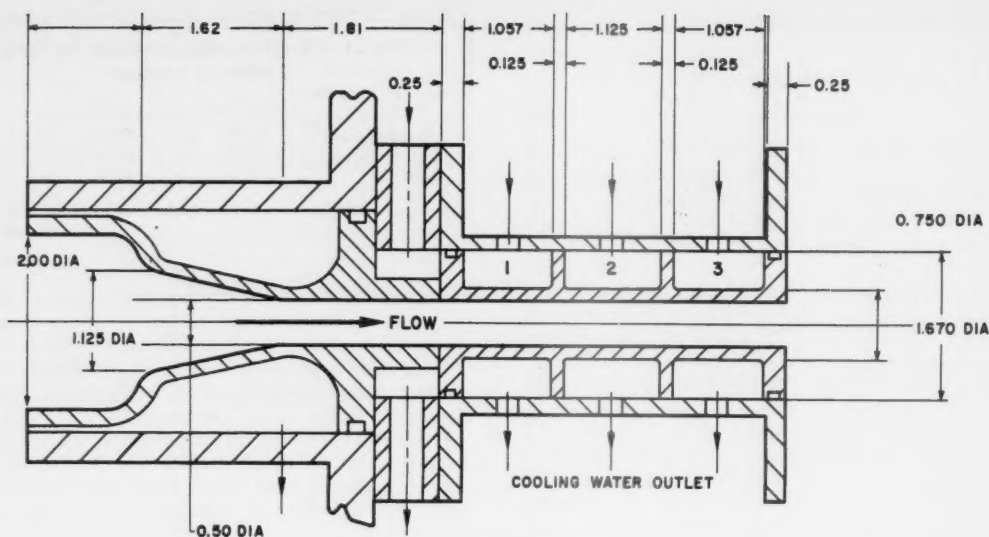


Fig. 1 Test configuration

separately instrumented water cooled calorimeters, and the heat transfer rates to these were measured during runs of 60 sec duration. A steady state heat transfer rate was generally attained in 10 to 15 sec. Complete energy balances were obtained in all the runs, and the enthalpy of the test gas was calculated from the difference between the power input and the energy losses to the various parts of the generator and the gas flow rate.

The thermodynamic properties of the test gases were calculated by T. Munson,⁵ and the main constituents present at 3400 K and 1 atm are shown.

Species	Mole fraction
H ₂	0.2612
H	0.2389
O ₂	0.0007
O	0.0098
H ₂ O	0.0454
OH	0.0169
HCl	0.0758
Cl	0.0462
NO	0.0013
CO	0.2347
CO ₂	0.0051
N ₂	0.0638

The actual composition of the gas differed slightly from this because of carbon injection from the cathode of the plasma generator. Although the added carbon would change the chemical reactivity of the gas, the mass transfer characteristics would remain essentially unchanged.

Experimental Results

The experimentally determined, convective transfer coefficients for the dissociated gas, $q/\Delta H$, are plotted in Figs. 2-4. The best straight lines through the experimental points are fully drawn. Corrections were made in these calculations for the differences in the enthalpy of the gas in the three calorimeters. The Reynolds numbers varied between 3360 and 7720 in the runs reported here, and the results, therefore, pertain to the turbulent flow regime in the 1/2 in. pipe. The observed convective transfer coefficients may be compared with those calculated from one of the correlations for

fully developed turbulent flow

$$q/\Delta H = 0.023 \frac{G}{Re^{0.2} Pr^{0.6}} \quad [1]$$

where

- q = heat transfer rate
- ΔH = enthalpy difference between the gas and the cold wall
- G = mass flow rate in the tube
- Re = Reynolds number
- Pr = Prandtl number

This equation is reduced to $q/\Delta H = 0.0065G^{0.8}$ when we employ a Prandtl number of 0.89 and a viscosity of 5.2×10^{-5}

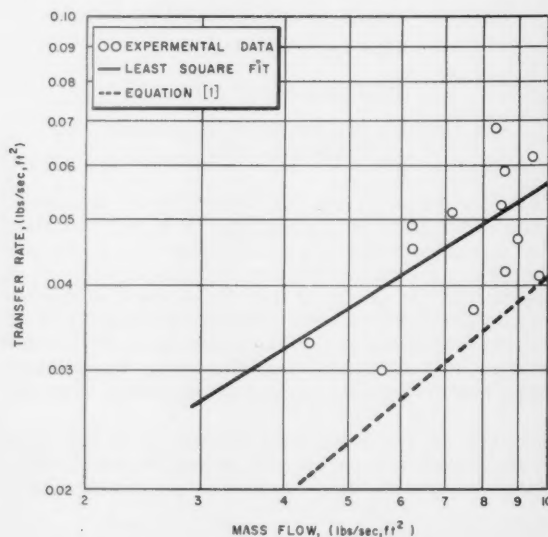


Fig. 2 Transfer rate in section 1

(Continued on page 433)

